Organic Semiconducting Polymers for Organic Electrochemical Transistors with Bioelectronic Applications



Sophie Griggs

Worcester College
University of Oxford

Supervised by
Iain McCulloch
Submitted: Michaelmas Term

16th December 2022

This thesis is submitted to the Department of Chemistry, University of Oxford, in partial fulfilment of the requirements for the degree of Doctor of Philosophy.

I Declaration

The work described in this thesis was carried out in the Department of Chemistry at Imperial College London and in the Department of Chemistry at the University of Oxford between October 2019 and December 2022 under the supervision of Professor Iain McCulloch. I declare that this thesis is entirely my own work, and except where otherwise stated, describes my own research.

Sophie Griggs, December 2022

II Abstract

Organic electrochemical transistors (OECTs) are a promising technology for bioelectronic devices, with applications in neuromorphic computing and sensing in healthcare settings. The active component enabling an OECT is the organic mixed ionic-electronic conductor (OMIEC), the optimisation of which is critical for realising high-performing devices. This thesis further develops structure-property relationships of OMIECs, by exploring their electrochemical activity and OECT performance.

This work aims to understand in greater depth the effectiveness of currently employed approaches, as well as proposing novel design strategies and additional factors that impact the performance of OECTs. By using both a p-type polythiophene and an n-type naphthalene diimide (NDI)-based polymer, the impact of purity and molecular weight were investigated. It was found that whilst molecular weight has negligible impact on OECT performance, the degree of purity, specifically the removal of palladium, is able to improve both OECT performance by over seven times. Next, a novel series of n-type NDI-based copolymers were designed, with the aim of improving the degree of delocalisation, and therefore electron mobility. Reducing the size of the comonomer and improving planarity, by utilising vinyl and alkynyl motifs, was observed to increase the degree of crystallinity and improve the OECT electron mobility by over 200 times compared to the typical thiophene comonomer, to achieve a mobility of 2.40 x 10^{-2} cm^2 V^{-1} s^{-1}. The final series was designed as a model system to better understand the ionic conductivity of OMIECs, by employing the electronically insulating pyromellitic diimide (PMDI) unit for a series of copolymers. By varying the hydrophilic sidechain content and composition, it was found that the capacitance is proportional to the percentage of sidechains that are hydrophilic, providing this segment terminates the sidechain.

III Acknowledgements

I am exceptionally grateful to a number of people from whom I have had the opportunity to learn from and work alongside during my PhD. Without these people, this journey would not have been remotely enjoyable or even possible. Firstly, I want to thank my supervisor, Iain McCulloch, for supporting me throughout my PhD and for encouraging me to think independently and creatively.

I thank Petruta Maria for all her support during the first two years of my PhD, for nurturing my knowledge of OECTs and bioelectronics and for her leadership of the subgroup. I also thank Cath Aitchison for her many hours explaining tricky concepts and providing constant encouragement, particularly when things weren't working. A special mention must also go to Flo Moruzzi for always making time for a chat, providing positive vibes to the entire lab and just generally making my PhD a much more enjoyable experience. Huge thanks to all the other McCulloch group members, especially Ben Willner for his absolutely incredible baking skills and Junfu Tian for always making time to help me out with a new measurement. Thank you to Kate Chamberlain for allowing me to guide her through her MChem project, it was a pleasure to work with her.

I am very grateful for the support of George Malliaras, who allowed me to spend time working with his lab and cleanroom to learn how to fabricate OECT substrates. I also thank Sophia Bidinger and Sanggil Han for their time and patience in showing me these new techniques. Thanks also go to Jonathan Rivnay and his group, particularly Reem Rashid, Dilara Meli, Emily Schafer and Bryan Paulsen for their assistance in measuring my materials and the many fruitful discussions and idea generation sessions we have had over the past three years. Thanks also go to Sahika Inal and her group members, particularly David Ohayon, Jacob Surgailis and

Tania Hidalgo Castillo, for their collaboration over the years in designing and characterising new materials. I also thank Achilleas Savva for his time and knowledge in developing our OECT set up. His on-call troubleshooting and willingness to help was very much appreciated and made the process far smoother. Thank you to Karl Thorley for always having time to run my calculations and providing insightful feedback and explanations along the way. I want to thank Ana De La Fuente Durán for her assistance with galvanostatic measurements and all her time discussing science (particularly electrochemistry) with me. A huge thank you also goes to Tyler Quill, he has not only been the most efficient collaborator but also a great friend over the last year. His time, particularly at the beamline but also in explaining GIWAXS to me for the nth time, is very much appreciated!

Finally, a very special thanks goes to my friends and family who made this PhD possible. To my wonderful friends, especially Beth, Sophie and Sarah, who have always been so supportive of me in everything I do, I couldn't have done this without your encouragement. To my family, Mum, Dad, Will, Grandma and Grandad, thank you for always taking an interest in my PhD even when you have no clue what I'm talking about, and for your constant love and support. No matter how far apart we are, I know you are always at the end of the phone and will do your best to help me solve any problem, I love you always. Lastly, to Adam and our gorgeous dog, Chevy, thank you for always listening to my rants, for celebrating the little wins with me and for reading my thesis cover to cover. I'm honoured to call you both my family and I love you forever.

Contents

I Declaration....2
II Abstract....3
III Acknowledgements....4
IV Abbreviations....9
V Publications....12
Chapter 1....14
1.1 Organic Electronics....15
1.2 Conjugated polymers....15
1.2.1 Introduction to organic semiconducting polymers....15
1.2.2 Charge transport in organic semiconductors....17
1.2.3 Molecular design strategies for tuning conjugated polymer properties....20
1.2.4 Doping of conjugated polymers....25
1.2.5 Synthesis of conjugated polymers....27
1.3 Organic Mixed Ionic-Electronic Conductors....28
1.4 Organic Electrochemical Transistors....30
1.4.1 From Organic Field-Effect to Organic Electrochemical Transistors....30
1.4.2 Performance metrics of an OECT....37
1.5 OECT active layer materials....38
1.5.1 P-type active layer materials....39
1.5.2 N-type active layer materials....44
1.5.3 Applications of OECT active layer materials....50
1.5.4 Design considerations of n-type materials....53
1.6 Thesis aims and outline....55
Chapter 2....58
2.1 General information and attributions....59
2.2 Introduction....59
2.3 Synthesis of the polymers....63
2.4 Molecular weight separation and determination....66
2.5 Properties of the polymers....67
2.5.1 Optoelectronic and physical properties....67
2.5.2 GIWAXS analysis....71
2.5.3 Electrochemical activity in aqueous electrolytes....74
2.5.4 OECT characteristics....77

2.6 Discussion 82
2.7 Conclusion 87
Chapter 3 89
3.1 General information and attributions 90
3.2 Introduction 90
3.3 Density Functional Theory (DFT) calculations 93
3.4 Synthesis of the polymers 98
3.5 Properties of the polymers 111
3.5.1 Optoelectronic and physical properties 111
3.5.2 GIWAXS analysis 113
3.5.3 Electrochemical activity in aqueous electrolyte 115
3.5.4 OECT characteristics 120
3.6 Discussion 125
3.7 Conclusion and future work 126
Chapter 4 129
4.1 General information and attributions 130
4.2 Introduction 130
4.3 Density Functional Theory (DFT) calculations 133
4.4 Synthesis 135
4.4.1 Synthesis of the sidechains 135
4.4.2 Synthesis of the PMDI monomers 137
4.4.3 Synthesis of the bithiophene monomers 138
4.4.4 Synthesis of the polymers 139
4.5 Properties of the polymers 141
4.5.1 Optoelectronic and physical properties 141
4.5.2 GIWAXS analysis 147
4.5.3 Cyclic voltammetry in aqueous electrolyte 151
4.5.4 Galvanostatic charging measurements 155
4.6 Conclusion and future work 158
Chapter 5 161
5.1 General experimental 162
5.2 Synthetic procedures for Chapter 2 168
5.3 Synthetic procedures for Chapter 3 175
5.4 Synthetic procedures for Chapter 4 186
Bibliography 205

Appendix 222
A1 General information and attributions 223
A2 Introduction 223
A3 P-type functionalisable polymer 228
A3.1 Synthesis 228
A3.2 Polymer functionalisation 233
A3.3 Optoelectronic, electrochemical and physical properties 236
A3.4 OECT characteristics 242
A3.5 Proof-of-concept functionalisation data 244
A3.6 Conclusions and future work 247
A4 N-type functionalisable polymer 248
A4.1 Synthesis 248
A4.2 Polymer functionalisation 250
A4.3 Optoelectronic and physical properties 253
A4.4 Electrochemical activity in aqueous media 256
A4.5 OECT characteristics 258
A4.6 Conclusions and future work 259
A5 Experimental procedures for Appendix 261
A5.1 General experimental 261
A5.2 Synthetic procedures for the p-type polymer 261
A5.3 Synthetic procedures for the n-type polymer 271
A6 References 285

IV Abbreviations

δ	chemical shift
λ	wavelength
°	degrees
μ	mobility
Å	angstrom
BT	benzo[c][1,2,5]thiadiazole
br.	broad
C	celsius
C^*	volumetric capacitance
calc.	calculated
CB	chlorobenzene
CV	cyclic voltammetry
d	channel thickness
$Đ$	dispersity
DCM	dichloromethane
DFT	density functional theory
DMF	*N*,*N*'-dimethylformamide
DPP	diketopyrrolopyrrole
DSC	differential scanning calorimetry
EA	electron affinity
E_g	bandgap
EI	electron ionisation
EIS	electrochemical impedance spectroscopy
equiv.	equivalents
EQCM-D	electrochemical quartz crystal microbalance with dissipation monitoring
eV	electron volt
FTIR	Fourier-transform infrared spectroscopy
GIWAXS	grazing incidence wide-angle X-ray scattering
glycol	oligo(ethylene glycol)

g_m	transconductance
g_m'	thickness normalised transconductance
GPC	gel permeation chromatography
HOMO	highest occupied molecular orbital
HRMS	high-resolution mass spectrometry
ICT	intramolecular charge transfer
I_D	drain current
IP	ionisation potential
IR	infrared
ITO	indium tin oxide
J	coupling constant
L	channel length
LUMO	lowest unoccupied molecular orbital
m/z	mass to charge
MALDI	matrix-assisted laser desorption/ionization
MeCN	acetonitrile
MeOH	methanol
M_n	number averaged molecular weight
MS	mass spectrometry
M_w	weight averaged molecular weight
NBS	*N*-bromosuccinimide
n-BuLi	*n*-butyllithium
NDI	naphthalene diimide
NDTI	naphthodithiophene diimide
NIR	near-infrared
NMR	nuclear magnetic resonance
NTI	naphtho[2,3-b]thiophene diimide
OECT	organic electrochemical transistor
OFET	organic field effect transistor
OLED	organic light emitting diode
OMIEC	organic mixed-ionic electronic conductor
OPV	organic photovoltaics
ORR	oxygen reduction reaction

OSC	organic semiconductor
P(*o*-tol)$_3$	tri(*o*-tolyl)phosphine
$Pd_2(dba)_3$	tris(dibenzylideneacetone)dipalladium(0)
PESA	photoelectron spectroscopy in air
PPh_3	triphenylphosphine
PMDI	pyromellitic diimide
Ppm	parts per million
redox	oxidation-reduction reaction
Rpm	revolutions per minute
S_N2	second-order nucleophilic substitution
S_NAr	nucleophilic aromatic substitution
T2	bithiophene
$TBAPF_6$	tetrabutylammonium hexafluorophosphate
T_d	decomposition temperature
TGA	thermogravimetric analysis
THF	tetrahydrofuran
TLC	thin layer chromatography
ToF	time-of-flight
Ts	tosyl
UV-Vis	ultraviolet-visible
v/v	volume by volume
V_D	drain voltage
V_G	gate voltage
V_T	threshold voltage
W	channel width

V Publications

(1) **S. Griggs**, A. Marks, H. Bristow, and I. McCulloch, N-Type Organic Semiconducting Polymers: Stability Limitations, Design Considerations and Applications. *J. Mater. Chem. C* **2021**, *9* (26), 8099–8128. https://doi.org/10.1039/D1TC02048J.

(2) A. A. Szumska, I. P. Maria, L. Q. Flagg, A. Savva, J. Surgailis, B. D. Paulsen, D. Moia, X. Chen, **S. Griggs**, J. T. Mefford, R. B. Rashid, A. Marks, S. Inal, D. S. Ginger, A. Giovannitti, J. Nelson, Reversible Electrochemical Charging of N-Type Conjugated Polymer Electrodes in Aqueous Electrolytes. *J. Am. Chem. Soc.* **2021**, *143* (36), 14795–14805. https://doi.org/10.1021/jacs.1c06713.

(3) R. B. Rashid, W. Du, **S. Griggs**, I. P. Maria, I. McCulloch, and J. Rivnay, Ambipolar Inverters Based on Cofacial Vertical Organic Electrochemical Transistor Pairs for Biosignal Amplification. *Sci. Adv.* **2021**, *7* (37). https://doi.org/10.1126/sciadv.abh1055.

(4) M. Moser, Y. Wang, T.C. Hidalgo, H. Liao, Y. Yu, J. Chen, J. Duan, F. Moruzzi, **S. Griggs**, A. Marks, N. Gasparini, A. Wadsworth, S. Inal, I. McCulloch, W. Yue, Propylene and Butylene Glycol: New Alternatives to Ethylene Glycol in Conjugated Polymers for Bioelectronic Applications. *Mater. Horizons* **2022**, *9* (3), 973–980. https://doi.org/10.1039/D1MH01889B.

(5) A. Marks*, **S. Griggs***, N. Gasparini, and M. Moser, Organic Electrochemical Transistors: An Emerging Technology for Biosensing. *Adv. Mater. Interfaces* **2022**, *9* (6), 2102039. https://doi.org/10.1002/admi.202102039.

(6) A. Marks, X. Chen, R. Wu, R. B. Rashid, W. Jin, B. D. Paulsen, M. Moser, X. Ji, **S. Griggs**, D. Meli, X. Wu, H. Bristow, J. Strzalka, N. Gasparini, G. Costantini, S. Fabiano, J. Rivnay, I. McCulloch, Synthetic Nuances to Maximize N-Type Organic Electrochemical Transistor and Thermoelectric Performance in Fused Lactam Polymers. *J. Am. Chem. Soc.* **2022**, *144* (10), 4642–4656. https://doi.org/10.1021/jacs.2c00735.

(7) J. Gladisch, V. K. Oikonomou, M. Moser, **S. Griggs**, I. McCulloch, M. Berggren, E. Stavrinidou, An Electroactive Filter with Tunable Porosity Based on Glycolated Polythiophene. *Small Sci.* **2022**, 2100113. https://doi.org/10.1002/SMSC.202100113.

(8) S. T. M. Tan, G. Lee, I. Denti, G. LeCroy, K. Rozylowicz, A. Marks, **S. Griggs**, I. McCulloch, A. Giovannitti, A. Salleo, Tuning Organic Electrochemical Transistor Threshold Voltage Using Chemically Doped Polymer Gates. *Adv. Mater.* **2022**, 2202359. https://doi.org/10.1002/adma.202202359.

(9) I. P. Maria, **S. Griggs**, R. B. Rashid, B. D. Paulsen, J. Surgailis, K. Thorley, V. N. Le, G. T. Harrison, C. Combe, R. Hallani, A. Giovannitti, A. F. Paterson, S. Inal, J. Rivnay,, I. McCulloch, Enhancing the Backbone Coplanarity of n-Type Copolymers for Higher Electron Mobility and Stability in Organic Electrochemical Transistors, *Chem. Mater.* **2022**, *34* (19), 8593-8602. https://doi.org/10.1021/acs.chemmater.2c01552.

(10) X. Wu, S. Chen, M. Moser, A. Moudgil, **S. Griggs**, A. Marks, T. Li, I. McCulloch, W. Lin Leong, High Performing Solid-State Organic Electrochemical Transistors Enabled by Glycolated Polythiophene and Ion-Gel Electrolyte with a Wide Operation Temperature Range from −50 to 110 °C, *Adv. Funct. Mater.* **2022**, 2209354.

https://doi.org/10.1002/adfm.202209354.

(11) J. Song, G. Tang, J. Cao, H. Liu, Z. Zhao, **S. Griggs**, A. Yang, N. Wang, H. Cheng, C. K. Liu, I. McCulloch, F. Yan, Perovskite Solar Cell-Gated Organic Electrochemical Transistors for Flexible Photodetectors with Ultrahigh Sensitivity and Fast Response, *Adv. Mater.* **2022**. https://doi.org/10.1002/adma.202207763.

(12) **S. Griggs**, A. Marks, D. Meli, G. Rebetez, O. Bardagot, B. D. Paulsen, H. Chen, K. Weaver, M. I. Nugraha, E. A. Schafer, J. Tropp, C. M. Aitchison, T. D. Anthopoulos, N. Banerji, J. Rivnay, I, McCulloch, The effect of residual palladium on the performance of organic electrochemical transistors, *Nat. Commun.*, **2022**, *13* (1), 7964. https://doi.org/10.1038/s41467-022-35573-y.

(13) J. Song, H. Liu, Z. Zhao, X. Guo, C. Liu, **S. Griggs**, A. Marks, Y. Zhu, H. K. Law, I. McCulloch, F. Yan, 2D metal-organic frameworks for ultraflexible electrolyte-gated transistors with high transconductance and fast response speeds, *Sci. Adv.*, **2023**, *9* (2), eadd9627. https://doi.org/10.1126/sciadv.add9627.

(14) H. Chen, S. Y. Jeong, J. Tian, Y. Zhang, D. Naphade, M. Alsufyani, W. Zhang, **S. Griggs**, H. Hu, S. Barlow, H. Y. Woo, S. R. Marder, T. D. Anthopoulos, I. McCulloch, Y. Lin, A 19% efficient and stable organic photovoltaic device enabled by a guest nonfullerene acceptor with fibril-like morphology, *Energy Environ. Sci.*, **2023**. https://doi.org/10.1039/d2ee03483b

(15) D. Ohayon, D. Renn, S. Wustoni, K. Guo, V. Druet, A. Hama, X. Chen, I. P. Maria, S. Singh, **S. Griggs**, B. C. Schroeder, M. Rueping, I. McCulloch, S. Inal, Interactions of Catalytic Enzymes with n-Type Polymers for High-Performance Metabolite Sensors, *ACS Appl. Mater. Interfaces*, **2023**, *15* (7), 9726–9739. https://doi.org/10.1021/acsami.2c20502

(16) G. M. Matrone, E. R.W. van Doremaele, **S. Griggs**, G. Ye, I. McCulloch, F. Santoro, Y. van de Burgt, Organic neuromorphic spiking circuit for retina-inspired sensory coding and neurotransmitter-mediated neural pathways, **2022**, submitted.

(17) I. Uguz, D. Ohayon, A. Taal, **S. Griggs**, R. Sheelamanthula, I. McCulloch, S. Inal, K. L. Shepard, Tunable Electrical Characteristics of Organic Electrochemical Transistors for Complementary Operation in Front-end Amplifier Circuits Integrated in Flexible Neural Implants, **2022**, submitted.

(18) I. Uguz, D. Ohayon, V. Arslan, R. Sheelamanthula, **S. Griggs**, I. McCulloch, S. Inal, K. L. Shepard,' A Flexible and Switch-Matrix Addressable Active Electrode Array Based on Complementary Organic Electrochemical p-n Diode and Transistor Technology, **2022**, submitted.

(19) A. D. L. F. Duran, A. Y. L. Liang, I. Denti, H. Yu, D. Pearce, A. Marks, E. Penn, K. Weaver, L. Turaski, I. P. Maria, **S. Griggs**, X. Chen, A. Salleo, W. C. Chueh, J. Nelson, A. Giovannitti, J. T. Mefford, Origins of hydrogen peroxide selectivity during oxygen reduction on organic mixed ionic-electronic conducting polymers, **2022**, submitted.

(20) V. Druet, D. Ohayon, C. E. Petoukhoff, Y. Zhong, N. Alshehri, A. Koklu, P. D. Nayak, L. Salvigni, L. Almulla, J. Surgailis, **S. Griggs**, I. McCulloch, F. Laquai, S. Inal, A single n-type semiconducting polymer-based photo-electrochemical transistor, **2023**, submitted.

Chapter 1

Introduction

1.1 Organic Electronics

The demand for electronic devices with flexible and low-cost components has led to huge advances in the field of organic electronics in the last few decades, with numerous commercial applications for organic light emitting diodes (OLEDs). OLEDs are found in virtually every area of lighting, including smartphones and televisions,[1–3] whilst electrochromic displays have been demonstrated in Boeing's dimmable windows.[4] Organic semiconductors (OSCs) also have a wide range of other usages, including in organic photovoltaics (OPV),[5] field-effect transistors (OFET)[6] and organic thermoelectric (OTE) generators,[7] among others. Whilst in many of these cases, OSCs are not able to outperform their inorganic counterparts, an emerging area of bioelectronics looks to capitalise on the specific advantages of organic materials, such as their flexibility and compatibility with biological media. The field of organic bioelectronics aims to couple organic electronics with biological systems for healthcare monitoring, diagnostics and therapy.

1.2 Conjugated polymers

1.2.1 Introduction to organic semiconducting polymers

Traditionally, an inorganic semiconductor is best understood by explaining the concept of band structure, which sets out a model of bonding and conduction (**Figure 1.1(a)**).[8] Chemical bonding occurs through a collection of overlapping molecular orbitals (MOs), along which electrons are delocalised. These MOs, broadly speaking, have a bonding or an anti-bonding character and are more commonly called the valence band and the conduction band, respectively, with the separation between the bands known as the bandgap (E_g).

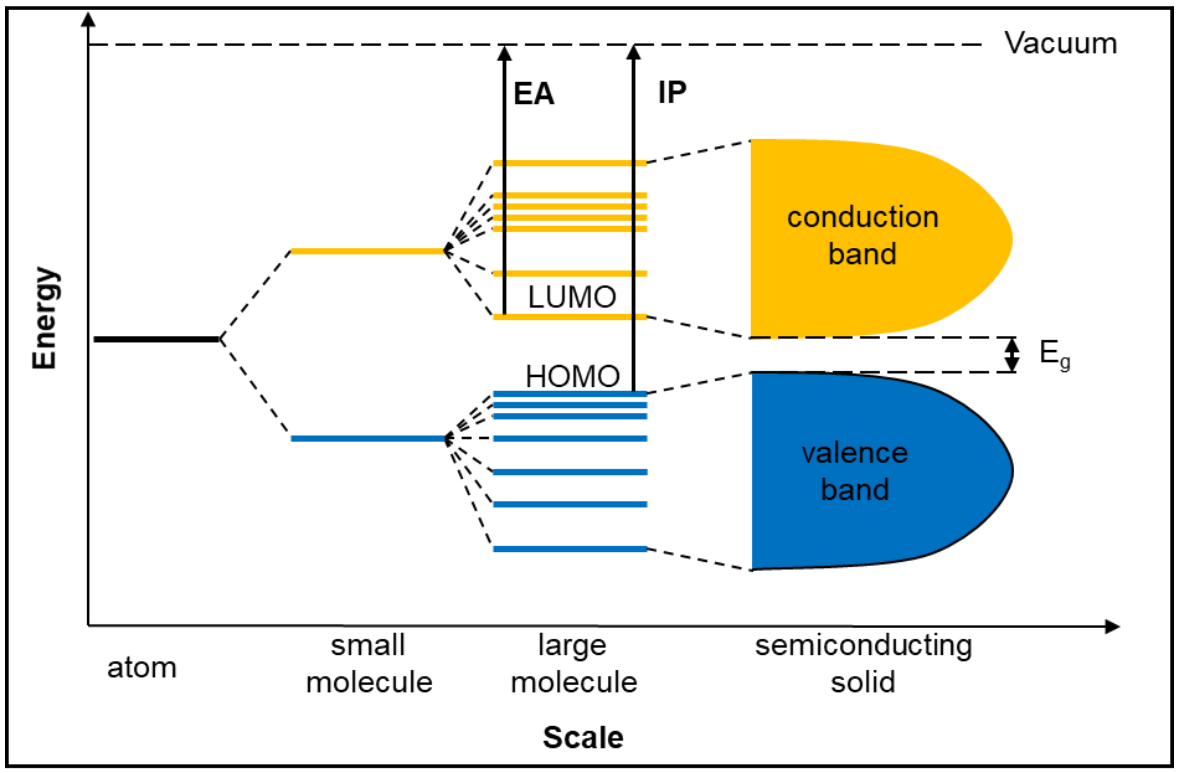


Figure 1.1. Energy level diagram (excluding electrons) to show how energy levels differ with the scale of a material, from an atom to a semiconducting solid. The blue levels represent orbitals with a bonding character, while yellow represent antibonding character.[9]

This model can be adapted to organic materials by dissecting the bands into their constituent molecular orbitals. The defining factor of an organic semiconductor is a series of alternating single and double bonds, comprised of sp^2-hybridised centres. The remaining unhybridised p_z orbitals sit perpendicular to the σ-framework and overlap, to create a π-framework. As an organic material extends from a small molecule to a conjugated polymer, band theory becomes more applicable as the material has more sp^2-hybridised centres, and the previously discrete energy levels begin to "blur". An extended π-framework causes a broadening of the highest occupied and lowest unoccupied molecular orbitals (HOMO and LUMO, respectively), and moves the organic material towards the model of electronic bands traditionally used for inorganic semiconductors, where the HOMO correlates to the valence band, and the LUMO to the conduction band (**Figure 1.1**).[10,11] The energy between these, the band gap, is a material

property that is exploited by optoelectronic devices as it corresponds to the wavelength of light required to promote electrons from the HOMO to the LUMO (absorption) and the wavelength of light released upon radiative decay (emission). Organic semiconductors typically absorb light in the visible part of the spectrum, resulting in band gaps between 1 and 4 eV.[12]

As an approximation, the HOMO can be estimated as the ionisation potential (IP, the energy required to remove an electron from the valence band) and the LUMO as the electron affinity (EA, the energy released when an electron is added to the conduction band of a neutral molecule),[10,11] where the energy difference is an estimate of the band gap.[13] In organic polymers, the band gap decreases as the degree of polymerisation increases, until the effective conjugation length is reached, at which point, the band gap remains constant regardless of increasing polymer chain length.[14]

Organic semiconductors are materials that can act as both an insulator and a conductor, with "switching" between these two states typically occurs via doping. Naturally occurring (semi)conducting organic materials have an excess of either electrons or holes with which they are able to transport charge.[8,15] However, most organic materials are relatively good insulators in their pristine states, and rely upon doping, which introduces either electrons into the conduction band (LUMO) or holes into the valence band (HOMO), giving rise to electrical conductivity.

1.2.2 Charge transport in organic semiconductors

Charge carrier mobility (μ) is a measure of the speed at which charges can be transported under an applied electric field and is the main performance measure of a semiconductor. Charge can be transported through polymeric OSC materials via both intrachain or interchain transport, facilitated by the delocalised π-framework and π-π stacking, respectively (**Figure 1.2**). Intrachain transport is the dominant mode of transport in conjugated polymers, so charge

mobility is limited by interchain transport. As such, the ease of interchain transport is measured by the interchain transfer integral, *t*, and is associated with the splitting of an energy level when going from a solitary chain to a multi-chain system.[16]

Due to the weak van der Waals interactions between polymer chains, the degree of delocalisation of charge carriers is mainly limited by structural disorder,[17,18] rather than charge diffusion across molecules through delocalised wavefunctions, as described by the Boltzmann band model.[17,19,20] In this case, interchain charge transport occurs via a series of thermally activated "hops". There have been some examples identified of an intermediate regime, whereby there is a transient localisation of charge on timescales shorter than that of intermolecular vibrations, indicating this would provide a faster mode of charge transport.[18,21]

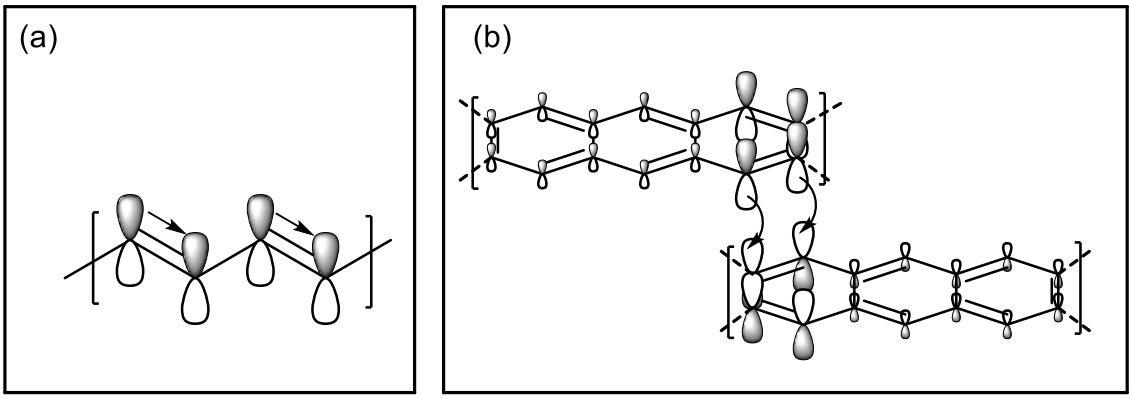


Figure 1.2. (a) Intrachain charge transport along a conjugated polymer backbone and (b) Interchain charge transport between two sections of conjugated aromatic polymer backbones, through the hybridised π-framework.

The efficiency of charge transport is governed by a number of factors aside from temperature, including but not limited to, the molecular weight of the polymer,[22] charge carrier density[23] and the molecular packing and disorder.[19] The most relevant of these factors for the work in **Chapter 2** of this thesis is the impact of polymer molecular weight on the performance of a material. The interrelated nature of molecular weight and performance (usually observed

through the charge carrier mobility) can be explained by noting that longer polymer chains act as connectors between crystalline regions within the microstructure, as well as increasing the chance of forming tie chains (**Figure 1.3**).[24,25] Without these, clear paths between ordered domains are limited and mobility is greatly reduced. This trend can be seen with the material poly(didodecylquaterthiophene-alt-didodecylbithiazole) (**PQTBTz-C12**), where an increase in molecular weight from 13 to 41 kDa resulted in a three-fold increase in mobility.[22] The same trend has also been seen with poly(3-hexylthiophene) (**P3HT**), where a ten-times increase in the degree of polymerisation resulted in a four-fold increase in hole mobility.[26]

Organic semiconducting polymers commonly consist of regions of crystallinity of both long- and short-range order, dispersed within an amorphous matrix (**Figure 1.3**).[27] Charge transport occurs preferentially throughout the most ordered regions as much as possible to avoid the large energy barrier associated with charge moving from ordered to amorphous regions. As such, materials that efficiently transport charge generally contain significant portions of high order, with short connecting sections of amorphous material, or with tie-chains, bridging the ordered domains.[17,28,29] However, transport through disordered regions is unavoidable and often creates a bottleneck for charge transport in organic semiconductors.

An example of a high-mobility n-type polymer is the branched NDI derivate poly{[*N*,*N'*-bis(2-octyldodecyl)naphthalene-1,4,5,8-bis(dicarboximide)-2,6-diyl]-alt-5,5'-(2,2'-bithiophene)} (**p(NDI2OD-T2)**), where large regions of crystallinity have been observed.[30] This polymer also takes advantage of a face-on packing texture, with the aromatic polymer backbones stacked directly on top of each other, parallel to the substrate. This provides a readily available hopping mechanism between chains, due to a stronger orbital overlap and interchain interaction. In summary, more efficient packing leads to short close contact distances, improving charge carrier transport, which is recorded as higher mobilities.[31,32–35] Factors which may alter the

packing of a material include strong dipole-dipole interactions[36,37] and the planarity or the polymer backbone, which can be controlled via steric locking.[38,39]

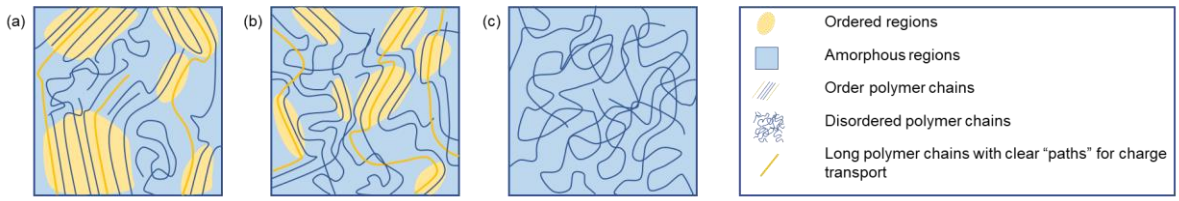


Figure 1.3. Graphic representation of the microstructure of a variety of polymeric materials. (a) Semi-crystalline polymer, (b) partial order due to short-range aggregates and (c) an amorphous structure. The yellow shading indicates ordered regions, and long polymer chains, indicated in yellow, represent clear "paths" for charge transport, significantly improving charge transport. Figure adapted from literature.[40]

1.2.3 Molecular design strategies for tuning conjugated polymer properties

The first synthetic technique for tuning the energy levels of a conjugated polymer is through the selection of the conjugated building blocks. These usually include aromatic motifs, such as benzene or thiophene. Aromatic units exhibit two different resonance forms, the aromatic and the quinoidal form (**Figure 1.4**), whereby the quinoidal structure is more planar due to the double bond character between the cyclic portions. The aromatic form is energetically more stable than the quinoidal, thus aromatic moieties with a greater affinity to the quinoidal resonance structure have destabilised energy levels, raising the HOMO and lowering the LUMO energy levels.[41] When comparing polythiophene with polybenzene, a single thiophene has a lower resonance stabilisation energy than a single benzene (122 kJ mol^{-1} *c.f.* 152 kJ mol^{-1}) thus the true structure of polythiophene has a more quinoidal structure, making it more planar, with an increased degree of delocalisation, than polybenzene.

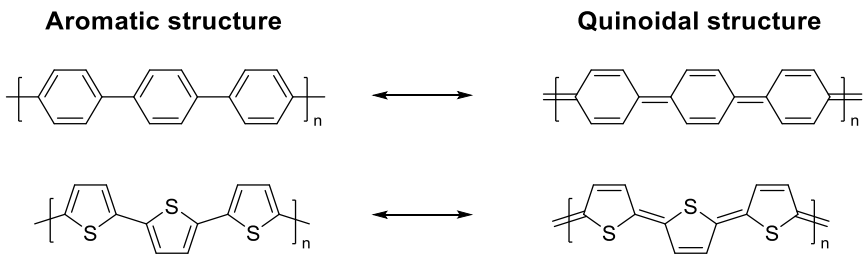


Figure 1.4. Equilibria of polyphenylene and polythiophene between the aromatic and quinoidal structures.

Another key consideration for extending the conjugation length is the planarity of the polymer backbone, as this is a requirement for aromaticity. Where aromatic units are linked by single σ-bonds, steric requirements of bulky units may lead to a backbone twist, which inhibits the conjugation. This issue can be highlighted by examining the coupling of two benzene rings compared to two thiophene rings. The benzene rings results in a relatively large torsional angle of 35-45°,[42] while this is reduced for the bithiophene counterpart, to ~25°.[43,44] This is on account of the hydrogen atoms in the *ortho* positions of the benzene rings sterically "clashing", which is largely relieved when a five-membered thiophene ring is used instead. This could also reflect a greater tendency for delocalisation as noted above.

The most common type of OSC polymers consist of an alternating electron rich donor and an electron deficient acceptor component, predominantly due to the early applications of OSC polymers. These materials were designed to mimic silicon, thus the bandgap was required to be as narrow as possible (~1.1 eV). Perturbation theory dictates that the orbitals of donor-acceptor polymers (also known as "push-pull" polymers) hybridise by combining the HOMOs and the LUMOs of the constituent monomers, redistributing their energy levels and in turn the energy of the occupying electrons, narrowing the bandgap (**Figure 1.5**).[45,46] As shown by numerous DFT calculations, the HOMO wavefunction is usually distributed along the polymer backbone, while the LUMO wavefunction is generally much more localised on the acceptor monomer.[47,48] This enables synthetic control and optimisation of these energy levels with

relative ease and specificity by modifying the relevant location of the molecule to tune the associated energy level and/or bandgap of the material to suit the application.

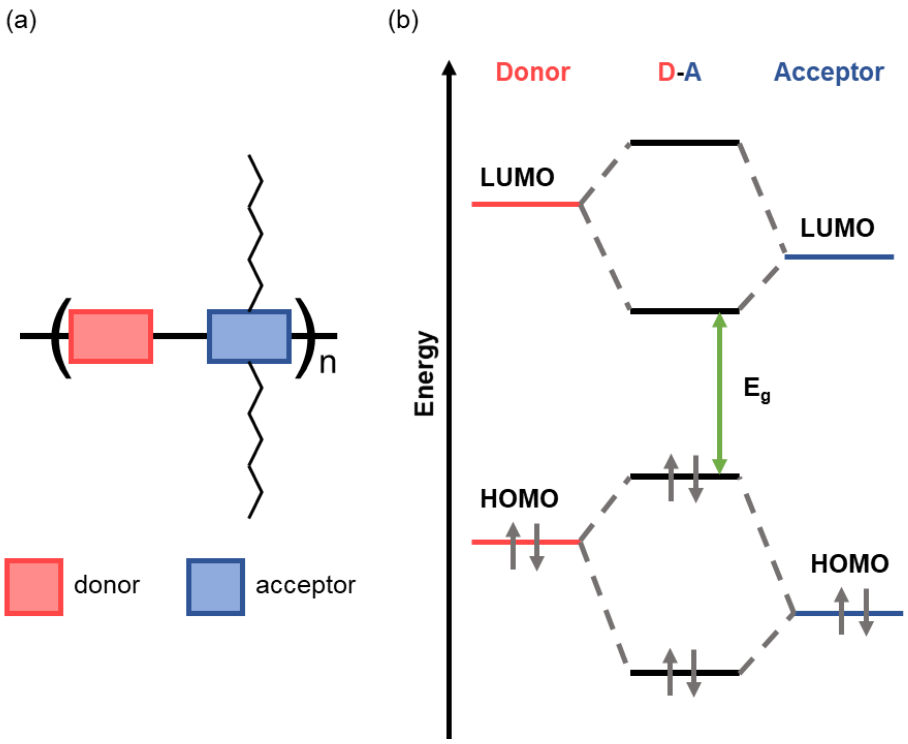


Figure 1.5. (a) Schematic of a donor-acceptor ("push-pull") polymer and (b) molecular orbital diagram to demonstrate the impact of synthesising a donor-acceptor copolymer from a donor and an acceptor unit, indicating the resultant HOMO resembles that of the donor and the LUMO that of the acceptor.

Some typical cores that have been employed to achieve the donor-acceptor conjugated polymer backbone structure include thiophene (T) and bithiophene (T2),[49] naphthalenediimide (NDI),[50] diketopyrrolopyrrole (DPP),[51] lactam[52] and isoindigo (**Figure 1.6**).[53]

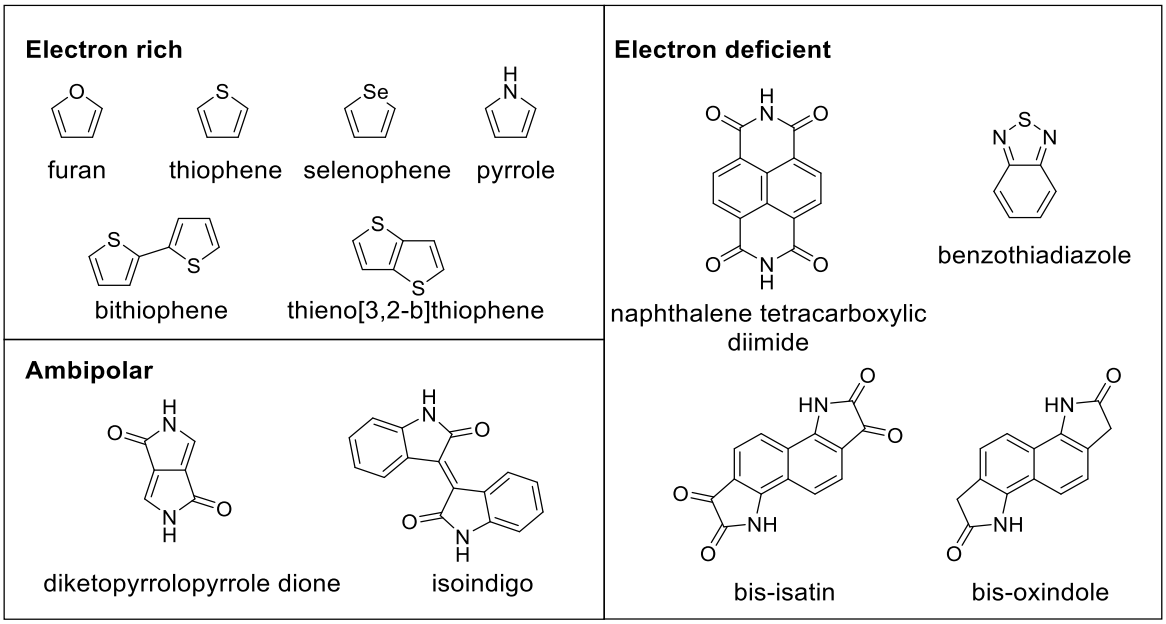


Figure 1.6. Typical electron rich, ambipolar and electron deficient building blocks for the synthesis of conjugated polymers.

Further synthetic techniques for manipulating a polymer's energetics include: extending the conjugation length,[54,55] increasing backbone planarisation through backbone rigidity or non-covalent interactions,[38,56,57] introducing heteroatoms into the polymer backbone,[58–60] adding electron donating or withdrawing groups to manipulate the HOMO or LUMO levels[61,62,60] and including solubilising sidechains to control packing into a highly ordered arrangement (**Figure 1.7**).[63,54]

Extending the conjugation length can be achieved by increasing the number of atoms per monomer over which the conjugation extends.[64] Rigidification of the polymer backbone can also lead to an increased conjugation length by increasing the planarity of a polymer. There are a number of strategies for this, such as introducing intra-chain planarising interactions[65,66] or linking monomers with inflexible double bonds, conformationally locking the backbone.[52] This both reduces the bandgap and also reduces backbone disorder, thus aiding the intermolecular close packing of chains and improving charge transport throughout the material.[38] The use of heteroatoms throughout the backbone can also be used to alter electron density, with research

commonly focussing on the chalcogens. Here, the trend observed is a deepening of the LUMO level when descending the group on account of the increasing C-X bond length.[59,60]

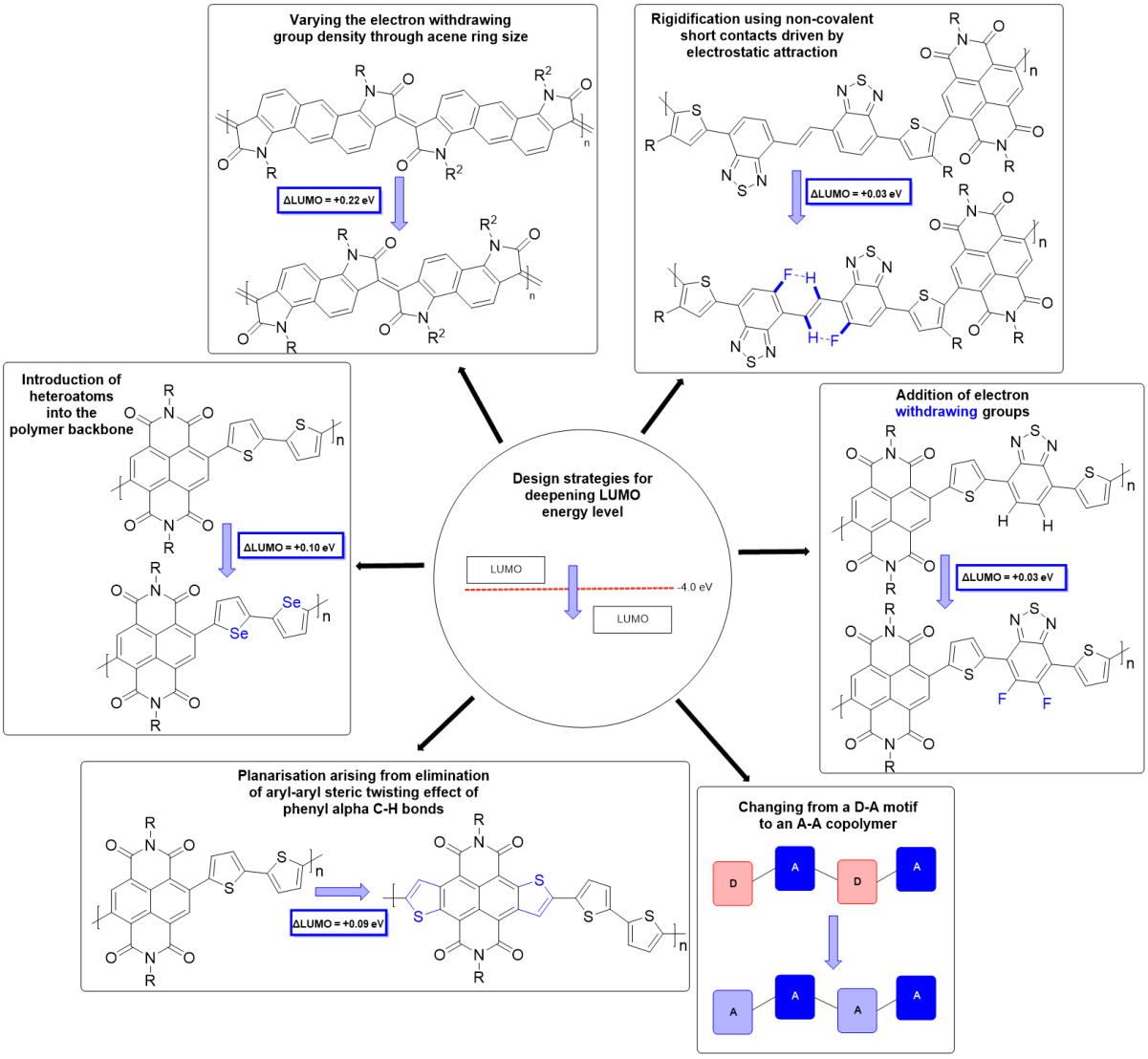


Figure 1.7. Summary of design strategies improve n-type stability by deepening the LUMO level. Figure taken from literature.[40]

Electron donating or withdrawing groups can also be used to almost exclusively either raise the HOMO or lower the LUMO energy levels, respectively, through either inductive or resonance effects. Electron donating groups include: alkyl, alkoxy, alkylthio, amine and aryl groups, while examples of electron withdrawing substituents are: nitro, carboxyl, halogeno, sulfo or cyano functionalities. These groups can also be combined with the use of alternating

donor and acceptor monomers, to increase the electron density of the donor or reduce the electron density of the accepting component.[67]

It should be noted that while a minimum degree of solubility is crucial for both the synthesis (to achieve high molecular weight materials) and device fabrication of a polymer (to allow solution processing, such as inkjet printing or spin coating), sidechains also impact the optoelectronic properties. Notably, the addition of alkyl chains act to donate electron density and typically raise the HOMO level of the polymer. This must be accounted for in the polymer design, with a material that seeks to balance the optoelectronic effects of such sidechains with the necessity of a soluble backbone. Other solubilising sidechains have also been explored in the field of OSCs,[68] including those with ionic functionalities,[69] hydrosilanes[70] and most notably oligo(ethylene glycol) ("glycol") chains,[71–73] which will be employed throughout this thesis as they are most applicable for use in OECTs.

1.2.4 Doping of conjugated polymers

A semiconductor is a material that can act as both a conductor and an insulator, and this is typically controlled through a process referred to as doping. Doping is the concept of introducing unpaired charges, either by removing electrons from the HOMO to create holes (p-doping or oxidation) or by inserting electrons into the LUMO (n-doping or reduction). Further classification can also be made to denote how the charges are introduced to the material, namely chemically or electrochemically.

More specifically, chemical doping occurs from an electron transfer between the conjugated polymer and a dopant molecule. This process can take place either in solution or in the solid state. In the former, the dopant and polymer are dissolved in a solvent of choice, which results in the oxidation or reduction of the polymer. The material is then processed from solution to deposit a film as normal, however as the dopant remains present, the polymer microstructure

can be greatly disrupted, reducing the order of the film, thus reducing charge transport properties.[12,74] The latter process avoids this and the deposited thin film is treated with dopants in the vapour phase (vapour deposition) to allow the dopant to diffuse into the bulk of the conjugated polymer, where oxidation or reduction can take place.[74]

On the other hand, electrochemical doping occurs when an electron transfer takes place between a semiconductor and a metal electrode, leaving a residual charge in the semiconductor (**Figure 1.8**). Charge neutrality across the semiconductor is maintained in this case by the presence of ions in the electrolyte compensating the electronic charges in the semiconductor. The mode of doping depends on the application of the semiconductor, where chemical doping is preferred for thermoelectric generators, whilst electrochemical doping is required in transistor applications.[75]

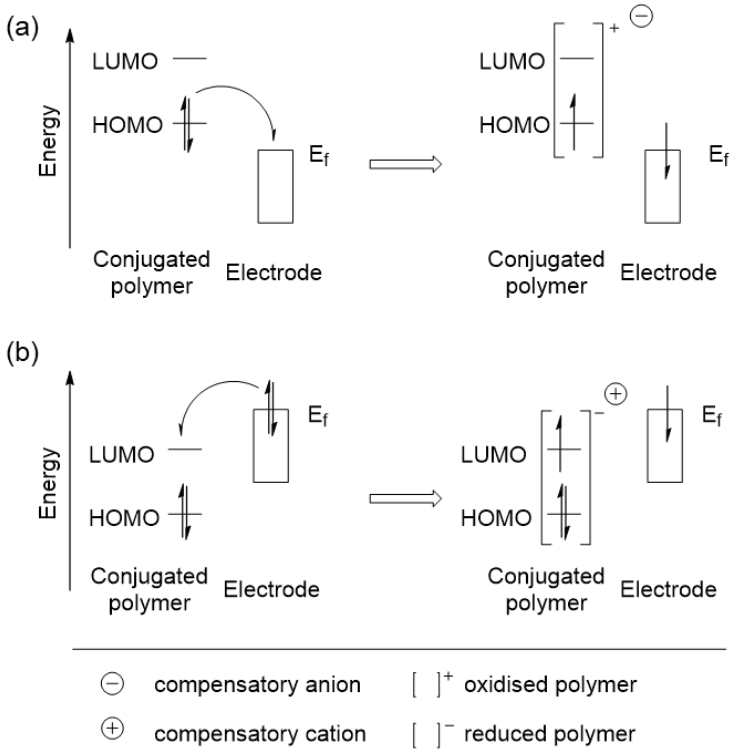


Figure 1.8. Mechanism of electrochemical doping for (a) p-type and (b) n-type conjugated polymer, indicating the oxidised or reduced polymer and the associated compensatory ion. E_f is the Fermi energy of the electrode.

1.2.5 Synthesis of conjugated polymers

Solution-based C-C coupling reactions tend to be favoured due to the method's versatility, enabling access to a great variety of structures.[11] Whilst oxidative polymerisations[76–78] and, more recently, Grignard Metathesis (GRIM)[79,80] are favoured for highly regioregular homopolymers, such as poly(3-alkylthiophenes), to date, the majority of conjugated polymers have been synthesised by palladium cross-couplings, namely Stille[81] and Suzuki[82] (**Figure 1.9**). These techniques have been demonstrated to be compatible with a huge number of aromatic moieties, giving rise to a wide range of both homo- and copolymers. Stille couplings confer good tolerance to a range of functional groups, though depend upon highly toxic organo-tin reagents.[81] On the other hand, Suzuki polymerisations utilise the typically non-toxic boronic acid functionalities, though these monomers are not stable with electron rich moieties, such as thiophenes, resulting in extremely poor molecular weights.[83] Employing a boronic ester enables the use of Suzuki conditions with electron rich monomers and allows good molecular weights to be achieved.[84] For both polymerisation conditions, an oxygen-free environment is necessary to avoid deactivation of the active Pd(0) catalyst species. **Figure 1.9(a)** shows the proposed reaction cycle for a Pd-mediated C-C coupling via Stille conditions. Initially, the Pd(0) catalyst inserts into the R^1-X bond, where X is typically a halogen, such as Br or I, in a step called oxidative addition. Then, the transmetallation step replaces X with another aromatic carbon (R^2), producing a trialkyltin halide derivative as a byproduct. Finally, through reductive elimination, the desired C-C bond is formed between the R^1 and R^2 aromatic units, and the Pd(0) is regenerated for the next cycle. Suzuki polymerisation conditions follow a similar cycle (**Figure 1.9(b)**), though the product of transmetallation is R_2BX and the catalyst may experience ligand exchange with the base to displace the halide with a hydroxide.[85] The boronic acid or ester also forms an intermediate complex, which then undergoes transmetallation, and concludes with a reductive elimination to form the new C-C bond. A final polymerisation

technique worth noting is Aldol polycondensations, which avoids the use of precious transition metal catalysts and toxic reagents, as well as generating only water as a benign byproduct (**Figure 1.9(c)**).[38,52,86]

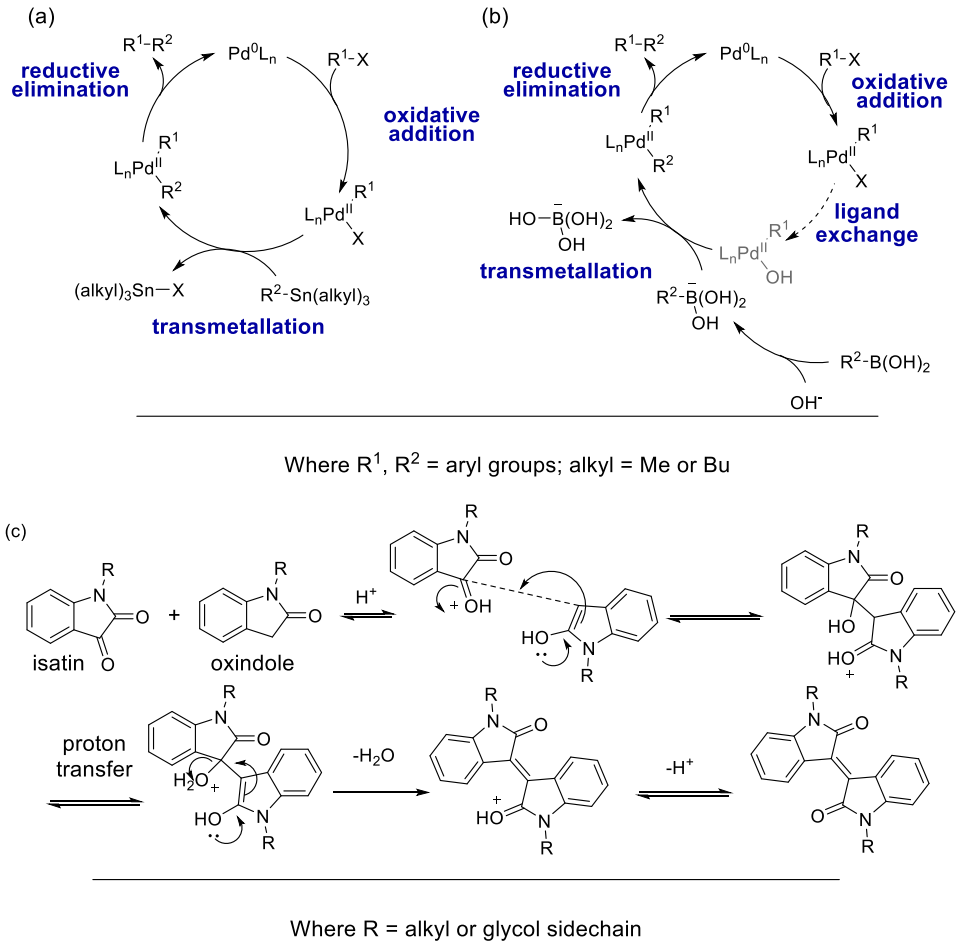


Figure 1.9. Proposed reaction cycle for (a) a Stille cross coupling reaction (b) a Suzuki cross coupling reaction and (c) the mechanism of an acid-catalysed aldol condensation.

1.3 Organic Mixed Ionic-Electronic Conductors

When OSCs are employed in a range of applications, as already mentioned, these generally only require the conduction of electronic charge carriers. Organic mixed ionic-electronic conductors (OMIECs) are materials that are capable of conducting both ionic and electronic charge carriers when operated in an aqueous electrolyte (or ionic liquid), and function in the bulk phase rather than an interfacial regime. These properties enable efficient charge storage

or signal transduction, making OMIECs applicable to a plethora of applications, including actuators,[87,88] sensors,[89,90] and electrophysiological recorders.[91,92]

On account of this, OMIECs are particularly suited to the channel material in organic electrochemical transistors (OECTs) due to their ability to transduce an ionic signal into an electronic output.[93] The most researched OMIEC is the conjugated polymer-polyelectrolyte blend, poly(3,4-ethylenedioxythiophene):polystyrenesulfonate (**PEDOT:PSS**) (**Figure 1.10(a)**).[94,95] In **PEDOT:PSS**, the **PEDOT** backbone is conjugated and allows for the transport of hole charge carriers, while the polyanionic PSS component allows for the uptake of water and ions into the bulk of the material, conferring ionic transport properties. This provides an indication that by increasing the hydrophilicity of a material, it improves its ionic conduction (**Figure 1.10(b)** and **(c)**). However, as the ionic conductivity increased, a detrimental impact on the electronic charge carrier mobility was noted, which was attributed to the disruption of the microstructure.[96] Further evidence for the conflicting design parameters of OMIECs was observed by *in situ* electrochemical microscopy, where, unsurprisingly, electronic transport was superior in the most ordered domains, however ionic transport was enabled by the less ordered domains.[97] This provides challenges when designing appropriate OMIECs.

One potential strategy to this is through the addition of hydrophilicity to the existing library of OSC materials. This can be achieved by introducing more hydrophilic oligo(ethylene glycol) sidechains directly to these monomer units, in place of the traditional alkyl chains.[98,99] This allows for the solubility to be maintained in typical organic solvents, whilst also enabling ionic transport into the bulk of these OSCs, turning them into OMIECs. These single component systems give greater synthetic freedom compared to **PEDOT:PSS** and allow for substantial structure-property relationships to be established.

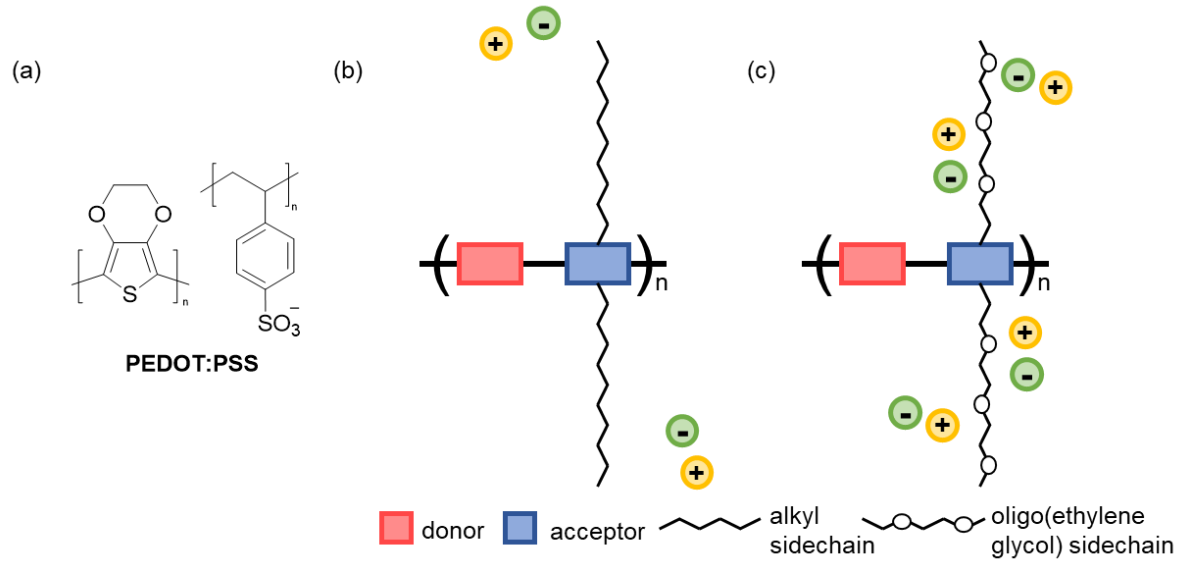


Figure 1.10. (a) The structure of **PEDOT:PSS** and a schematic illustration of the influence of (b) alkyl or (c) oligo(ethylene glycol) sidechains on ionic migration into the bulk of the material (i.e. the ability of the sidechain to facilitate ionic transport).

1.4 Organic Electrochemical Transistors

1.4.1 From Organic Field-Effect to Organic Electrochemical Transistors

A transistor uses a semiconductor to amplify a signal or to act as a switch to control the electron flow by changing the applied potential of the gate electrode. The introduction of this circuit component allowed for the development of much more complex circuits, including those of a computer chip.[100] Traditionally, transistors were made of silicon due to both cost and abundance, though the use of organic materials in transistors dates back to 1986, when a relatively poor charge carrier mobility on the order of 10^{-5} cm^2 V^{-1} s^{-1} was reported.[101] The field is now well-established,[102–104] and they act as a common characterisation tool for benchmarking the performance of organic semiconductors, by comparing the extracted charge carrier mobilities.[105,106]

An organic field effect transistor (OFET) employs a three-electrode system; a source, drain and gate, with the active channel OSC layer deposited between the source and drain electrodes (**Figure 1.11**). Electrodes are typically a high work function metal, such as gold or silver, because these inert metals match the energy levels of OSCs to facilitate charge injection and extraction.[107] The OSC layer is capped with a dielectric material, such as silicon dioxide, poly(methyl methacrylate) or benzocyclobutene-based polymers,[108,109] which are electronically conducting but ionically insulating. Applying a potential at the gate electrode, which is separated from the active channel by a dielectric layer, acts to switch the device ON and OFF. Aside from research into the dielectric and electrode materials, significant research efforts have contributed to huge numbers of novel active channel materials, as is well documented in literature reviews.[110,111] These materials can be broadly classified into two categories, based on the charge carrier transport they facilitate; p-type (hole transporting) or n-type (electron transporting) materials.

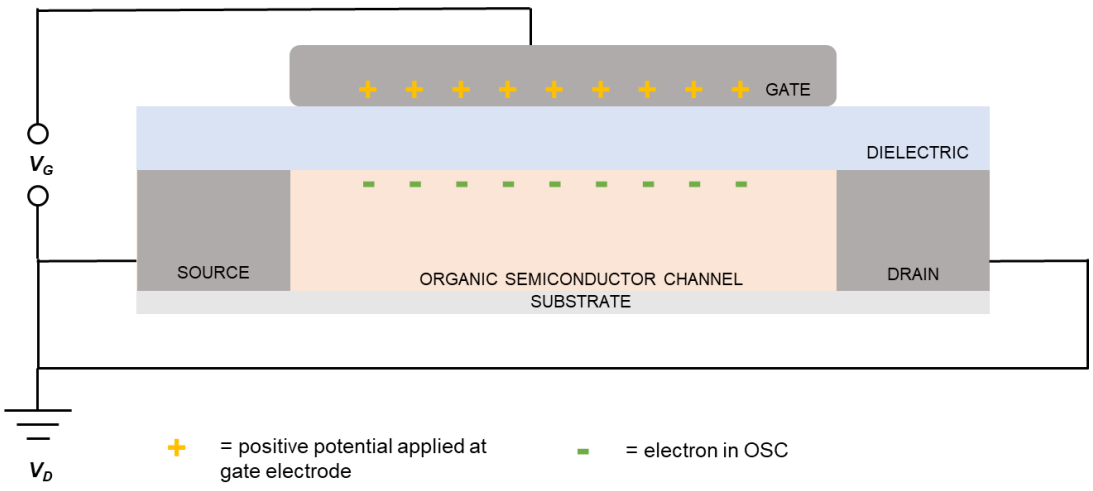


Figure 1.11. A schematic circuit diagram of the commonly utilised top-gate bottom-contact OFET device, with an n-type OSC layer, where V_D is the drain voltage and V_G is the gate voltage.

By using a high resistance semiconductor material, which gives a near-zero output current upon applying a potential between the source and drain terminals, the pristine device is in the OFF state. An applied gate voltage (V_G) polarises the dielectric layer and charge carriers accumulate at the semiconductor-dielectric interface. These charge carriers cause the semiconductor to become conductive, and upon applying a drain voltage (V_D), the charge carriers move between the source and drain electrodes, switching the device ON and generating a drain current (I_D). The main criterion to switch the device ON is the application of a gate voltage that is greater than the threshold voltage (V_T). The threshold voltage originates from the filling of trap states in every OSC, which must occur before the material is able to transport a charge.

When V_D is less than [V_G-V_T], the transistor operates in the linear regime, whereby the recorded drain current exhibits a linear trend with drain voltage, as predicted by Ohm's law. When V_D equals [V_G-V_T], the "pinch-off" point is reached as the charge carriers near the drain electrode are depleted. If V_D is further increased, the transistor reaches the saturation regime, where the area of OSC that is depleted of charge increases in size, towards the source electrode. These two regimes are neatly summarised by the Schockley equations **(1)** and **(2)**:

$$I_{D,lin} = \frac{W}{L}\mu_{lin}C(V_G - V_{Th})V_D \qquad \textbf{(1)}$$

$$I_{D,sat} = \frac{W}{2L}\mu_{sat}C(V_G - V_{Th})^2 \qquad \textbf{(2)}$$

Where I_D = the drain current in the specified regime, W = channel width, L = channel length, μ = charge carrier mobility and C = capacitance of the gate dielectric.

The current-voltage characteristics of OFETs can be graphically represented through the output and transfer characteristics (**Figure 1.12**). The output plot depicts the I_D as a function of V_D, at different V_G, where the linear and saturation regimes can be identified. The transfer characteristics plot the I_D as a function of V_G for a specified V_D, either in the linear or saturation regime.

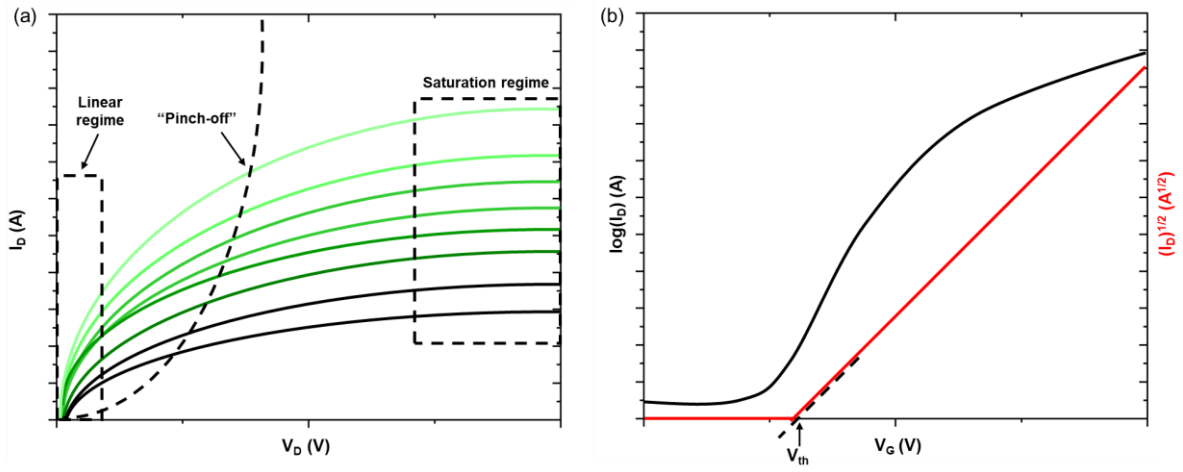


Figure 1.12. Current-voltage characteristics of a typical OFET. (a) Output plot showing the drain current as a function of the drain voltage for different gate voltages, highlighting the linear and saturation regimes. (b) Transfer plot in the saturation regime, showing drain current as a log function of gate voltage (black), and as a square root (red), extrapolating for the threshold voltage.

From the output and transfer graphs, a number of key performance metrics can be derived, to understand the device and channel material. These include the ratio of the maximum I_D recorded at a particular V_D in the ON and OFF states (I_{ON}/I_{OFF}), V_T and the linear and saturation mobilities. I_{ON}/I_{OFF} relates to the switching ability of the device, where a high OFF current (thus low I_{ON}/I_{OFF}) indicates ambient doping of the semiconductor material or leakage current. V_T of a device can be extracted by extrapolating a plot of $\sqrt{I_D}$ against V_G, to find the intercept with the y-axis (**Figure 1.12**).

The equations to calculate mobility in OFETs are derived from the Schockley equations, using the gradual channel approximation. The mobility in the linear and saturation regimes are found by solving equations **(3)** and **(4)**:

$$\mu_{lin} = \frac{L}{WCV_D}\frac{\partial I_{D,lin}}{\partial V_G} \qquad \textbf{(3)}$$

$$\mu_{sat} = \frac{2L}{WC}\left(\frac{\sqrt{I_{D,sat}}}{\partial V_G}\right)^2 \qquad \textbf{(4)}$$

The linearity of I_D against V_G in the linear regime or $\sqrt{I_D}$ against V_G in the saturation regime is required for accurate determinations of μ.[112] This is often not observed, with "kinks" in the transfer characteristics on account of contact resistance, resulting in non-ideal characteristics and inflated values for μ.[40,110] Additionally, OFETs typically require high V_G to switch devices between the ON and OFF states, which results in inefficient devices in practice due to high power consumptions. One route of investigation to overcome this is through the use of alternative dielectric materials, including electrolytes which are ionically conducting but electronically insulating. Their use in transistors gave rise to a novel device, the electrolyte-gated organic field-effect transistor (EG-OFET) (**Figure 1.13**).

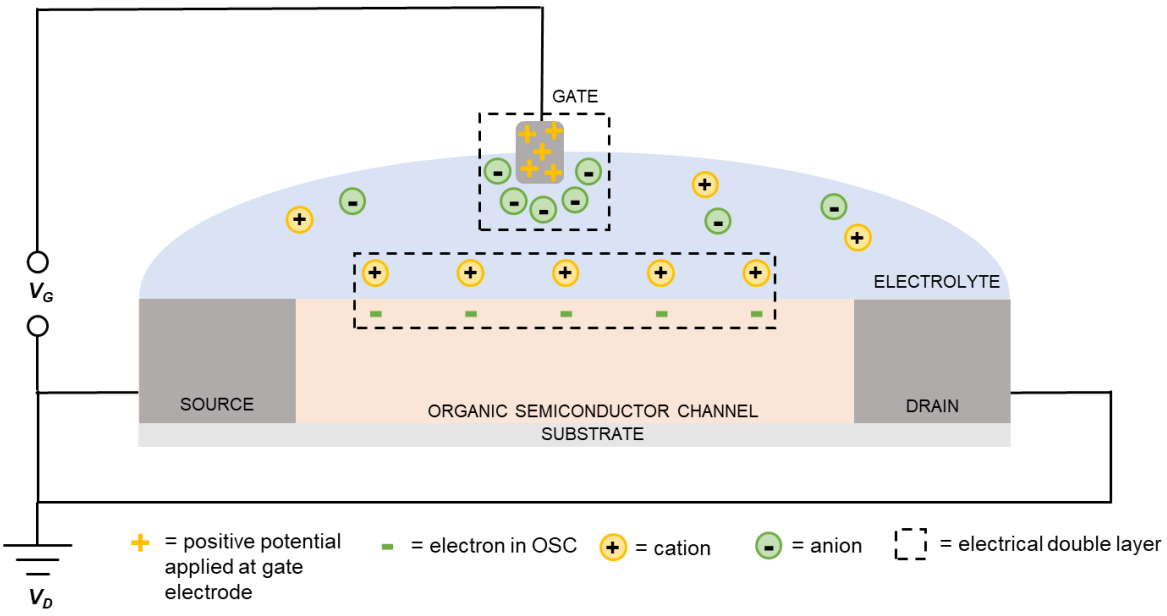


Figure 1.13. A schematic circuit diagram of an electrolyte-gated organic field-effect transistor (EG-OFET) device, with an n-type OSC layer, where V_D is the drain voltage and V_G is the gate voltage.

EG-OFETs have similar operating principles to conventional OFETs, relying on the application of V_G to control the number of charge carriers in the active channel layer and operating in an

interfacial regime. The main difference between these two types of transistors is that in an EG-OFET, the charges injected into the active channel are compensated by electrolyte ions which migrate to both the OSC-electrolyte and gate-electrolyte interfaces. Particularly notable, is the high electric double layer (EDL) capacitance at the OSC-electrolyte interface, which significantly reduces the operating voltages to below 1 V, due to the decreased contact resistances.[113,114]

To further take advantage of the lower contact resistance and operational voltages conferred by electrolyte gating, organic electrochemical transistors (OECTs) were developed in the 1980s.[115] OECTs consist of the same three-terminal architecture as an EG-OFET, however they employ an OSC layer that are both ionically and electronically conducting, i.e. the OSC is an OMIEC (**Figure 1.14**). As described for conjugated polymers, OMIECs can be divided into p-type and n-type materials, and can also be categorised based on their ambient level of doping. A material that is not doped when $V_G = 0$ operates in accumulation mode, whilst an OSC that is doped when $V_G = 0$ operates in depletion mode.[93,99] To illustrate the operation of an OECT more clearly, an n-type material with a deep LUMO, **P-90**, is used as an example.[116] **P-90** has a relatively high electron affinity (*EA*) and ionisation potential (*IP*), such that ambient doping does not occur, thus the material operates in accumulation mode.[116] When a positive drain bias is applied when $V_G = 0$, electrons are not injected into the OMIEC, because the structure is not able to support charge in this state. Application of a negative gate bias is required for the device to be switched ON, as cations from the electrolyte penetrate into the bulk of the OMIEC to compensate for the electrons injected by the drain when $V_D > 0$ (**Figure 1.14**).

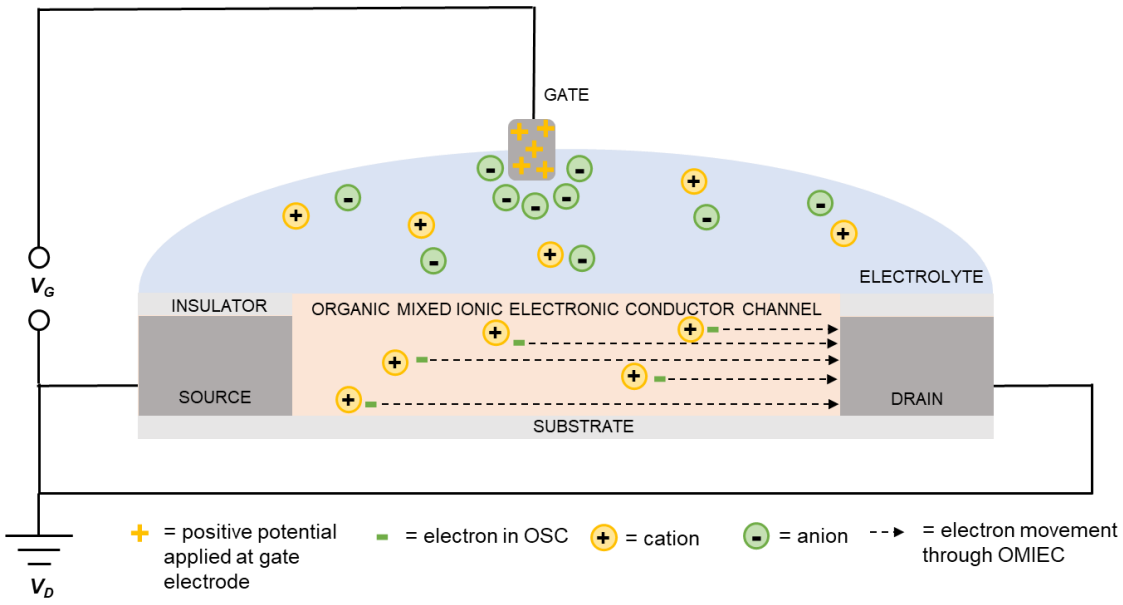


Figure 1.14. A schematic circuit diagram of an OECT device, with an n-type OMIEC layer, e.g. **P-90**, where V_D is the drain voltage and V_G is the gate voltage.

As demonstrated by these operating principles, OECTs are favoured over EG-OFETs due to their ability to amplify the signal by taking advantage of volumetric electrochemical doping,[71,117] rather than being limited by the EDL in EG-OFETs, which improves device sensitivity.[98] This makes OECTs the ideal device to amplify aqueous ionic signals typically found in biology into readable electronic ones, on account of their low operational voltages within the electrochemical window of water.[72]

Volumetric electrochemical doping of the OMIEC also introduces the hydration sphere associated with each migrating ion, resulting in solvent molecules being introduced into the organic layer.[118] This is also referred to as swelling. In typical transistor OSC layers, amorphous regions are usually viewed as detrimental to the charge carrier transport properties, however in OECTs, some amorphous regions are required to accommodate the compensatory ions and their hydration shells. This does however, prevent facile movement of charge carriers between crystalline regions[119] as the solvent molecules introduce "free volume", which enables

rapid ion migration.[120] This indicates that a balance must be found to maximise the ionic transport to a point where the electronic transport is not limited, and vice versa.

1.4.2 Performance metrics of an OECT

Originally, OECT performance was measured by comparing the transconductance, g_m, which is calculated using equation **(5)**:

$$g_m = \frac{\partial I_D}{\partial V_G} \qquad \textbf{(5)}$$

Seminal work from Bernards and Malliaras involved the development of a model of the steady-state performance of OECTs, which separates the overall device into two circuits, the electronic circuit (i.e. charge carrier transport in the OSC layer) and the ionic circuit (i.e. the movement of ions in the electrolyte).[121] By drawing comparisons between these circuits and metal oxide semiconductor field-effect transistors (MOSFETs), this model allows for the derivation of OECT transconductance in the saturation regime as equation **(6)**:

$$g_m = \frac{Wd}{L}\,\mu C^*(V_T - V_G) \qquad \textbf{(6)}$$

Where W = width, d = thickness and L = length of the active layer, μ = charge carrier mobility, C^* = volumetric capacitance V_T = threshold voltage and V_G = gate voltage. From this equation, the transconductance can be seen to be dependent on the device geometry, hence increasing the device volume can improve the g_m value obtained. In practice, this usually comes from an increase in channel thickness because devices are required to be on the micro-scale to be relevant for many bioelectronic applications.[117] Increased device thicknesses do however negatively impact the device response times, which limits the device's operational frequencies. This led to the more recent introduction of the μC^* product as the favoured figure of merit, as it is geometry independent and relies on optimising the ionic and electronic transport in OMIECs.[122] Furthermore, by removing device related terms, it provides a useful value for the

benchmarking of OMIECs, to allow for valid comparisons when deriving structure-property relationships.

Whilst both g_m and μC^* are key properties for understanding the steady-state performance of OMIECs, there are also some transient properties that are critical to the development of high performing and useful materials. These include the response time of a device, and its operational stability. A device's response time is particularly important for applications involving the monitoring of rapid signals, such as brain oscillations, where frequencies tend to range from 0.5-200 Hz.[123] This is usually identified through the transient response time of a device, which is the time taken for the device to reach 90% and 10% of the maximum ON and OFF currents, respectively.[124] Finally, stability is critical for OECTs to realise practical application in healthcare settings, for both device safety and efficiency. Stability is measured by repeated cycling or pulsing of the gate voltage, where the retention of the I_D is the metric of interest.[49,125,126] Typically the gate voltage chosen is that where the highest transconductance value is obtained, to ensure valid comparisons between materials can be drawn.

1.5 OECT active layer materials

As mentioned previously, OMIECs are the natural choice for the OECT active layer due to their ability to conduct both electronic and ionic charges. As the field of bioelectronics has realised the potential of OECT devices, significant research effort has turned to developing novel high performing OMIEC materials. There are several ways to classify these materials, including by their structure, by their ambient level of doping or by their charge carrier properties.[127] Structure classification differentiates between structures whereby the ions are chemically bonded to the OMIEC structure, for example in conjugated polymer/polyelectrolyte blends (**PEDOT:PSS**)[94,95] and conjugated polyelectrolytes,[69,128,129] or where the structure enables free ions to penetrate into the material upon device operation, for example in

conjugated polymers with appropriately selected sidechains.[71,116,125] The ambient doping level of a material leads to its operation in either a depletion or accumulation mode device.[93,99] In depletion mode devices, the OMIEC is intrinsically doped in ambient conditions (usually on account of ions chemically bonded to the OMIEC) and require an applied gate voltage to turn off the device, whilst the opposite is true for accumulation mode devices. In principle, accumulation mode devices are preferable for bioelectronic sensing applications due to their ability to turn on as the biomarker increases in concentration, potentially allowing for a wider sensing regime.[130]

As introduced in **Section 1.4**, the materials herein will be categorised by their charge transport regime, namely, p-type (hole transport) or n-type (electron transport). In some cases, materials may exhibit both hole and electron transporting capabilities, denoting them as ambipolar.

1.5.1 P-type active layer materials

The most widely employed channel material in OECT devices to date is **PEDOT:PSS**, since it was first used in 2002.[131] **PEDOT:PSS** is commercially available as an aqueous dispersion, where the hydrophobic, conjugated PEDOT backbone is stabilised by the hydrophilic, polyanionic PSS (**Figure 1.*10*(a)**). **PEDOT:PSS** shows good performance, with transconductance in the mS range, on account of the π-stacking observed when **PEDOT:PSS** is cast, allowing for good interchain charge transport.[132] The use of co-solvents, such as ethylene glycol, have then further improved the performance of **PEDOT:PSS** by encouraging aggregation in solution, which increases the size of the PEDOT crystallite domains, causing tighter π-stacking and increasing hole transport properties.[96] Unfortunately, this negatively impacted the ionic conductivity, as ionic movement throughout the highly ordered domains was reduced, highlighting the need to balance the electronic and ionic conductivities.[96] When employing ethylene glycol as an additive, the optimal performance was found at 5 vol%, which resulted in a maximum g_m of ~9 mS.[96]

Despite the benefits of **PEDOT:PSS**, there are a number of disadvantages, including the acidity of the PSS component, limiting its compatibility with implantation, the electrically insulating PSS polyanion, which limits the volumetric capacitance (< 100 F cm^{-3}),[122] and the complex microstructure, which limits its suitability for determining structure-property relationships of OMIECs. Typically, the self-doped nature of **PEDOT:PSS** results in unfavourable depletion mode operation, however **PEDOT:PSS**-based OECTs have been demonstrated to operate in accumulation mode when aliphatic amines are added to the polymer dispersion as de-dopant molecules, allowing for accumulation mode operation and tuning of V_T.[133]

In order to tackle the issues associated with conjugated polymer/polyelectrolyte blends, such as **PEDOT:PSS**, single component systems have since been synthesised, where the ion conducting component is covalently attached to the conjugated polymer backbone. These new OMIECs typically make use of either a polythiophene or PEDOT backbone, both of which are known for their high hole mobilities. Combining these with charge-bearing sidechains, such as sulfonates, results in a new class of OMIECs, called conjugated polyelectrolytes (**Figure 1.15**).

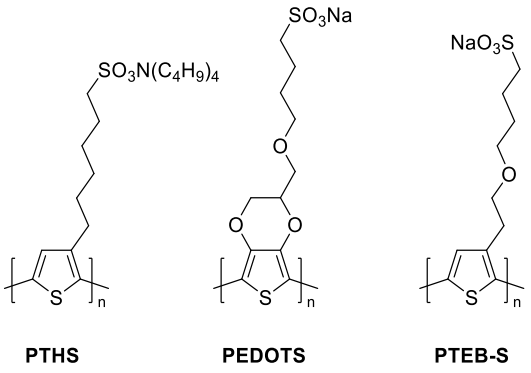


Figure 1.15. Examples of conjugated polyelectrolytes used as p-type OECT active layer materials.

Due to the self-compensating sidechain (i.e. the positive sulfonate compensates the negative tetrabutylammonium ion), **PTHS** has semiconducting capabilities and operates in accumulation mode. Additionally, it achieves performance in a comparable range to

PEDOT:PSS, with a maximum g_m of 2 mS.[134] **PEDOTS** and **PTEB-S** (**Figure 1.15**) both make use of anionic sidechains, thus they compensate charges on the polymer backbone, and operate in depletion mode.[124] Pristine **PEDOTS** is able to achieve a high g_m of 16.2 mS as the OECT active layer. Interestingly, by blending **PEDOTS** with **PTEB-S**, the mode of operation of the OECT device can be altered to achieve a hybrid accumulation/depletion mode, although a slight decrease in the transconductance was observed, with a peak g_m of 12.0 mS reported.[124] Unfortunately, this still results in either a polymer blend, with a complex microstructure, or a depletion mode device, both of which come with the aforementioned disadvantages. Furthermore, due to the additional sidechain of **PEDOTS** compared to the original PEDOT core, this polymer has high aqueous solubility, so an ionic liquid ($BMIM^+BF_4^-$) must instead be employed, limiting its biological applications.[124]

The last six years have focused on expanding the library of accumulation mode OECT active layer materials, by making use of conjugated polymers with uncharged sidechains. This design principle has focused on replacing the typical alkyl chains used in OFET active layer materials with oligo(ethylene glycol) chains. This retains solubility in organic solvents necessary for synthesis and device fabrication, but also introduces hydrophilicity required to convert an electrically conducting, ionically insulating material into an OMIEC.[49,71,73,135,136] Additionally, this allows for a translation of knowledge of OFET charge transport along these same polymer backbones into the lesser understood field of OECTs.

This design strategy was first reported by Nielsen et al., where a series of p-type backbones containing benzothithiophene (BDT) or bithiophene (T2) motifs were selected and decorated with triethylene glycol sidechains.[73] The study aimed to investigate the effect of backbone conformation and sidechain density on p-type OECT operation. The authors found that increasing the glycol sidechain density of the BDT-based polymers unfavourably increased the π-π stacking distances and displayed a predominantly edge-on orientation in the solid state.

These combined factors were attributed to the lower hole mobility and transconductance values observed for these polymers. However, polymers containing the glycolated T2 unit exhibited significantly lower oxidation potentials (i.e., the device is easier to switch ON) and increased electrochemical stability in aqueous electrolytes than the BDT-based polymers. Additionally, the thiophene-based polymer, **p(g2T-T)** (**Figure 1.16**) displayed higher g_m than **PEDOT:PSS** in all tested active layer dimensions, with a peak g_m of 21 mS.[73] This provided the motivation to continue developing this design strategy, as such Giovannitti et al. worked to improve **p(g2T-T)** by substituting the thiophene comonomer with a thieno[3,2]thiophene (TT) unit, to create **p(gT2-TT)** (**Figure 1.16**).[71] This improved the planarity of the material, due to the rigidity conferred by the TT monomer, and reduced the π-π stacking distance, resulting in a further increase in both hole mobility and transconductance, with values of 0.95 $cm^2\ V^{-1}\ s^{-1}$ and 27 mS, respectively. **p(gT2-TT)** was then benchmarked by Inal et al. against other state-of-the-art OECT channel materials, by comparing devices of various dimensions, and was confirmed to outperform all other p-type active layer materials to date, with a μC^* of $261 \pm 29\ F\ cm^{-1}\ V^{-1}\ s^{-1}$.[122]

A recent study looking further into the operation of **p(gT2-TT)**, however, revealed that the de-doped films are able to spontaneously catalyse the oxygen reduction reaction (ORR) when immersed in aqueous electrolytes. This generates hydrogen peroxide via the two-electron process, and is potentially detrimental to the films themselves, worsening device sensitivity and limiting energy storage applications, as well as having toxic effects on surrounding biological media in sensors. To minimise the spontaneous catalysis of ORR, Giovannitti et al. suggests that p-type materials with IPs higher than 4.9 eV are required to increase the oxidation onset potential to greater than 0.15 V (versus Ag/AgCl in pH 7).[137] To this end, **p(gPyDPP-OMeT2)** was developed (**Figure 1.16**), with an IP ~4.92 eV, and showed no formation of hydrogen peroxide during device operation. Additionally, **p(gPyDPP-OMeT2)** experienced

OFF currents two orders of magnitude lower than **p(gT2-TT)** when operated in ambient conditions.[137]

Two other approaches to improving the operational stability of p-type OMIECs have been employed by Moser et al.[49] and Wang et al.[126] Firstly, Moser et al. conducted a sidechain redistribution on the common homopolymer, **p(g3T2)**, whereby the ethylene glycol length on one T2 unit was increased by one repeat unit, with the neighbouring T2 simultaneously decreasing by one glycol repeat unit (**Figure 1.16**). This provided control over the degree of water uptake of the polymers, with C^* broadly decreasing as the distribution increased, but hole mobility increasing, again reflecting the balance between μ and C^*. Electrochemical quartz crystal microbalance with dissipation monitoring (EQCM-D) measurements aligned with these findings, indicating that active swelling was the smallest for the polymers with the smallest C^* (**p(g1T2-g5T2)** and **p(g0T2-g6T2)**), with volume increases of only 10% and 4% reported, respectively. When translating this to OECT operational stability, this was dramatically improved for these two polymers, which both retained 98% of their initial current, when cycling over two hours.[49]

Wang et al. were similarly motivated to control the hydrophilicity of a series polymers, this time utilising a donor-acceptor motif, with isoindigo and EDOT. Their approach instead employed a range of polymers containing alkyl-only, glycol-only and mixed alkyl-glycol hybrid sidechain to modulate this property.[126] The authors observed that **PIBET-AO** (**Figure 1.16**), the mixed alkyl-glycol derivative, provided enhanced operational stability and substrate adhesion (i.e. prevented delamination) when devices were operated in aqueous electrolytes, compared to the glycol-only derivatives.[126]

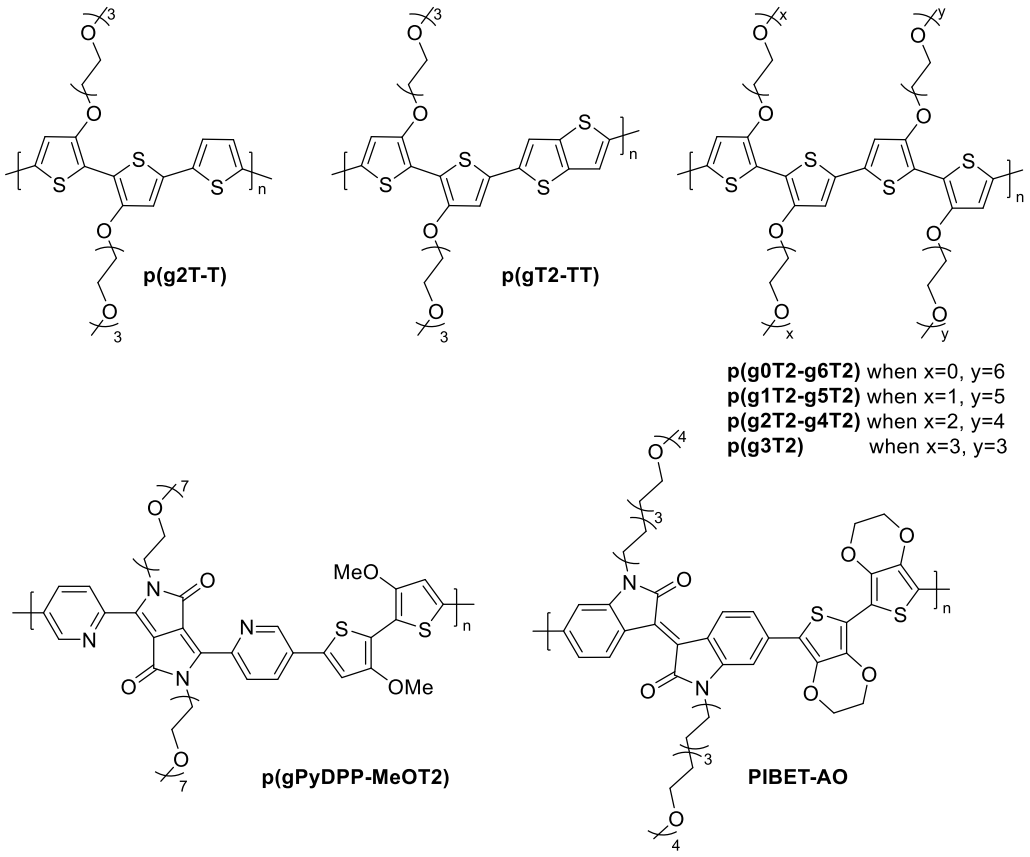


Figure 1.16. Examples of p-type OMIEC polymers used as OECT active layer materials.

1.5.2 N-type active layer materials

Until recently, literature has been dominated by high performing p-type OMIECs, with water-stable n-type materials only developed in 2016.[72] The first example, by Giovannitti et al. employed the same glycolation strategy, with an electron deficient naphthalene diimide (NDI) core, as commonly seen in other organic electronic applications.[40] The glycolated NDI was copolymerised with a bithiophene unit to product **p(gNDI-gT2)** (**Figure 1.17**), which was able to withstand long-term pulsing experiments, but had a low μC^* product, several orders of magnitude lower than the p-type values discussed in the previous section. The product was decoupled through further analysis to indicate that the poor performance was attributed to a low electron mobility of 3.1 x 10^{-4} cm^2 V^{-1} s^{-1} (**Table 1.1**).[72]

After the development of **p(gNDI-gT2)**, the impact of glycol sidechain density on n-type OECT performance was investigated on the same NDI-T2 backbone. In this case, the T2 unit remained free from sidechains, resulting in a unipolar n-type material (*c.f.* **p(gNDI-gT2)**, which is ambipolar). The series was based on the high performing OFET polymer, **N2200**,[30] which bears hydrophobic 2-octyldodecyl sidechains, which were exchanged with heptakis(ethylene glycol) sidechains in varying percentages to generate seven random copolymers, ranging from **P-0** (0% glycol chain) to **P-100** (100% glycol chain) (**Figure 1.17**).[116] Electrochemical impedance spectroscopy (EIS) identified two discrete charging regimes: an interfacial regime for **P-0** to **P-50** and a volumetric regime for **P-75** to **P-100**. This indicates a clear trend between increasing hydrophilicity of the polymer and the ability of aqueous ions to penetrate into the bulk of the semiconductor. This was supported by the observation that polymers **P-75** to **P-100** displayed a high degree of swelling, and a minimum requirement of 50% glycol density for OECT operation.[116] In terms of performance metrics, as the glycol density was increased, the C^* values increased, however electronic mobility was hindered on account of the disruption to the microstructure when hydrated ions were brought into the polymer. This resulted in an optimal glycol density occurring for **P-90**, which revealed the highest μC^* and thickness-normalised g_m (**Table 1.1**).

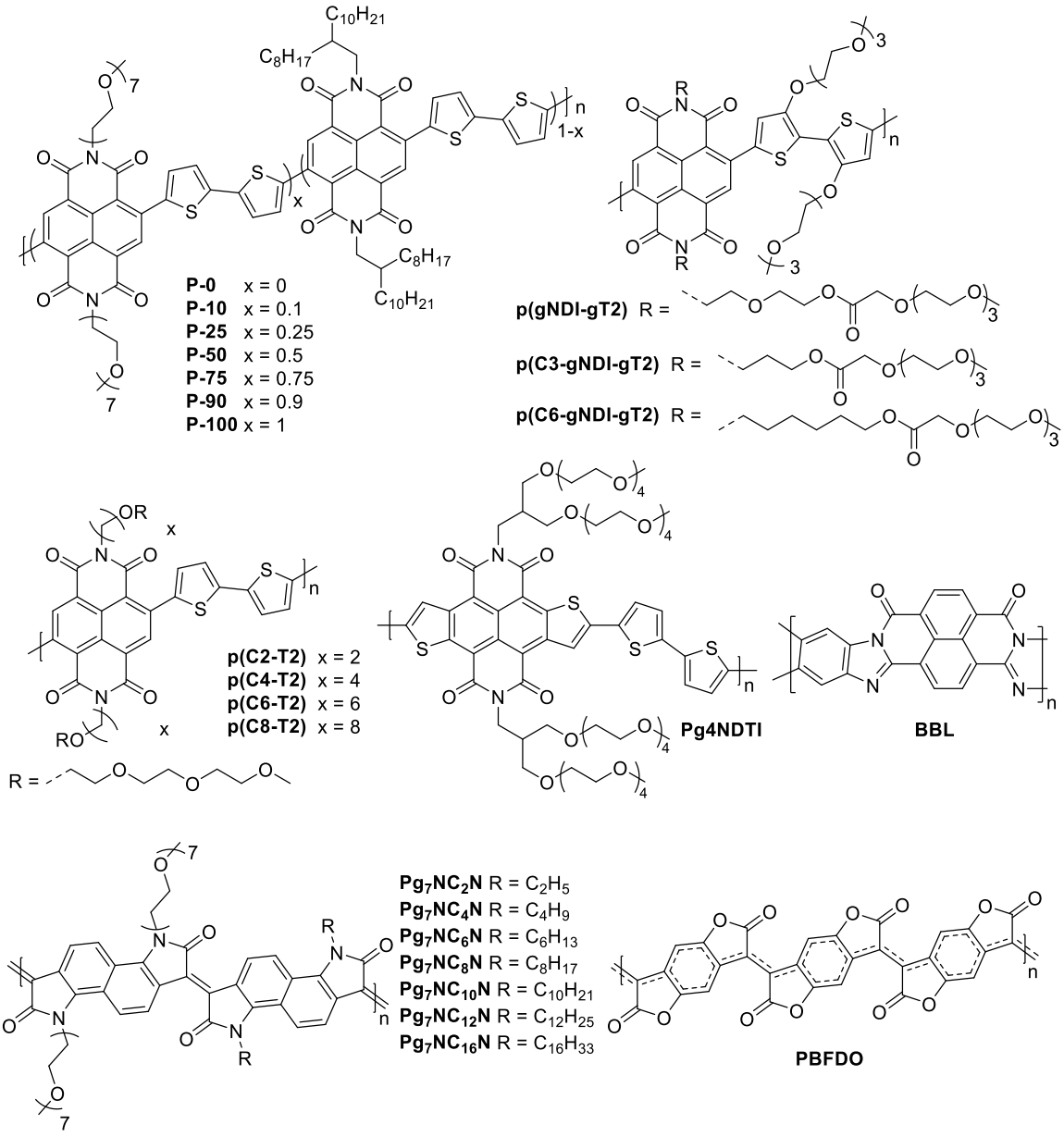


Figure 1.17. Examples of n-type OMIEC polymers used as OECT active layer materials.

Table 1.1. A summary of n-type OMIEC performance, including the electron affinity (EA), the electron mobility (μ_e), volumetric capacitance (C^*), μC^* and thickness normalised transconductance (g_m').

Material	EA (eV)[a]	μ_e (cm^2 V^{-1} s^{-1})	C* (F cm^{-3})	[μC*] (F cm^{-1} V^{-1} s^{-1})	gm' (S cm^{-1})[b]	Ref
p(gNDI-gT2)	4.12	1.00 x10^{-5}	397	-	1.085	[72,138]
P75	4.20*	1.46 x10^{-4}	188	-	0.141	[116]
P-90	4.23*	2.38 x10^{-4}	198	-	0.210	[116]
P-100	4.17*	1.96 x10^{-4}	192	-	0.204	[116]
p(C3-gNDI-gT2)	4.10	-	72	0.13	0.34	[138]
p(C6-gNDI-gT2)	4.00	-	59	0.16	0.37	[138]
p(C_2-T2)	4.10*	3.97 x 10^{-4}	492	0.20	0.40	[139]
p(C_4-T2)	4.10*	1.90 x 10^{-3}	158	0.30	0.63	[139]
p(C_6-T2)	4.20*	4.74 x 10^{-3}	272	1.29	2.28	[139]
p(C_8-T2)	4.20*	3.76 x 10^{-4}	342	0.13	0.15	[139]
P4gNDTI	4.17	1.42 x 10^{-3}	167	0.27	0.47	[140]
BBL	4.00	2.14 x 10^{-3}	731	1.99	0.815	[141]
PBFDO	4.67	-	-	180	1,970	[142]
PgNgN	4.35	1.89 x10^{-4}	239	0.04	0.007	[52]
p(g_7NC_2N)	4.26	2.00 x10^{-3}	180	0.36	0.069	[75]
p(g_7NC4N)	4.28	1.46 x10^{-3}	126	0.18	0.035	[75]
p(g_7NC_6N)	4.25	2.29 x10^{-3}	150	0.34	0.065	[75]
p(g_7NC_8N)	4.26	6.01 x10^{-3}	199	1.19	0.240	[75]
p($g_7NC_{10}N$)	4.23	1.20 x10^{-2}	153	1.83	0.370	[75]
p($g_7NC_{12}N$) (PgNaN)	4.22	6.50 x10^{-3}	100	0.66	0.212	[52,75]
p($g_7NC_{16}N$)	4.29	3.80 x10^{-3}	86	0.33	0.047	[75]

[a]EA is an estimation of the LUMO, although neglects the electron binding energy. Those indicated with * were measured by subtracting the optical bandgap from the IP (measured by PESA). Otherwise, these values were measured with cyclic voltammetry in 0.1 M $TBAPF_6$ acetonitrile solution, using the onset of reduction to calculate

the EA. [b]g_m' represents the thickness normalised transconductance; where this was not explicitly reported, it has been calculated by dividing the transconductance by the thickness. Table is updated from literature.[40]

Beyond this, two other studies have been conducted to investigate the use of hybrid alkyl-glycol sidechains on n-type OMIECs (similar to those seen for p-types in **Section 1.5.2**). The first of these modified **p(gNDI-gT2)** by introducing alkyl "spacer" units between the NDI unit and the glycol sidechain (**Figure 1.17**) as a method to modulate unfavourable swelling properties.[138] As expected, when the propyl and hexyl spacers were introduced, the C^* value decreased significantly from 397 F cm^{-1} to 72 and 59 F cm^{-1}, respectively (**Table 1.1**), and fewer ions were stored within the polymer microstructure, as determined by EQCM-D.[138] Notably, this reduction in swelling also contributed to an increase in OECT stability, where no decrease in current was observed when switching the device ON and OFF for two hours for **p(C6-gNDI-gT2)**.[138] The second study applied a similar approach, inserting an alkyl spacer of varying lengths (C2 to C8) between the backbone and the glycol part of the sidechain (**Figure 1.17**).[139] Here, no clear trend in C^* was observed, however both μC^* and g_m are optimised for **p(C$_6$-T2)**, where the highest NDI-based OECT performance is reported, with μC^* = 1.29 F cm^{-1} V^{-1} s^{-1}. This is on account of the increase in electron mobility observed for this polymer, which is attributed to increased long-range order from interconnected crystallite regions.[139]

A final noteworthy attempt at improving the OECT performance of NDI-based polymers involved the extension of the aromatic area of the NDI to introduce fused thiophenes onto the core to form naphthodithiophene diimide (NDTI).[140] Whilst this larger core required branched glycol sidechains to maintain solubility, it conferred improvements in electron mobility compared to the NDI derivative by almost three orders of magnitude, reaching a value of 1.42 x 10^{-3} cm^2 V^{-1} s^{-1} and translating to a μC^* product of 0.27 F cm^{-1} V^{-1} s^{-1}.[140] This increase in mobility was attributed to the extended effective π-conjugation length and improved planarity of the polymer backbone.[140]

Alternatives to NDI-based OMIECs for n-type OECT active layer materials consist of the use of a fully or partially fused backbone, with or without glycolated sidechains.[75,142–144] **BBL** was originally reported over 50 years ago[145] and has since found application in OECTs on account of its high EA, which enables stable operation in aqueous electrolytes. It is also able to achieve a C^* of between 731 and 930 F cm^{-3}, almost three times that of glycolated materials (**Table 1.1**),[141,146] due to the lack of sidechains, which enables **BBL** to store compensatory ions in closer proximity to its backbone, and therefore more easily accommodate electronic charge. Additionally, due to the rigid, planar nature of the backbone, the electronic mobility is significantly improved over other NDI-based OMIECs. Overall, this combines to give an impressive μC^* of 1.99 F cm^{-1} V^{-1} s^{-1}, and provides design strategies to improve n-type OMIEC performance, particularly electron mobility, through increasing backbone planarity and rigidity. Since then, efforts to realise another sidechain-free conformationally locked backbone has results in the creation of **PBFDO**, which was reported to achieve a μC^* two orders of magnitude greater, at 180 F cm^{-1} V^{-1} s^{-1} in the optimal conditions.[142] It should however be noted that no volumetric capacitance or OECT mobility are independently reported, rendering an understanding into the origin of this supreme performance impossible. Whilst solubility of this polymer is not possible in volatile solvents such as chloroform, it retains solubility in DMF and DMSO, meaning processing remains possible. It is thought that this is due to a strong interaction between the negatively charged backbone and the very polar solvents.[142]

However, as previously discussed, sidechains are often required to impart more convenient solubility (i.e. in chloroform) and enable the use of traditional solution-based polymerisation techniques and processing, such as spin coating and drop casting. For example, for the dissolution of **BBL**, aggressive acids, such as methanesulfonic acid, are required, which creates hazards when processing. Another downfall of this material is its poor response times of ~ 1 s, on account of a slow diffusion of ions throughout the active layer.[146,147] In an effort to bypass

these disadvantages but retain the valuable increase in electron mobility that this material confers, novel "rigid rod" materials were developed (**pgNgN** and **p(g$_7$NC$_x$N)**, **Figure 1.17**), incorporating a fully fused structure with the added benefit of sidechains.[52,75] Chen and Marks et al. first verified that some alkyl content was necessary to module swelling,[52] then optimised the ratio of glycol:alkyl sidechain content via the use of two monomers polymerised under aldol condensation conditions, varying the length of the alkylated monomer.[75] Of these eight materials, the peak performance was observed for **p(g$_7$NC$_{10}$N)**, which reported a μC^* of 1.83 F cm^{-1} V^{-1} s^{-1}, rivalling **BBL** (**Table 1.1**). Similar to the trend for the NDI spacer series, **p(g$_7$NC$_{10}$N)** offered the ideal microstructure for electronic transport, with a mixed face-on/edge-on orientation, which has been shown to improve 3D charge transport.[127,148] This proves particularly useful in OECT devices, where charge transport is required throughout the bulk of the OMIEC. Perhaps most notably, these "rigid rods" are synthesised by a metal-free aldol condensation, which does not require the use of a precious metal catalyst, nor toxic alkyl tin derivatives, making them ideal materials for use in safe bioelectronic devices.

Unfortunately, as demonstrated by the performance metrics in **Table 1.1**, n-type performance still lags significantly behind their p-type counterparts. Improvements in n-type materials are necessary to allow for the creation of more complex circuits, built with well-matched p-type materials, which lower the static power consumption, enabling faster circuit speeds and increased operational stability.[146,147]

1.5.3 Applications of OECT active layer materials

Previously, inorganic materials were favoured for semiconductors due to their high efficiencies and fast switching speeds.[149] However, organic materials offer several key advantages specific to bioelectronic applications, such as their flexibility and cheap large-scale production capabilities. This, combined with the biological compatibility conferred by organic materials,

renders OECTs a promising technology for sensing applications in healthcare settings,[150,151] as well as neuromorphic computing.[152,153]

OECTs have been employed as neural recording elements,[91,123,154] ion sensors,[155,156] biomolecule detectors[150,157,158] and cell activity monitors,[159,160] amongst many others. In this respect, OECTs offer an appealing solution to develop highly sensitive biosensors. Excitingly, a number of these examples make use of conjugated polymer OMIEC active layers, instead of the commercially available conjugated polymer-polyelectrolyte, **PEDOT:PSS**.[89,130,150] The most common examples of biosensors employing conjugated polymer OMIEC active layers utilise the polymer **P-90** (**Figure 1.17**), in OECT-based enzymatic sensors.[150] By using lactate oxidase (LOx), drop-cast onto the **P-90** channel, the presence of lactate in the electrolyte causes a shift in gate voltage, which modulates the conductivity of the channel and alters the drain current. The device is able to detect successive increases in lactate concentration, with a range of 10 μM to 100 mM, giving a wide sensing regime.[150] This concept was also translated to a glucose sensor, instead using glucose oxidase (GOx) as the enzyme for catalytic reduction of glucose in situ, where the authors suggest that the sensing mechanism is dictated by the spontaneous transfer of electrons from the enzyme to **P-90**.[161] Furthermore, the GOx functionalised **P-90** was employed as an anode, while a p-type polymer, **p(EDOT-co-EDOTOH)**, was the cathode, enabling the development of an enzymatic biofuel cell.[161] This setup allowed the system to convert the chemical energy of glucose and oxygen into electrical energy to power the sensor itself.[161]

Typically, n-type materials are more commonly used in enzymatic sensors due to their compatibility in accepting the electrons generated by the redox reaction of the enzyme. However, recently, a p-type conjugated polymer, **p(g0T2-g6T2)** (**Figure 1.16**), was reported in a state-of-the-art COVID-19 OECT-based sensor.[89] This used a gate electrode functionalised with a specific nanobody protein, and enabled high specificity and single-molecule detection

from 5 µL of unprocessed sample in only 10 minutes.[89] Additionally, these OECT-based biosensors offered sensor accuracy and sensitivity rivalling typical PCR tests, and this technology can be easily translated to other target proteins, if the corresponding nanobody can be sourced.[89] These viral sensors operate in a similar way to that described for enzymatic sensors, whereby the presence of the virus in the electrolyte shifts the gate voltage and modulates the channel conductivity, changing the drain current response.

Another application for OMIEC active layers is in inverters, whereby transistors with opposing charge transport regimes are paired to produce a complementary inverter, offering lower power consumption and reduced noise.[146] The first example of this was reported by Sun et al., where the p- and n-type materials (poly(3-carboxy-pentyl-thiophene, **P3CPT** and **BBL**, respectively) were on separate substrates to allow performance to be matched by controlling the active layer thicknesses. This allowed for a peak gain of 12 at 0.6V,[146] and this was further improved by substituting the p-type layer for **PEDOT:PSS**, to achieve a gain of ~60.[90] This disadvantage of these two devices however, is the scale, where both are on the millimetre scale, making the wider application impractical. Instead, Rashid et al. reported a vertical inverter, which reduces the form factor, and requires the application of a single ambipolar OMIEC, **p(C_4T2-C_0-EG)**.[139,162] This device recorded a peak gain of ~28, whilst also presenting practical application in recording electrocardiograms (ECGs) in healthy patients, with a gain of 10.[162]

Beyond these examples, due to the flexibility conferred by the organic nature of these devices, OECTs have been demonstrated in various wearable technologies, including integrating an OECT into a single fibre for weaving into clothing[163,164] or through OECT patches, to measure biomolecules in sweat.[165,166] Unfortunately, none of the applications discussed have yet had vast commercial success, however this provides opportunities to further understand the operation of OMIECs, which can inform design strategy and develop novel materials for relevant and scalable applications.

1.5.4 Design considerations of n-type materials

To discuss the design considerations of n-type materials, first the fundamental challenges with n-type materials and why high performing n-type materials are scarce should be addressed.[167] It should be noted that theoretically the transport mechanisms utilised by electrons and holes is identical, so is not the limiting factor in the inferior performance of n-type materials.[106]

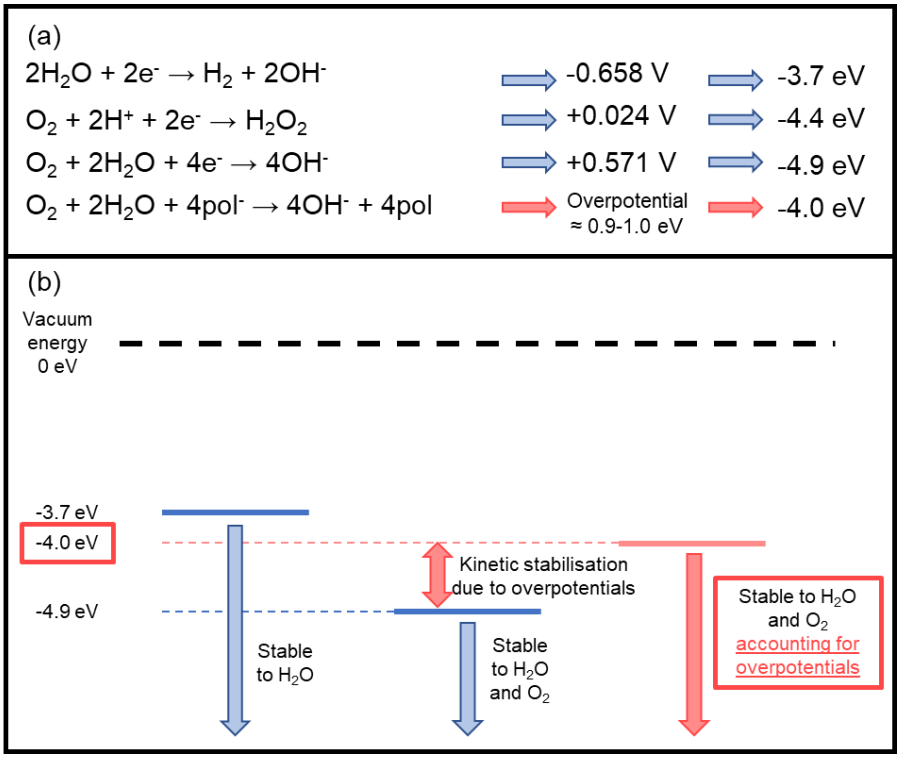


Figure 1.18. (a) The key reduction equations, and associated energies, that cause inherent n-type instability. The redox potentials are measured versus the standard calomel electrode (SCE) at pH = 7.[168] The corresponding LUMO levels have been approximated from these redox potentials using the equation $E_{LUMO} = E_{red} + 4.4$ V.[168] pol^- represents the anionic polymer species undergoing the redox reaction and pol is the neutral polymer after quenching by the ambient species. (b) A schematic representation of the stability requirement of the LUMO energy level of an n-type material, accounting for an overpotential of 0.9-1.0 eV. Adapted from literature.[40]

Rather than an inherent chemical instability, the problems associated with n-type materials originates from reactions with moisture and oxygen generated electron traps which impede electron mobility.[40,168,169] The most important reactions are those occurring with oxygen and water, as these potentials reside within the electrochemical window of most common n-type OSCs (**Figure 1.18**).[168,170] When accounting for the overpotentials of these redox reactions (the energetic barrier originating from penetration of an ambient species into an OSC),[171] a LUMO below ~-4 eV is required to introduce ambient stability.[172] This must be kept in mind as a design strategy for the advancement of stable n-type OSCs, and specifically OMIECs.

The performance of OMIECs is further complicated by the design requiring volumetric penetration of hydrated ions, ideally without disruption to the charge transport pathways. Typically, this cannot be avoided, and electrochemical doping leads to swelling and distortions to the microstructure as the film accommodates the additional ions and their hydration shells.[119,173–176] Flagg et al. postulated that during electrochemical doping of **P3HT**, a hydrophobic polymer, each chloride anion, found in typical aqueous OECT electrolytes, is accompanied by ~10-13 water molecules, whilst larger anions, such as PF_6^- and $TFSI^-$, are accompanied by no or almost no hydration shell.[174] This effect is therefore expected to be amplified in polymers designed to incorporate hydrophilicity. This is typically achieved through the introduction of glycol sidechains, with these polymers showing crystal lattice expansion[119] and swelling[177] even before being subjected to an applied bias.

Studies by Flagg et al. and Giridharagopal et al. indicate that water molecules are best accommodated in the amorphous regions of the polymers, while the ions themselves are able to penetrate closer to the polymer backbone, residing in the sidechain regions during OECT operation.[97,174] With this lattice expansion due to excessive swelling, charge transport is hindered by the disruption of connectivity between crystalline domains,[174,177,178] however,

some hydration is required to allow for ionic transport and to maximise g_m and μC^* figures of merit, once again indicating the necessity of balancing ionic conductivity and charge transport. Additionally, as the ions are compensating the electronic charge on the polymer backbone, it may be possible that their proximity to the charge on the backbone could impede charge transport by localising it, because ions have restricted movement due to obstruction from the sidechains. Design strategies to optimise the distance between the ion and the charged backbone have been employed in both p- and n-type polymers, and have demonstrated an effective method for improving electronic transport, whilst also controlling the degree of swelling.[126,138,139]

The numerous considerations highlighted through this section indicate the complexity of designing effective materials for high performing OECT devices, as well as further decoupling the relationship between electronic and ionic transport, to develop stronger knowledge of structure-property relationships of OMIECs.

1.6 Thesis aims and outline

The overarching aim of this thesis is to develop thorough structure-property relationships of mixed ionic-electronic conductors (OMIECs) for application in organic electrochemical transistors (OECTs). By investigating three series of copolymers, this work aims to improve understanding of both material design and other neglected factors, such as material purity, on the performance of OECTs, with a primary focus on n-type (electron transporting) OMIECs. This is done both through the design of novel materials and using existing libraries of materials as well as employing alternative techniques to improve performance.

Chapter 2 presents two common OMIEC polymer backbones, namely a polythiophene and a naphthalene diimide (NDI) copolymer and introduces preparative GPC as a method of molecular weight separation and purification. By using optoelectronic and structural analysis

and OECT measurements, the impact of the molecular weight, dispersity and degree of polymer purity is decoupled. The work in this chapter indicates that the molecular weight of the OMIEC polymer has limited impact on OECT performance, providing it is above a minimum value to allow for the interconnection of crystalline regions. Instead, the impact of residual Pd from the polymerisation is deemed detrimental to the OECT performance, specifically the mobility. This is found to differ from the impact of Pd on a field effect transistor and potential mechanisms are described.

Chapter 3 details the design and computational modelling using DFT calculations of seven novel NDI-based copolymers (and includes a further two reported polymers as benchmarks), to understand the impact of the size, electron density and planarity of the comonomer on the degree of delocalisation and OECT performance. From these findings, a series of three polymers were synthesised and fully characterised, where the planarity and size of the comonomer were revealed as the most important factors in improving OECT performance. By examining the OECT mobility and correlating it to the GIWAXS data, the degree of delocalisation was inferred.

Chapter 4 explores a "model system" for understanding the ionic conductivity of OMIEC materials. Whilst the mobility of OECTs is relatively well understood from its similarity to field effect transistors, ionic conductivity is often disregarded as a critical factor for optimisation. By designing six novel copolymers containing the electronically insulating pyromellitic diimide (PMDI) monomer unit, the impact of the sidechain and the comonomer on ionic conductivity were investigated. Using electrochemical and structural measurements, this chapter sets out some considerations for the design of future materials to optimise ionic transport in OECTs. Beyond their design as a "model system" for OECTs, these materials show promise in aqueous battery applications through galvanostatic measurements to understand the

charging and discharging mechanism, which may occur via a Faradaic process for two of the six polymers.

The appendix proposes novel p- and n-type polymers with reactive end groups for functionalisation with biorecognition elements, such as aptamers or enzymes. By designing polymers with reactive end groups, they are able to undergo post-polymerisation functionalisation to introduce the desired functionality under biocompatible conditions. In this case, a functionalisable polythiophene-based polymer was successfully reacted under mild, non-toxic conditions with a fluorescent marker, which enabled the process to be tracked via fluorescence spectroscopy. An n-type NDI-based copolymer was synthesised and functionalised with a covalently-attached ferrocene derivative and its ability to act as an electron mediator with glucose oxidase in the presence of glucose, was investigated. These conjugated polymers are the first of their kind to present sidechain end groups with biocompatible reactivity and show promise for the development of OECT-based biosensors whereby the sensing element is covalently bound to the OMIEC.

Chapter 2

The Effect of Polymer Purification and Molecular Weight on Organic Electrochemical Transistor Performance

2.1 General information and attributions

Polymer **p(g$_4$T2-TT)** used for this study was provided by Dr Adam Marks (McCulloch Group, University of Oxford) and synthesised as reported in **Chapter 5**. GPC measurements in chloroform were performed by Dr Hu Chen (McCulloch Group, KAUST) and measurements in DMF were performed by the author. Spectroelectrochemical measurements were conducted by Dr Olivier Bardagot and Dr Gonzague Rebetez (Banerji Group, University of Bern). ICP-MS measurements were conducted by Dr Adam Marks and Dr Karrie Weaver (Stanford University). OECT substrates were fabricated by Emily Schafer (Rivnay Group, Northwestern University) and OECT measurements were performed by Dilara Meli (Rivnay Group, Northwestern University). GIWAXS measurements were performed by Dilara Meli and Dr Bryan Paulsen, and analysis was performed by Dr Joshua Tropp (Rivnay Group, Northwestern University). OFET devices were fabricated and tested by Dr Mohamad Nugraha (Anthopoulos Group, KAUST).

2.2 Introduction

The difference between the three-dimensional operation of OECTs and the interfacial regime of organic field effect transistors (OFETs)[75] presents new challenges to current understanding and indicates that previous assumptions on the similarity of OFETs and OECTs may not hold true.[116] Two factors that are relatively well known in OFET literature, and more widely in other organic semiconducting polymer applications, such as organic photovoltaics (OPV), which impact device performance, are the molecular weight and the conjugated polymer purity.[17,179–185]

There are several types of molecular weight, however typically in the field of organic transistors, M_n is the most widely reported.[49,52,135,136,138,139] The number average molecular weight (M_n) is defined as the total weight of polymer divided by the total number of polymer

chains, and the dispersity (*Đ*) is a measure of the distribution of the molecular weights, with *Đ* = 1 indicating all polymer chains are of equal length. There is also the weight average molecular weight metric (M_w), which is defined as the sum of the weights of all the chains divided by the number of chains.

The dependence of OPV and OFET performance on molecular weight has been known for a decade, with the polymer poly(hexyl-3-thiophene) (**P3HT**) being the focus of most of this research.[179–183] In OPV studies, a wider range of **P3HT** molecular weights have been investigated, ranging from 17 kDa to 111 kDa.[180] In this case, blends of **P3HT**:**O-IDTBR** were fabricated from four different **P3HT** batches, whereby an intermediate molecular weight was observed to maximize performance, hypothesised to provide the ideal blend morphology and component separation. More specifically, a weight average molecular weight (M_w) of 34 kDa of the donor polymer was found to optimize the power conversion efficiency (PCE), short-circuit current density and charge generation efficiencies, whilst a M_w value both above and below this showed a decrease in performance.[180]

For OFET applications, the relationship between performance and molecular weight is usually attributed to morphological factors.[17,24,179,185] It has been repeatedly demonstrated that increasing the M_n of **P3HT** from ~3 kDa to 36 kDa vastly improves OFET performance on account of increasing the field-effect hole mobility by up to four orders of magnitude.[182,183] There are two reasons postulated for this, namely the conformation of the polymer chains, and the frequency and prominence of the grain boundaries between crystalline regions. With higher molecular weights, polymer backbones are able to adopt more planar conformations, allowing smaller interchain distances, promoting both inter- and intrachain mobility.[182] Conversely, the lower molecular weight batch is thought to have smaller crystalline regions and more pronounced grain boundaries, resulting in an increase in unfavourable hopping events, limiting the overall field-effect mobility.[183]

Further studies in OFETs have used blends of different molecular weights to establish that higher molecular weights have longer polymer chains that can act as "tie chains", providing charge transport pathways through amorphous regions and connecting crystalline domains (**Figure 1.3**).[17] Where longer polymer chains are not present to act as tie chains, charges are instead forced to hop unfavourably between crystalline regions, which severely reduces charge carrier mobility.[183] Whilst intuition may lead to the assumption that low molecular weights cause poor charge transport properties, OFET studies indicate that an intermediate molecular weight may be optimal due to the formation of the most favourable morphology.[181]

Despite this relationship being shown in other semiconducting applications, less is known about this in OECT applications, where the three-dimensional operation through swelling and bulk doping of the OMIEC differs significantly from OFET devices. It is generally assumed that a higher molecular weight results in improved OECT performance, as has been shown for ladder-type polymers,[144] however the link between molecular weight and performance has not been demonstrated for other conventional OECT materials, such as polythiophene or naphthalenediimide (NDI) backbones.

Another consideration that may impact OECT performance is the purity of the OMIEC material. Typically, these conjugated polymers are only purified by Soxhlet extraction in numerous solvents, which removes limited amounts of residual metal impurities. In Stille polymerisations, the reaction conditions make use of 3,000-5,000 ppm of Pd, with Soxhlet reducing these values by about an order of magnitude.[186] Studies have demonstrated that these levels have a detrimental impact on OPV performance,[184] as Pd is able to trap charges and reduce charge transport (**Figure 2.1(a)**).[186,187] Pd is also known to act as a co-catalyst for redox reactions of ambient species, which makes its presence particularly applicable to OECT (but not OFET) applications. Specifically, this includes the oxygen reduction reaction (ORR),

which generates hydrogen peroxide, that is toxic to biological media, presenting another limitation of impure OMIECs for bioelectronic applications.

This chapter investigates the impact of molecular weight and purity (the level of residual Pd) of a polythiophene and an NDI-based polymer on the OECT performance. The specific structures are presented in **Figure 2.1(b)**. In particular, this study aims to understand the benefits of polymer purification as a strategy for improving OECT performance, which is readily available to the existing library of OMIECs.

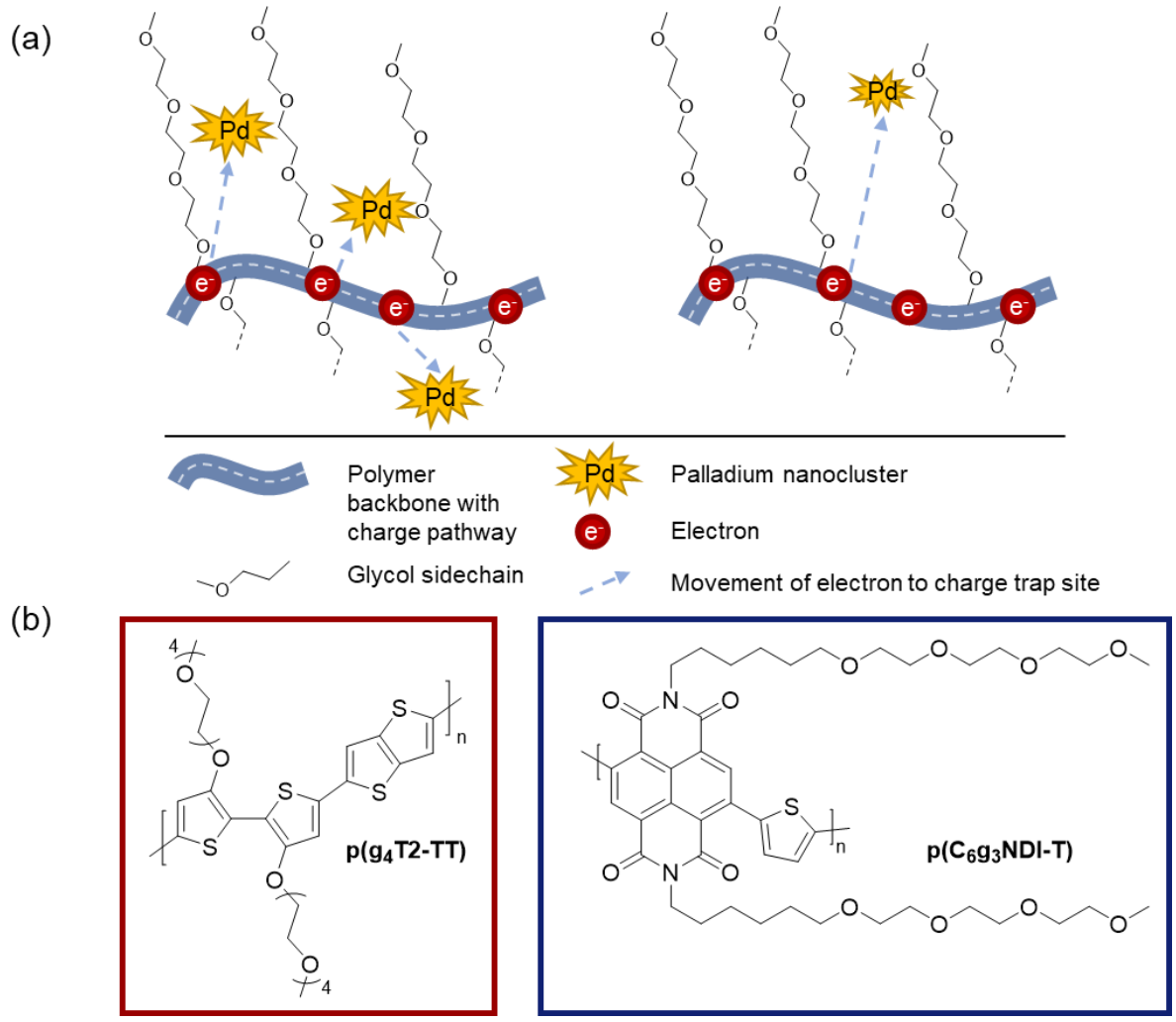


Figure 2.1. (a) Schematic of the impact of palladium nanocluster residues on the charge transport of conjugated polymer OMIECs and (b) the structures of the two polymers under investigation.

2.3 Synthesis of the polymers

The two polymers were selected due to the prevalence of polythiophene-based polymers as the standard p-type OMIEC,[49,71,73,148] and n-type literature being dominated by NDI-based polymers.[40] **p(g$_4$T2-TT)** offers a variation of the commonplace p-type polymer **p(gT2-TT)**,[71] with the longer sidechains selected to make higher molecular weight polymers more accessible. The synthesis of **p(g$_4$T2-TT)** was adapted from literature,[73] affording the monomer in two steps from commercially available starting materials, rather than the typical three step procedure that is widely reported (**Figure 2.2**).[49,71,148]

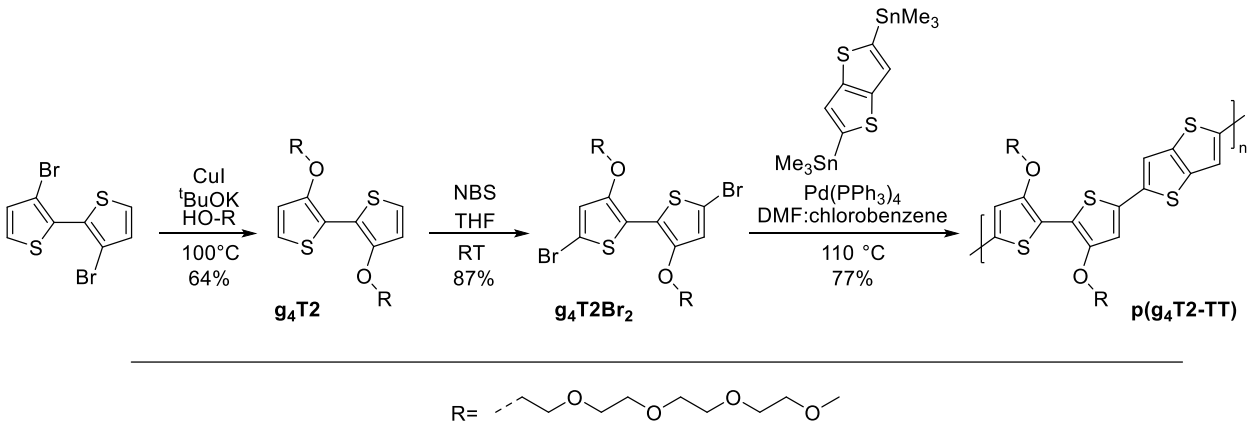


Figure 2.2. Synthetic route to **p(g$_4$T2-TT).**

The first step involved a copper(I) mediated coupling to introduce the tetraethylene glycol sidechains, in a reasonable yield of 64%. As this single step removes two relatively low yielding steps from the conventional synthesis (overall 29-52% yield)[49,148], this is considered to be beneficial for future synthesis of glycolated polythiophenes. In some respects, this synthesis can also be considered greener due to the lack of solvent required, and the ability to recover excess sidechain during column chromatography. The monomer was then brominated using typical conditions, to yield the monomer in an overall yield of 56%, the formation of which was confirmed by NMR and HRMS, both of which agreed with literature.[49,188]

p(g$_4$T2-TT) was prepared via Stille cross-coupling polymerisation using the synthesised brominated and commercially available stannylated monomer, to achieve an A-B-A-B coupling pattern (**Figure 2.2**). The polymerisation was carried out in a 1:1 v/v mixture of chlorobenzene:DMF to allow for higher reaction temperatures to be used than DMF alone, with the aim of maximising the molecular weight. The polymer exhibited good solubility in chloroform at room temperature, thus molecular weight separation and purification using the preparative GPC remained possible, as well as allowing for convenient processing.

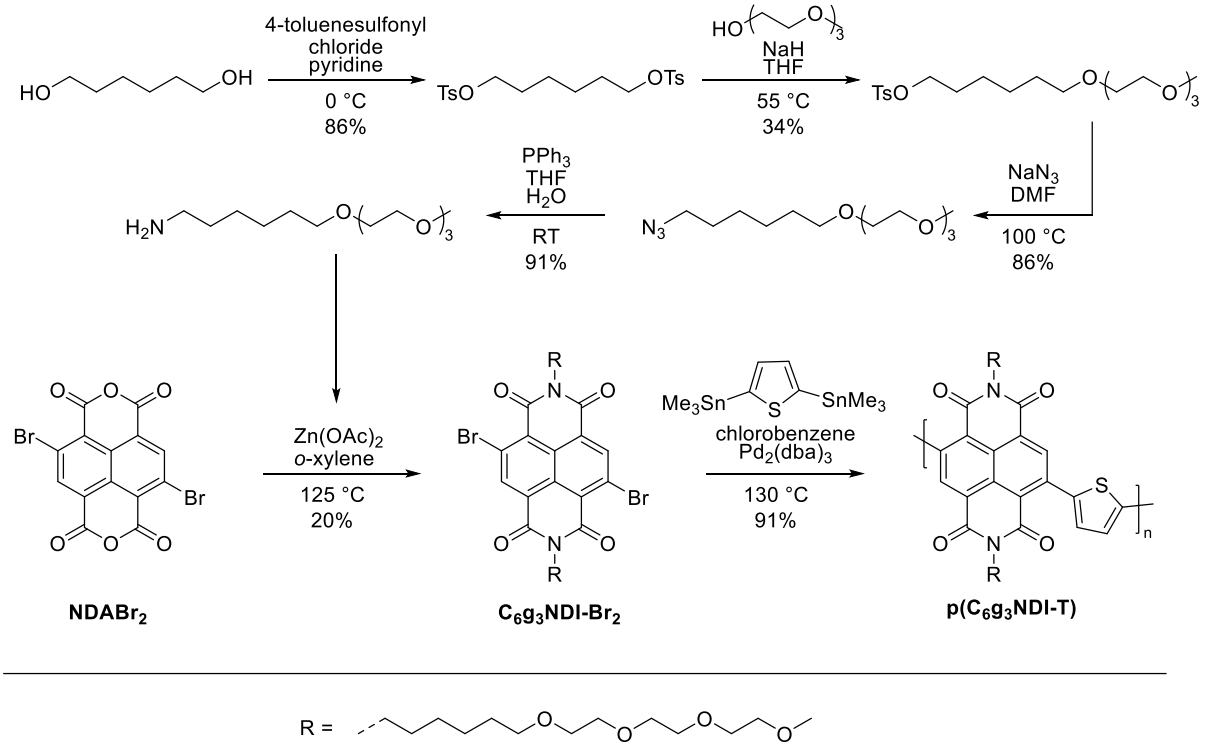


Figure 2.3. Synthetic route to **p(C$_6$g$_3$NDI-T)**.

Synthetic efforts towards **p(gC$_6$g$_3$NDI-T)** began with work to optimise the sidechain formation, as existing literature was found to be unreproducible (**Figure 2.3**).[139] Following a simple ditosylation, the condensation reaction between one tosyl group and the alcohol group of the triethylene glycol monomethyl ether was developed, as the initial attempt using DMF as the solvent failed, with the crude NMR displaying no product. It was found that by exchanging the solvent to THF to allow for heating of the deprotonation of triethylene glycol monomethyl

ether by sodium hydride, the pure product could be obtained in a yield of 34%. The low yield is attributed to the formation of the disubstituted product, which was separable by column chromatography, though its formation likely could have been reduced by further altering the equivalents of the ditosylate. From this key intermediate, the final sidechain could be obtained in good yields in a two-step procedure, using S_N2 substitution with sodium azide, then Staudinger conditions to transform the azide into a primary amine, with no further purification required. The azide underwent simple purification, through the addition of copious amounts of ethyl acetate to precipitate the excess azide and sodium byproducts, followed by an aqueous work up to ensure all azide had been quenched and removed. The final amine also required minimal purification due to the hydrophilic nature of the sidechain, along with the additional hydrophilicity of the amine, making it soluble in water. This allowed for the reaction to be diluted with water, followed by washing of the aqueous phase using diethyl ether to remove any phosphine derivatives, resulting in a pure product. This sidechain was then used directly in the formation of the monomer, **C_6g_3NDI-Br_2**, by condensation of commercially available 2,6-dibromonaphthalenedianhydride (**$NDABr_2$**) with the primary amine.[116,139] The particularly low yield of this reaction is common in literature and was attributed to the formation of the core-substituted amine, by S_NAr with the bromine atoms,[189] the products of which were visible by crude NMR and TLC. Fortunately, these were separable by column chromatography, resulting in the pure monomer, as verified by NMR and HRMS.

p(C_6g_3NDI-T) was also prepared via Stille cross-coupling polymerisation, reacting **C_6g_3NDI-Br_2** with commercially available 2 5-bis(trimethylstannyl)thiophene (**Figure 2.3**), in chlorobenzene, which allowed reaction temperatures up to 130 °C. This polymer also exhibited good solubility in chloroform at room temperature, thus molecular weight separation and purification using the preparative GPC remained possible, as well as allowing for convenient processing.

2.4 Molecular weight separation and determination

Each polymer was initially purified using the traditional Soxhlet purification method. Whilst this has been documented as a method for separating molecular weights,[190] the disadvantage is that fractions eluting later will likely have a higher purity than those eluted more quickly. Furthermore, as was the case with these polymers, no material was soluble in the Soxhlet washing solvents (hexane, ethyl acetate, acetone, methanol, tetrahydrofuran and dichloromethane), only dissolving in chloroform, therefore this separation technique was not viable. Instead, preparative GPC was employed to separate a single batch of polymer into four molecular weight fractions, collecting such that each fraction contained approximately the same amount of material, with the first fraction collected (fraction 1) being of highest molecular weight (**Figure 2.4**). Preparative GPC can also be viewed as an additional method of purification, as remaining impurities (typically palladium from the catalyst) are of lower molecular weight than any polymer chains and so are discarded after the elution of the polymer.

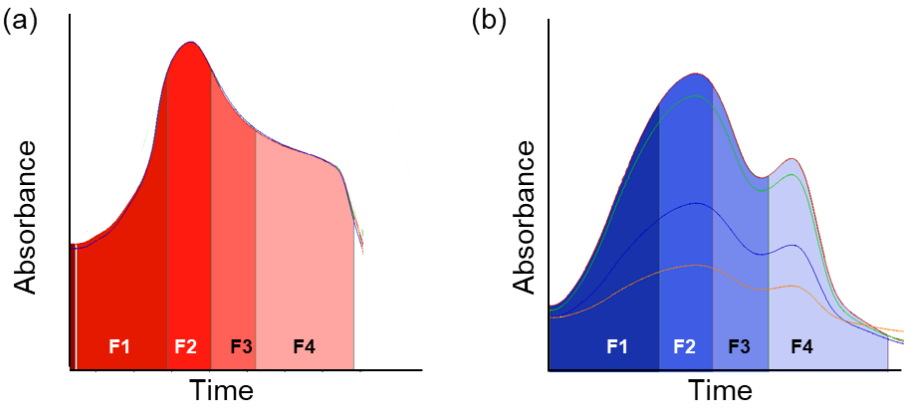


Figure 2.4. The preparative gel permeation chromatography trace for (a) **p(g$_4$T2-TT)** and (b) **p(C$_6$g$_3$NDI-T)** showing the second cycle, where the polymer is collected into four separate fractions, F1-4.

The molecular weight can be measured in various ways, including through gel permeation chromatography (GPC),[191–193] matrix-assisted laser desorption/ionization-time of flight

(MALDI-ToF)[116,139] and nuclear magnetic resonance (NMR) end group analysis.[194] Each method comes with limitations, for example, GPC is a relative technique, calibrated to polystyrene standards, which may not be a good comparison for polymers with different hydrodynamic volumes. The resulting inaccuracies make it difficult to compare different polymers by this method. Additionally, data may be inflated in the case of aggregation, or poor data analysis can lead to over-integration of bimodal distributions. Conversely, MALDI-ToF is likely to be an underestimation as heavier polymer chains may not 'fly'. Molecular weight analysis via NMR end group analysis often involves significant extra synthetic workload to develop model systems for comparison, and when the molecular weight is too high, the deterministic end group may not be visible, or accurately integratable, by NMR.

In this case, GPC was chosen as it avoided the need to synthesise additional model systems for end group analysis and was readily accessible. The measurements were conducted at 40 °C with respect to polystyrene standards, using either dimethylformamide (**p(g$_4$T2-TT)**) or chloroform (**p(C$_6$g$_3$NDI-T)**) as the eluent. It is not uncommon for glycolated polymers to display a bimodal distribution by GPC,[116,138] however these polymers, particularly once fractionated, showed ideal unimodal traces. This is unsurprising on account of the use of preparative GPC for fractionation, as it relies upon the same size exclusion method as the analytical GPC.

2.5 Properties of the polymers

2.5.1 Optoelectronic and physical properties

The two series' optoelectronic properties are summarized in **Table 2.1**. Cyclic voltammetry (CV) in 0.1 M tetrabutylammonium hexafluorophosphate ($TBAPF_6$) in acetonitrile was used to determine the ionization potential (IP) of **p(g$_4$T2-TT)**, which remains unchanged across the fractions at ~4.25 eV (**Figure 2.5(a)**), providing an estimate for the highest occupied molecular

orbital (HOMO).[13] The electron affinity (EA) of **p(C$_6$g$_3$NDI-T)** also shows no significant variation at ~4.18 eV (**Figure 2.5(b)**) and provides an estimate for the lowest unoccupied molecular orbital (LUMO). Each polymer exhibits discrete reduction or oxidation behavior, thus the limits of CV (due to redox of ambient species) result in being unable to obtain the EA for **p(g$_4$T2-TT)** and IP for **p(C$_6$g$_3$NDI-T)** using this method.

Table 2.1. Summary of the properties of **p(g$_4$T2-TT)** and **p(C$_6$g$_3$NDI-T)**.

Polymer		M_n (kDa) [$Đ$] [a]	$E_{g,opt}$ (eV)[b]	$\lambda_{max,\ sol}$ (nm)[c]	EA (eV)[d]	IP (eV)[d]
p(g$_4$T2-TT)	Neat	83.3 [1.36]	1.67	610, 915	-	4.23
	F1	180.1 [1.30]			-	4.24
	F2	107.9 [1.12]			-	4.25
	F3	61.3 [1.25]			-	4.24
	F4	18.4 [1.15]			-	4.26
p(C$_6$g$_3$T2-T)	Neat	42.4 [2.13]	1.65	323, 540	4.19	-
	F1	211.0 [1.95]			4.18	-
	F2	99.8 [1.34]			4.18	-
	F3	46.2 [1.67]			4.17	-
	F4	17.6 [1.48]			4.19	-

[a] Number-average molecular weight (M_n) and dispersity ($Đ$) measured by GPC vs polystyrene standards in dimethylformaldehyde for **p(g$_4$T2-TT)** or chloroform for **p(C$_6$g$_3$T2-T)** at 40 °C. [b] Optical band gap estimated from thin film UV-Vis absorption onset. [c] Peak wavelength obtained from solution UV-Vis absorption spectra in chloroform. [d] Calculated from the onset of the cyclic voltammogram of polymer thin films on glassy carbon electrode with 0.1 M tetrabutylammonium hexafluorophosphate as the supporting electrolyte using a platinum rod counter electrode and a silver/silver chloride reference electrode.

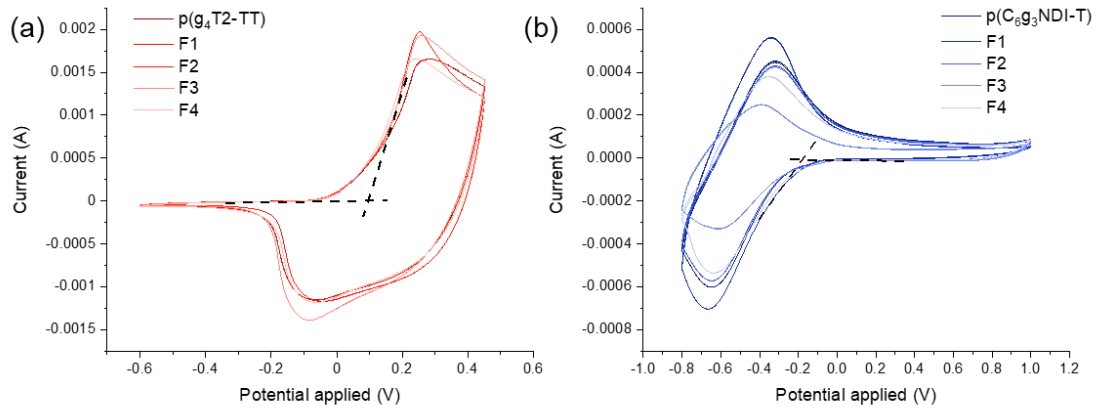


Figure 2.5. Cyclic voltammograms of neat and F1-4 of (a) **p(g4T2-TT)** and (b) **p(C6g3NDI-T)** determined by cyclic voltammetry of the polymer thin films on a glassy carbon working electrode vs Ag/AgCl in acetonitrile with 0.1 M tetrabutylammonium hexafluorophosphate as the supporting electrolyte, using a platinum rod counter electrode. The tangents on each graph indicate the method used for estimating the IP and EA with the intercept of the two tangents used as E_O and E_R (the oxidation and reduction onset potentials, respectively) in: $IP = 4.8 + E_O - E_f$ or $EA = 4.8 + E_R - E_f$, respectively. E_f is the average potential of the oxidation and reduction peaks in ferrocene and was found to be 0.44 V.

The UV-Vis absorption spectra of the polymers in chloroform solutions and as thin films are presented in **Figure 2.6**. **p(g4T2-TT)** presents a characteristic absorption profile as seen in previous reports of similar polymers,[71] where the λ_{max} (≈ 600 nm) is attributed to the π–π* transition (HOMO-LUMO transition), while the small lower energy band (≈ 950 nm) is most likely attributed to ambient-induced polarons (**Figure 2.6(a)**). The spectra for **p(C6g3NDI-T)** also matches previously reported literature,[139,195] with the π–π* transition ≈ 325 nm and the ICT energy band ≈ 600 nm (**Figure 2.6(b)**). The lack of spectroscopic shoulders present on the ICT bands in the UV-Vis absorption spectra in solution for either polymer series indicates that strong aggregation is not occurring in these materials, potentially due to fractionation.[196] The optical bandgaps ($E_{g,opt}$) were estimated from the absorption onset of the thin film spectra,

resulting in consistent bandgaps across each of the series. The normalised UV-Vis data supports the uniformity noted by CV for each polymer series, providing almost identical spectra across the molecular weights. This is unsurprising, given that no impact on the bandgap is expected above the effective conjugation limit.

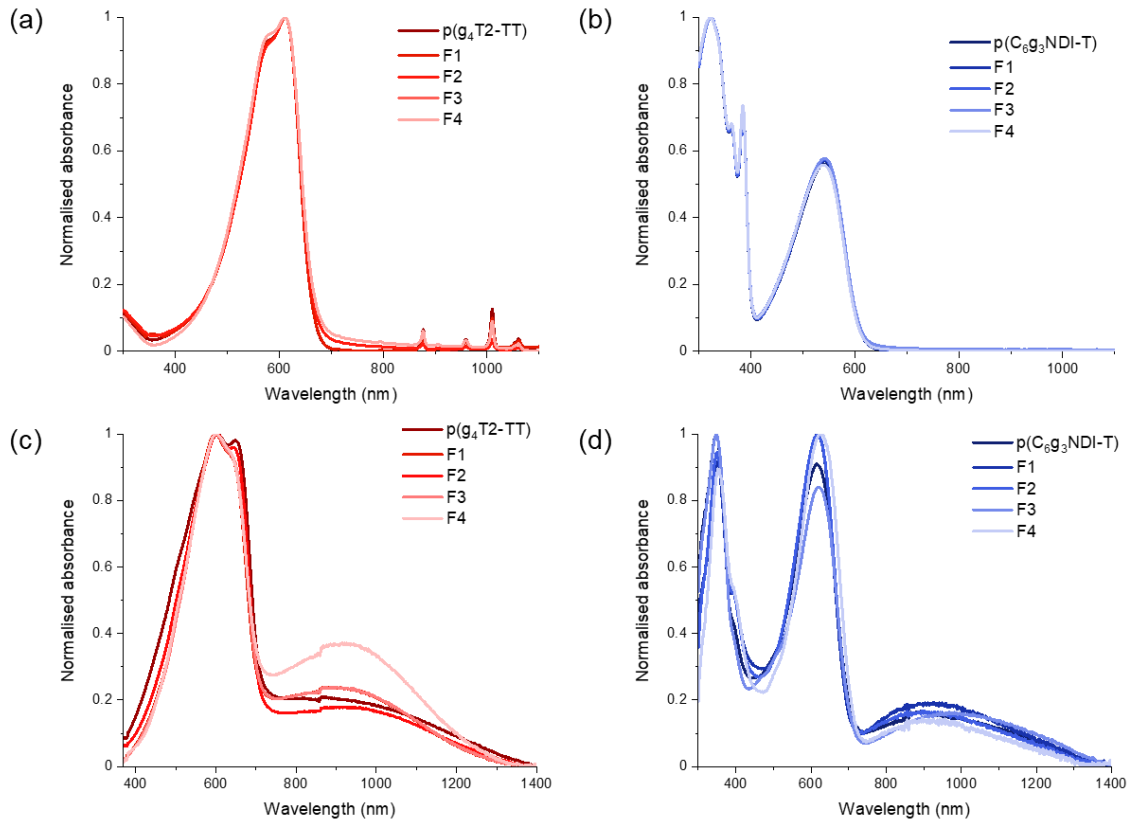


Figure 2.6. Normalised UV-Vis-NIR absorption spectra in chloroform solution of (a) **p(g$_4$T2-TT)** and (b) **p(C$_6$g$_3$NDI-T)** and as thin films on glass substrates of (c) **p(g$_4$T2-TT)** and (d) **p(C$_6$g$_3$NDI-T)**.

To understand the impact of residual palladium on the performance of the two polymers, the neat batch and each fraction underwent inductively coupled plasma mass spectrometry (ICP-MS) to calculate the concentration of Pd. Pd originates from the catalysts ($Pd_2(dba)_3$ or $Pd(PPh_3)_4$) employed for Stille polymerisations, which is typically used at around 2 mol%, which equates to ~3,000 ppm for **p(g$_4$T2-TT)** and ~4,900 ppm for **p(C$_6$g$_3$NDI-T)**. The Soxhlet

washing alone reduces the levels to around 25%, however preparative GPC fractionation is able to reduce levels by up to 97%, to 39 ppm (**Table 2.2**).

Table 2.2. Relating the method of purification and the concentration of residual palladium.

Polymer		M_n [kDa] [a]	Method of purification	Conc of Pd [ppm] [b]
p(g_4T2-TT)	Neat	83.3	Soxhlet	1769
	F1	180.1	Soxhlet + prep GPC	323
	F2	107.9		370
	F3	61.3		157
	F4	18.4		73
p(C_6g_3NDI-T)	Neat	42.4	Soxhlet	1176
	F1	211.0	Soxhlet + prep GPC	197
	F2	99.8		39
	F3	46.2		112
	F4	17.6		540

[a] Number-average molecular weight (M_n) measured by GPC vs polystyrene standards in dimethylformaldehyde for **p(g_4T2-TT)** or chloroform for **p(C_6g_3T2-T)** at 40 °C (as reported in **Table 2.1**). [b] Calculated from inductively coupled plasma mass spectrometry (ICP-MS, details in **Chapter 5**).

2.5.2 GIWAXS analysis

Grazing incidence wide angle X-ray scattering (GIWAXS) measurements of thin films spin cast onto p+ doped silicon wafer substrates were carried out to investigate the morphology of the polymer films ex situ. Line cuts of the untreated as-cast films are shown in **Figure 2.7** and the peak parameters are summarised in **Table 2.3**.

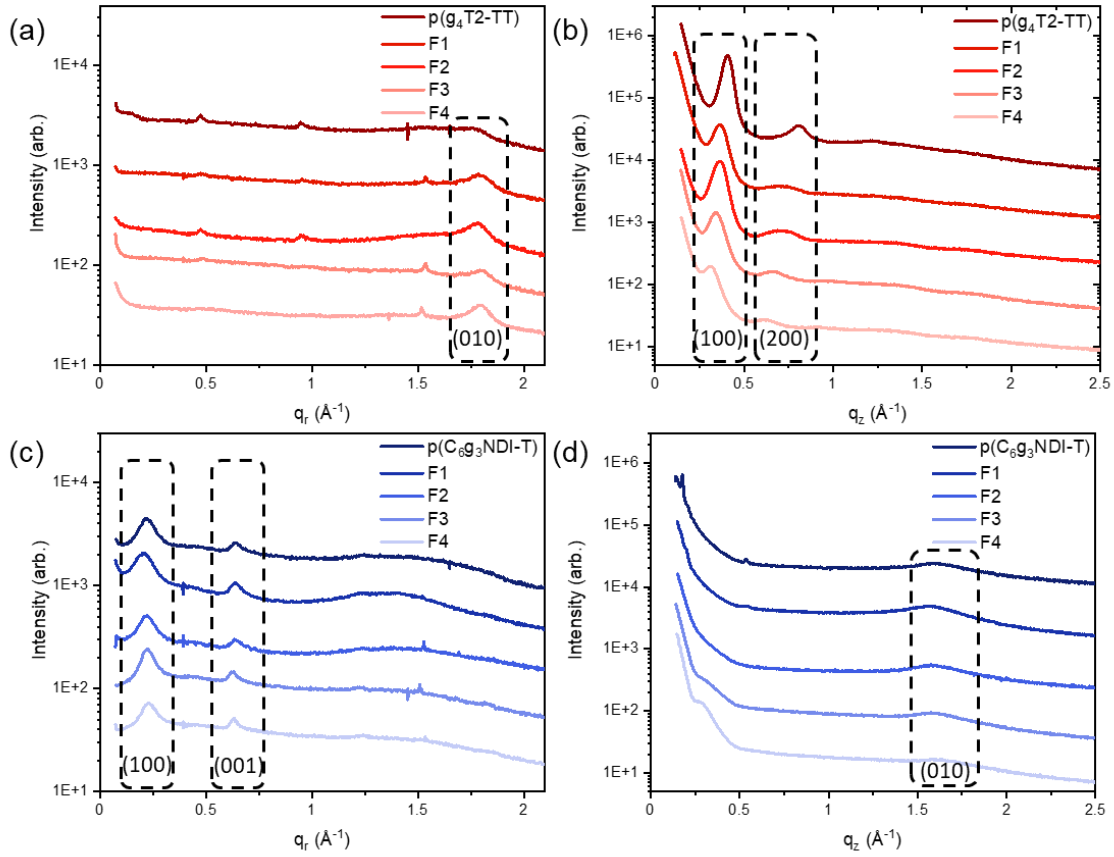


Figure 2.7. GIWAXS data of untreated as-cast films showing (a) in-plane (q_r) and (b) out-of-plane (q_z) line cuts of each fraction of **p(g$_4$T2-TT)** and (c) in-plane and (d) out-of-plane line cuts of each fraction of **p(C$_6$g$_3$NDI-T)**.

The general microstructure of **p(g$_4$T2-TT)** presents in an edge-on orientation and is similar to previously reported glycolated polythiophene polymers.[49,73] The process of fractionation acted to resolve the π-stack, compared to the neat batch, which may be due to the influence of a large dispersity. Additionally, after fractionation, the in-plane π-stack exhibited a contraction of between 0.05 and 0.09 Å and narrower diffraction peaks (which translates to a longer coherence length) in the backbone direction compared to the neat polymer. Finally, the polythiophene polymer showed two orders of out-of-plane lamellar scattering (100 and 200 in **Figure 2.7(b)**), with the fractions showing expanded lamellar spacings and reduced coherence lengths compared to the neat polymer.

Table 2.3. GIWAXS peak parameters for **p(g$_4$T2-TT)**.

Polymer		M_n [kDa] [a]	π-π stacking [b]		lamellar stacking [c]		lamellar stacking [d]
			d (Å)	L_c (Å)	d (Å)	L_c (Å)	d (Å)
p(g$_4$T2-TT)	Neat	83.3	3.58	25.0	15.5	102	15.6
	F1	180.1	3.51	35.1	17.0	90.2	17.5
	F2	107.9	3.53	47.0	17.4	74.9	17.3
	F3	61.3	3.49	68.7	18.4	71.5	18.9
	F4	18.4	3.50	65.3	19.8	75.8	20.2

[a] Number-average molecular weight (M_n) measured by GPC vs polystyrene standards in dimethylformaldehyde at 40 °C (as reported in **Table 2.1**). [b] In-plane π-stack scattering peak (010). [c] Out-of-plane lamellar scattering peak (100). [d] Second order out-of-plane lamellar scattering peak (200).

The n-type polymer, **p(C$_6$g$_3$NDI-T)**, was oriented face-on, as is typical for NDI polymers in literature.[116,138,173] On account of the broad and relatively weak (010) out-of-plane π-stack peaks (**Figure 2.7(d)**), the material is thought to have a high degree of paracrystalline disorder.[27] A subtle trend was also observed, with a small expansion in the out-of-plane *d*-spacing (π-stack) and lamellar stack with increasing M_n. NDI-based materials typically have two different packing configurations, namely either Form I or Form II.[197] The Form I polymorph occurs when one NDI unit has cofacial registration with the NDI unit of another chain, while Form II occurs when the NDI unit aligns with the bithiophene unit of another chain.[197] Here, the polymer shows exclusively Form I, due to the (001) in-plane backbone spacing ~20.0 Å correlating with the length of an NDI-T repeat unit (**Table 2.4**). This is also expected for the NDI-T motif because the length of the single thiophene does not allow for cofacial registration with NDI due to the difference in size, as the Form II polymorphs are typically observed with NDI-T2 motifs.

Table 2.4. GIWAXS peak parameters for **p(C$_6$g$_3$NDI-T)**.

Polymer		M_n [kDa] [a]	π-π stacking [b]		lamellar stacking [c]	backbone stacking [d]
			d (Å)	L_c (Å)	*d* (Å)	*d* (Å)
p(C$_6$g$_3$NDI-T)	Neat	42.4	3.92	3.60	28.3	19.6
	F1	211.0	3.99	10.3	30.4	19.6
	F2	99.8	3.97	10.8	28.4	19.6
	F3	46.2	3.95	16.5	27.7	20.0
	F4	17.6	3.90	-	26.7	19.9

[a] Number-average molecular weight (M_n) measured by GPC vs polystyrene standards in chloroform at 40 °C (as reported in **Table 2.1**). [b] Out-of-plane π-stack scattering peak (010). [c] In-plane lamellar scattering peak (100). [d] In-plane backbone scattering peak (1'00).

2.5.3 Electrochemical activity in aqueous electrolytes

To understand the electrochemical operation of OMIEC materials in aqueous electrolytes is of the utmost importance when rationalising their behaviour in OECTs. Ideally, reduction and oxidation onset potentials close to zero are desired for aqueous operation to minimise the energy required to operate the device, as well as to avoid electrochemical redox processes of ambient species, such as oxygen and water. To first investigate the reversibility (i.e. stability) and any trend in redox onset potentials, CVs were performed in 0.1 M NaCl aqueous electrolyte. As displayed in **Figure 2.8**, the polymers can be reversibly charged and discharged in the aqueous electrolyte, with the redox onset potential remaining constant across all fractions of each polymer. For **p(g$_4$T2-TT)**, this gives an oxidation onset potential of ≈ -0.1 V vs Ag/AgCl (**Figure 2.8(a)**), whilst for **p(C$_6$g$_3$NDI-T)**, this results in a reduction onset potential of ≈ -0.1 V vs Ag/AgCl (**Figure 2.8(b)**).

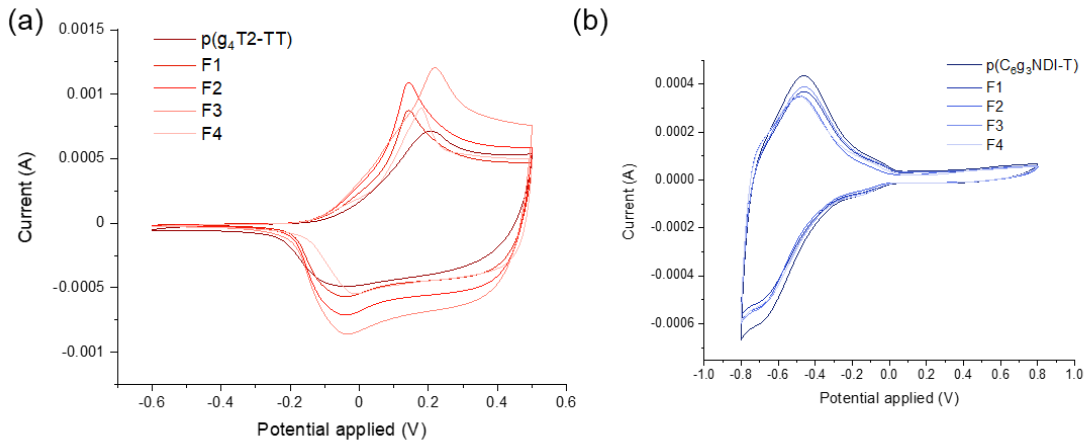


Figure 2.8. Cyclic voltammograms of the polymer films on the glassy carbon electrode, in degassed 0.1 M NaCl aqueous solution with a scan rate of 0.1 V s^{-1}, using a Pt rod counter and Ag/AgCl reference electrode, where (a) is **p(g$_4$T2-TT)** and (b) is **p(C$_6$g$_3$NDI-T)**.

The doping process in this aqueous electrolyte was further probed by spectroelectrochemical measurements, whereby the progression of the UV-Vis spectra was monitored as each polymer underwent electrochemical redox (**Figure 2.9**). For **p(g$_4$T2-TT)**, the polymer was initially fully de-doped (i.e. the ambient-induced polarons were removed) by applying a potential of -0.2 V vs Ag/AgCl. The presence of the ambient-induced polaron is supported by the negative oxidation onset potential observed by aqueous CV and the small, broad polaron peak observed at ~950 nm in the thin film UV-Vis spectra (**Figure 2.6(c)**). Charging in 0.1 V intervals between -0.2 and +0.2 V vs Ag/AgCl resulted in bleaching of the π-π* peak at ~600 nm. As potentials became positive, the peak at ~950 nm reappeared, which provides further evidence of its attribution to the polaronic species.[49,191] As potentials were further pushed into the positive regime, the polaronic peak decreased in intensity, and a new peak at higher wavelengths appeared, which is attributed to the bipolaronic species.

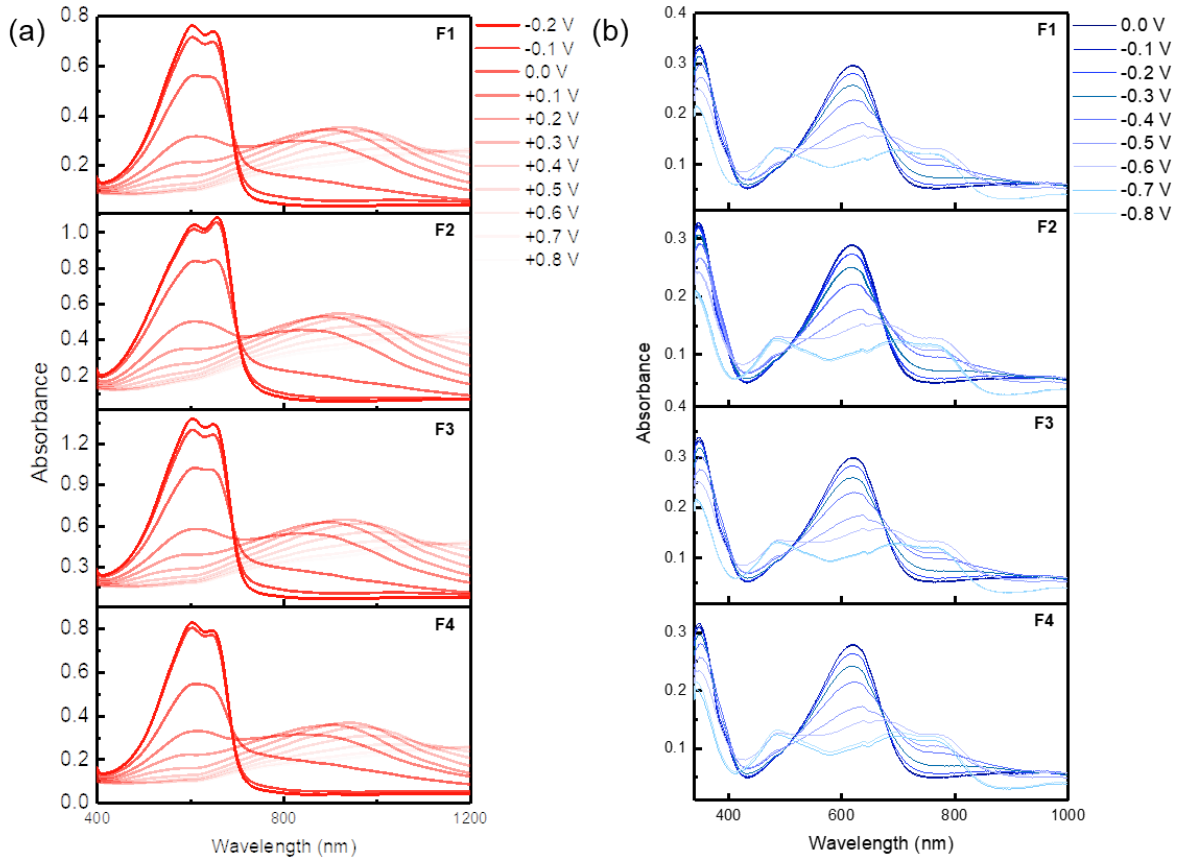


Figure 2.9. Progression of the UV-Vis absorption spectra for fractions 1-4 of (a) **p(g$_4$T2-TT)** during charging between -0.2 and +0.8 V and (b) **p(C$_6$g$_3$NDI-T)** during charging between 0 and -0.8 V, in 0.1 V steps, in degassed 0.1 M NaCl aqueous electrolyte.

For **p(C$_6$g$_3$NDI-T)**, the polymer was charged between 0 and -0.8 V vs Ag/AgCl. There was no need to charge the polymer with positive potentials because the neutral state exhibited fully de-doped characteristics (i.e. no polaronic peak). Progressive charging to -0.8 V causes a significant decrease in the intensity of the ICT band, whilst two new absorption features appear at ~480 and 790 nm. These can be thought of as the new π-π* and ICT transitions, whereby additional charge in the molecule alters the energy of the S1 energy level, which causes these shifts to be observed from the neutral UV-Vis absorption spectra, as corroborated by literature.[195]

For both materials, a large extent of doping was observed, which was consistent across all fractions. After spectroelectrochemical measurements, both polymers were returned to the initial applied voltage (-0.2 or 0 V for **p(g$_4$T2-TT)** or **p(C$_6$g$_3$NDI-T)**, respectively) and all fractions of both materials showed full de-doping, with this trace directly overlaying the initial spectra in all cases. This indicates excellent reversibility of these polymers in aqueous media, with no degradation observed.

2.5.4 OECT characteristics

Next, the effect of molecular weight on OECT performance was investigated by employing devices with a geometry of W = 100 µm and L = 10 µm. These devices were fabricated and the films cast as per the procedure in **Chapter 5**. Mimicking the aqueous CVs, all devices were operated in a degassed 0.1 M aqueous NaCl electrolyte, with an Ag/AgCl pellet gate electrode. The devices were operated with no post-deposition treatments (i.e. the materials were not annealed), and as expected for these backbones, all devices were found to operate in accumulation mode. The OECT characteristics show good agreement with aqueous CV measurements, where the measured V_T broadly correlates to the observed redox onset potentials (**Table 2.5**).

Table 2.5. Steady-state OECT performance of the polymers

Polymer		Conc of Pd [ppm] [a]	μ_{OECT} [$cm^2\ V^{-1}\ s^{-1}$] [b]	C^* [$F\ cm^{-3}$] [c]	[μC^*] [$F\ V^{-1}\ cm^{-1}\ s^{-1}$] [d]	g_m' [$S\ cm^{-1}$] [e]	V_T [V] [f]
p(g$_4$T2-TT)	Neat	1769	3.13 ± 0.52	120 ± 9	374 ± 67	295 ± 57	0.16 ± 0.014
	F1	323	5.65 ± 0.19	123 ± 15	694 ± 87	494 ± 17	0.085 ± 0.008
	F2	370	5.31 ± 2.65	246 ± 21	1308 ± 662	838 ± 438	0.041 ± 0.015
	F3	157	6.53 ± 0.065	308 ± 20	2008 ± 130	1457 ± 6	0.067 ± 0.003
	F4	73	8.53 ± 0.40	114 ± 14	972 ± 127	626 ± 38	0.019 ± 0.002
	F3 + $Pd_2(dba)_3$	2157	3.02 ± 0.26	287 ± 18	860 ± 56	602 ± 21	0.10 ± 0.010
	Mixed [g]	236	4.75 ± 1.12	123 ± 17	451 ± 124	231 ± 56	-0.064 ± 0.008
p(C$_6$g$_3$NDI-T)	Neat	1176	$1.02 \times 10^{-3} \pm 3.79 \times 10^{-4}$	222 ± 79	0.227 ± 0.117	0.055 ± 0.021	0.29 ± 0.005
	F1	197	$3.57 \times 10^{-3} \pm 2.94 \times 10^{-4}$	129 ± 55	0.461 ± 0.202	0.127 ± 0.017	0.27 ± 0.014
	F2	39	$5.34 \times 10^{-3} \pm 3.40 \times 10^{-4}$	306 ± 127	1.632 ± 0.688	0.155 ± 0.020	0.22 ± 0.020
	F3	112	$6.06 \times 10^{-4} \pm 1.58 \times 10^{-4}$	521 ± 160	0.316 ± 0.127	0.095 ± 0.024	0.25 ± 0.006
	F4	540	$2.26 \times 10^{-3} \pm 2.53 \times 10^{-4}$	250 ± 78	0.563 ± 0.188	0.164 ± 0.018	0.24 ± 0.003
	F2 + $Pd_2(dba)_3$	2039	$1.10 \times 10^{-3} \pm 1.52 \times 10^{-4}$	124 ± 26	0.136 ± 0.0341	0.029 ± 0.003	0.36 ± 0.005
	Mixed [g]	198	$1.96 \times 10^{-3} \pm 2.25 \times 10^{-4}$	257 ± 101	0.503 ± 0.205	0.110 ± 0.012	0.28 ± 0.004

[a] Calculated from inductively coupled plasma mass spectrometry (ICP-MS, detailed in **Chapter 5**). [b] OECT mobility calculated from the transistor saturation [μC^*] product using the respective C^* values. [c] C^* values extracted from Randles circuit fits from electrochemical impedance curves of the polymers coated on Au electrodes in 0.1 M aqueous NaCl solution. [d] [μC^*] calculated for the highest performing channel from the slope of g_m with known channel dimensions and applied bias. [e] Peak OECT transconductance normalized by thickness. [f] Threshold voltage extracted from a plot of $\sqrt{I_D}$ versus V_G. [g] Formed by combining a mass ratio of 1:1.4:1.4:1 of F1:F2:F3:F4, which resulted in M_n = 90.6 kDa and M_w = 142.3 kDa for **p(g$_4$T2-TT)** and M_n = 61.2 kDa and M_w = 102.1 kDa for **p(C$_6$g$_3$NDI-T)**.

To understand the impact of residual Pd on the OECT performance, and separate its effect from molecular weight, the concentration of Pd can be compared with the charger carrier mobility, which shows a near-perfect correlation with the concentration of Pd (**Table 2.5** and **Figure 2.10(a)**). Seven out of the eight fractions very clearly follow this trend where, as the

concentration of Pd is reduced, the charge carrier mobility increases. As for these two polymers, the vast library of OMEICs available are synthesised via cross coupling conditions, which, in the case of Stille and Suzuki polymerisations, employs a molecular Pd catalyst.[71,73,116,138,139] Previous studies indicate that residual Pd present in semiconducting polymers predominantly exists in the form of Pd(0) nanoclusters,[184,198,199] which are able to trap electrons, due to the low work function of Pd, compared to the LUMO energy of many polymers. Specifically, the LUMO of **p(C$_6$g$_3$NDI-T)** is ~-4.18 eV, considerably shallower than the value of -5.1 to -5.2 eV attributed to Pd,[200,201] allowing favourable charge transfer to the Pd nanoclusters (**Figure 2.10(b)**). Not only are the electrons transferred to the Pd, but they are also then used to catalyse the oxygen reduction reaction (ORR), due to the device's operation in ambient conditions.

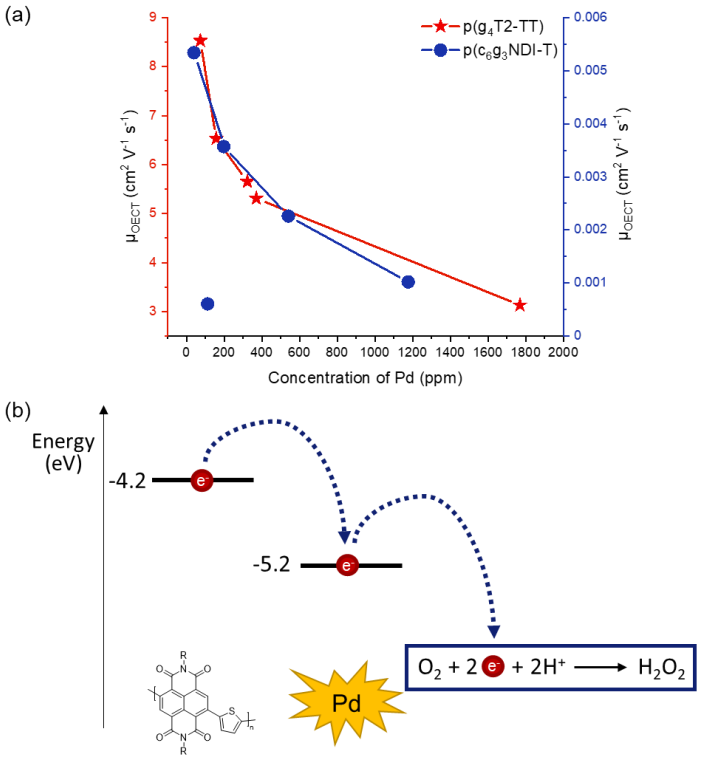


Figure 2.10. (a) μ_{OECT} vs concentration of Pd for **p(g$_4$T2-TT)** and **p(C$_6$g$_3$NDI-T)** and (b) the proposed mechanism for residual Pd to trap electrons, thus reducing charge carrier mobility.

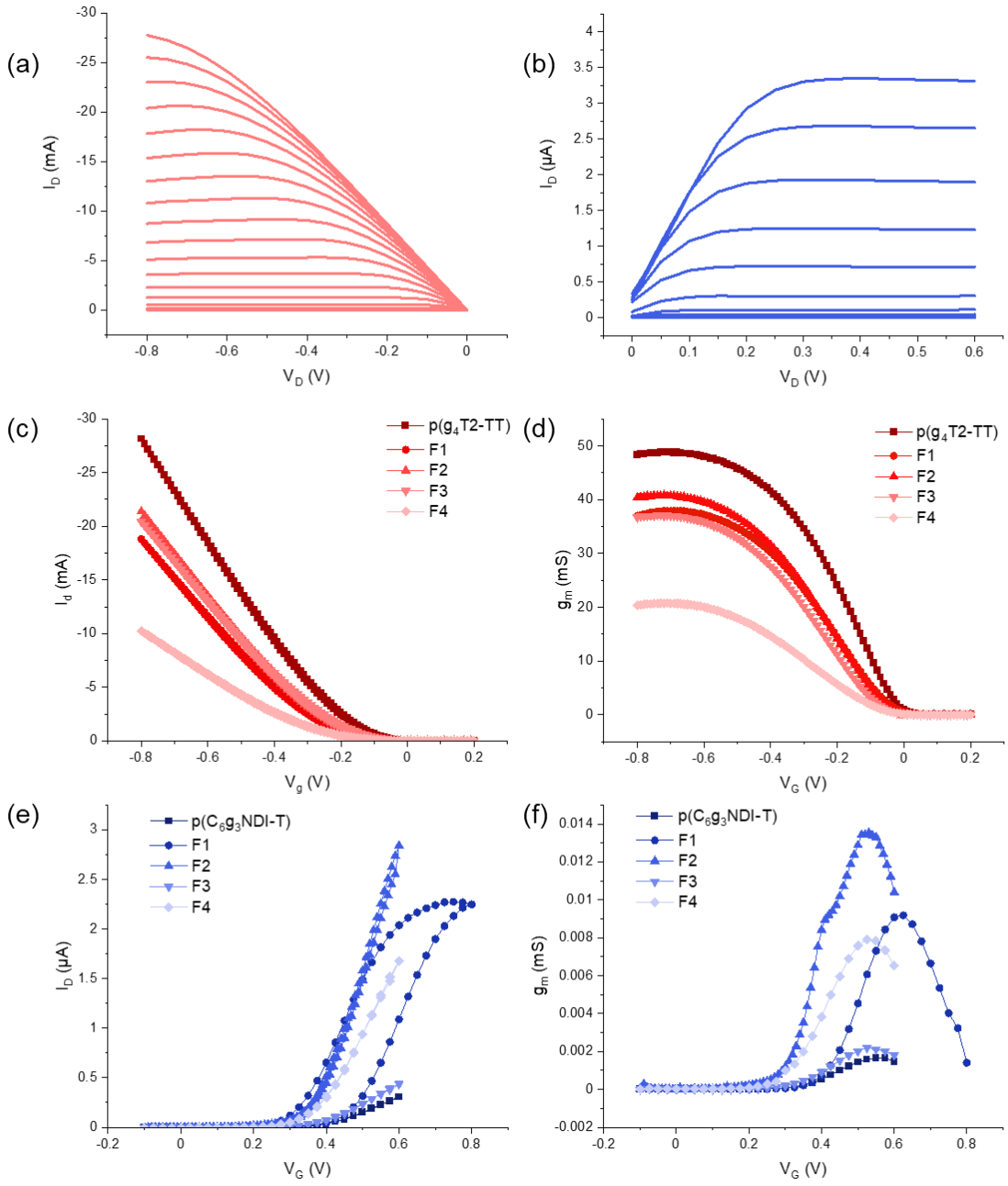


Figure 2.11. Performance of the OECTs (W = 100 μm, L = 10 μm, sweep rate of 0.1 V s^{-1}) in an aqueous 0.1 M NaCl solution in ambient conditions showing the output characteristics for (a) fraction 3 of **p(g_4T2-TT)** (V_G = 0.0 to 0.8 V, ΔV_G = 0.05 V) and (b) fraction 2 of (V_G = 0.0 to 0.6 V, ΔV_G = 0.05 V) for **p(C_6g_3NDI-T)**, (c) transfer curves and (d) transconductance vs V_G for **p(g_4T2-TT)** and (e) transfer curves and (f) transconductance vs V_G for **p(C_6g_3NDI-T)**.

As expected, the polythiophene-based polymer exhibited pure p-type behaviour, whilst the NDI-based polymer showed only n-type characteristics (**Figure 2.11**). For the **p(g$_4$T2-TT)** series, the thickness normalized transconductance increased to a peak of 1457 S cm^{-1} for fraction 3 (M_n = 61.3 kDa), then decreased as the M_n further increases. A similar trend is observed for **p(C$_6$g$_3$NDI-T)**, where the highest normalized transconductance was observed for fraction 2 (M_n = 99.8 kDa), at 0.155 S cm^{-1}. Interestingly, for both series, all values were larger than that of the unfractionated batch, which correlates to the higher charge carrier mobilities observed due to the reduced levels of Pd.

This trend was supported by [μC^*], where, again, all fractions were higher than the neat batch (see the dotted line on **Figure 2.**). Similarly, the trend across the fractions of both polymers is comparable, with an intermediate molecular weight appearing optimal for OECT performance in both cases. The [μC^*] value for the p-type increases from 694 (M_n = 180.1 kDa) to 1308 (M_n = 107.9 kDa) to 2008 F V^{-1} cm^{-1} s^{-1} (M_n = 61.3 kDa), a state-of-the-art OECT performance,[49,125,135,202–205] then decreases to 972 F V^{-1} cm^{-1} s^{-1} with decreasing M_n (**Figure 2.**). **p(C$_6$g$_3$NDI-T)** also mimicked the thickness normalized transconductance, with fraction 2 (M_n = 99.8 kDa) providing the maximal [μC^*] value at an impressive value of 1.632 F V^{-1} cm^{-1} s^{-1} (**Figure 2.**).

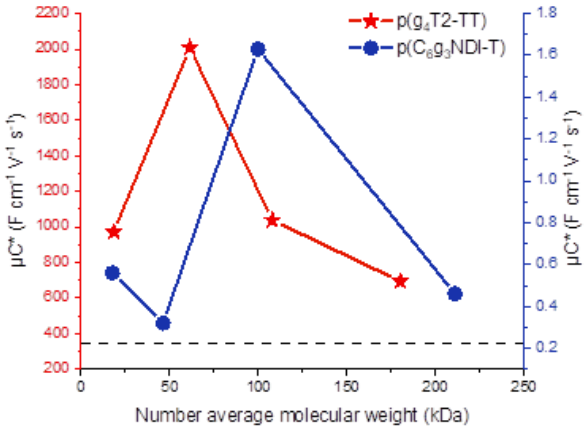


Figure 2.12. *[μC^*]* vs M_n for **p(g$_4$T2-TT)** and **p(C$_6$g$_3$NDI-T)**, where the dashed line indicates the performance of the polymer pre-fractionation.

To further understand these OECT characteristics, electrochemical impedance spectroscopy (EIS) was used to determine C^* at offset potentials of 0 to -0.8 V for **p(g$_4$T2-TT)** and of 0.3 to 0.8 V for **p(C$_6$g$_3$NDI-T)** vs Ag/AgCl in a 0.1 M aqueous NaCl electrolyte. For both the p- and n-type materials, C^* increased with increasing M_n, peaking at fraction 3, with C^* = 308 and 521 F cm^{-3}, respectively, dropping by over 50% in both cases as the molecular weight was further increased. High C^* values typically correlate with the polymer's ability to accommodate compensatory ions, however it is well-known that this comes at the cost of reduced charge mobilities, due to a disrupted microstructure.[49,177] This is partially validated with these materials, for example, fraction 3 of **p(C$_6$g$_3$NDI-T)** (M_n = 46.2 kDa) had the highest C^* value, but the lowest μ_{OECT} despite a lower concentration of electron trapping Pd. This neatly reveals that a subtle balance between C^* and μ_{OECT} is required to maximize OECT performance. Both polymer series indicate that there is an optimum M_n, above or below which, the performance drops, as evaluated by g_m and $[\mu C^*]$ (**Figure 2.**).

2.6 Discussion

Literature has previously reported that the microstructure of polymers used in OFET applications show significant differences at different molecular weights.[206] These differences were not observed in the GIWAXS images of these two polymer series, thus attributing the observed OECT performance solely to the molecular weight is incomplete. Instead, it remains likely that alternative factors are also at play, such as the purity of the materials. In OFET applications, the purity of polymers has been shown to have limited effect on device performance.[207] To understand the response of OFETs to the purity level of the two polymers, the neat and highest OECT performing fraction of each polymer was tested in a top gate/bottom contact OFET. Unfortunately, **p(g$_4$T2-TT)** acted as a conductor, thus did not respond to current modulations, and a mobility could not be extracted. Alternatively, **p(C$_6$g$_3$NDI-T)** displayed only low output currents, which translated to low electron mobilities for both the neat batch

and fraction 2, of 1.7 x 10^{-4} and 6.0 x 10^{-5} cm^2 V^{-1} s^{-1}, respectively (**Figure 2.13**). This data shows that for this n-type polymer, when operated in an OFET device, purity does not have a significant effect on performance, in fact, the performance is over two times higher for the polymer with higher contaminants. The difference in mobility here could instead be explained by the longer polymer chains in the neat batch providing a subtly preferable microstructure for OFETs, thus providing the dominant effect in terms of performance.

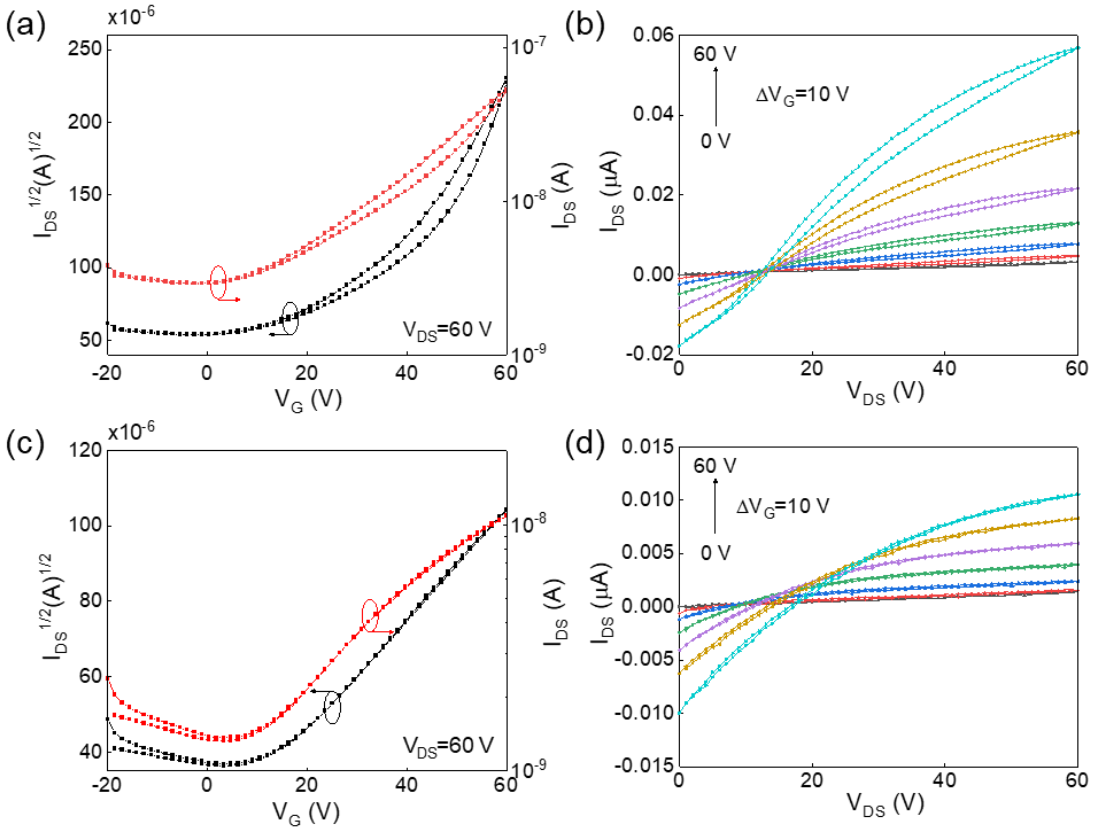


Figure 2.13. (a) The transfer curve and (b) output curve for neat **p(C_6g_3NDI-T)** and (c) the transfer curve and (d) output curve for F2 of **p(C_6g_3NDI-T)**. The transfer curves are recorded in the saturation regime, where V_{DS} = 60 V (black) and the mobility is calculated from the linear fit of the drain current square root (red). The output curves are measured for V_G = 0 V to V_G = 60 V in 10 V steps. The non-ideal output characteristics are attributed to the very low currents recorded.

Conversely, these subtle morphology differences do not appear to play a significant role in OECT mobility. One explanation for this is that the morphology of the material changes significantly during operation of an OECT (*c.f.* OFET operation), due to the swelling that occurs when the polymer is charged. It is therefore possible that these swelling-induced changes are more drastic than any initial differences in morphology, which hence are overridden during OECT operation. An additional difference between OECTs and OFETs is the use of an electrolyte vs a dielectric, respectively. As OFET measurements are often conducted under inert conditions, the effect of Pd is not observed in OFET applications as it is not able to catalyse ORR. By understanding this mechanism, it is possible to explain why the removal of Pd has such a large impact on the charge transport properties, particularly for the n-type polymer. Furthermore, ORR generates biologically toxic hydrogen peroxide, which hinders any application for these impure materials as a clinically safe bioelectronic sensor (**Figure 2.10(b)**).[137]

Interestingly, the mobility of the p-type material was also improved, although to a lesser degree, by the purification process. Whilst there were thought to be no accessible oxidation reactions that coincide with the energy of the hole polaron of **p(g$_4$T2-TT)**, impedance measurements on p-type polymers with similar energy levels reported that higher Pd levels can cause increased electrical resistance.[187] It is therefore hypothesised that Pd in the OMIEC polymers creates distortion in the semiconductor microstructure, and a subsequent local energetic disorder, reducing the charge carrier mobility in **p(g$_4$T2-TT).**

To decouple the impact of molecular weight vs palladium residues on the OECT performance of these polymers, two further experiments were conducted. In both cases, the OECT characteristics detailed in **Section 2.5.4** were repeated, firstly, with the best performing fraction of each polymer after the reintroduction of Pd, and secondly, by recombining a selected ratio

of the four fractions (**Table 2.5**). Through these measurements, it was possible to verify a causal relationship between the Pd content and the OECT performance, rather than just a correlation.

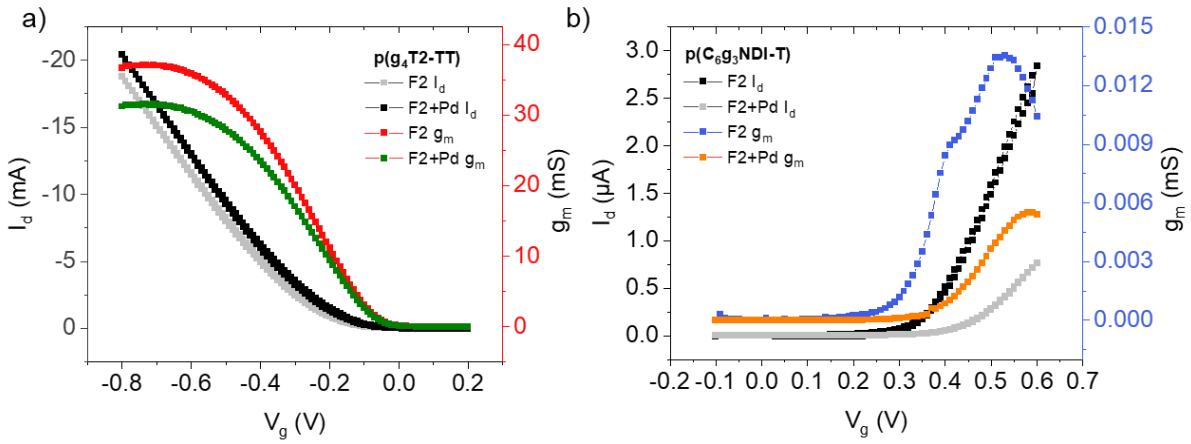


Figure 2.14. The transfer and transconductance curves for (a) fraction 3 of **p(g$_4$T2-TT)** before and after the reintroduction of 2,000 ppm of Pd and (b) for fraction 2 of **p(C$_6$g$_3$NDI-T)** before and after the reintroduction of 2,000 ppm of Pd.

The chloroform-soluble catalyst, $Pd_2(dba)_3$, was added to introduce 2,000 ppm of Pd to each of the two best performing fractions, fraction 3 of **p(g$_4$T2-TT)** and fraction 2 of **p(C$_6$g$_3$NDI-T)**, and the OECT characterisation was repeated (**Table 2.5**, **Figure 2.**). This offered one method to confirm that the improvement in charge carrier mobility could be attributed to the presence of Pd in the sample. In both cases, an increase in mobility was observed, with fraction 3 of **p(g$_4$T2-TT)** decreasing in hole mobility from 8.53 to 3.02 $cm^2\ V^{-1}\ s^{-1}$ upon reintroduction of Pd. This can primarily be ascribed to an increase in V_T from 0.067 to 0.10 V, and resulted in a deterioration in overall performance, with [μC^*] dropping by over 60%, from 972 to 361 $F\ V^{-1}\ cm^{-1}\ s^{-1}$. An even more dramatic effect was noted for fraction 2 of **p(C$_6$g$_3$NDI-T)**, where the mobility decreased five-fold, from 5.34 x 10^{-3} to 1.10 x 10^{-3} $cm^2\ s^{-1}\ V^{-1}$, again on account of an increase in V_T from 0.22 to 0.36 V. The increase in V_T which was observed for both materials with increased Pd levels can be explained by viewing Pd as charge trapping sites. These must be "filled" before the polymer contains excess charges which are then free to move.

Like the previous trend (**Figure 2.10**), the impact of Pd on the p-type polymer was less than that on the n-type polymer, for reasons suggested above.

Secondly, to ensure that the physical form of Pd was comparable (nanoclusters that naturally form during the work-up and processing of the polymer *c.f.* molecular Pd present when $Pd_2(dba)_3$ is added), the OECT characteristics were repeated for a final time on a device of combined fractions 1-4 of each polymer. The polymers were combined in a 1:1.32:0.16:1 mass ratio for **p(g$_4$T2-TT)** and in a 1:1.4:1.4:1 mass ratio for **p(C$_6$g$_3$NDI-T)** in an effort to maintain a Gaussian distribution for the GPC traces and are referred to as the "mixed" batch of each polymer. The Pd levels were calculated from the known ratio and Pd concentration of each of F1-4. The molecular weights were measured again to ensure the comparison was fair and were determined to be M_n mixed = 90.6 kDa vs M_n neat = 83.3 kDa for **p(g$_4$T2-TT)** and M_n mixed = 61.2 kDa and M_n neat = 42.4 kDa for **p(C$_6$g$_3$NDI-T)**. Due to the comparable M_n values and more accurate representation of the physical form of Pd, this method is also able offer a clearer understanding into the impact of Pd on OECT performance. Like the trend observed when reintroducing Pd to the highest performing fraction, the impact of purification appears to offer a greater improvement for **p(C$_6$g$_3$NDI-T)** than **p(g$_4$T2-TT)** (**Figure 2.15**). More specifically, the n-type sees a 92% increase in mobility from 1.02 x 10^{-3} to 1.96 x 10^{-3} cm^2 V^{-1} s^{-1}, compared to ~50% increase for the p-type, from 3.13 to 4.75 cm^2 v^{-1} s^{-1}, where both have comparable levels of Pd, at around 200 ppm. The mixed batches of both polymers show comparable C^* values to the neat batches, resulting in increases to [μC^*] that are very similar to those seen for mobility, boosting values from 0.227 to 0.503 F V^{-1} cm^{-1} s^{-1} for **p(C$_6$g$_3$NDI-T)** and from 374 to 451 F V^{-1} cm^{-1} s^{-1} for **p(g$_4$T2-TT)**. These results further verify that the removal of Pd is responsible for improving OECT performance.

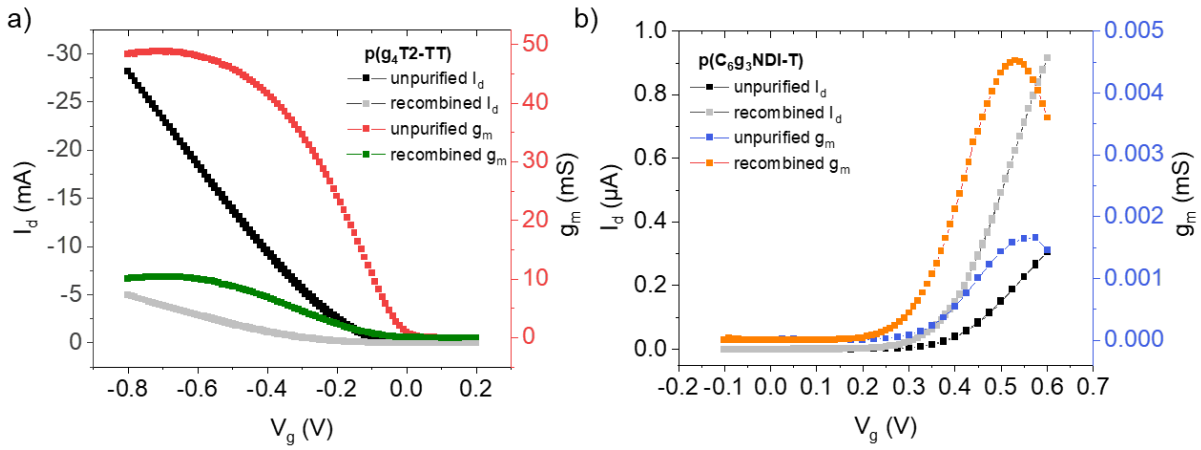


Figure 2.15. Transfer and transconductance characteristics for (a) neat and "mixed" **p(g$_4$T2-TT)** and (b) neat and "mixed" **p(C$_6$g$_3$NDI-T)**.

Whilst there may be some impact on the mobility due to differences in molecular weight, it is thought that in OMIECs, where charge transport pathways are severely disrupted by swelling,[119] the observed mobility variations are predominantly on account of the improved polymer purity.

2.7 Conclusion

This study presents a novel method for OMIEC purification, by more thoroughly removing by-products than only using traditional Soxhlet purification. Preparative GPC is also particularly useful for studying the impact of molecular weight as any batch-to-batch variations are removed. One batch is simply divided into several fractions of lower dispersity instead of synthesizing new batches through different reaction conditions, making this the most comprehensive method for comparing molecular weights.

By studying the optoelectronic, structural and transistor properties, the impact of the purity and molecular weight on OECT performance of two OMIECs, **p(g$_4$T2-TT)** and **p(C$_6$g$_3$NDI-T)**, was assessed. Conclusive trends could not be determined by solely examining the molecular

weight differences, thus the purity of the OMIECs was also considered, by measuring residual Pd concentrations of the purified and neat fractions using ICP-MS. By comparing the concentration of Pd to the OECT performance, a near perfect correlation was observed, with state-of-the-art performances recorded for both p- and n-type materials. To verify this relationship as causal, two further experiments were conducted, specifically, the reintroduction of Pd to the highest performing fractions, and by recombining the purified fractions. Together, these two methods confirmed that the removal of Pd was the cause of improved OECT performance, whereby reintroducing Pd, in the form of $Pd_2(dba)_3$, caused the mobility of the highest performing p- and n-type fractions to drop by almost three and five times, respectively. Additionally, the recombination of fractions allowed molecular weight variations to be removed, whilst ensuring a fair comparison between the physical form of Pd impurity (naturally occurring nanocusters *c.f.* molecular Pd added as $Pd_2(dba)_3$).

The residual Pd is thought to arrange in nanoclusters, which can both trap charge and act as a co-catalyst for ORR. This work is significant to the field of OECTs, and the wider use of OMIECs, because it emphasises safety concerns when applying these materials in biosensors, where the production of hydrogen peroxide results in unsafe devices. Furthermore, it highlights the issue that poor purification results in the underperformance of existing materials, hence preparative GPC offers a versatile method to achieve pure, safe and high performing p- and n-type materials.

Chapter 3

Calculations vs reality: Understanding the delocalisation length of NDI copolymers computationally and empirically

3.1 General information and attributions

DFT calculations were performed by Dr Karl Thorley (University of Kentucky). OECT and EIS measurements were carried out by Dilara Meli and Hans Xu (Rivnay Group, Northwestern University). GIWAXS measurements were performed and analysed by Dilara Meli and Dr Joshua Tropp (Rivnay Group, Northwestern University). The author would also like to thank Dr Bryan Paulsen (Rivnay Group, Northwestern University) for fruitful discussions throughout the evolution of the project.

3.2 Introduction

It is well understood in the field of OECTs that n-type material performance lags significantly behind their p-type counterparts, which is attributed to the reduced charge carrier mobility of electrons compared to holes in p-type materials.[40] This was indicated in **Section 1.5.4**, where the primary focus of the discussion was surrounding the stability of n-type materials to ambient operation. Instability can lead to reduced charge carrier mobility of n-type polymers, particularly if the electrons in the LUMO are of the appropriate energy to undergo side reactions. This results in the removal of electrons from the polymer, reducing charge carrier density and mobility.[208–211] Through careful selection of the monomers and/or with chemical modifications, the criterion of stability can typically be met, by designing materials with a LUMO deeper than -4.0 eV.[40,168]

Aside from stability, the poor charge transport properties of n-type materials can be understood by examining the delocalisation of the relevant molecular orbital across the backbone. Charge transport via delocalisation is preferred as it offers coherent transport pathways, whereas hopping relies on thermal energy to trigger charge movement between sites.[212] P-type polymers transport holes through the HOMO, whilst n-type polymers transport electrons through the LUMO. In high performing p-type materials, such as polythiophenes, the HOMO is generally

delocalised across the polymer backbone.[125] This is on account of the distribution of the electron density across the backbone, which is evenly spread, due to the equal "donor" characteristics of the repeating thiophene moiety (**Figure 3.11(a)**). This orbital delocalisation, combined with interchain orbital overlap, creates crystalline domains, improving charge transport pathways and boosting μ.[110]

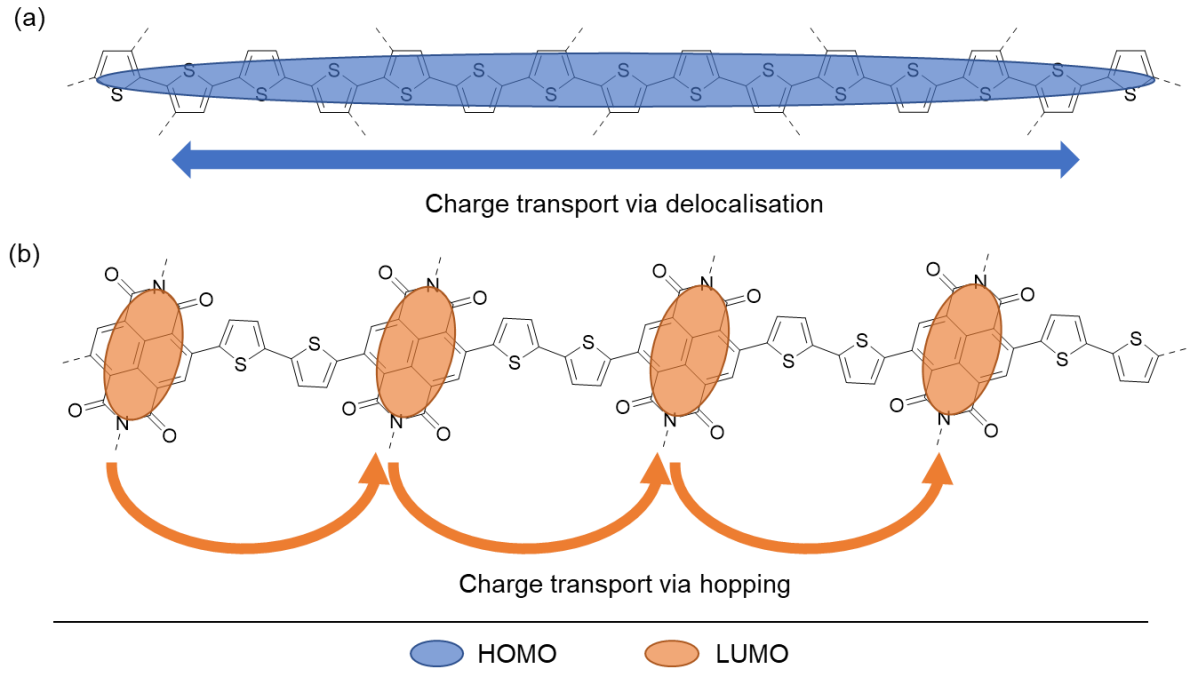


Figure 3.1. Schematics for (a) the delocalisation of the HOMO across a polythiophene polymer backbone, showing charge transport through the delocalised molecular orbital and (b) the localisation of the LUMO on the electron deficient NDI units along an NDI-T2 backbone, where electronic charge transport occurs via hopping between discrete sites.

This is not the case in common n-type materials, which typically employ a donor-acceptor (D-A) motif. Instead, the LUMO becomes highly localised on the electron deficient component, causing electrons to become confined to the lowest energy portions of the backbone, typically the acceptor units (**Figure 3.1(b)**).[213] This means that not only do charges have to hop between chains to continue transport pathways, but they must also hop intramolecularly from one electron deficient unit to the next. This is what is responsible for the poor electron mobilities

of many of the D-A n-type materials, such as NDI-T2 derivatives,[116,138,139] and motivated the work in this chapter. Another method to improve mobility involves reducing the number of trapping sites and subsequently decreasing the number of immobile charge carriers. This can be achieved by minimising the defects in the material (both arising in the microstructural arrangement and from miscouplings during the polymerisations) and improving the material purity.[40,211] By designing more planar structures, the microstructural defects can be reduced, theoretically improving charge carrier mobility.

NDI is the most prevalent n-type backbone, both within the field of OMIECs and beyond.[40] It was therefore selected as the primary candidate to understand, both theoretically and empirically, how to design new materials for improved electronic mobility. The proposed polymers are set out in **Figure 3.2** and aim to investigate the effect of the size (highlighted in blue), electron density (highlighted in yellow) and planarity (highlighted in green) of the comonomer on delocalisation of the LUMO and overall OECT performance.

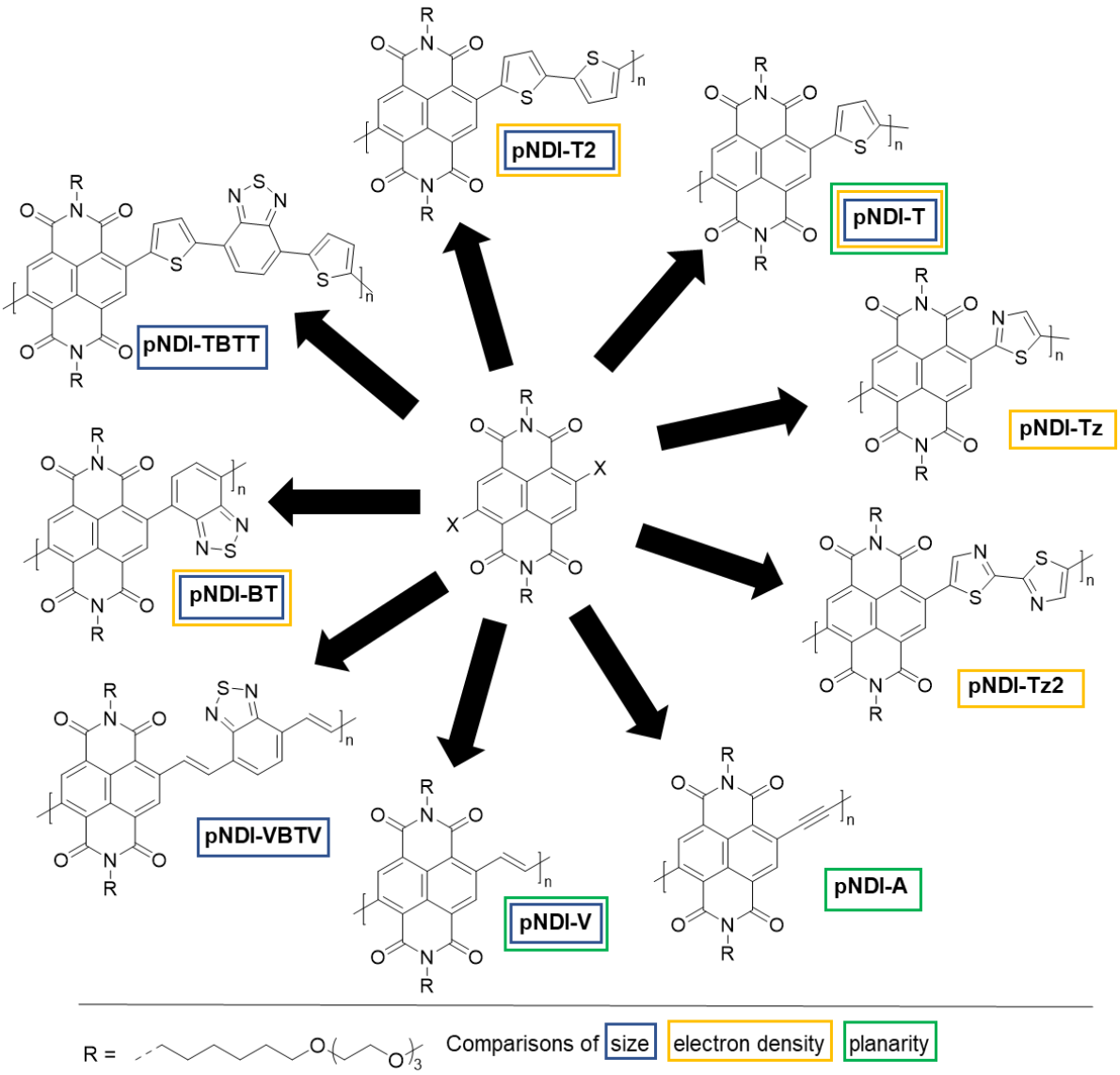


Figure 3.2. Structures of the nine proposed NDI-based polymers investigated in this chapter.

3.3 Density Functional Theory (DFT) calculations

Density Functional Theory (DFT) calculations of the nine different methyl-functionalised NDI-based tetramers were carried out at the ωB97XD/6-31G* level of theory to investigate the frontier orbital wave function distribution (i.e. the degree of delocalisation) and the planarity of the polymer backbone. This level of theory was selected due to its suitability as a good predictor of empirical results.[214] The distributions of the LUMO were examined in the three

different groupings indicated in **Figure 3.2**, comparing size, electron density and planarity of the comonomer.

To investigate the impact of the size of the comonomer on the delocalisation of the LUMO, six structures were compared, with the comonomer varying between 19 atoms and 2 atoms in size. By examining the LUMO delocalisation across these tetramers (**Figure 3.3**), qualitatively, the LUMO appears to be spread most evenly across the **NDI-V** structure. This indicates that its smaller size enables the LUMO to better delocalise. This observation could be partially attributed to the improved planarity offered by **NDI-V** compared to the other backbones, however interestingly, the **NDI-VBTV** also has a relatively low dihedral angle of 35.7° between the NDI and the vinyl group of the comonomer. It is likely that this is due to the smaller size of the flanking vinyl groups compared to the benzothiadiazole or thiophene comonomers.[215] However, this planarizing effect does not translate to a well delocalised LUMO for **NDI-VBTV**, likely due to the total size of the vinyl flanked benzothiadiazole being too large.[55] The reduced dihedral angle of both copolymers containing a vinyl group adjacent to NDI suggests that its moderate size prevents steric clash between itself and the NDI and is also able to act as a "spacer" between NDI-NDI or NDI and another bulky comonomer to reduce the steric hinderance.[216] Other comonomers, such as the thiophene-containing comonomers (e.g. **NDI-T**, **NDI-T2** and **NDI-TBTT**), are not able to do this effectively.

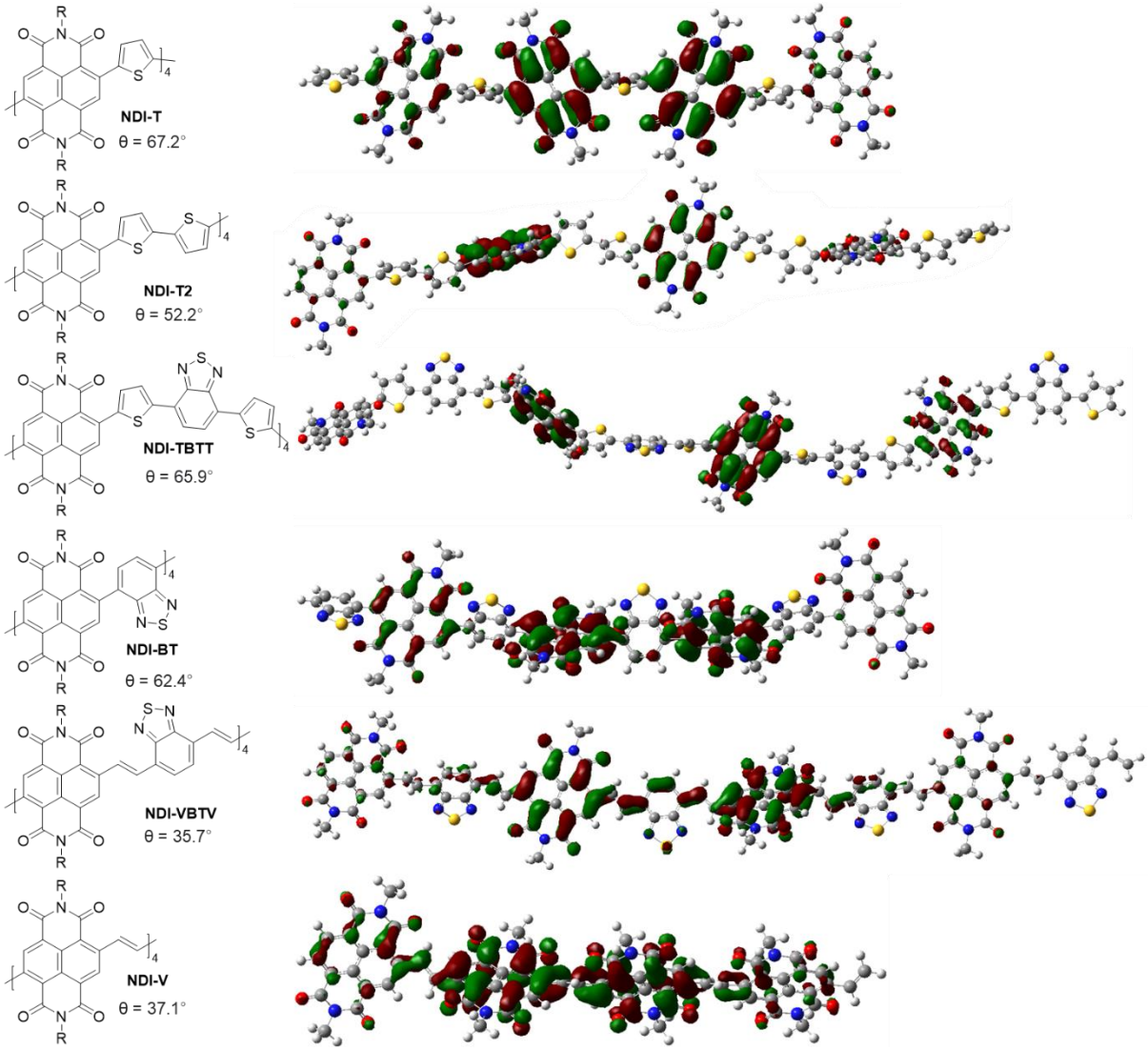


Figure 3.3. Investigating the impact of the size of the comonomer. DFT calculations of methyl-substituted NDI-based tetramers at the ωB97XD/6-31G* level of theory, showing the energy-minimised structures of the LUMO wave function distributions and the average dihedral angle across the NDI-X bond, allowing for comparison of the size of the comonomer.

Subsequently, the comonomer was varied to understand the impact of electron density on the LUMO delocalisation. Typically for NDI-based polymers, particularly in the field of OMIECs, literature precedent favours a D-A structure. To challenge this approach, acceptor-acceptor (A-A) structures were proposed. The five tetramers for comparison in this series were: **NDI-T** (D-A), **NDI-T2** (D-A), **NDI-BT** (A-A), **NDI-Tz** (A-A) and **NDI-Tz2** (A-A) (**Figure 3.4**).

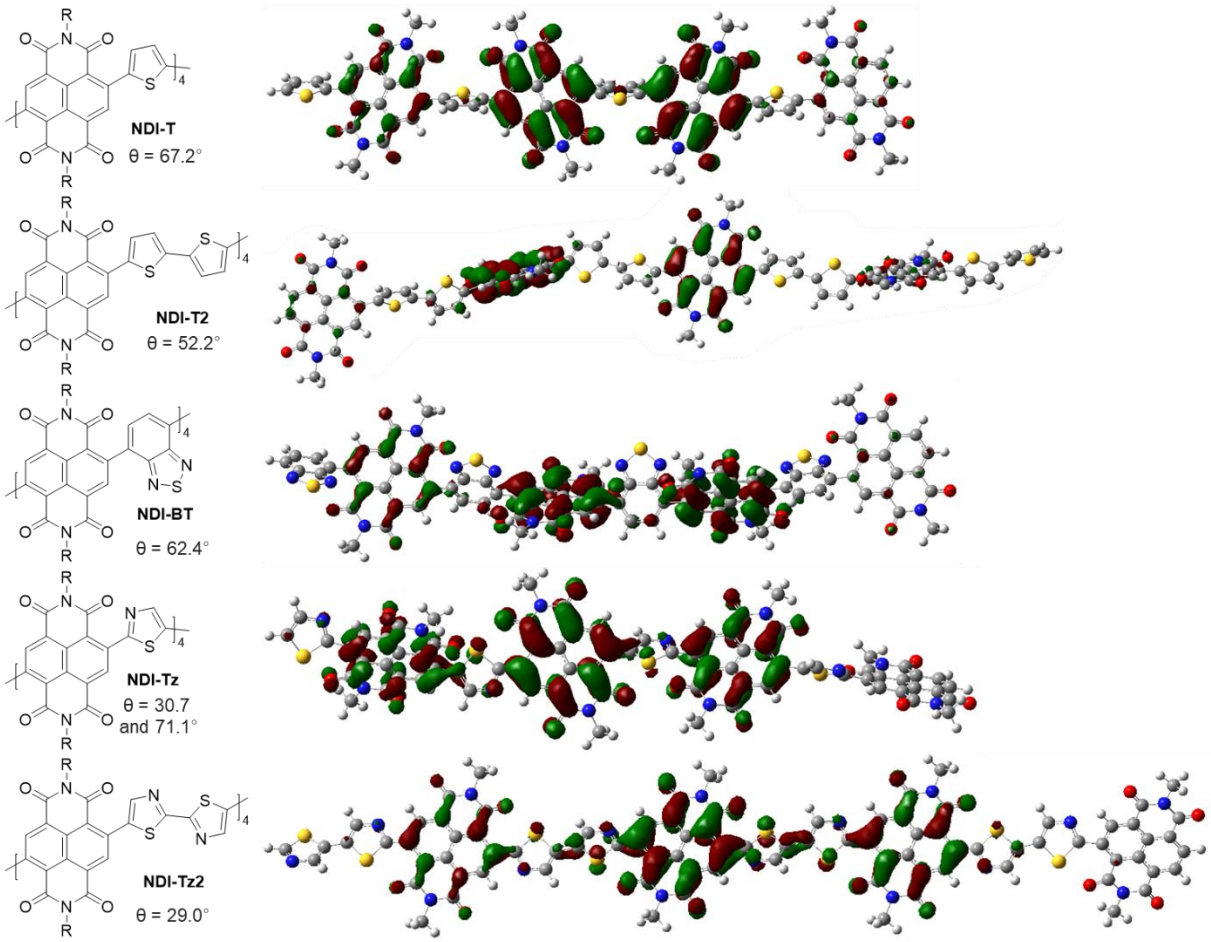


Figure 3.4. Investigating the impact of the electron density of the comonomer. DFT calculations of methyl-substituted NDI-based tetramers at the ωB97XD/6-31G* level of theory, showing the energy-minimised structures of the LUMO wave function distributions and the average dihedral angle across the NDI-X bond, allowing for comparison of the electron density of the comonomer.

This series qualitatively demonstrates that electron accepting character assists with improving the degree of delocalisation, where the BT and Tz comonomers show a better spread of the LUMO, both onto more NDI units and onto the comonomer to differing degrees. Unfortunately, due to the phenyl-phenyl linkage present in the **NDI-BT** system, the aromatic form dominates over the quinoidal, thus limited planarization is observed. This is expected to limit the degree of delocalisation, as planarity is required for optimal overlap of orbitals over the entire backbone, explaining why the A-A nature does not translate to a fully delocalised

LUMO. However, the A-A nature does make some contribution to delocalisation because although the thiophene and bithiophene comonomers have similar dihedral angles to the BT system, DFT predicts virtually no LUMO presence on any of the thiophene motifs, due to their D-A motif, whilst the BT system has a small LUMO contribution.

The degree of delocalisation appears to be further enhanced by the size of the comonomer, where the smallest and most electron poor comonomer, thiazole, appears to have the best degree of delocalisation of the five systems. However, due to its asymmetry, two distinct dihedral angles are observed, where the N of the thiazole has a planarizing effect when neighbouring the NDI core ($\theta = 30.7°$). Conversely, this does cause the dihedral angle to be larger for the opposite configuration ($\theta = 71.1°$), where NDI connects to the 5-position of thiazole (i.e. when the thiazole N is further from the NDI), causing a twisted conformation and somewhat reducing the degree of delocalisation. This twisting is avoided for the symmetrical 5,5'-bithiazole derivative (**NDI-Tz2**), where θ is equal throughout the backbone at 29.0°, however it is thought that the larger size of the comonomer is responsible for the poorer degree of LUMO delocalisation. The 2,2'-bithiazole derivative was also modelled, however the degree of twisting was larger at ~90°,[217] hence the 5,5'-bithiazole isomer was selected going forward.

Finally, the conformation of the model tetramer systems was further investigated. Taking into account the hypothesis that reducing the size of the comonomer appears to be beneficial in delocalising the LUMO, the smallest units with varying planarity were selected (**Figure 3.5**). The first in the series is **NDI-T**, where the large dihedral angle and strong D-A characteristics result in the LUMO being highly localised on the NDI unit. By replacing the thiophene with a vinyl, the dihedral angle is reduced and planarity increases along the backbone, encouraging the degree of delocalisation to increase. However, **NDI-V** is still able to access the relatively free rotation about the σ-bonds adjacent to the π-bond, which gives the molecule a "floppy" nature. By replacing the vinyl comonomer with an alkynyl unit, the increased planarity of the

backbone could be explored, while maintaining a similar electron density. Due to the sp hybridisation of the carbon centres in the alkyne bond, the contiguous atoms are held in the same plane as the triple bond, minimising the dihedral angle to as little as 7.2° from θ = 37.1° for **NDI-V**. Qualitatively, the LUMO delocalisation also appears to be superior for **NDI-A**, as it is able to take advantage of both its small and planar nature. From this data, it is evident that both the size and planarity of the comonomer are influential, with a smaller and more planar comonomer being preferrable to aid with delocalisation of the LUMO across the backbone.

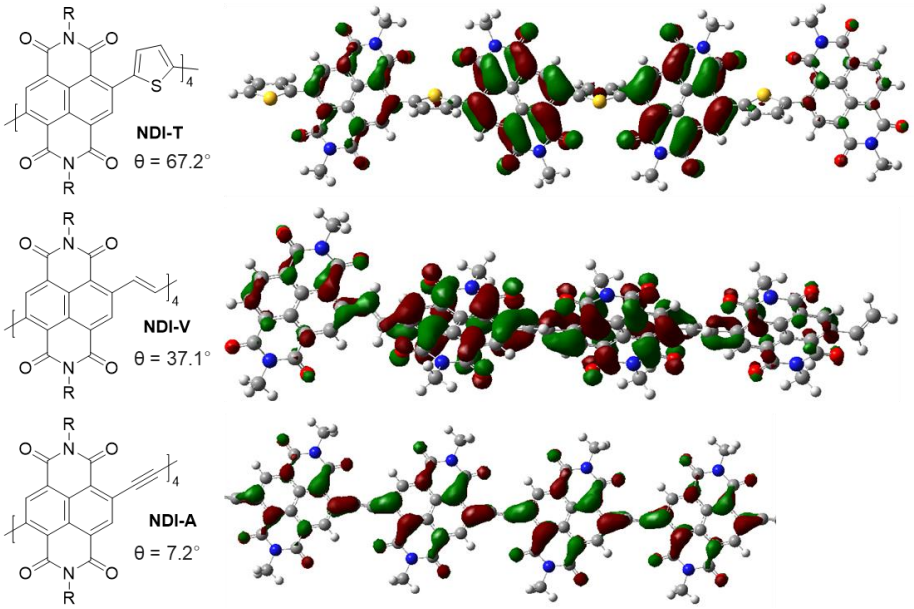


Figure 3.5. Investigating the impact of the planarity of the backbone. DFT calculations of methyl-substituted NDI-based tetramers at the ωB97XD/6-31G* level of theory, showing the energy-minimised structures of the LUMO wave function distributions and the average dihedral angle across the NDI-X bond, allowing for comparison of the planarity of the backbone.

3.4 Synthesis of the polymers

The sidechain utilised in this series was selected due to its superior OECT device performance with the NDI moiety.[139] This can be attributed to the ability of the hybrid sidechain to modulate swelling of the polymer to maximise the charge transport properties.[138,139] This was deemed an

important property because disturbance of the microstructure via swelling may also disrupt the degree of delocalisation. Furthermore, as the aim of extending delocalisation is to realise an improved electronic mobility, the alkyl "sheath" can act to maintain distance between the ion and the polaron, avoiding charge localisation and trapping.[138]

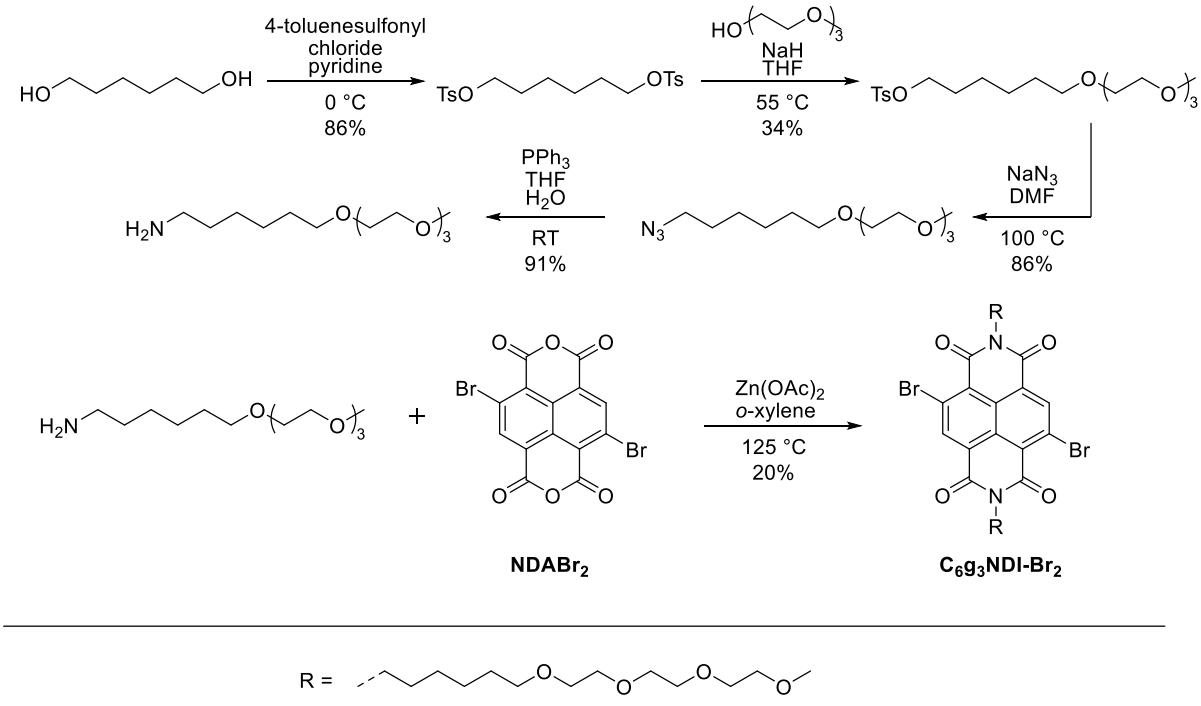


Figure 2.3. (adapted) Synthetic route to **C_6g_3NDI-Br_2**.

The sidechain and monomer, **C_6g_3NDI-Br_2**, were synthesised as per **Figure 2.3**. From this, a range of polymers were accessible via Stille and Suzuki polymerisation conditions (**Figure 3.6**).

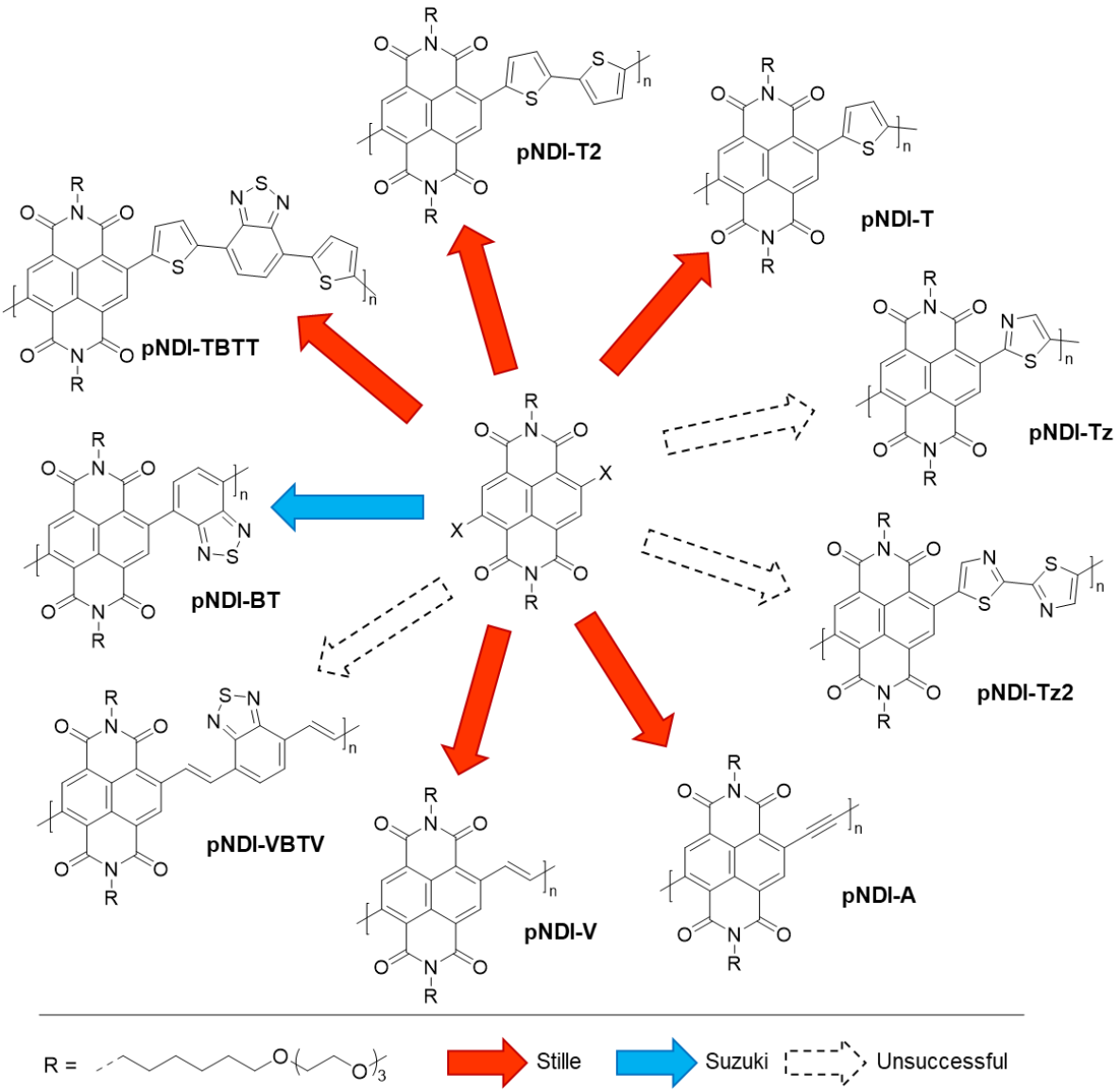


Figure 3.6. The successful synthesis of six polymers from the monomer **C$_6$g$_3$NDI-Br$_2$**, where the red arrows indicate synthesis by Stille polymerisation conditions and the blue arrow indicates synthesis by Suzuki polymerisation conditions. Dashed arrows indicate that the polymer was not successfully synthesised.

The thiophene, bithiophene, vinyl and alkynyl comonomers were all commercially available as bis(trimethyltin) derivatives. The thiophene derivatives were recrystalised and dried under high vacuum before use in the polymerisation, however, 1,2-bis(trimethylstannyl)ethene and 1,2-bis(trimethylstannyl)ethyne exist as liquids, thus were used directly in the polymerisation without further purification. It was found that a higher molecular weight and a lower dispersity

could be accessed by first weighing the liquid monomer directly into the reaction vial, then recalculating the other monomers to this mass, rather than calculating quantities using the density of the liquid monomer, as the micro-syringe did not convey sufficient accuracy. Of the four polymerisations, only the **pNDI-A** polymer proved problematic, with poor yields of 13% reported. This yield was ascribed to the insoluble nature of the polymer due to the rigidity of the backbone, conferred by the alkynyl unit. Trials involving reducing the reaction time and concentration as well as deliberately unbalancing the stoichiometry were carried out, however these resulted in significantly poorer molecular weights. The optimal M_n of 11.3 kDa was achieved with standard Stille reactions conditions (see **Chapter 5**), and whilst the molecular weight initially appears relatively low, the low mass of the alkynyl comonomer means that this M_n value equates to an average of nine repeat units per chain.

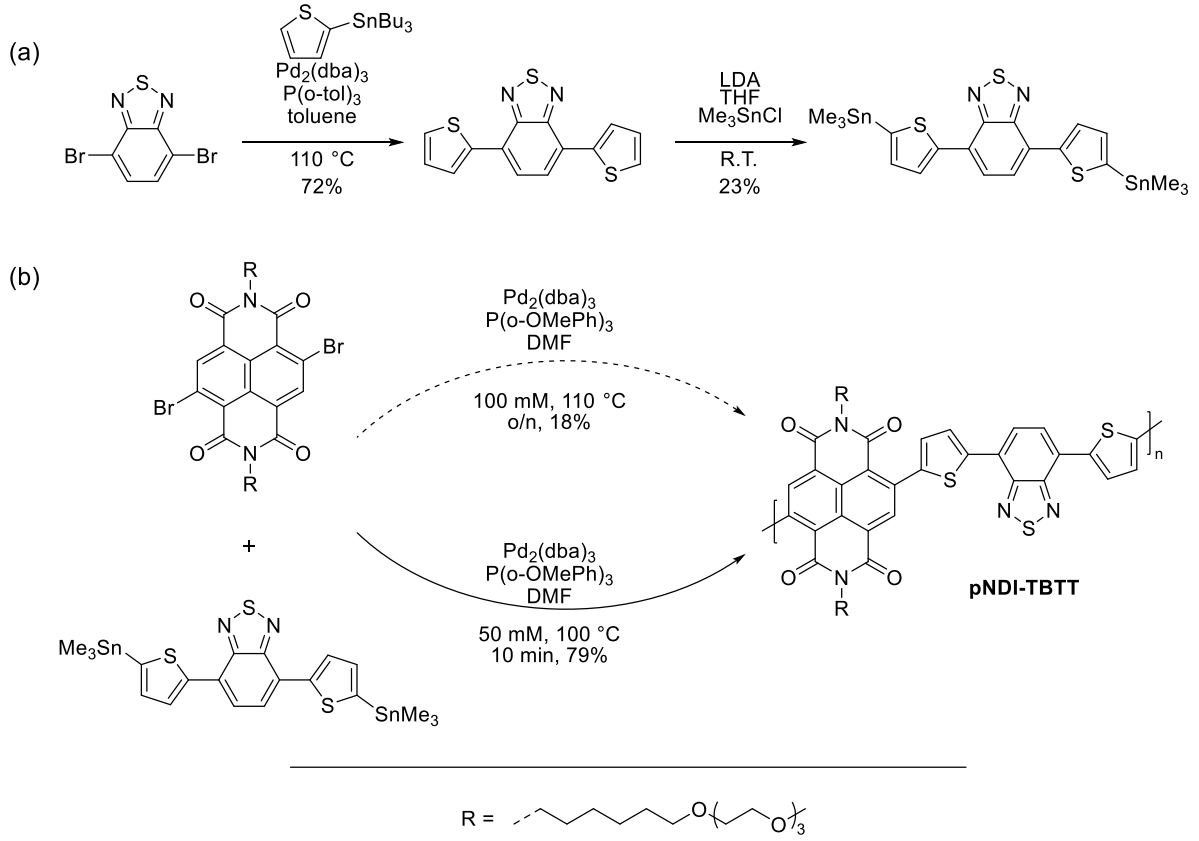


Figure 3.7. Synthetic route to **pNDI-TBTT** via monomer 4,7-bis(5-(trimethylstannyl)thiophen-2-yl)benzo[c][1,2,5]thiadiazole. The dashed reaction in (b)

indicates the first polymerisation attempt and the solid line denotes the optimised polymerisation conditions.

The thiophene flanked benzothiadiazole was synthesized in two steps from commercially available 4,7-dibromobenzo[c][1,2,5]thiadiazole in a combined yield of 17% (**Figure 3.7(a)**).[218] The poor cumulative yield can be attributed to the low yield of the stannylation step (23%), which is most likely due to a wet bottle of trimethyl tin chloride. This resulted in significant amounts of the mono(tributyltin) product being recovered during purification by preparative gel permeation chromatography. Promisingly though, the isolated product was very pure by ^{1}H and ^{13}C NMR and presented with the correct mass by HRMS (see **Chapter 5**). 4,7-Bis(5-(trimethylstannyl)thiophen-2-yl)benzo[c][1,2,5]thiadiazole was then used in typical Stille polymerization conditions to match those used for the four polymers above. The first attempt at the polymerization was left to react overnight, as is standard procedure for Stille conditions. Unfortunately, due to the large nature of the comonomer, the reaction mixture solidified, even at high temperatures, and the resultant material was predominantly insoluble. The small amount of material that was soluble in the chloroform Soxhlet fraction had an M_n of 2.1 kDa, which is equivalent to two repeat units. The polymerization was repeated, diluting the reaction mixture from ~0.1 mmol mL^{-1} to ~0.05 mmol mL^{-1}, and the reaction was only heated for 10 minutes (**Figure 3.7(b)**). On this occasion, when at 100 °C, the reaction mixture remained liquid, only gelling upon cooling. As the polymer remained in solution throughout the reaction, it allowed for the degree of polymerization to be controlled, such that the final polymer stayed soluble and processable. At the dilute concentration, the polymer was fully soluble in the chloroform fraction of the Soxhlet, with a 79% yield and M_n = 6.9 kDa achieved.

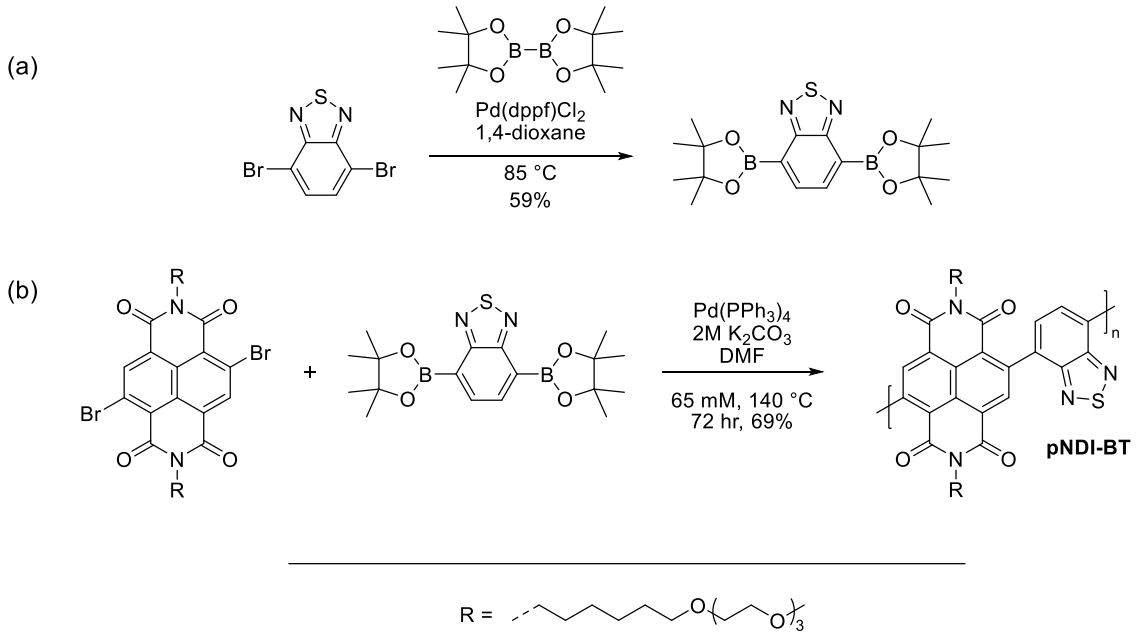


Figure 3.8. Synthetic route to polymer **pNDI-BT**, using Suzuki polymerisation conditions with monomer 2,1,3-benzothiadiazole-4,7-bis(boronic acid pinacol ester).

The final successfully synthesized polymer was made from 4,7-dibromobenzo[c][1,2,5]thiadiazole, which underwent a Miyaura borylation to form the monomer, 2,1,3-benzothiadiazole-4,7-bis(boronic acid pinacol ester) in one step, using literature conditions (**Figure 3.8(a)**).[219] This monomer required significant purification to be deemed pure enough for polymerisation, including by silica column chromatography and two recrystallisations from hexane. This monomer was then subjected to adapted Suzuki polymerisation conditions[219] with the brominated NDI monomer, **C$_6$g$_3$NDI-Br$_2$**, to afford polymer **pNDI-BT** (**Figure 3.8(b)**). With limited optimisation, a number average molecular weight value of 16.2 kDa was achieved, which is comparable to the other polymers, thus this procedure was not repeated.

Synthesis of the remaining three polymers intended to take advantage of either Stille or Suzuki conditions, however, this time using the NDI monomer as the organotin or organoborane component. This allowed for more freedom in designing the synthesis of the outstanding comonomers, requiring only halogenation at the polymerisation sites, rather than more

challenging stannylations or borylations. 2,5-Dibromothiazole is commercially available and was recrystallised from diethyl ether before use in a polymerisation. The planned synthetic pathways to the remaining two monomers, vinyl-flanked benzothiadiazole (4,7-bis(*[E]*-2-bromovinyl)benzo[c][1,2,5]thiadiazole) and bithiazole, are presented in **Figure 3.9**. 4,7-Bis(*[E]*-2-bromovinyl)benzo[c][1,2,5]thiadiazole was synthesised in two steps from 4,7-dibromobenzo[c][1,2,5]thiadiazole in a moderate yield of 27%, following a literature procedure.[220] The first step proceeded with significantly poorer yields than the reported 91%, however, this was due to insufficient stirring time during the acid-base purification, as considerable amounts of dark orange material were noted in the acidic filtrate the following day. These were then recovered and recrystallised from THF, and an additional 30% of product was recovered, increasing the yield to 69%.

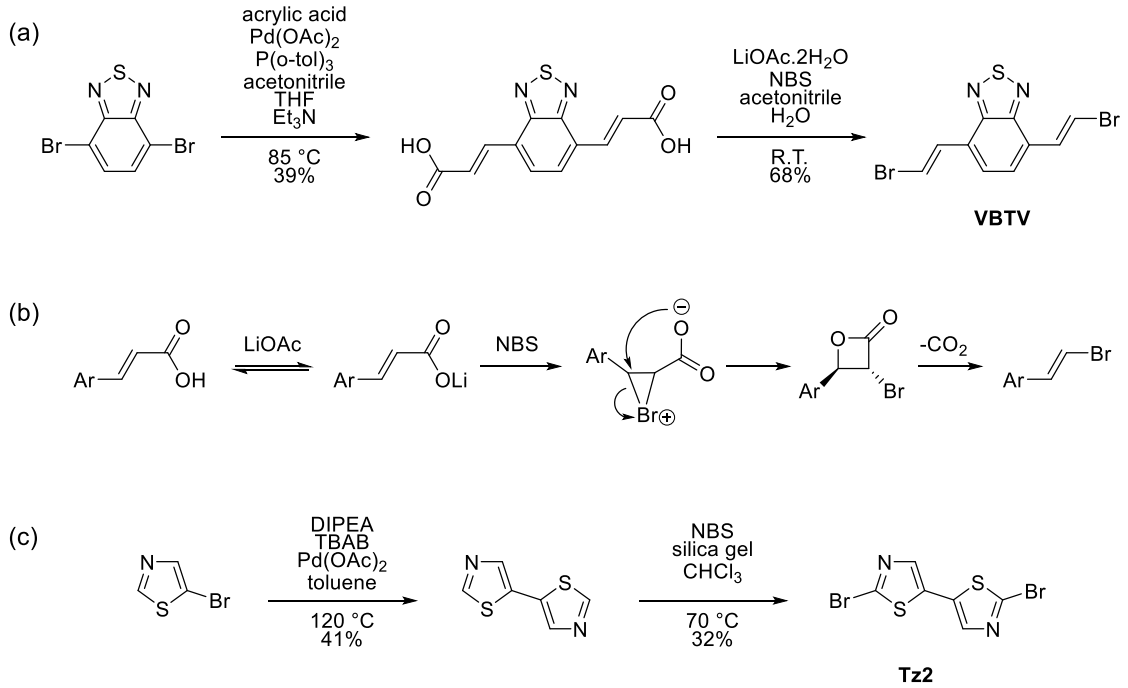


Figure 3.9. Synthetic pathway to (a) 4,7-bis([E]-2-bromovinyl)benzo[c][1,2,5]thiadiazole, (b) the mechanism for the transformation of the carboxylic acid functionalities into bromides, and (c) the synthetic route to 2,2'-dibromo-5,5'-bithiazole.

The bromination proceeded via the reaction mechanism depicted in **Figure 3.9(b)**, using the typical NBS brominating reagent, with the addition of catalytic amounts of lithium acetate.[221] NBS alone is not able to transform the electron deficient cinnamic acid derivative, it requires the formation of the lithium carboxylate, which can react with NBS to form the trans β-lactone. This intermediate is able to stereospecifically thermally decompose to produce only the trans-substituted product, **VBTV** (**Figure 3.9(b)**).[221]

The synthesis of 2,2'-dibromo-5,5'-bithiazole was streamlined from original literature, which requires four steps to reach the desired product.[222] Instead, Lui et al. reported a two-step synthesis in 2019,[223] which was reproduced in very similar yields (**Figure 3.9(c)**). Whilst higher yields have been reported, this involved the use of a synthesised organozinc complex,[224] which was not practical or within the remit of this project. Palladium acetate catalyses the coupling step and tetrabutylammonium bromide acts as a phase transfer agent. *N*,*N*-diisopropylethylamine, a hindered base, is required to regenerate the catalyst during the C-C bond forming reductive elimination step from the Pd^{II} to the Pd^{0} state. In the bromination step, 0.1 equivalents of silica gel were added to act as a catalyst, as has been demonstrated in several organic reactions,[225,226] as well as for brominations more specifically.[227,228] The reaction was initially attempted without silica and the starting material was completely recovered, with no product present, indicating that for this reaction to proceed, even at elevated temperatures, the catalyst is required. As verified by literature, stannylation of 5,5'-bithiazole was not possible,[223] likely due to the instability of the lithio-5,5'-bithiazole salts during the stannylation reaction.[222] This information confirmed that selecting the NDI unit for stannylation or Miyaura borylation was the best route to proceed.

There is scant literature precedent for the stannylation of the NDI core,[229] however due to the extremely electron deficient nature of the (bi)thiazole, this was deemed the preferential route. Synthetic efforts commenced by applying the literature procedure to the modified NDI core,

which achieved moderate yields of 34%, lower than the 48% reported in literature.[229] The literature procedure detailed the addition of the catalyst (0.05 equiv.) and ligand (0.20 equiv.) at both the start and after 24 hours of the reaction (trial 1, **Figure 3.10(a)**). After the second addition, the reaction was allowed to proceed for a further two days. Similar to the literature report, the mono(tributyltin) product was recovered, thus optimisation commenced with the aim of increasing the percentage conversion.

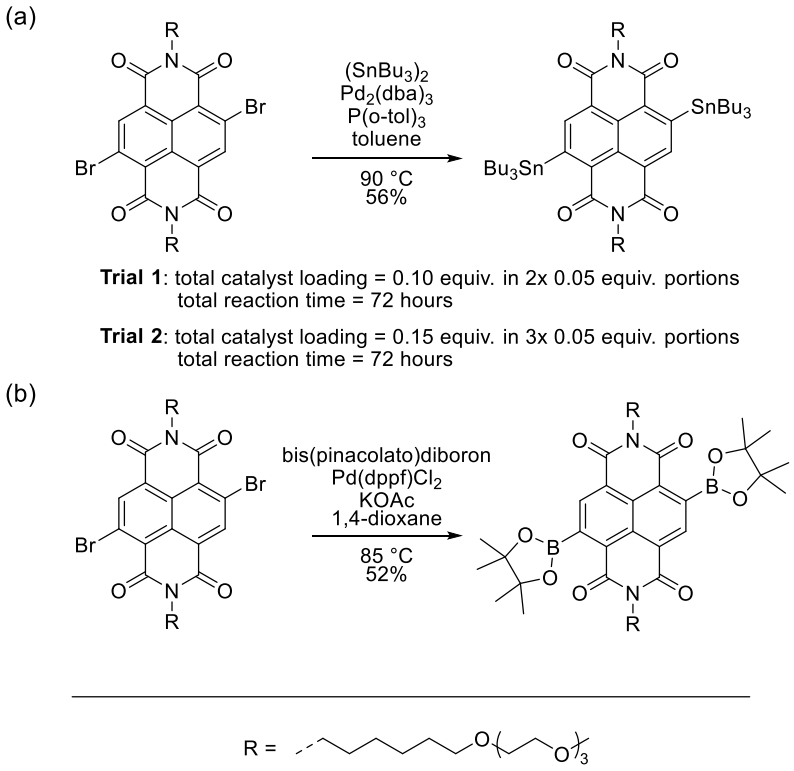


Figure 3.10. Synthetic pathways to bis(tributyltin) and bis(boronic ester) NDI monomers via (a) lithiation/stannylation and (b) Miyaura borylation.

In the repeat, the conditions were kept consistent, aside from the addition of a further portion of catalyst and ligand at t = 48 hours, after which, the reaction was allowed to proceed for another 24 hours, keeping the total reaction time constant (trial 2, **Figure 3.10(a)**). This resulted in a yield of 56% after purification of the desired product, with the mono(tributyltin) derivative being the most common side product. These conditions produced a sufficient mass of the monomer to progress, hence further optimisation of this step was not undertaken. It is thought

that the addition of extra catalyst and ligand throughout the reaction assists the yield because the catalyst becomes deactivated after a period of time, but unreacted starting material remains. The most likely reason for this would be mild leaks in the seals and joints of the vessel allowing external oxygen to enter the reaction, which oxidises the active catalytic species, $Pd[P(OPh)_3]_2$.[230] Overcoming this by reintroducing pre-catalyst periodically throughout the reaction appears to improve the conversion, thus increasing the yields beyond the values achieved here, this process could be repeated and the reaction time increased further.

The stannylated NDI monomer was then taken forward to react under Stille polymerisation conditions. Unfortunately, utilising the bis(tributyltin)-NDI did not yield successful polymerisations with any of the three comonomers. This was hypothesised to be on account of the combined electronics of the reaction, where the oxidative addition is able to proceed as normal, whilst the transmetallation is hindered by the electron deficient NDI core, which is unable to undergo the transfer from the Sn to the Pd. This may be attributed to the higher electron density and "post transition metal" nature of Sn, which is able to form stronger, more covalent-like bonds,[231] thus stabilising the NDI and preventing it from polymerising. Interestingly, there is a single literature report for the synthesis of a derivative of **pNDI-Tz2** using Stille conditions,[217] however several attempts were made to reproduce this without success.

In an attempt to bypass the failed Stille polymerisation, Suzuki conditions were instead selected, requiring the borylation of the NDI core (**Figure 3.10(b)**). There is some literature precedent to indicate that Suzuki couplings may be able to proceed with two moderately electron deficient units, as Bulfield and Huber demonstrated the coupling of trifluorobenzene with tetrafluorobenzene.[232] Whilst this system is not as electron deficient as the proposed **NDI-Tz** or **NDI-Tz2**, it provides insight that this is a reasonable route to attempt. Using the typical Miyaura borylation conditions employed to borylate benzothiadiazole, NDI was successfully

borylated, with the NMR peaks correlating with similar reports of diboronic ester-NDI compounds in literature.[233] Unfortunately, the Suzuki polymerisation attempts were also unsuccessful, including with the **VBTV** monomer, hence steric hinderance originating from the bulky NDI unit may also be a contributing factor in the failed reactions. Again, it was thought that the oxidative addition proceeded as usual, as this typically works well with electron deficient monomers, such as NDI or benzothiadiazole. It may instead be that the transmetallation with such a large substituent as the functionalised NDI motif is unable to reach the necessary proximity for orbital overlap with Pd to undergo the transmetallation. This may also be a contributing factor in the failed Stille reactions, where Pd in the same oxidation state is used, thus the steric effects are expected to be similar. There is one other synthetic procedure reported for the synthesis of a derivative of **pNDI-Tz2**, but this utilises active Zn, which was not accessible to the author due to the lack of a synthetic glovebox.[234] Furthermore, the use of the more accurate SCS-MP2 level of theory for the calculations into torsional potentials indicates that dihedral angles for NDI-Tz may actually be closer to 90°, making them non-ideal systems for improved delocalisation and electron transport.[217]

Taking into account the encountered synthetic constraints and using the knowledge inferred from the DFT calculations (**Section 3.3**) that both size and planarity appeared influential, the most promising series for further investigation were: **pNDI-T**, **pNDI-V** and **pNDI-A** (**Figure 3.11**). Whilst **NDI-T** appears the worst choice of the modelled oligomers, thiophene derivatives are the most common comonomer in NDI-based polymers,[116,138,139,162] thus its inclusion, along with two more promising candidates for advancing NDI-based materials, was deemed necessary.

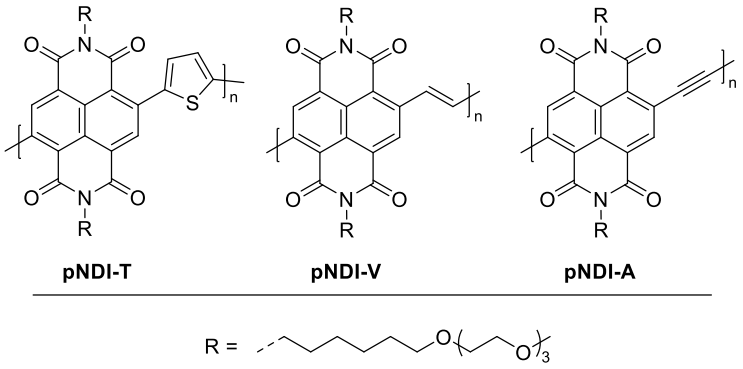


Figure 3.11. The selected polymers for further investigation into planarity of the comonomer and its impact on delocalisation.

Two further sets of calculations were conducted. Firstly, the three selected systems were modelled again using 16 repeat units to better understand the degree of delocalisation and to match more closely with the expected empirical molecular weights of these polymers. This revealed that in all cases, the charges could not be considered evenly distributed, and limited charge is predicted to delocalise onto the comonomer (**Figure 3.12**). However, the data does support the previous trend, with the charges more likely to delocalise over more NDI units when moving from **NDI-T** to **NDI-V** to **NDI-A**, with **NDI-T** showing high orbital population only on the central two NDI units, while **NDI-A** exhibits reasonable delocalisation across the central four NDI units (**Figure 3.12(c)**).

The calculations for the vinyl system were then repeated, with the σ-bonds adjacent to the vinyl artificially forced into a planar conformation. This enabled an understanding of whether the additional delocalisation of the alkynyl polymer originated from additional cumulene resonance forms, whether it is affected by planarization, or a combination of both. Interestingly, the charge distribution calculations predict that the planarized vinyl system behaves virtually the same as the **NDI-A** system (**Figure 3.12(d)**), revealing that the planarization appears to be more important in influencing delocalisation than additional cumulene resonance occurring on account of the alkynyl moiety. Whilst it is not possible to confirm this empirically (i.e. the vinyl

group cannot be forcibly planarised), this knowledge is useful in the future design of more delocalised systems.

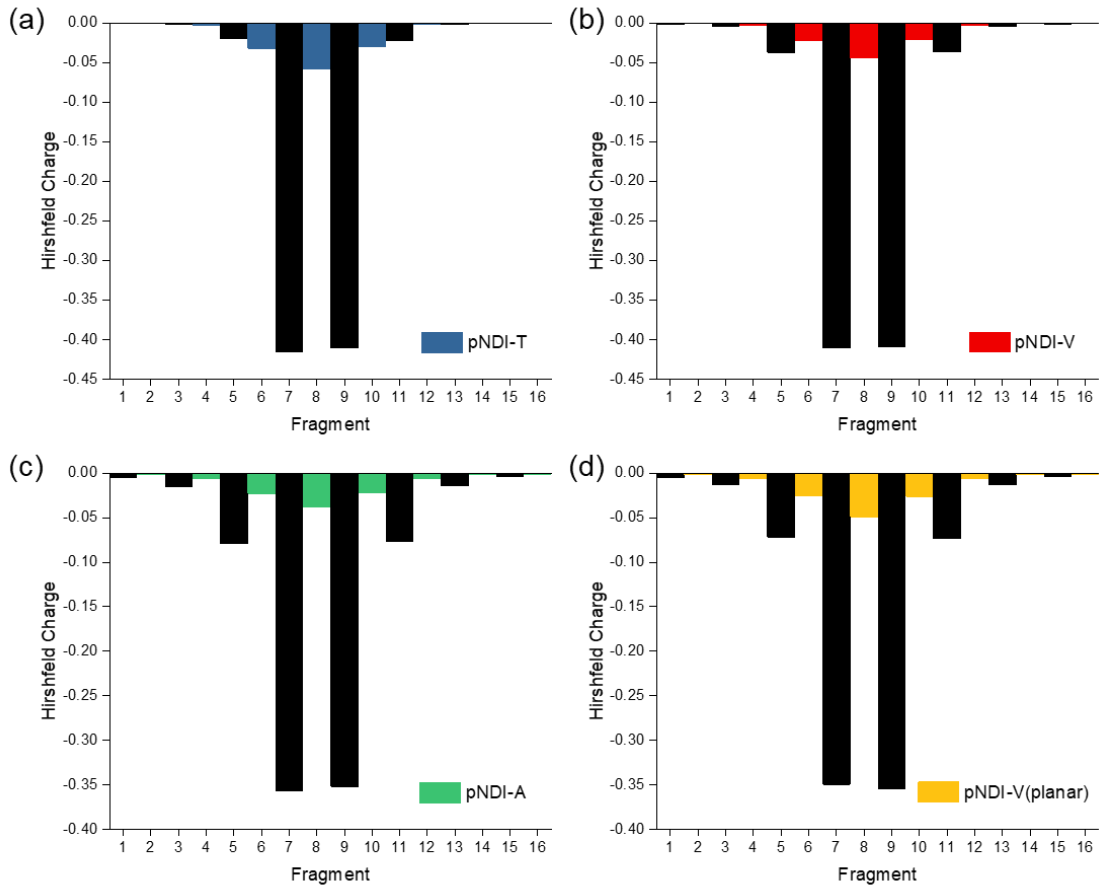


Figure 3.12. Hirshfeld charge distributions of hexadecamers of the four systems: **NDI-T**, **NDI-V**, **NDI-A** and planarized **NDI-V**. These calculations present the orbital population for the LUMO, divided into fragments along the polymer chain (black = NDI, colour = comonomer unit).

3.5 Properties of the polymers

3.5.1 Optoelectronic and physical properties

Table 3.1. Summary of the properties of **pNDI-T**, **pNDI-V** and **pNDI-A**.

Polymer	M_n (kDa) [Đ] [a]	$E_{g,opt}$ (eV) [b]	$\lambda_{max,\ sol}$ (nm) [c]	EA (eV) [d]	IP (eV) [e]
pNDI-T	17.4 [1.80]	1.72	323, 540	4.19	6.11
pNDI-V	18.8 [1.64]	1.91	329, 525	4.25	5.97
pNDI-A	11.3 [1.80]	1.99	329, 561	4.30	6.10

[a] Number-average molecular weight (M_n) and dispersity ($Đ$) measured by GPC vs polystyrene standards in chloroform at 40 °C. [b] Optical band gap estimated from thin film UV-Vis absorption onset. [c] Peak wavelength obtained from solution UV-Vis absorption spectra in chloroform. [d] Onset of the cyclic voltammogram of polymer thin films on glassy carbon electrode with 0.1 M tetrabutylammonium hexafluorophosphate as the supporting electrolyte using a platinum rod counter electrode and a silver/silver chloride reference electrode. The EA was calculated by finding the reduction onset potential and using it to calculate EA by: $EA = 4.8 + E_R - E_f$ where E_f = 0.44 V. [e] Measured by photoelectron spectroscopy in air.

The physical and optoelectronic properties of the three polymers are summarised in **Table 3.1**. The number average molecular weights were determined by GPC in chloroform at 40 °C with respect to polystyrene standards. The three polymers showed ideal unimodal traces, indicating that these are a reasonable reflection of their molecular weights. The M_n values are comparable across the series, and whilst **pNDI-A** is somewhat lower than the other two materials, this value still correlates to an average of nine repeat units per chain, which is sufficient to investigate the impact of planarisation and delocalisation of the backbone on OECT performance.

The UV-Vis absorption spectra of the polymers were measured both in dilute chloroform solutions and as thin films on glass substrates (**Figure 3.13 (a)** and **(b)**, respectively). Interestingly, the π–π* (HOMO-LUMO) transition in solution appears very similar for the three polymers, ≈ 325 nm, which is surprising given the measured shift in EA (and changes in IP) across the series (**Table 3.1**). Whilst **pNDI-T** and **pNDI-V** show no shoulder on the ICT band in solution, **pNDI-A** has a distinct shoulder, which can be ascribed to aggregation in solution.

This is unsurprising, due to the predicted rigid nature of the polymer making it less soluble, as noted during the synthesis and from the lower molecular weight achieved. Introduction of the vinyl or alkynyl comonomer causes a notable shift to lower wavelengths in the absorption onset of the ICT band, from ≈ 720 nm to 650-625 nm. This translates to a larger optical bandgap ($E_{g,opt}$) for these materials compared to **pNDI-T** (**Table 3.1**), opposite to the expected trend, if planarity and delocalization is increasing across the series. Conversely, a promising feature of note is that the peaks for **pNDI-A** in both solution and thin film UV-Vis appear sharper than the other two polymers. This could be attributed to the polymer having fewer rotational states available, thus fewer possible transitions.

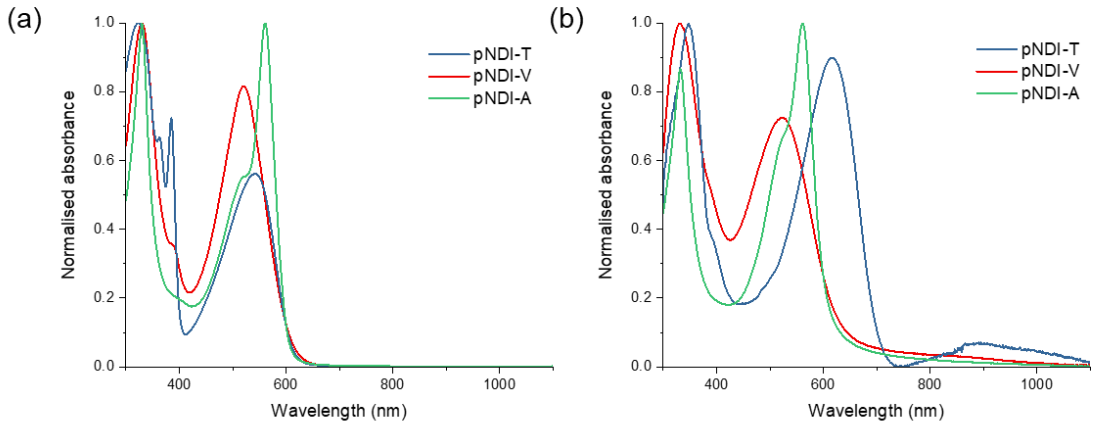


Figure 3.13. Normalised UV-Vis absorption spectra (a) in chloroform solution and (b) as thin films spin coated onto glass substrates at 600 rpm for 45 seconds for **pNDI-T**, **pNDI-V** and **pNDI-A**.

The LUMO energy level can be estimated from the electron affinity (EA), which is determined by conducing CV measurements in 0.1 M tetrabutylammonium hexafluorophosphate ($TBAPF_6$) in acetonitrile. The EA shows an increasing trend across the series when moving from the thiophene comonomer, to smaller and more planar vinyl and alkynyl comonomers, increasing from 4.19 eV to 4.30 eV (**Table 3.1**). All three EA values are considered sufficiently

deep to ensure the stability of the material when operating in aqueous environments, and only a handful of ladder-type rigid polymers have exhibited EAs ~4.30 eV.[52,75,235] All three polymers displayed discrete reduction behaviour within the limits of CV, indicating that they are n-type backbones, rather than ambipolar, as expected.

It would be expected that the ionisation potential (IP), determined by photoelectron spectroscopy in air (PESA) measurements, would decrease with increasing conjugation, particularly as the electron donating thiophene unit has been replaced. Instead, there is no clear trend in IP, with the value decreasing for the vinyl polymer, but the alkynyl derivative remaining consistent with the benchmark material, **pNDI-T**, at ~6.1 eV. The optoelectronic properties alone have not provided conclusive evidence for an increasing degree of delocalisation and planarity of the backbone across the series, although there are some strong indications that the materials behave differently.

3.5.2 GIWAXS analysis

Ex-situ grazing incidence wide angle X-ray scattering (GIWAXS) measurements of the thin films were carried out on silicon wafers to investigate the polymer morphology. The thickness-normalised GIWAXS images and the in-plane and out-of-plane line cuts are set out in **Figure 3.14**, and the extracted peak parameters are detailed in **Table 2.3**.

All three polymers present with a predominantly face-on orientation with varying degrees of order. **pNDI-T** is the least ordered material, with a relatively weak GIWAXS image (**Figure 3.14(a)**) and no identifiable peak for d(200) (**Figure 3.14(d)**). Both **pNDI-V** and **pNDI-A** show strong (100) and (200) peaks, indicating a higher degree of order in the lamellar direction. When extracting the peak parameters for these, the coherence lengths in the lamellar direction increase from **pNDI-T** < **pNDI-A** < **pNDI-V** (52.1 < 87.7 < 138 Å). There are several possible reasons for this trend, including that the background for **pNDI-V** is considerably noisier than

the other two materials, which may result in the peak being assumed to be less broad, thus a larger coherence length is calculated. Nonetheless, the broadest peak is observed for **pNDI-T**, which could be indicative of less regular crystallites, smaller crystallites, or a combination of both.[236] Whilst the degree of crystallinity in the lamellar direction is useful for understanding the three-dimensional morphology of the material, a long in-plane coherence length does not necessarily correlate to better charge transport properties as charge transport does not occur in that direction. A large coherence length in the lamellar direction does however suggest that the overall material morphology may have larger crystallites (or more crystallites, or both).

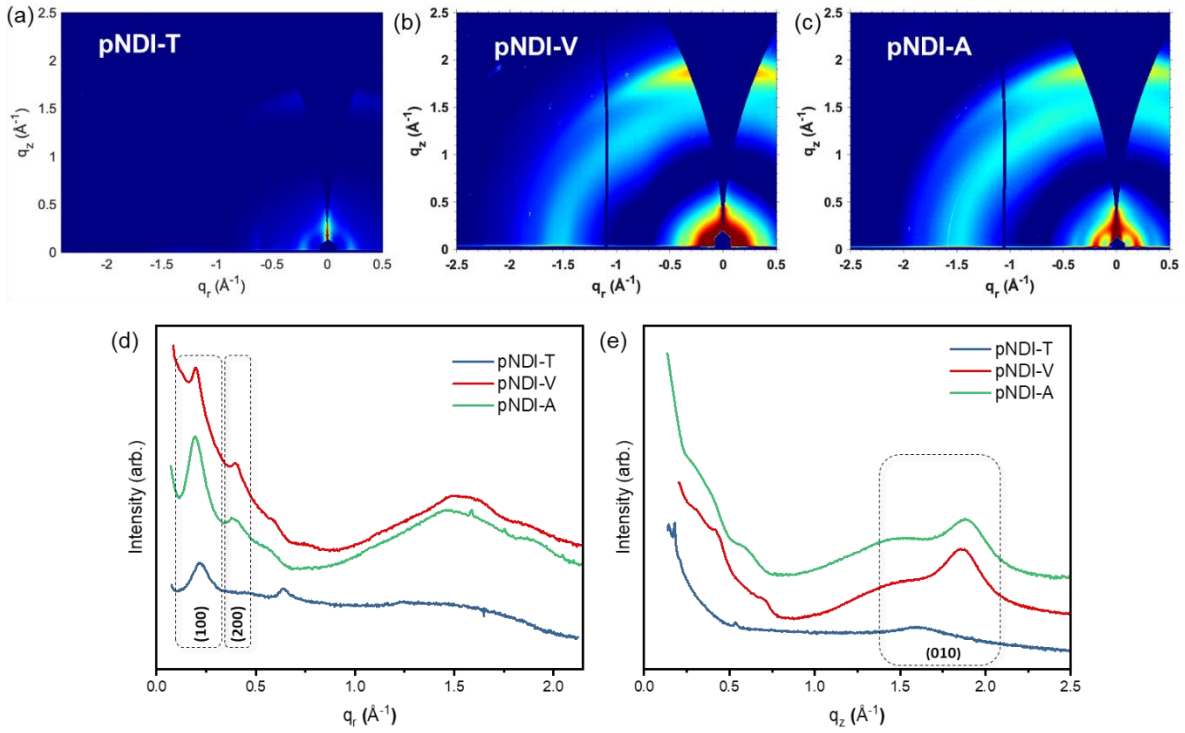


Figure 3.14. Thickness-normalised ex-situ GIWAXS images of neat as-cast films for (a) **pNDI-T**, (b) **pNDI-V** and (c) **pNDI-A** and the (d) in-plane (q_r) and (e) out-of-plane (q_z) line cuts of each polymer.

Looking next to the out-of-plane π-stacking peak, the π-stack decreases with increasing planarity of the polymer backbone, from 3.92 Å for the twisted thiophene derivative, to 3.33 Å for the virtually planar alkynyl derivative, with **pNDI-V** also offering a relatively tight π-stack

of 3.39 Å (**Table 3.2**). The attribution of the closer π-π distance to planarity is further supported by the significant increase in the coherence lengths in the out-of-plane direction for the vinyl and alkynyl derivates, where L_c increases up to 37.2 Å for **pNDI-V** (**Table 3.2**). The more planar backbones of **pNDI-V** and **pNDI-A** enable neighbouring chains to pack more closely together, giving rise to better π-orbital overlap, which will in turn further improve planarity and theoretically result in good intra and interchain electron transport. Interestingly, by comparing **Figure 3.14(b)** and **(c)**, it is also possible to examine the intensity of the π-scattering peak as the images are thickness normalised. **pNDI-V** exhibits a more intense signal, which is ascribed to a larger number of π-π stacks compared to **pNDI-A**. By measuring the materials in an OECT, it will be possible to see whether the number of π-π stacks or the π-π distance is more important in impacting the electron mobility.

Table 3.2. GIWAXS peak parameters for the three NDI-based copolymers.

Polymer	lamellar stacking [a]		π-π stacking [b]	
	L_c (Å)	d (Å)	L_c (Å)	d (Å)
pNDI-T	51.2	28.3	3.60	3.92
pNDI-V	138	31.5	37.2	3.39
pNDI-A	87.7	32.1	35.9	3.33

[a] In-plane lamellar scattering peak (100). [b] Out-of-plane π-stack scattering peak (010).

3.5.3 Electrochemical activity in aqueous electrolyte

The electrochemical activity of the three polymers was then examined using cyclic voltammetry in aqueous electrolyte (0.1 M NaCl aqueous solutions) to better represent the operation conditions of OECT devices. Similar to the CVs in organic electrolyte, all three polymers showed discrete reduction behaviour, with reversible cycling stability, which can be observed from the cycles perfectly overlaying each other (**Figure 3.15**). The reduction onset potential of a material is an indicator of the ease of electron transfer from the electrode to the material, as well as the aptitude for ion penetration.[138] It might be expected that as the electron

affinity of the materials increases when moving from **pNDI-T** to **pNDI-V** to **pNDI-A**, the reduction onset potential would decrease due to increasing ease of charge injection. This is not what is observed, and there is no clear trend in the reduction onset potentials, as **pNDI-T** has a reduction onset potential of ~ -0.11 V, **pNDI-V** = ~ -0.16 V and **pNDI-A** = ~ -0.09 V. Promisingly, one of the novel materials, the one with the highest electron affinity, does present with the lowest reduction onset potential, an important property to optimise, as low reduction potentials are desired for stable operation in aqueous environments without the electrolysis of water or reduction of oxygen.[168] The electron affinity for **pNDI-V** remains relatively high (4.25 eV), thus the more negative reduction onset potential of this material may instead indicate that the energetic barrier for ionic penetration is larger. As the sidechains are the same for the three polymers, it is unlikely that the hydrophobic content is changing significantly enough to affect the reduction onset potential by that extent,[116,178] thus the different reduction potentials may be attributed to the microstructure. For example, the higher intensity of the π-π scattering peak for **pNDI-V** may indicate that the material is significantly more crystalline, which in turn makes the material less accommodating to ions from the electrolyte.

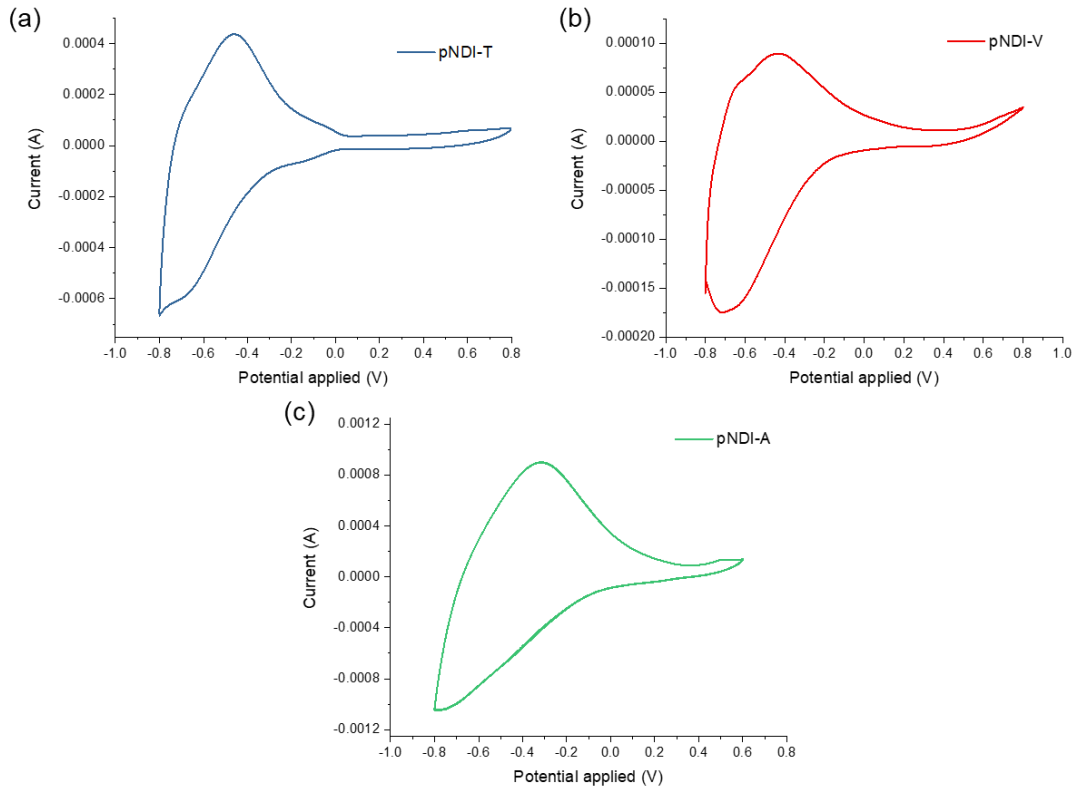


Figure 3.15. Cyclic voltammetry of (a) **pNDI-T**, (b) **pNDI-V** and (c) **pNDI-A** drop cast onto a glassy carbon working electrode, using an Ag/AgCl reference and platinum wire counter electrode. The electrolyte was degassed 0.1 M $NaCl_{(aq)}$ solution and a scan rate of 0.1 V s^{-1} was used. Three cycles are shown, the second, third and fourth cycles. The first cycle is not presented as this cycle is typically associated with the reorganisation of polymer chains or break-in effects.[237,238]

Interestingly, **pNDI-T** and **pNDI-V** showed more subtle features within the redox peaks, which were not observed with **pNDI-A**. For example, **pNDI-T** shows small redox peaks at low potentials ($E_{red,aq}$ = ~ 0 V), whilst **pNDI-V** presents a subtle additional reduction peak around -0.6 V. This may be attributed to the higher current recorded for **pNDI-A**, which indicates that the film is likely thicker than for the other two materials. This means that the voltammogram for this material may not reflect the response of the full thickness of the material. Attempts were made to vary the thickness of **pNDI-A** to verify this, however when both drop casting

smaller volumes and lower concentrations of solution onto the glassy carbon electrode, as well as spin coating onto an ITO slide, repeats of this CV showed the same broadness. Therefore, instead of relating to film thickness, the shape of this voltammogram may be the result of a higher degree of superposition of the redox states, which leads to better delocalisation of the polaron over the extended π-system,[140,238,239] as predicted by the DFT calculations (**Section 3.3**).

The aqueous electrochemical activity of the three polymers was further probed by spectroelectrochemical measurements. The progression of the UV-Vis spectra was monitored during electrochemical reduction occurring under an applied potential between 0 and -0.8 V, in 0.1 V increments, versus the Ag/AgCl reference electrode. These measurements were conducted using thin films spin coated on ITO as the working electrode, using a Pt mesh counter electrode, and the results are presented in **Figure 3.16**.

The three polymers all showed a decrease in the intensity of the ICT band and a concomitant appearance of two new absorption features, straddling the original ICT band, at ~ 420-500 nm and ~700-750 nm (**Figure 3.16**). The observed modulations in the spectra are corroborated by literature,[138,140,239] indicating the formation of a radical anion, or polaron species. Alkylated NDI-based copolymers (specifically NDI-T2 backbones) have also been demonstrated to exhibit a dianion species at more negative potentials. This is typically observed as a decrease in the peaks associated with the anion, and the appearance of two further red shifted features.[239] Whilst **pNDI-T** and **pNDI-V** do not show any evidence of the formation of the bipolaronic species in the electrochemical window examined, **pNDI-A** does develop new absorption features ~810 nm and ~1100 nm, although the latter is not clear due to the limitations of the UV-Vis spectrometer. These peaks, particularly the one at ~1100 nm, seem unusually red shifted for the bipolaronic species, however they may provide evidence that the alkynyl comonomer encourages formation of the bipolaron within the electrochemical window of

water. Time-dependent DFT calculations on the predicted spectrum of the bipolaron are ongoing and will allow more conclusive agreement of this theory.[69]

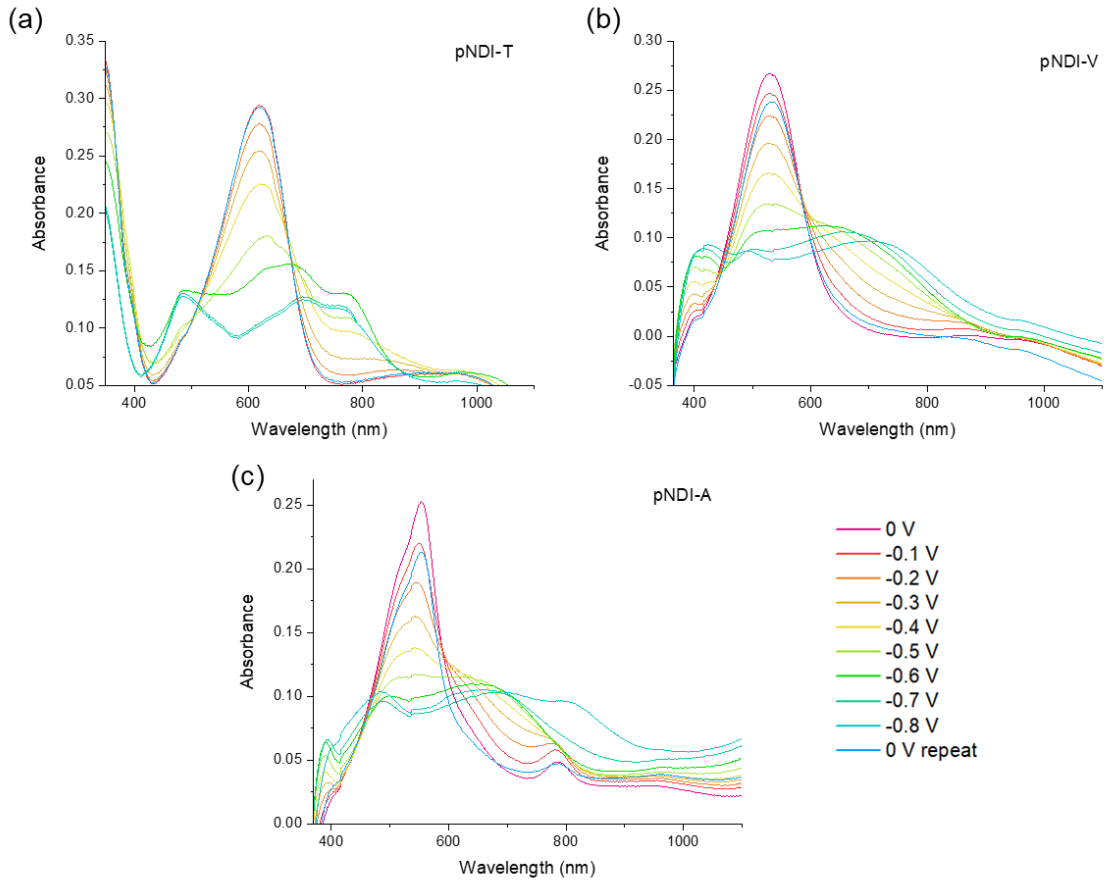


Figure 3.16. Spectroelectrochemical measurements during charging between 0 and -0.8 V versus Ag/AgCl for (a) **pNDI-T**, (b) **pNDI-V** and (c) **pNDI-A** in 0.1 M $NaCl_{(aq)}$ electrolyte, in 0.1 V steps.

The final point of note is regarding the stability of the materials. **pNDI-T** shows excellent reversibility, with the shape and intensity of the original spectra being restored when the potential is returned to 0 V. Polymers **pNDI-V** and **pNDI-A** show a good return to the original shape of the graph, however do not reach the original intensity, indicating that there may be some degree of degradation or other instability (such as delamination) of these materials.

3.5.4 OECT characteristics

OECT devices were measured in 0.1 M $NaCl_{(aq)}$ in ambient conditions using an Ag/AgCl pellet as the gate electrode to understand the impact of the comonomer on the mixed ionic-electronic transport. The performance parameters are summarised in **Table 3.3** and the output and transfer characteristics are displayed in **Figure 3.17**. Polymer **pNDI-T** is the same material as that used in **Chapter 2** and was remeasured due to the variation in molecular weight between the batches. The data for **pNDI-T** presented in **Table 2.5** is that of the batch used in this chapter, however its similarity to the neat batch of **Chapter 2** further verifies the conclusions that the impact of molecular weight is relatively insignificant for OECT performance.

Table 3.3. Steady-state OECT performance of the polymers.

Polymer	V_T [V] [a]	d [nm] [b]	g_m' [S cm^{-1}] [c]	[μC^*] [F V^{-1} cm^{-1} s^{-1}] [d]	C^* [F cm^{-3}] [e]	μ_{OECT} [cm^2 V^{-1} s^{-1}] [f]
pNDI-T *	0.20 ± 0.006	55.2 ± 12.9	0.065 ± 0.020	0.228 ± 0.108	220 ± 47	1.04 x 10^{-3} ± 2.11 x 10^{-4}
pNDI-V	0.26 ± 0.003	69.0 ± 26.8	1.38 ± 0.533	3.70 ± 1.18	154 ± 49	2.40 x 10^{-2} ± 9.62 x 10^{-4}
pNDI-A	0.09 ± 0.004	41.3 ± 6.79	0.667 ± 0.146	1.47 ± 0.654	112 ± 43	1.31 x 10^{-2} ± 2.94 x 10^{-3}

[a] Threshold voltage extracted from a plot of $\sqrt{I_D}$ versus V_G. [b] Thin film thickness measured by Dektak profilometer. [c] Peak OECT transconductance normalized by thickness. [d] [μC^*] calculated for the highest performing channel from the slope of g_m with known channel dimensions and applied bias. [e] C^* values extracted from Randles circuit fits from electrochemical impedance curves of the polymers coated on Au electrodes in 0.1 M aqueous NaCl solution. [f] OECT mobility calculated from the transistor saturation [μC^*] product using the respective C^* values. * The values for **pNDI-T** were remeasured for the new batch of polymer due to the variations in molecular weight but performance was virtually identical to the neat polymer presented in **Chapter 2**.

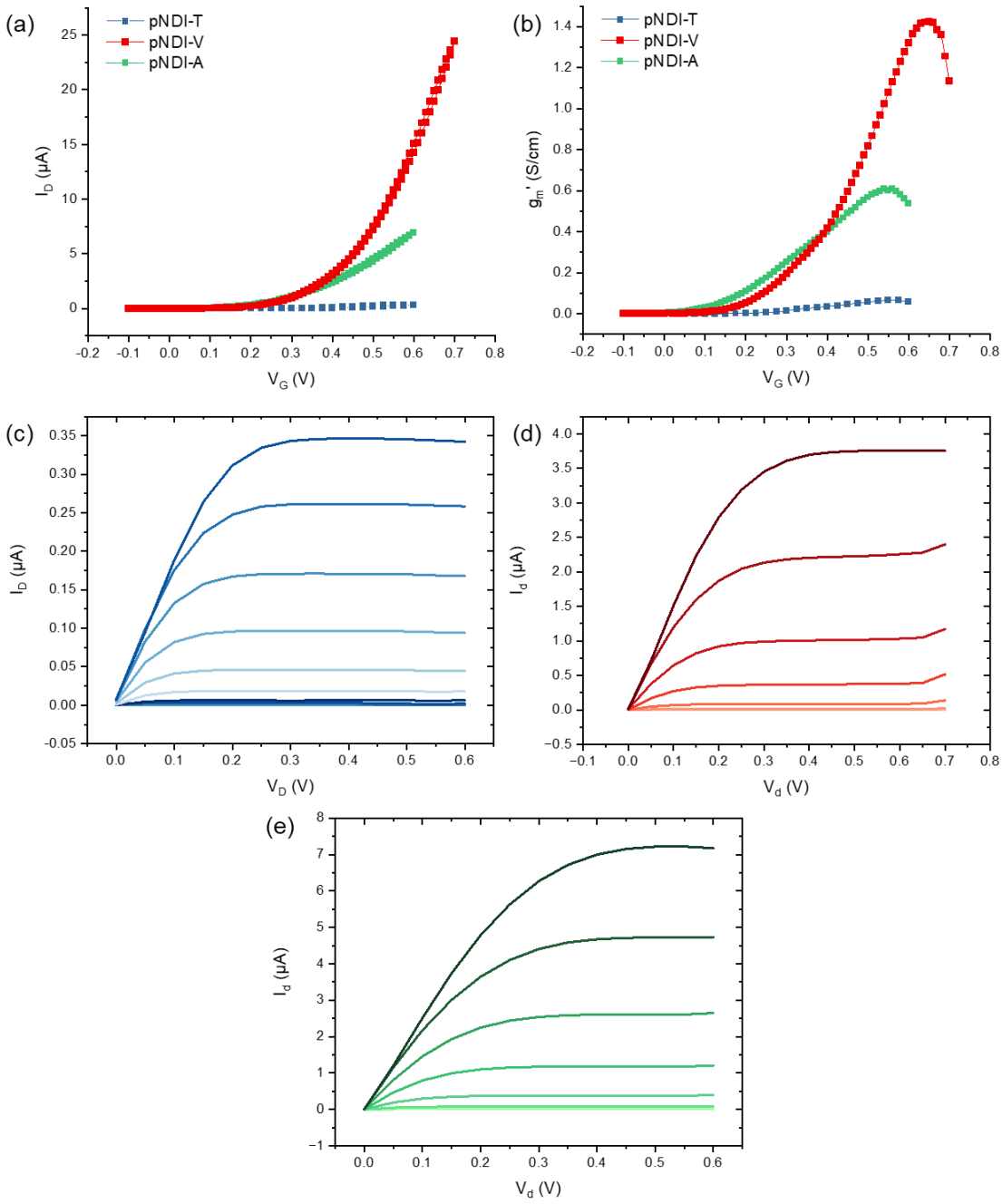


Figure 3.17. Performance of OECTs averaged across 6 devices, where W = 100 µm and L = 10 µm in aqueous 0.1 M NaCl solution in ambient conditions. The panels present (a) transfer curves, (b) thickness-normalised transconductance (g_m') vs gate voltage (V_G), and the output characteristics of (c) **pNDI-T**, (d) **pNDI-V** and (e) **pNDI-A** OECT devices.

Similar to **pNDI-T**, **pNDI-V** and **pNDI-A** also demonstrated pure n-type, accumulation mode OECT operation. The threshold voltages were extracted from the transfer characteristics and corroborate the trend found in the reduction onset potentials in aqueous electrolyte, with **pNDI-A** being the easiest to switch ON, with V_T = 0.09 V. This can be considered a low threshold voltage for NDI-based polymers,[116,138–140] which is extremely advantageous as it results in lower power consumption, making the device operable at voltages closer to zero, without experiencing ambient doping.[168] As the three copolymers have virtually the same degree of hydrophilicity (i.e. the same sidechain), the variation in V_T is associated with the ease of ionic penetration, which is likely influenced by both the energetics and crystallinity of the materials. Like the reason given for the difference in the reduction onset potentials for aqueous CVs, it is possible that the crystallinity of **pNDI-V** makes the material more inaccessible to ions from the electrolyte, resulting in larger voltages required to drive ions into the bulk of material.

pNDI-V and **pNDI-A** offer access to significantly improved OECT performance compared to **pNDI-T**, with the thickness-normalised transconductance increasing by a factor of 20 and 10, respectively. This also translates to an increased μC^* product for the two novel materials, rising from 0.228 F V^{-1} cm^{-1} s^{-1} for **pNDI-T** to 3.70 and 0.667 F V^{-1} cm^{-1} s^{-1} for **pNDI-V** and **pNDI-A**, respectively.

In order to decouple the effect of electron mobility and volumetric capacitance on the μC^* product, electrochemical impedance spectroscopy (EIS) was conducted to determine C^*. These measurements were performed using a 600 µm x 600 µm polymer coated gold electrode as the working electrode, and an Ag/AgCl pellet as the gate electrode. From this setup, changes in the impedance magnitude and phase were recorded (**Figure 3.18**), such that a phase, φ, between 0° and -45° indicates resistive character, whilst φ between -45° and -90° denotes capacitive behaviour.[240] At low frequencies, all three polymers show capacitive behaviour, as expected, due to the hydrophilic nature of the sidechains (**Figure 3.18**). The phase for **pNDI-V** and

pNDI-A appears to move towards resistive character more quickly than for **pNDI-T**. This could indicate that the ionic capacity more quickly reaches saturation because the smaller comonomer for the vinyl and alkynyl derivatives translates to less amorphous regions, or less "space" to accommodate the ions,[177] which aligns with the structural characterisation obtained by GIWAXS.

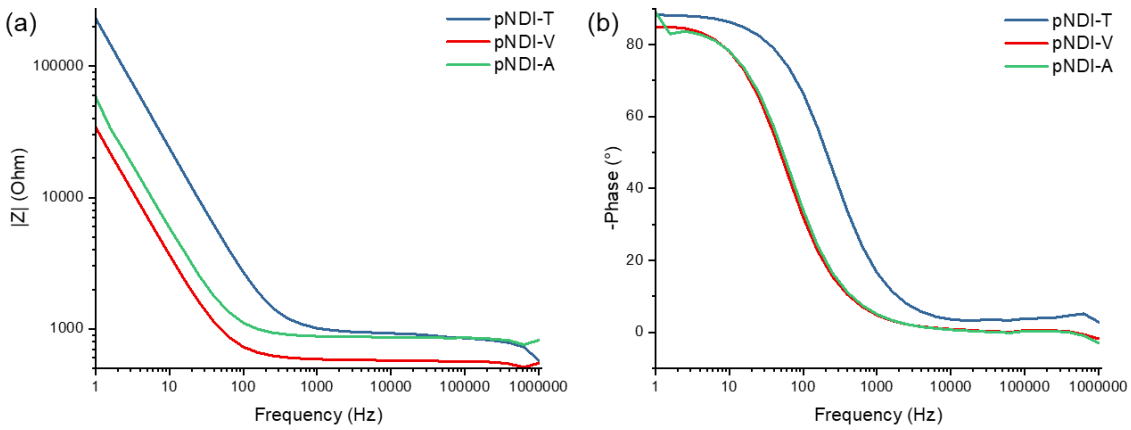


Figure 3.18. Electrochemical impedance spectroscopy of the polymers at the OECT gates in 0.1 M $NaCl_{(aq)}$ (L = W = 600 μm, V = 0.6 V vs Ag/AgCl). (a) The impedance magnitude, and (b) the impedance phase.

The Randles circuit fits of the EIS data were used to extract the capacitance for each of the polymers, which could then be normalised by the known volume, to obtain C^*.[117] Unsurprisingly, the polymer with the least crystalline microstructure by GIWAXS, **pNDI-T**, showed the largest C^* of 220 F cm^{-3}, as the more amorphous microstructure, with the largest π-π stacking distances, allows for the easier penetration of ions into the bulk of the OMIEC.[119] Following this logic, as the π-π stacking distance of the polymer decreases (as observed by GIWAXS), the volumetric capacitances decreases, such that C^* = 154 F cm^{-3} for **pNDI-V** and C^* = 112 F cm^{-3} for **pNDI-A**. Despite the lower C^* values for **pNDI-V** and **pNDI-A**, the larger g_m' and μC^* product indicate that the overall increase in performance can be ascribed to improved electronic mobilities, μ. With known C^* values, μ was calculated from the transistor

saturation μC^* product and resulted in impressive n-type mobilities, particularly for NDI-based copolymers, of 0.0240 and 0.0131 $cm^2\ V^{-1}\ s^{-1}$.

For the realisation of bioelectronic devices based on OECTs, the operational stability of the transistor is paramount. To test this, stability measurements were carried out by monitoring the drain current upon cycling the gate voltage between 0 and 0.6 V (ΔV_G = 0.6 V) over 30 minutes. The upper limit was selected based on the applied gate voltage at which the maximum transconductance was recorded. The benchmark polymer, **pNDI-T** showed poor stability, with the current changing by 36% across the 30 minutes of cycling. This large change in ON current indicates that it would not be suitable for long-term sensing applications, where this degradation could interfere with current fluctuations of the biological system, making it impossible to distinguish the true signal from the instability of the device. Fortunately, not only do **pNDI-V** and **pNDI-A** outperform **pNDI-T** in terms of absolute OECT performance, but they are also significantly more stable under operation (**Figure 3.19**). Notably, both **pNDI-V** and **pNDI-A** show only a 3% change in drain current over 30 minutes of cycling. This makes them promising candidates for bioelectronic sensing applications, although their stability should be further tested in longer cycling measurements, over the course of several hours.

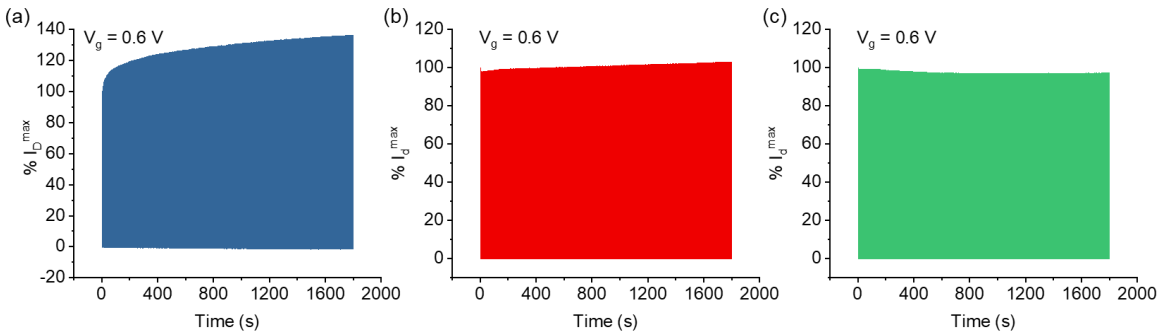


Figure 3.19. Stability measurements conducted by cycling the gate potential between 0 V and the applied gate potential at which the peak transconductance was recorded for that material. The recorded drain currents over 30 minutes are presented for (a) **pNDI-T**, (b) **pNDI-V**, and (c) **pNDI-A** carried out in OECT channels in aqueous 0.1 M NaCl solution.

3.6 Discussion

The most likely explanation for the significant increase in charge carrier mobility by more than an order of magnitude, from 0.00104 $cm^2 V^{-1} s^{-1}$ for **pNDI-T**, to 0.0240 and 0.0131 $cm^2 V^{-1} s^{-1}$ for **pNDI-V** and **pNDI-A**, respectively, is the realisation of the DFT-predicted improvement in planarity and increased delocalisation (**Figure 3.5** and **Figure 3.12**). This most likely translates to fewer defects in the microstructure, which minimises trapping sites, allowing a greater proportion of the electrons to move freely. This is also supported by the GIWAXS data, which indicates that both **pNDI-V** and **pNDI-A** have a higher degree of planarity, which enables the observed closer π-π stacking distances. Furthermore, the increased intensity of the **pNDI-V** π-scattering may be ascribed to a higher degree of crystallinity, where more polymer chains are stacked in the out-of-plane direction. This planarity allows for better intrachain charge transport, and the conferred additional orbital overlap is also likely to improve interchain charge transport events. It appears that in this case, the number of π-stacking occurrences for **pNDI-V** outweighs the slight enhancement in the π-stacking distance of **pNDI-A**, due to the significantly higher mobility of the vinyl derivative.

There is, however, another factor to consider. As these polymers, **pNDI-V** and **pNDI-A**, are more planar (as inferred by DFT calculations, GIWAXS and OECT mobility) than **pNDI-T**, the polymer discussed in **Chapter 2**, it is possible that molecular weight does somewhat impact performance, more similar to rigid rod-like polymers, such as BBL.[144] As the polymer backbones are more planar and the charge is predicted to be more delocalised (**Figure 3.12**), it is possible that for **pNDI-V**, which has a higher M_n, the charge transport is improved due to an increased length of the chain. Intrachain transport will always be the energetically favourable route for charges where there is sufficient delocalisation, thus the longer chains in **pNDI-V** compared to **pNDI-A** may also play a role in the recorded OECT mobility. Unfortunately, due to solubility limits, **pNDI-A** of higher molecular weights could not be accessed, thus for a valid

comparison, a lower molecular weight batch of **pNDI-V** would need to be synthesised, despite this potentially purposely being detrimental to performance.

Beyond the mobility, it should be noted that the degree of swelling does not correlate with OECT performance. In fact, the material with the highest ion uptake, **pNDI-T**, exhibited the poorest overall OECT performance. With this in mind, future design strategies should focus more closely on boosting n-type OECT mobility to maximise performance, through reducing the size of the comonomer and improving planarity of the polymer backbone.

3.7 Conclusion and future work

In this study, nine polymers were designed and DFT calculations were carried out to understand the effect of the size, electron density and planarity of the comonomer on the OECT performance, specifically the electronic mobility, of NDI-based copolymers. Taking into account the DFT calculations, it was predicted that both size and planarity significantly impact the charge delocalisation, whereby more planar and smaller comonomers overall have a positive effect. With this in mind, and considering synthetic constraints, three polymers were synthesised for further investigation, namely **pNDI-T**, **pNDI-V** and **pNDI-A**. It was found that by reducing the size and increasing the planarity of the comonomer, the OECT performance was significantly improved, such that record NDI-based polymer mobilities were reported, as high as 2.40 x 10^{-2} cm^2 V^{-1} s^{-1} for the vinyl derivative.

By examining the GIWAXS data for the three polymers, both **pNDI-V** and **pNDI-A** indicated more order and a higher degree of crystallinity, with comparable crystallite sizes in the out-of-plane π-stacking direction for the two materials. Whilst **pNDI-A** had a slightly tighter π-π stacking distance than **pNDI-V** (Δd_{010} = 0.06 Å), the intensity of the π-scattering for **pNDI-V** was significantly more than **pNDI-A**, which indicates that there is a higher degree of π-stacked chains in the sample. When examining the charge carrier mobilities of the two materials, it's

possible to see that the greater extent of π-stacking outweighs the tighter π-stacking distance and is reflected by a two-fold increase in μ. Additionally, the OECT stability is significantly improved from the benchmark polymer, **pNDI-T**, which saw a 36% change in drain current over 30 minutes of cycling. This was reduced to $\Delta I_D = 3\%$ for both **pNDI-V** and **pNDI-A**, thus these novel polymers not only present higher performance, but also more stable OECT devices. These learnings can be taken forward as useful design strategies that minimising the size of the comonomer and increasing the planarity of the polymer backbone acts to improve OECT mobility and stability through reducing the number of trapping sites and increasing the degree of delocalisation.

The final part of this study involves making a direct comparison between the predicted and empirical degree of delocalisation. This has only been demonstrated once comprehensively in literature, for polythiophene materials,[214] thus this part of the study would significantly increase its impact. There are two methods, electron spin resonance (ESR) and optical conductivity measurements, currently underway to create custom setups to conduct these measurements.[241] ESR can be used to measure spin delocalisation, which can be probed by electron nuclear double resonance (ENDOR). By looking to the width of the hyperfine coupling of the ENDOR spectrum, the extent of delocalisation can be predicted. These polarons are typically generated using a dopant,[242,243] but can also be generated via a field effect or using a solid electrolyte.[244] Conversely, optical conductivity measurements involve either the generation of excitons using a strong pump beam, which dissociate into polarons, or the generation of polarons using a field-effect. This can then be examined by FTIR to further understand the degree of crystallinity in the material and the extent of polaron delocalisation, when compared to a modelled spectrum. This method has also been used when the polaron is generated by a field-effect,[245,246] however limited examples exist for either technique using an aqueous electrolyte in place of the dielectric. The ability to generate the polaron via the same method (i.e. electrochemically) is

critical to draw meaningful conclusions about the polaron in the OECT device, thus until these custom setups are completed by collaborators, these measurements are on hold.

Chapter 4

Isolating ionic transport: A model system to understand ionic conductivity in organic mixed ionic electronic conductors

4.1 General information and attributions

Aqueous CV measurements were performed by Dr Adam Marks (Salleo Group, Stanford University). GIWAXS measurements and analysis were carried out by Dr Adam Marks and Tyler Quill (Salleo Group, Stanford University). Galvanostatic measurements were conducted by Ana De La Fuente Durán (Cheuh Group, Stanford University). The author would also like to thank Dr Alexander Giovannitti (Salleo Group, Stanford University) for constructive discussions regarding project direction.

4.2 Introduction

The product μC^* is an important figure of merit for OECTs, which comprises of contributions from the charge carrier mobility, μ, and the volumetric capacitance, C^*. It is widely accepted that the device physics of OFETs offers a reasonable system for understanding charge carrier transport properties in OECTs.[93] Both devices require the application of a drain and gate voltage for a (accumulation mode) device to switch on and a drain current to be generated.[93,99] **Chapter 2** indicated that there are some differences in the models for charge carrier mobilities in OFETs compared to OECTs, which mainly arise from the three-dimensional nature of OECTs. This means that where in OFETs, molecular weight is more significant and purity levels may have a negligible impact, because a higher degree of crystallinity is of utmost importance to performance,[179,182,183] these same factors do not have the same influence on OECT performance.[211] Instead, molecular weight is less impactful on OECT performance because charges are able to take advantage of the bulk of the OMIEC to find a connected pathway through the semiconducting layer. Additionally, the degree of crystallinity, hence the charge transport pathways, vary due to the swelling of the OMIEC that occurs in OECTs under operation,[119] which is not something that OFET models account for.

The other equally important parameter impacting OECT performance is the ionic conductivity of the OMIEC, which is measured as the volumetric capacitance, C^*. For ionic conductivity, there is currently no appropriate model system. The property cannot be modelled using OFET device physics, even for basic understanding, as OFETs rely solely upon 2D charge transport and are not able to conduct ions. This is the fundamental difference between two the devices, thus an alternative model is required. A model system would enable a better understanding of ionic conductivity and the ability to isolate discrete factors that impact this property.

Current studies that have been shown to impact ionic conductivity (thus C^*) mainly involve sidechain modifications, such as the density and composition of the sidechain. For example, Moser et al. increased the carbon spacing between each oxygen of the classic ethylene glycol sidechain to create propylene and butylene glycol derivatives.[191] Through this, C^* was modulated as the new derivatives caused a decrease in ionic conductivity, due to increased hydrophobic content. However, C^* was not the only affected property, and mobility, particularly for the butylene glycol derivative, increased by 66%, on account of the more porous microstructure, as observed by atomic force microscopy.[191] Other examples include the use of hybrid sidechains, where increasing the length of the alkyl spacer whilst maintaining the glycol content again increases the hydrophobicity of the sidechain, thus C^* decreases.[138,139] This again interferes with the OECT mobility, indicating that volumetric capacitance and charge carrier mobility are clearly linked, as a reduction in C^* means that charge transport pathways are less likely to be disrupted by swelling, thus mobility exhibits an increase. Whilst it is important to note that these properties are intertwined, to develop useful design strategies for improving ionic conductivity, these parameters need to be decoupled.

This chapter aims to decouple ionic and charge carrier transport in OMIECs by presenting a series of polymers with essentially no charge carrier mobility. By varying the electronics and sidechains, it will then be possible to understand the impact of these properties on ionic

conductivity. For this electronically insulating system, the pyromellitic diimide (PMDI) core was selected due to its known ability to act as an efficient energy storage device.[247] PMDI-based polymers have been demonstrated to turn on in OFET devices, although only very small electronic mobilities, on the order of 10^{-4} – 10^{-5} cm^3 V^{-1} s^{-1}, have been achieved.[248] From this, two series of polymers, set out in **Figure 4.1**, were developed to investigate both the impact of systematically changing the backbone composition (i.e. energetics, series 1) and the sidechain composition (series 2).

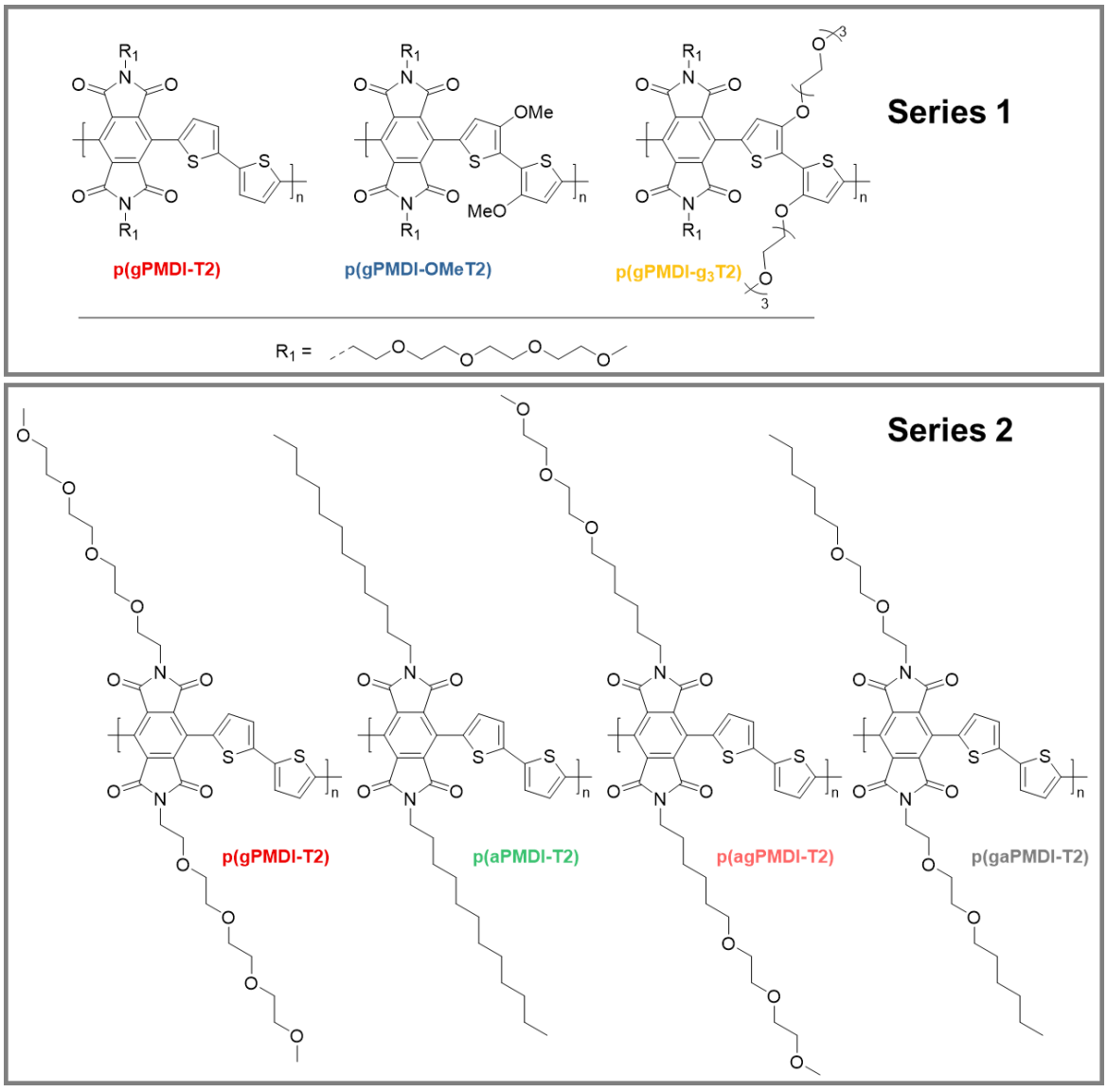


Figure 4.1. Structures of the six PMDI-based copolymers, separated into the two series, where series 1 examines the impact of changing the energetics of the backbone through comonomer

exchange, and series 2 focuses on the impact of the sidechain. Note, **p(gPMDI-T2)** is presented in both series.

4.3 Density Functional Theory (DFT) calculations

Due to the computational intensity required for Density Functional Theory (DFT) calculations, it is typical to examine the polymer backbone alone, using methyl-terminated repeat units. This enables understanding of the conjugated system but does not provide insight into the impact of different sidechains. In the context of this study, this limits the models to the methyl-terminated PMDI-T2 and PMDI-OMeT2 derivatives. The use of such calculations is therefore somewhat constrained to indicating the degree of delocalisation of the charge along the backbone, as well as predicting energy levels and torsional angles. Calculations of this level of theory are therefore not able to make predictions about the interaction of various sidechains with a wider system (i.e., ions in the electrolyte). With this in mind, DFT calculations were carried out at the ωB97XD/6-31G* level of theory on octadecamers of the two derivatives, and the aforementioned properties were examined. These derivatives behave similarly, with severely limited conjugation, such that the LUMO is very localised. By examining the Hirshfeld charge distribution, the negative polaron exhibits >90% chance of being localised to one pyromellitic unit of the nine modelled in both systems. This indicates that these systems will fulfil the requirement of limiting charge transport, so that ionic transport can be decoupled and examined independently.

Whilst the electron affinities of the two systems are predicted to be very similar, at 2.73 and 2.67 eV for PMDI-T2 and PMDI-OMeT2, respectively, on account of the localised LUMO and polaron, the ionisation potentials vary drastically, with a larger IP of 6.50 eV for PMDI-T2, compared to 5.13 eV for PMDI-OMeT2. Whilst DFT calculations at this level of theory can be used to predict the energy levels of a polymer, they are better able to offer a trend between

materials rather than necessarily providing the absolute number, as measured by photoelectron spectroscopy or cyclic voltammetry.[249] To better understand the localisation of the LUMO, the torsional energy profiles were calculated using B3LYP-D3/6-31G* in the gas phase along the dihedral coordinate connecting a thiophene or methoxy-thiophene ring with the PMDI unit. The atoms about which the dihedral is measured, and the resulting profiles are presented in **Figure 4.2**. Both polymers display a double well potential, although the angles of the stable conformations vary slightly, with PMDI-T2 at ~60° and ~120° and PMDI-OMeT2 at ~50° and ~130°. The energetic barrier for rotation is lower than that seen for NDI-T2 copolymers,[140] at 0.4 kcal/mol and 0.9 kcal/mol for PMDI-T2 and PMDI-OMeT2, respectively. Conversely, the energy required to approach the planar conformation of either system is between 4.4 and 7.5 kcal/mol, which provides a huge energetic barrier. This signifies that although rotation between the two conformations is relatively easy, this would proceed via the perpendicular conformer, rather than the planar conformer. This lack of planarity inhibits conjugation and can be held responsible for the almost complete localisation of the LUMO and negative polaron.

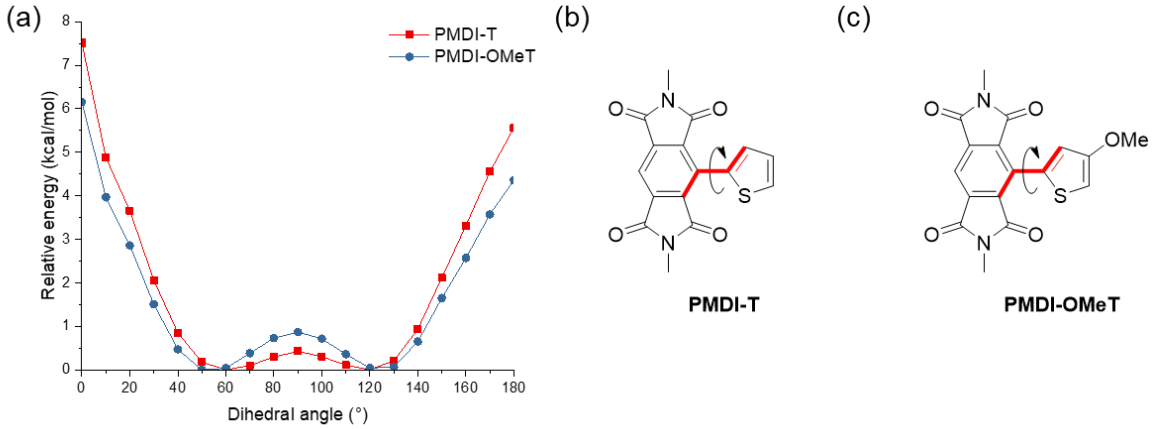


Figure 4.2. (a) Torsional energy profiles for PMDI-T and PMDI-OMeT, calculated using B3LYP-D3/6-31G* in the gas phase. The rotatable bonds (i.e., the bonds over which the dihedral angle was calculated) are highlighted in red for the 0° conformer for (b) PMDI-T and (c) PMDI-OMeT.

4.4 Synthesis

4.4.1 Synthesis of the sidechains

Efforts towards the novel polymers commenced with synthesis of the sidechains. To evaluate the variations of the sidechain on ionic transport properties, the most common sidechains in transistors were selected, namely a fully alkylated (for OFET applications) and fully glycolated derivative (for OECT applications). Of the two, it could be expected that the glycolated material is able to allow ions to penetrate into the bulk of the material, whilst the hydrophobic alkyl sidechains prevent ion uptake, making these materials suitable solely for charge transport, such as that of OFETs.[71,116] The initial choice of sidechain was made due to the comparative size of the PMDI core versus the NDI core. Its smaller nature indicated that a shorter total chain length would be more appropriate to ensure solution processability of the polymer, without advocating excessive swelling. As NDI-based copolymers are typically soluble with a heptakis(ethyleneglycol) sidechain, it was deemed that a tetrakis(ethyleneglycol) sidechain should be appropriate, thus synthesis of 2,5,8,11-tetraoxatridecan-13-amine was completed according to a modified literature procedure (**Figure 4.3(a)**).[116] When selecting the fully alkylated sidechain, efforts were made to keep the length comparable to the previous candidate (13 atoms), thus dodecanamine was chosen (**Figure 4.3(b)**).

To add to the series, based on the prior knowledge that alkyl spacers act to modulate swelling and maximise electronic charge transport by preventing the polarons from localising next to ions,[126,138,139,250] a hybrid sidechain with a hexyl spacer and a diethylene glycol component was selected. Similar to the sidechain synthesised for **Chapters 2** and **3**, the ditosylated hexanediol was subjected to a mono-substitution reaction to introduce the diethylene glycol monomethyl ether tail (**Figure 4.3(c)**). Encouragingly, the yield observed for this (62%) was almost double that achieved when the sidechain was synthesised with triethylene glycol monomethyl ether for **Chapters 2** and **3**. This may be due to the dryness of the glycol sidechain, which in this

case was rigorously dried under high vacuum for 3 hours before use. The remaining tosyl group was reacted with sodium azide, before undergoing Staudinger conditions to generate the final sidechain in an overall yield of 22%. The final step should ideally be refined to improve yield, as this previously was a high yielding step, however sufficient amounts of the sidechain were synthesised in the first attempt, thus optimisation was not necessary.

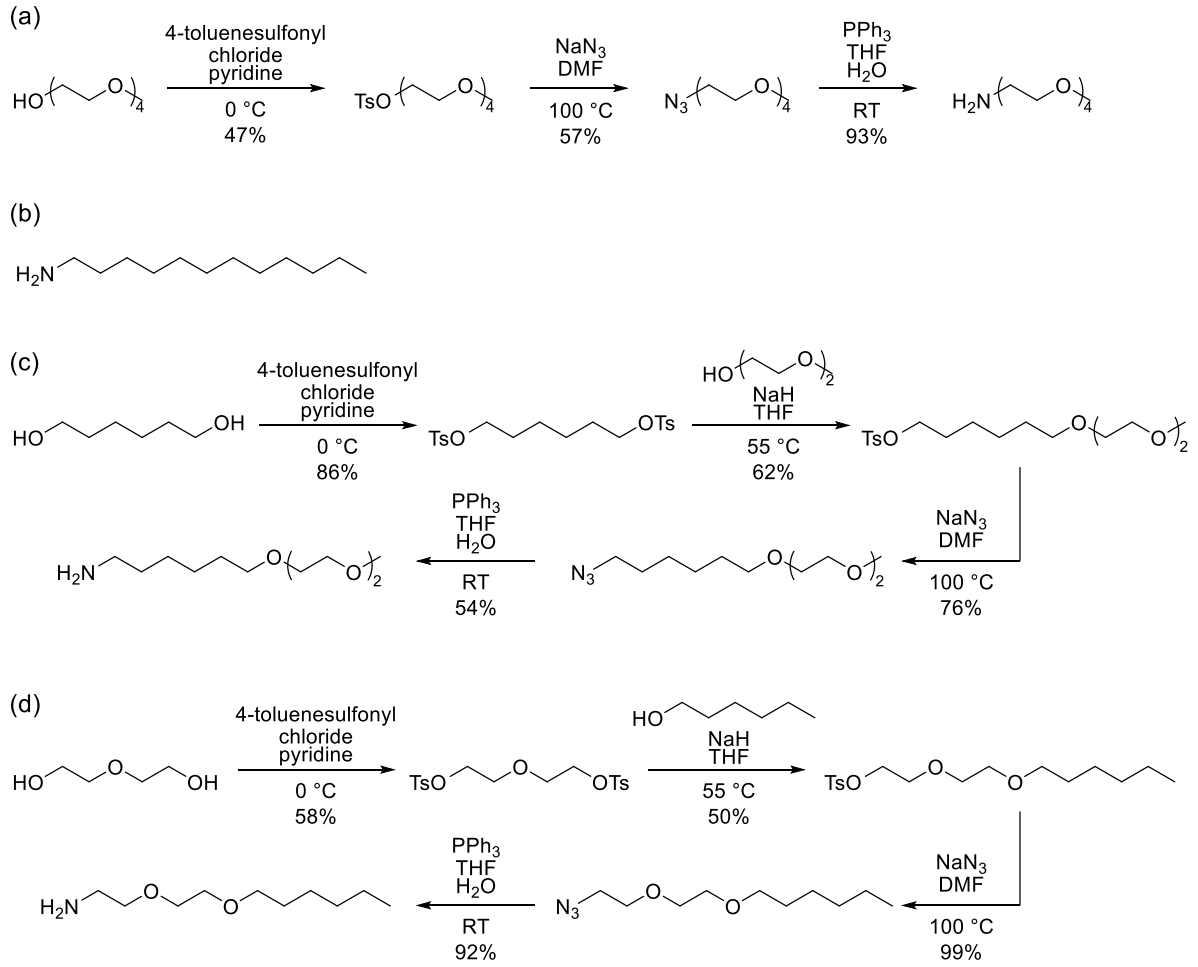


Figure 4.3. Synthetic route to the chosen three sidechains. (a) 2,5,8,11-tetraoxatridecan-13-amine, (b) dodecanamine, (c) 6-(2-(2-methoxyethoxy)ethoxy)hexan-1-amine and (d) 2-(2-(hexyloxy)ethoxy)ethan-1-amine. Dodecanamine was procured from commercially available sources.

Finally, the reverse sidechain was synthesised, meaning the hydrophobic alkyl section of the sidechain was instead present as a "tail". This has not been widely explored in literature, with very limited reports of any glycolated sidechains with anything other than a methyl terminus.[251]

It was therefore deemed a useful contribution to the field to better understand the impact of the location of the spacer, rather than just present/not present, particularly as this series is focussing solely on ionic conductivity. The same reaction conditions were used for this route, though notably, the Staudinger conditions on this occasion were able to achieve impressive yields of 92%, resulting in a yield of 26% for the four-step synthesis (**Figure 4.3(d)**).

4.4.2 Synthesis of the PMDI monomers

Initially, the conditions used for the synthesis of NDI cores with glycolated sidechains (zinc acetate and *o*-xylene)[116,140] were trialled due to the similarity of the PMDI system. This however produced a very small amount of product (~5% yield), potentially due to the increased electron density of the PMDI core compared to NDI, which instead required a stronger acid than the weak Lewis acid of zinc acetate. Typically, during the synthesis of glycolated NDI cores, zinc acetate and a non-polar solvent is employed to minimise the undesired S_NAr side reaction, which causes sidechain substitution on the aromatic core.[116] It appears that in the case of PMDI, this effect is much less observed, thus there is no need to avoid polar solvents. For example, the TLC only showed two spots, one for the desired product, and one for unreacted sidechain, whilst TLCs of the same reaction for NDIs, especially when using a polar solvent such as acetic acid, shows three NDI spots, with yellow being the desired product, and orange and pink spots indicating the S_NAr products (**Figure 4.4**).

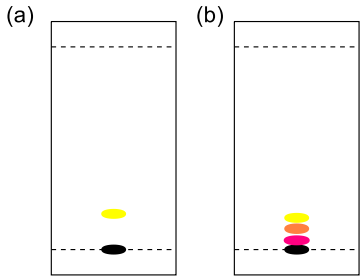


Figure 4.4. TLC visualisation of the crude mixtures of (a) PMDI and (b) NDI when a polar solvent is employed. In both cases, the yellow spot is the desired product and the black spot

resembles unreacted sidechain. In reality, the PMDI product spot is barely visible by eye as the pure product is a white solid.

Instead, with reference to literature,[248] acetic acid was used as both the catalyst and solvent for the reaction (**Figure 4.5**). The reported procedure was adapted to introduce the sidechain at elevated temperatures (80 °C), before further heating the reaction mixture to 120 °C overnight. In the case of the fully alkylated and fully glycolated sidechains, these conditions produced the pure product after silica plug or column chromatography in good yields of 68-72%. Unfortunately, the synthesis with the hybrid sidechains resulted significantly poorer yields of 23-24%, although the pure product was isolated following silica column chromatography and a recrystallisation.

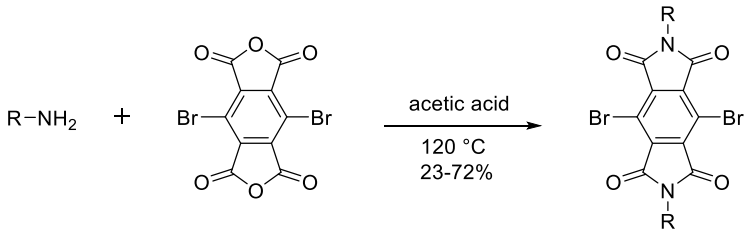


Figure 4.5. General synthetic conditions for formation of the functionalised PMDI monomers.

4.4.3 Synthesis of the bithiophene monomers

Initially, bithiophene (T2) was selected as the comonomer of choice due to its commercial availability as 5,5′-bis(trimethylstannyl)-2,2′-bithiophene. To understand the impact of the positions of the HOMO and LUMO levels on the ionic conductivity, two additional comonomers were selected to manipulate the energetics. These were both bithiophene derivatives, namely **OMeT2** and **g$_3$T2** (**Figure 4.6(a)** and **(b)**, respectively), to minimise the impact on other variables. These bithiophene derivatives were both synthesised using adapted literature procedures,[49] from commercially available 3-methoxythiophene. (3,3'-dimethoxy-[2,2'-bithiophene]-5,5'-diyl)bis(trimethylstannane) was synthesised in two steps, in a 35% yield, whilst (3,3'-bis(2-(2-(2-methoxyethoxy)ethoxy)ethoxy)-[2,2'-bithiophene]-5,5'-

diyl)bis(trimethylstannane) involved a three-step synthesis, which achieved a 24% yield. The additional step for the stannylated **g$_3$T2** originates from the incorporation of the glycol sidechains, which were introduced via an acid-catalysed transetherification reaction, where the methyl group of the methoxy functionality was replaced by the glycol chain. The limiting step to reach stannylated **OMeT2** was the iron-mediated coupling, which has notably poorer yields than the same step involving triethylene glycol sidechains (**Figure 4.6**). This may be due to the slower reactivity of the thiophene unit when solubility is reduced through the lack of sidechains, thus the yield may have been optimised by allowing the reaction to continue over a longer timeframe.

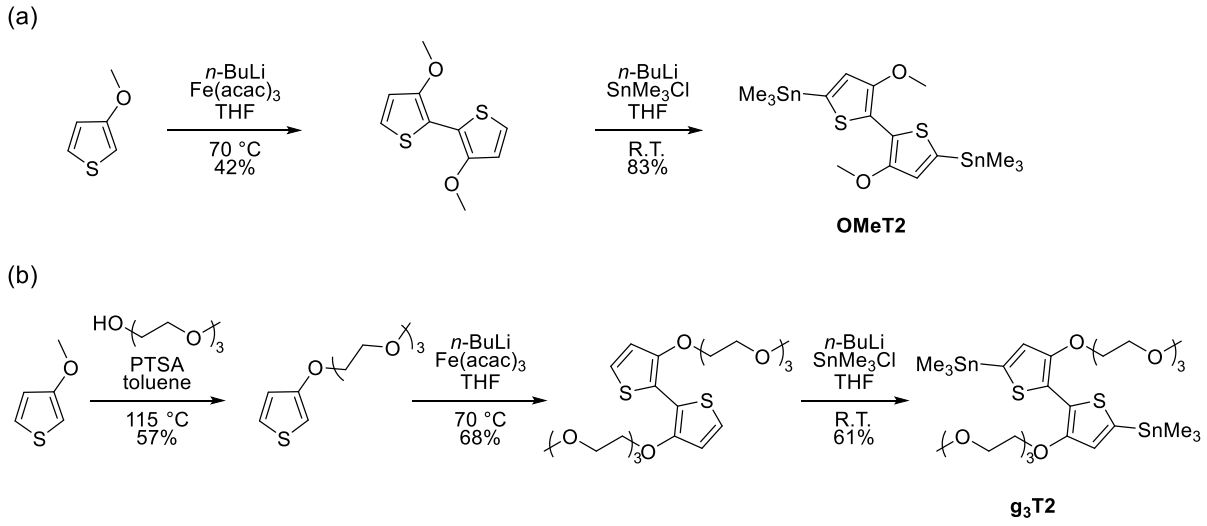


Figure 4.6. Synthetic route to (a) (3,3'-dimethoxy-[2,2'-bithiophene]-5,5'-diyl)bis(trimethylstannane) (**OMeT2**) and (b) (3,3'-bis(2-(2-(2-methoxyethoxy)ethoxy)ethoxy)-[2,2'-bithiophene]-5,5'-diyl)bis(trimethylstannane) (**g$_3$T2**).

4.4.4 Synthesis of the polymers

The monomers above were subjected to classic Stille polymerisation conditions, specifically $Pd_2(dba)_3$ and tris(*o*-methoxyphenyl)phosphine in DMF at 110 °C overnight, in an attempt to produce the desired D-A polymer structure. Unfortunately, during the Soxhlet purification process, initial trials with the **p(gPMDI-T2)** system resulted in a very low molecular weight,

such that the entirety of the "polymer" dissolved in the acetone and methanol washes. Efforts were made to improve the molecular weight of the polymers by increasing the reaction time in increments up to 96 hours, as well as increasing the concentration to from 0.1 to 0.3 M. Additionally, the solvent was switched from DMF to chlorobenzene to enable the use of higher temperatures, up to 130 °C (the full details of the optimisation reactions can be found in **Table 4.2**). Whilst these factors did improve the molecular weight, such that ~3-6 mg of polymer was collected in the chloroform fraction of the Soxhlet, M_n remained low, <6 kDa (**Table 4.2**).

Table 4.2. Trial conditions in the optimisation of PMDI polymerisations.

Trial	Solvent	Temp (°C)	Time (hours)	Conc (M)	Heat/MW	M_n (kDa)
1	DMF	110	16 h	0.1	Heat	N/A*
2	DMF	110	16 h	0.3	Heat	N/A*
3	DMF	110	48 h	0.3	Heat	N/A*
4	DMF	110	96 h	0.3	Heat	3.1
5	CB	130	96 h	0.3	Heat	5.4
6	CB	135	4 h	0.1	MW	28.5

The trials were conducted with polymer **p(gPMDI-T2)**. * No material was soluble in the chloroform fraction of the Soxhlet extraction, so a number average molecular weight could not be obtained. "Heat" denotes the use of an oil bath, heated to the stated temperature and monitored by an in-built thermometer, "MW" indicates the reaction was microwave-assisted.

For D-A polymers synthesised using Stille conditions, microwave-assisted polymerisation has previously been demonstrated as an alternative method, typically increasing the molecular weight.[73,252,253] As such, a final endeavour to increase the molecular weight of these polymers was made (**Figure 4.7**), which saw yields of up to 88%, with exclusively the chloroform fraction of the Soxhlet extraction collected. An additional benefit to this method is that the reaction time can be dramatically reduced, to as little as an hour. For optimal yields and

molecular weights, the polymers were reacted for 2.5-4 hours, though this is still significantly faster than the 3-4 days that produced the optimal results for the standard heat-based polymerisation conditions.

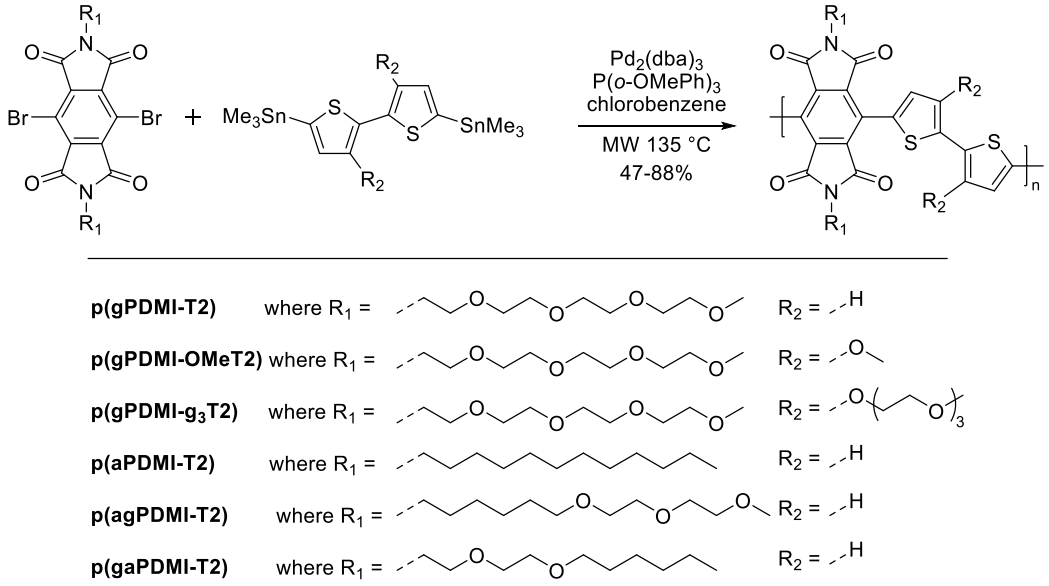


Figure 4.7. Synthesis route to the PMDI-T2 copolymers.

4.5 Properties of the polymers

4.5.1 Optoelectronic and physical properties

The optoelectronic and thermal properties of the six polymers are set out in **Table 4.2**. The number average molecular weights (M_n) were measured by GPC in chloroform, using polystyrene standards at 40 °C. All polymers displayed a unimodal GPC trace, however the broad traces in most cases resulted in high dispersities being calculated. This indicates that there is a high degree of variability in the lengths of the polymer chains in each sample. For step growth polymerisations, the Flory-Huggins model predicts that the dispersity, $Đ = 1 + p$, where p is the extent of the reaction and $Đ$ increases until its value plateaus at 2.[254] This indicates that for $Đ<2$, the reaction has not run to completion, which can be for a number of reasons, including the partially formed polymer chains becoming insoluble, or the reaction time being inadequate. The lowest molecular weight polymer, **p(aPMDI-T2)**, is most likely due to

the lack of solubility conferred by this sidechain. Typically, alkylated NDI-based copolymers employ a substantial branched octyldodecyl sidechain, hence the selected dodecyl chain alone may not be sufficient to enable the polymer to remain in solution for long enough during the synthesis to achieve a higher M_n.

Table 4.2. Summary of the optoelectronic and thermal properties of the six PMDI-based D-A copolymers.

Polymer	M_n (kDa) [$Đ$] [a]	$E_{g,opt}$ (eV) [b]	$\lambda_{max,\ sol}$ (nm) [c]	IP (eV) [d]	T_d (°C) [e]
p(gPMDI-T2)	28.5 [1.54]	2.22	415	5.84	382
p(gPMDI-OMeT2)	30.9 [2.32]	2.08	492	5.36	347
p(gPMDI-g$_3$T2)	21.6 [1.70]	2.00	485	5.08	338
p(aPMDI-T2)	13.1 [1.71]	2.02	419	5.73	409
p(agPMDI-T2)	19.7 [1.29]	2.07	421	5.43	374
p(gaPMDI-T2)	36.8 [1.65]	2.12	421	5.84	318

[a] Number-average molecular weight (M_n) and dispersity ($Đ$) measured by GPC vs polystyrene standards in chloroform at 40 °C. [b] Optical band gap estimated from thin film UV-Vis absorption onset. [c] Peak wavelength obtained from solution UV-Vis absorption spectra in chloroform. [d] Measured by photoelectron spectroscopy in air. [e] Temperature for 5% weight-loss (i.e., decomposition) from thermogravimetric analysis.

The UV-Vis absorption spectra of the six polymers are shown in **Figure 4.8**, both in chloroform solutions and as thin films on glass substrates. For series 1, a bathochromic shift is noted when the comonomer is exchanged both in solution and thin films. One potential reason for this is a more planar conformation,[248] however it is more likely due to the increased electron density of the OMeT2 or g$_3$T2 compared to T2. This observation can be ascribed to the increased donor character of the copolymer, which acts to raise the HOMO, as predicted by DFT calculations. This results in a narrower optical bandgap as the electron donating ability of the comonomer increases: T2<OMeT2<g$_3$T2 ($E_{g,opt}$ = 2.25, 2.07, 1.95 eV, respectively).

For series 2, as expected, the PMDI-based polymers showed two absorption features, with the higher of the two energy bands attributed to the π-π* transition, and the lower energy band

attributed to intramolecular charge transfer (ICT).[248] Unsurprisingly, the spectra in solution overlay perfectly for the same PMDI-T2 backbone with varying sidechains, as the electronic properties of these polymers are not expected to have significant differences. As thin films, there is some variation in the UV-Vis absorption spectra, with a bathochromic shift occurring for λ_{max} as the alkyl content increases. When the optical bandgap is calculated from absorption onset, the same trend is observed, with **p(gPMDI-T2)** presenting the largest bandgap of ~2.22 eV, and **p(aPMDI-T2)** recording the smallest bandgap of the four polymers, of 2.02 eV.

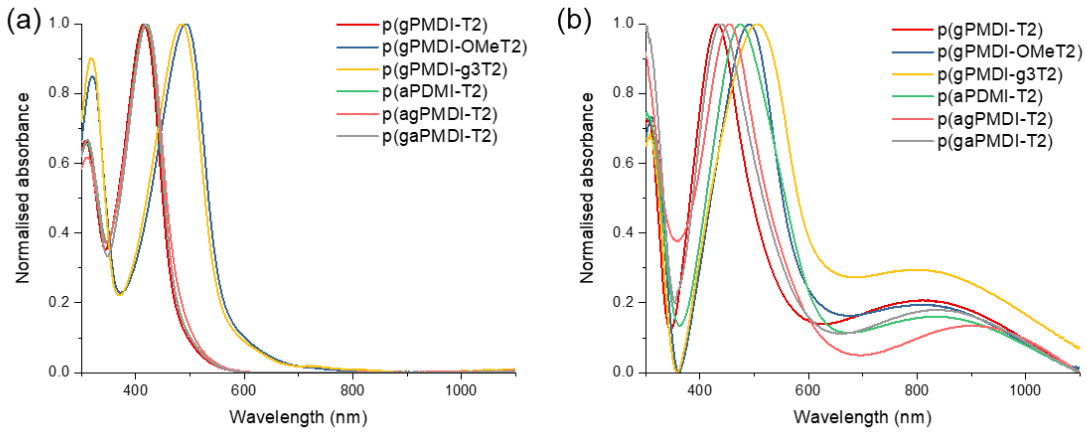


Figure 4.8. UV-Vis spectra of the polymers in (a) dilute chloroform solutions and (b) as thin films on glass substrates.

Next, the thermal stability of the six polymers was investigated using thermogravimetric analysis (TGA). The polymers were subjected to heating up to 600 °C under nitrogen to obtain the degradation temperature of the polymers, which was defined as the temperature at which a 5% mass loss was observed. The values are indicated in **Table 4.2**, and the traces are depicted in **Figure 4.9**. From the data, all polymers exhibit good thermal stability with T_d >300 °C. The fully alkylated and fully glycolated polymers reveal the best thermal stability, with T_d = 409 and 382 °C, respectively, with the mixed sidechains and alternative comonomers acting to hamper this property.

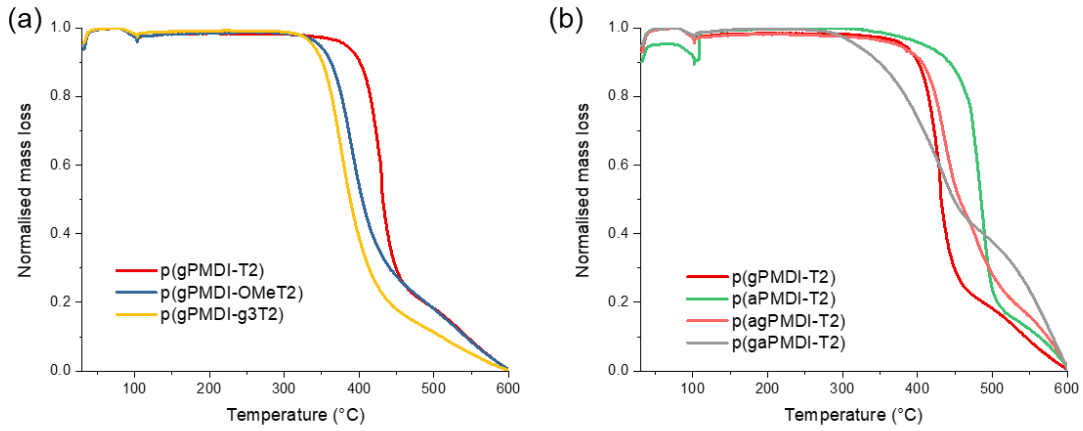


Figure 4.9. Thermogravimetric analysis traces of the polymers of (a) series 1 and (b) series 2. **p(gPMDI-T2)** is displayed on both graphs for comparative purposes. Polymers were heated under nitrogen flow (50 mL/min), using the following conditions: [1] 30.0 to 105.0 °C, 34.99 K/min, [2] hold at 105.0 °C for 10.00 min, [3] 105.0 to 600.0 °C, 10.00 K/min. The artifact at ~100 °C are attributed to the equipment and are present in all spectra.

With a known thermal degradation temperature for each material, the polymers can then safely be investigated using differential scanning calorimetry (DSC), whereby the materials were cycled between -30 and 300 °C under a nitrogen atmosphere. It is critical to conduct TGA measurements in advance to know that the polymers will remain stable throughout the DSC measurements, or to appropriately adjust the DSC conditions to within the thermal stability of the material. DSC was carried out to measure the melting and crystallisation temperatures (if any) of the polymers (**Figure 4.10**). The "crystallisation" peaks at ~65 °C are artifacts attributed to contamination within the machine. This conclusion was reached due to the peak appearing in all spectra, including those that are otherwise featureless, and because there is no corresponding melting peak.

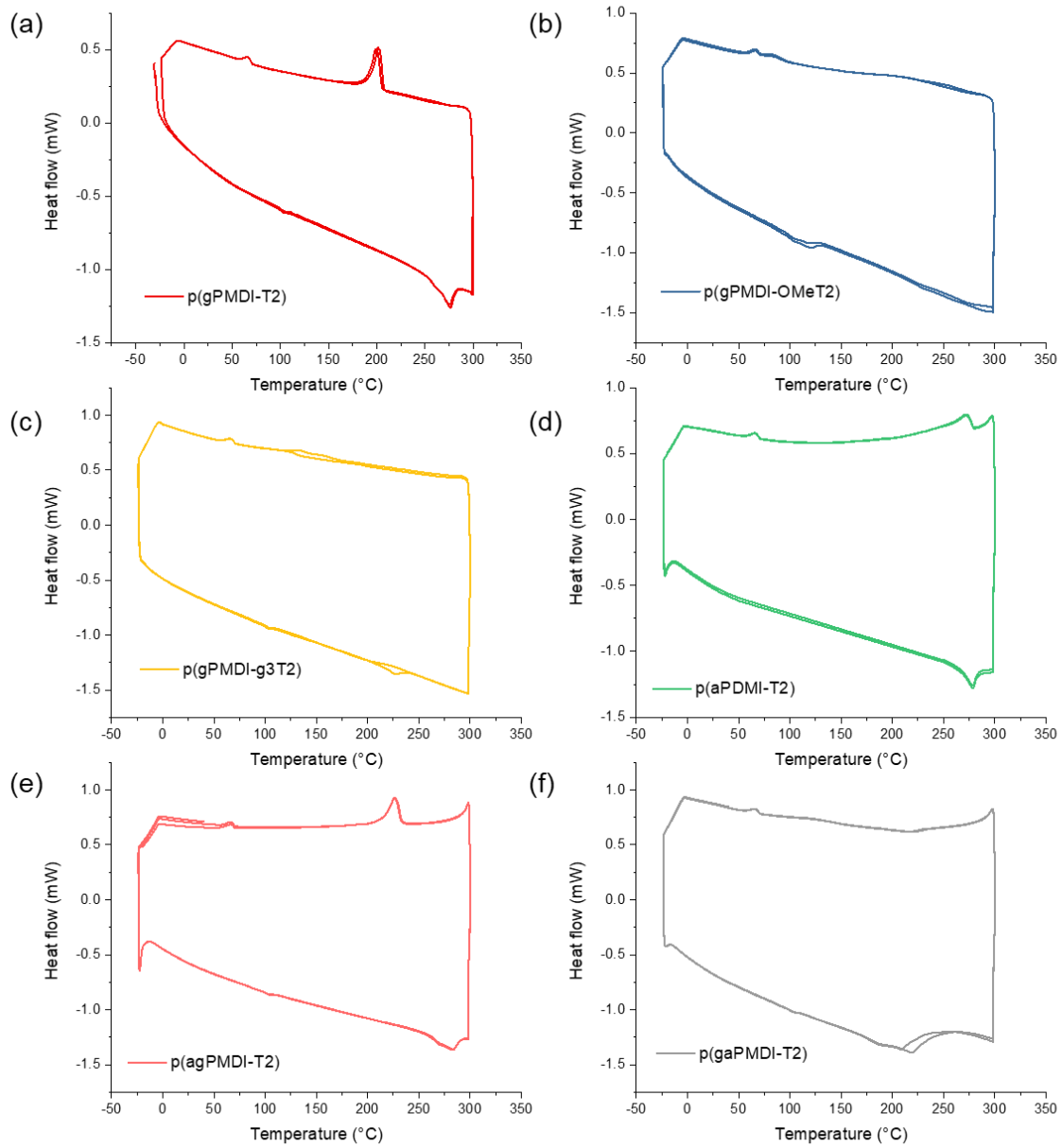


Figure 4.10. Differential scanning calorimetry (DSC) traces of the six polymers. Polymers were heated/cooled at 10 K/min in a nitrogen atmosphere from -30 to 300 °C. The second and third cycles only are presented to remove any variations attributed to processing effects in the first cycle. The peaks at ~65 °C are artifacts present is all measurements and are not related to events during the heating/cooling cycles.

As the sidechains of these polymers are liquids at room temperature, it would not be expected to see sidechain melt and crystallisation within the temperature range of these measurements.

Instead, three of the polymers, **p(gPMDI-T2)**, **p(aPMDI-T2)** and **p(agPMDI-T2)** display clear melting and crystallisation transitions, which are most likely ascribed to backbone phase transitions. The other polymer with the same backbone, **p(gaPMDI-T2)**, also displays some melt transition, although its consistency is questionable and there is no clear corresponding crystallisation peak. It does, however, appear that by replacing the comonomer with OMeT2 or g_3T2, the transition becomes much less prominent, and shifts to lower temperatures, which corresponds with the lower decomposition temperatures found by TGA for these two materials.

Focussing on the three polymers with clear transitions, the temperatures progressively increase with increasing alkyl content. This trend is relatively unsurprising, as alkyl content, particularly adjacent to the backbone, is likely to induce an ordering effect, resulting in higher temperatures being required to melt the backbone.[255] What is surprising are the clear melting and crystallisation features for polymers containing >10% glycol content, particularly **p(gPMDI-T2)**, but also **p(agPMDI-T2)**. Typically, glycolated polymers display very limited, if any, thermal transitions by DSC,[116,125,192,256] with minimal exceptions.[195]

From the DSC traces, it is also possible to extract the enthalpy of a transition by integrating the area under the peak and normalising by mass. This information gives an insight into the energy required for the transition, and highlights that either there are more crystallites present in the sample, or that each crystallite requires more energy to undergo the transition, or both. Integrating the peaks for **p(gPMDI-T2)**, **p(aPMDI-T2)** and **p(agPMDI-T2)**, the enthalpy of each transition was acquired, and is presented in **Figure 4.11**. **p(gPMDI-T2)** and **p(agPMDI-T2)** both exhibit greater melting enthalpies compared to the fully alkylated variant, which, again, is surprising, and is indicative of a relatively ordered microstructure.

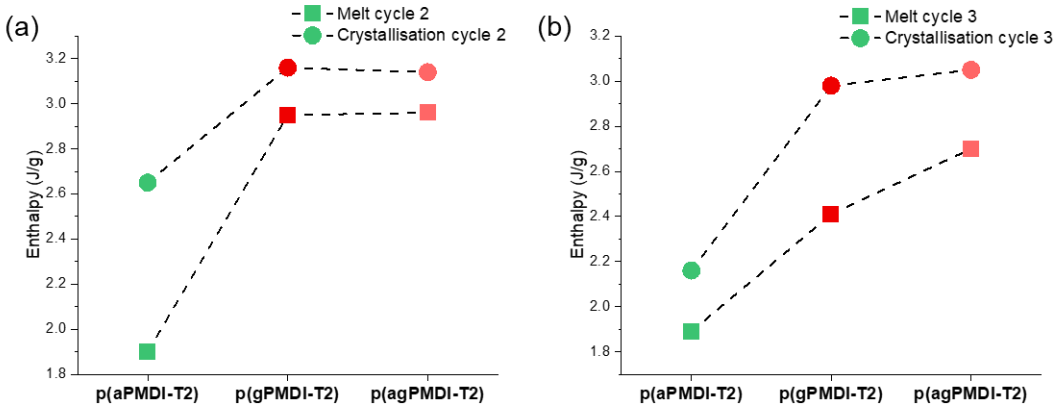


Figure 4.11. Melting and crystallisation enthalpies of **p(gPMDI-T2)**, **p(agPMDI-T2)** and **p(aPMDI-T2)** from (a) the second heating/cooling cycle and (b) the third heating/cooling cycle of DSC measurement.

4.5.2 GIWAXS analysis

Grazing incidence wide angle X-ray scattering (GIWAXS) was conducted on the six PMDI-based copolymers ex situ to understand their morphology. The GIWAXS images and line cuts are set out in **Figure 4.12** and **Figure 4.13**, and the extracted GIWAXS parameters are set out in **Table 4.3**. The first point of note is the similarity in the lamellar stacking distance for all six polymers. This is critical when examining the ion conductivities of polymers with different sidechains, as large variations in lamellar spacings would indicate significant differences in the length or packing of the sidechains. The molecular design of these polymers ensured that the sidechains were of comparable lengths (by the number of atoms), and this data verifies that the packing is also comparable, although not identical. The slight differences may occur from the more linear conformation of the fully alkylated sidechain, compared to the glycol sidechain which is thought to adopt a somewhat helical structure.[135] This leads to a length difference of ~1.4 Å, or 7%.

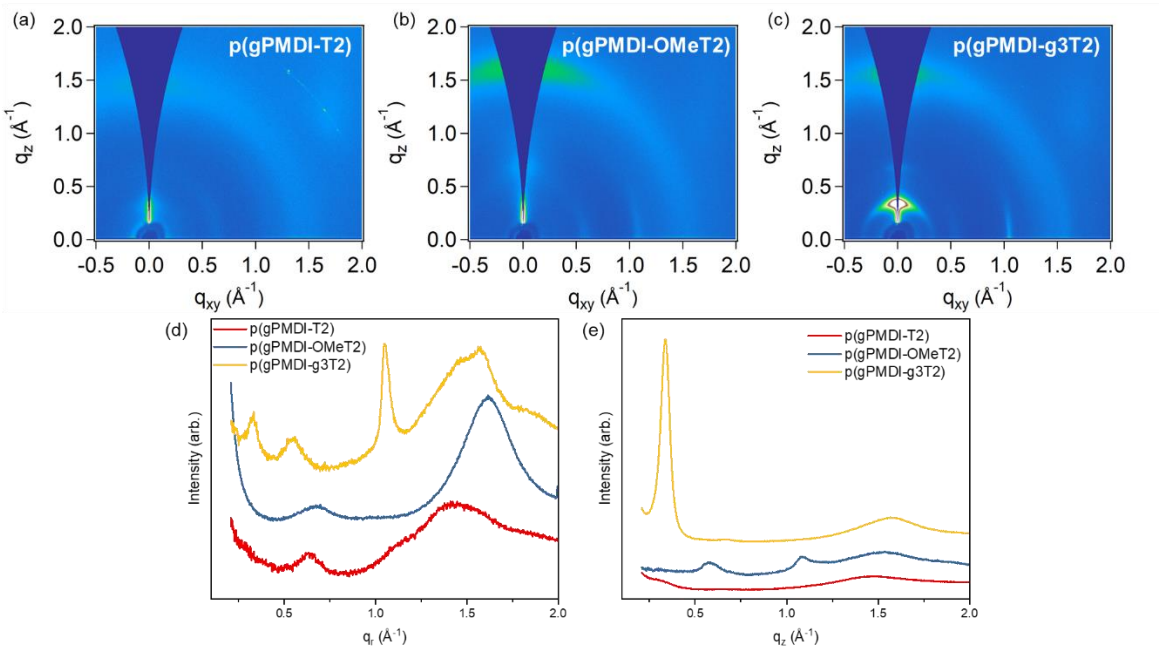


Figure 4.12. Ex-situ GIWAXS images of neat as-cast films for (a) **p(gPMDI-T2)**, (b) **p(gPMDI-OMeT2)** and (c) **p(gPMDI-g3T2)** and the (d) in-plane (q_r) and (e) out-of-plane (q_z) line cuts of each polymer of series 1.

The three polymers of series 1 present a mixed edge on/face on texture (**Figure 4.12**). On account of this, the q_z plane was used to extract the lamellar distances to avoid misinterpretation of any peaks related to the backbone. From both the GIWAXS images (**Figure 4.12**), and the peak parameters (**Table 4.3**), it is possible to observe that the polymer becomes more ordered with increasing glycol content on the bithiophene unit. This is seen through the increasing intensity of both the lamellar and π-stacking signals, as well as by the sharper (100) lamellar peak and clear definition of the (200) peak in the linecuts. This translates to a longer coherence length of the lamellar spacing of 106.8 Å for **p(gPMDI-g3T2)**, compared to 35.2 Å for **p(gPMDI-OMeT2)**. For the least ordered of the series, **p(gPMDI-T2)**, it was not possible to extract a lamellar spacing due to the poorly defined structure. Further evidence of the increasing order across series 1 is the decrease in the π-π stacking distance, from 4.20 Å for **p(gPMDI-T2)**, to 4.02 Å for **p(gPMDI-g3T2)** (**Table 4.3**). The bare T2 copolymer displays an

amorphous texture and introducing planarising oxygens adjacent to the bithiophene unit increases planarity, allowing neighbouring chains to pack more closely. This supports the hypothesis that the DFT calculations predicted, suggesting that some additional planarity is conferred by the OMeT2 unit, reducing the dihedral angle between the PMDI and T2 units upon introducing the methoxy groups.

Table 4.3. GIWAXS peak parameters for the six PMDI-based copolymers.

	Polymer	lamellar stacking [a]		π-π stacking [b]
		L_c (Å)	d (Å)	d (Å)
Series 1	**p(gPMDI-T2)**	-*	-*	4.20
	p(gPMDI-OMeT2)	35.2†	18.7†	4.09
	p(gPMDI-g3T2)	106.8	18.7	4.02
Series 2	**p(aPMDI-T2)**	107.8	20.1	3.99
	p(agPMDI-T2)	79.3	19.0	4.05
	p(gaPMDI-T2)	44.6	19.3	4.29

[a] In-plane lamellar scattering peak (100). [b] Out-of-plane π-stack scattering peak (010). * **p(gPMDI-T2)** had a poorly defined structure from GIWAXS pattern, therefore the (100) coherence length and lamellar spacing could not be calculated. † **p(gPMDI-OMeT2)** coherence length and lamellar spacing was calculated from (200) as (100) could not be separated from the baseline at low q values. Coherence lengths for the π-stacking peaks were not extracted as the (010) peak could not be clearly separated from the baseline.

The remaining three polymers of the second series all present a predominantly edge on orientation, with the alkylated derivative revealing the most ordered microstructure, when examining both the π-stacking distance and the coherence length of the lamellar stacking. Further to this, the data indicates that having alkyl chains flanking the backbone confers a higher degree of order, with **p(agPMDI-T2)** reporting a lamellar coherence length of almost double the inverted sidechain of **p(gaPMDI-T2)**, with L_c = 79.3 Å and 44.6 Å, respectively, whilst having very similar lamellar *d*-spacings (**Table 4.3**). It is also the case that some alkyl content in the sidechain appears beneficial when (qualitatively) compared to the fully glycolated derivative, as **p(gaPMDI-T2)** shows more order than **p(gPMDI-T2)** (**Figure 4.13**).

Similar to the previous series, the longer coherence length is also corroborated by shorter π-stack distances, which is smallest for **p(aPMDI-T2)**, at 3.99 Å, increasing to 4.05 Å for **p(agPMDI-T2)**, then 4.29 Å for **p(gaPMDI-T2)**. Interestingly, the inverted hybrid sidechain derivative (**p(gaPMDI-T2)**) reports a larger π-stack than **p(gPMDI-T2)**, however as the intensity of the signal for **p(gPMDI-T2)** is poor, extracting the spacing from the linecut may consist of some error.

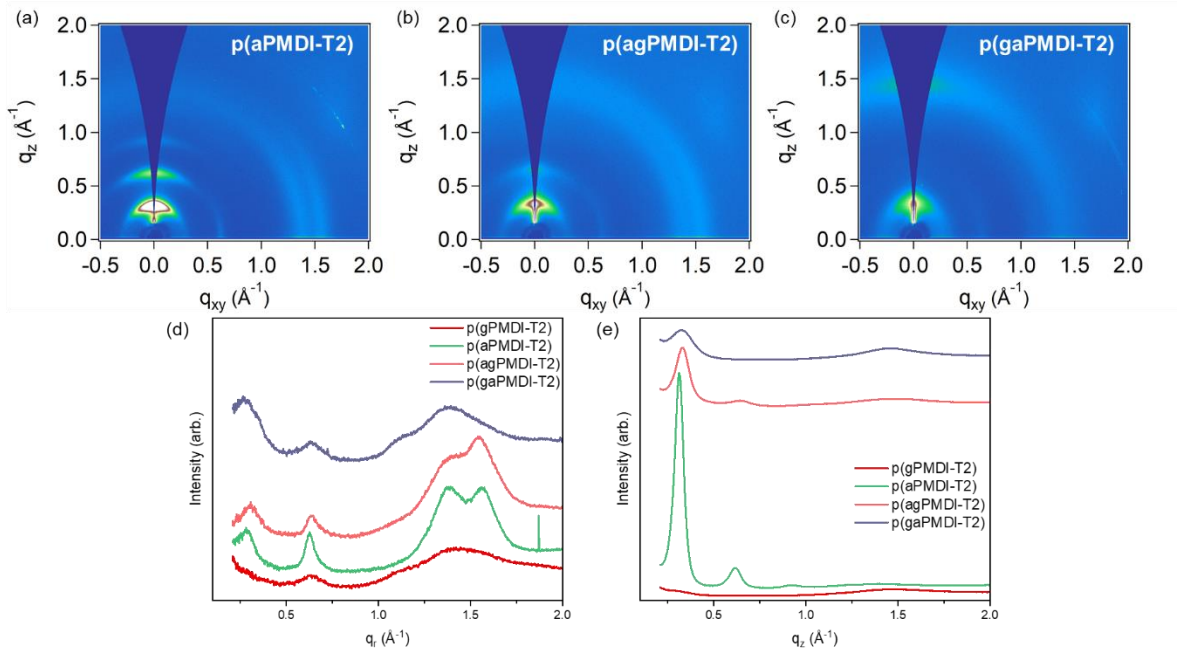


Figure 4.13. Ex-situ GIWAXS images of neat as-cast films for (a) **p(aPMDI-T2)**, (b) **p(agPMDI-T2)** and (c) **p(gaPMDI-T2)** and the (d) in-plane (q_r) and (e) out-of-plane (q_z) line cuts of each polymer of series 2 (including **p(gPMDI-T2)** reproduced.

The morphology of the microstructure found by GIWAXS can be related to the DSC data reported and discussed in **Section 4.5.1**. By GIWAXS, **p(agPMDI-T2)** and **p(aPMDI-T2)** appear the most ordered of the six PMDI polymers, which is therefore expected that they both display melting and crystallisation transitions by DSC. However, GIWAXS finds **p(gPMDI-T2)** to be a predominantly amorphous material, with limited order, thus it is initially surprising that this material exhibits any transitions by DSC. The cycles presented in **Figure 4.10** are the

second and third cycles only, hence the polymer has already undergone one heating/cooling cycle. It is therefore likely that the transitions observed by DSC are due to crystallisation occurring after the initial melt. To confirm this attribution, the first DSC cycle was examined, and no peaks were observed, which indicates that crystallisation does not occur during the spin-casting process for **p(gPMDI-T2)**, and instead happens when cooling after melting. This begs the question of the impact of annealing, a process that is not commonly exploited for these mixed conductors, particularly in relation to ionic transport. There are assumptions within the field that annealing of OMIECs prior to their operation in OECTs would minimise the volumetric capacitance recorded, due to the increased ordering of the polymer, such that larger crystallites do not allow free volume to accommodate aqueous ions in the bulk of the material.[119] In fact, this is a property that requires further evaluation, particularly in the context of ionic transport, to understand the impact it has on OECT performance.

4.5.3 Cyclic voltammetry in aqueous electrolyte

By using cyclic voltammetry in 0.1 M KCl aqueous electrolyte, the electrochemical activity of the two series of polymers was probed. The CVs were conducted using a polymer coated ITO slide as the working electrode, with a Pt wire and Ag/AgCl counter and reference electrode, respectively. The six CVs are presented in **Figure 4.14**. From these voltammograms, it appears that of the six polymers, only **p(gPMDI-T2)** and **p(agPMDI-T2)** showed reversible reduction and oxidation in aqueous electrolyte. This can be seen by the roughly equal intensity of the peaks associated with reduction (resulting in a negative current) and oxidation (recorded as a positive current). It is thought that these materials have sufficient hydrophilic glycol content and composition, particularly at the interface of the material with the electrolyte (i.e., at the end of the sidechains: **p(agPMDI-T2)** *c.f.* **p(gaPMDI-T2)**), that they are able to accommodate aqueous ions, and are also able to expel the ions under a potential within the electrochemical window of water. This is particularly apparent as **p(gaPMDI-T2)** did not show reversible redox

features despite having the same chain, albeit in an inverted configuration. The terminal alkyl sidechain segment likely acted as a hydrophobic barrier, shielding the polymer from aqueous ion penetration and preventing reversible redox.

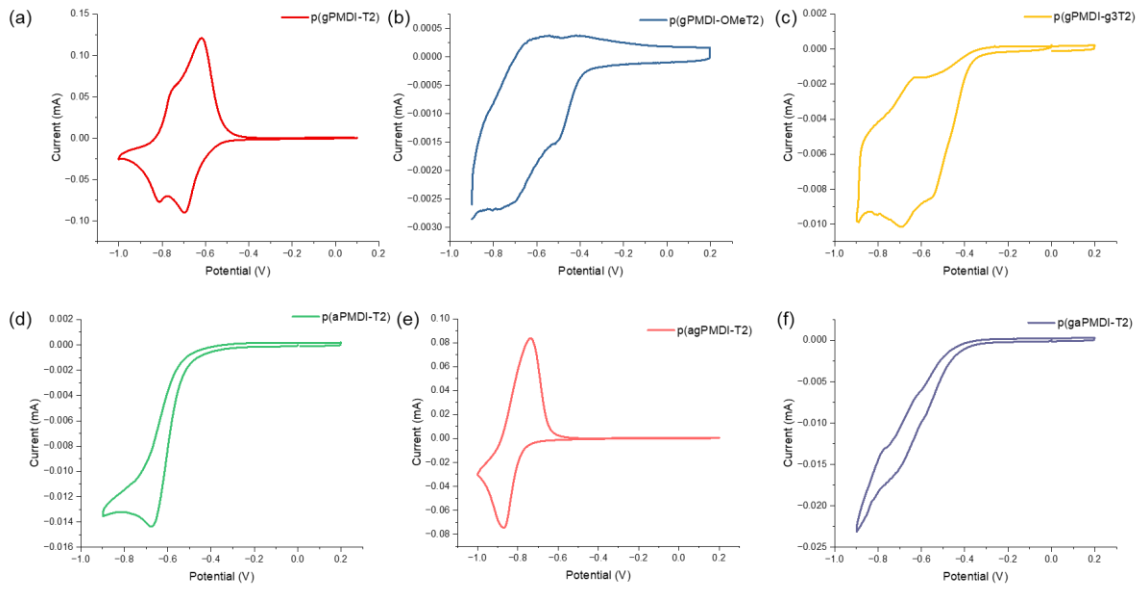


Figure 4.14. Cyclic voltammetry of (a) **p(gPMDI-T2)**, (b) **p(gPMDI-OMeT2)**, (c) **p(gPMDI-g3T2)**, (d) **p(aPMDI-T2)**, (e) **p(agPMDI-T2)** and (f) **p(gaPMDI-T2)** spin cast onto an ITO-coated glass slide as the working electrode, using an Ag/AgCl reference and platinum wire counter electrode. The electrolyte was degassed 0.1 M $KCl_{(aq)}$ solution and a scan rate of 5 mV s^{-1} was used. For **p(gPMDI-T2)** and **p(agPMDI-T2)** three cycles are shown, the second, third and fourth cycles. For the other four voltammograms, the second cycle only is shown as there was a significant decrease in current with each subsequent cycle.

For the other materials, a clear reduction is observed, however there is no oxidation to recover the neutral state. This is to be expected for the fully alkylated **p(aPMDI-T2)**,[116] and it can be concluded that the terminal alkyl sidechains of **p(gaPMDI-T2)** does not allow for the free movement of aqueous ions, hence an irreversible electrochemical doping process. For the other two polymers, **p(gPMDI-OMeT2)** and **p(gPMDI-g3T2)** it is possible that the hydrophilic content is in fact too high, causing the ions to easily penetrate, then remain within the bulk of

the polymer as there is insufficient driving force to expel them. Successive cycles of all the irreversible polymers produced smaller and smaller reduction currents, which may be ascribed to the fact that there is less neutral polymer to reduce on each subsequent cycle. This could be verified by bubbling oxygen into the electrolyte and repeating the measurements. If the CV returns to the original shape, then the polymer is capable of oxidation via direct electron transfer, but not using aqueous ions.

All the voltammograms except **p(agPMDI-T2)** show, to varying extents, at least two different reduction peaks. This is indicative of the formation of the polaron and bipolaron within the electrochemical window of water. The bipolaron formation for **p(agPMDI-T2)** is expected to be at a potential greater than -1 V due to the negatively shifted reduction onset potential (and entire spectrum) compared to the other materials. Within series 1, the reduction onset potential decreases (i.e., it moves closer to zero) with increasing glycol content on the bithiophene unit, moving from -0.59 V to -0.40 to -0.37 V. This follows literature precedent, where introducing glycol chains onto the bithiophene donor unit of NDI-based polymers decreases the reduction onset potential.[72] However, the values for these PMDI polymer are around two times larger, indicating that either ionic or electronic doping of PMDI is more difficult, or both. Additionally, whilst it was proposed that changing the comonomer to a more electron rich bithiophene moiety (e.g., in **p(gPMDI-OMeT2)** and **p(gPMDI-g3T2)**) may introduce some ambipolar character,[72,138] this was not found to be the case when extending the potential cycles to +0.8 V.

For series 2, the reduction onset potential does not provide a logical trend, with **p(gPMDI-T2)** and **p(agPMDI-T2)** displaying comparatively large reduction onset potentials of -0.59 V and -0.74 V, respectively. This is somewhat surprising as it would be expected that electrochemical doping of **p(gPMDI-T2)** and **p(agPMDI-T2)** would be easier than that of **p(aPMDI-T2)**, due to the hydrophobic alkyl sidechains preventing aqueous ion migration into the bulk. Instead,

the alkylated derivative presented an aqueous reduction onset of -0.51 V, and **p(gaPMDI-T2)** had the lowest of the series, at -0.45 V. Whilst these materials were designed solely as a model system of ionic conductivity, rather than usable OMIECs for OECTs, these values are all very large if an energy efficient transistor was the end goal.

By comparing the onset of reduction obtained from the organic and aqueous CVs, it would be possible to use the difference between these numbers to estimate the ion penetration (i.e., $E_{red,org} - E_{red,aq}$).[71,191] Unfortunately, obtaining CVs in organic electrolyte was not possible due to both dissolution and delamination issues, thus this method could not be exploited.

Aqueous CVs can also be used to extract the bulk capacitance of the material across the potential window under dynamic conditions. On the other hand, electrochemical impedance spectroscopy (EIS) is a particularly useful technique for understanding the capacitance of a material at a certain voltage (i.e., steady-state conditions), such as the operational potential of the OECT device. From the low frequency EIS measurements, the potential-dependant pseudocapacitance can be extracted, which is attributed to reversible faradaic redox processes.[237] The bulk capacitance, extracted from the CV, has both faradaic and capacitive contributions.[237] This method assumes that the material is acting as a capacitor and does not denote the potentials at which more or less charges can be stored, however for understanding the differences between comonomers or sidechains, this approach is sufficient. Furthermore, as these materials are hypothesised to have little to no charge carrier mobility, OECT devices are unlikely to turn on, hence their "operational voltage" is unknown and using EIS is not practical or necessary.

By integrating half a cycle of the voltammogram (i.e., either the reduction or oxidation peak, as the area under each peak should be equal), the bulk capacitance can be obtained using Equation **(7)**:[257]

$$C_{bulk} = \frac{\int IVdV}{2x\Delta V} \qquad (7)$$

Where C_{bulk} is the bulk capacitance, x is the scan rate of the CV and ΔV is the potential window. This method was only applied to **p(gPMDI-T2)** and **p(agPMDI-T2)** as these were the only polymers with reversible CVs. As these materials are n-type in nature, the reduction peak of the second cycle was selected for integration. For **p(gPMDI-T2)** this resulted in a C_{bulk} of 2.13 mF and 1.03 mF for **p(agPMDI-T2)**. As the same solution concentrations and spin conditions were used, it is assumed that the film volumes were comparable. The values are as expected when examining the glycol content of the two polymers, whereby the hydrophilic glycol content of **p(gPMDI-T2)** is double that of **p(agPMDI-T2)**, therefore enabling more aqueous ions to penetrate the material. This results in the material having the ability to store approximately double the charge, hence having double the C_{bulk}. Using this technique, it is not possible to determine the type of redox process (i.e., faradaic or non-faradaic), but this gives an insight into the significant contribution that mild variations in the sidechain composition may have (e.g., regular vs inverted hybrid sidechains), and verifies that glycol content (*c.f.* alkyl sidechains) is critical in the volumetric capacitance parameter of OECT performance.

4.5.4 Galvanostatic charging measurements

Following on from this, these two materials (**p(gPMDI-T2)** and **p(agPMDI-T2)**) were inserted into OECT devices to understand their ability to act as an OMIEC. Somewhat expectedly, the OECT devices containing these materials did not turn on, indicating that these materials conducted no electronic charge, thus cannot be classified as OMIECs and are not suitable materials for OECT applications. However, as these materials have been demonstrated to conduct ions, it is possible that they could instead be applied to battery technology, as other PMDI-based materials have been previously.[247,258] By performing galvanostatic charging

measurements, this concept can be probed, as well as gaining an insight into the faradaic/non-faradaic nature of the redox process.

Galvanostatic charging/discharging is a technique that applies a constant current to charge/discharge a material within a specified voltage range. This can be used to understand the rate of charging or discharging of a material (i.e., how quickly it is able to store or release charge) and allows understanding of its practical use as an energy storage device, such as a battery. It also provides an insight of whether the material is charging via a faradaic or non-faradaic process. Faradaic charging is a process whereby charge transfers from one bulk phase to another, such as from the electrode to/from the polymer.[259] Empirically, this is recorded as a constant voltage after the application of a constant current, which is visualised as a plateau in the galvanostatic charging profile. A non-faradaic process instead involves the gradual storage of charge, which would be portrayed as a constant slope in the galvanostatic charging profile.

These measurements are only possible for materials with clear redox behaviour by CV, as oxidation back to the neutral polymer is required to enable discharging of the material. The galvanostatic charging profiles in 0.1 M aqueous KCl solution for **p(gPMDI-T2)** and **p(agPMDI-T2)** are presented in **Figure 4.15**. By taking measurements using a current which equates to full charging of the material in one hour (C), and a current which equates to full charging of the material in two hours (C/2), the charging process can be evaluated. By referring to the peaks of the CVs for the two polymers (**Figure 4.14**), **p(gPMDI-T2)** presented reduction peaks at -0.05 V and -0.18 V, which correlate to the potentials of the plateaus observed in **Figure 4.15(a)**, which is indicative of Faradaic charging. Similarly, **p(agPMDI-T2)** presents a reduction peak by CV at ~-0.2 V, which corresponds to the plateau in galvanostatic charging, again suggesting that Faradaic charging may be occurring.

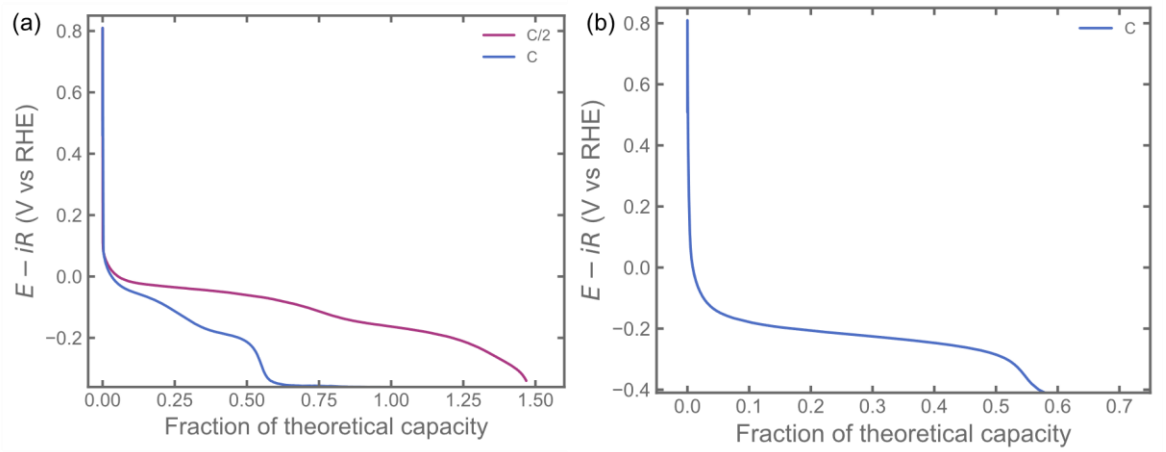


Figure 4.15. Galvanostatic charging profiles for (a) **p(gPMDI-T2)** and (b) **p(agPMDI-T2)** with an applied current that would fully charge the material in one hour (C) or in two hours (C/2) conducted in 0.1 M aqueous KCl solution. This was calculated based on the number of electrons a monomer unit can hold and the number of monomer units on the electrode, which resulted in a current of 5.16 nA for charging of **p(gPMDI-T2)** over one hour and 4.44 nA for charging of **p(agPMDI-T2)** over one hour.

After the galvanostatic charging measurements were conducted, the CVs for both polymers were repeated, and are set out in **Figure 4.16**. It is clear to see that the redox features of the original CVs, which appeared stable over 4 cycles, have been lost. This indicates that applying a constant current for over two hours (the length of time required to conduct the galvanostatic measurements at a C/2 charging rate) is not conducive with these materials as there is an irreversible process occurring that reduces stability. This suggests that whilst these materials are able to store charge, they are not yet optimised for real battery applications.

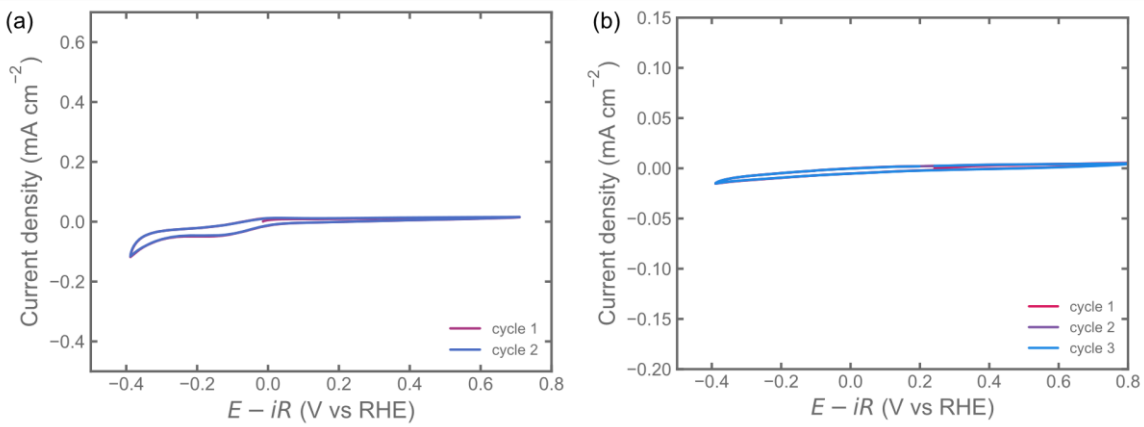


Figure 4.16. Cyclic voltammograms of (a) **p(gPMDI-T2)** and (b) **p(agPMDI-T2)** after galvanostatic measurements, spin cast onto an ITO-coated glass slide as the working electrode, using an Ag/AgCl reference and platinum wire counter electrode. The electrolyte was again degassed 0.1 M $KCl_{(aq)}$ solution and a scan rate of 5 mV s^{-1} was used.

4.6 Conclusion and future work

The work in this chapter involved the design, synthesis and characterisation of six novel PMDI-based copolymers with the aim of isolating ionic transport to better understand the role of ionic conductivity. Successful synthesis was completed to produce polymers containing comonomers of different electron densities (bithiophene, bis(methoxy)bithiophene and bithiophene functionalised with two triethylene glycol chains), as well as using glycolated, alkylated and hybrid sidechains on the PMDI core. The polymers all achieved similar molecular weights, and the solution and thin film UV-Vis absorption spectra were comparable for the same polymer backbone, only showing redshifted behaviour when increasing the electron density of the donor component.

The thermal properties of the polymers were investigated using TGA, with all polymers showing good stability and a thermal degradation temperature above 300 °C. From this, DSC measurements were conducted to evaluate the crystallinity of the materials through the observation of melting and crystallisation transitions. Three of the six polymers exhibited such

transitions, namely, **p(gPMDI-T2)**, **p(aPMDI-T2)** and **p(agPMDI-T2)**, which are likely attributed to backbone phase transitions. The microstructure was then examined with GIWAXS, which showed **p(aPMDI-T2)** and **p(agPMDI-T2)** to be well ordered materials, which explains the phase transitions by DSC. However, **p(gPMDI-T2)** presented an amorphous microstructure, and upon further inspection, the phase transitions only occurred after the first heating/cooling cycle, as crystallisation occurs only after melting, not from spin coating, for this material.

Aqueous CVs revealed that only two of the six polymers (**p(gPMDI-T2)** and **p(agPMDI-T2)**) were stable to repeated redox, due to their optimal glycol content and configuration which could reversibly accommodate aqueous ions to reduce and re-oxidise the material. By integrating the CVs and calculating the bulk capacitance, **p(gPMDI-T2)** has double the capacitance of **p(agPMDI-T2)**, indicating that double the amount of hydrophilic glycol content results in twice the ability to conduct and store charges. This indicates that a degree of glycol content is a critical design strategy for ionic conductivity. Furthermore, subtle variations in the sidechain composition can have significant impacts on the material's ability to store charges, with glycol content at the sidechain termini deemed a necessary requirement. Next, these two materials were trialled in OECT devices. These transistors could not be switched on, verifying that there was insufficient electronic charge. Instead, these materials were subjected to galvanostatic measurements to understand their capabilities as energy storage materials, whereby a constant current is applied across a selected voltage window. By comparing the aqueous CVs and the galvanostatic profiles, it was possible to connect the CV reduction peaks with the potentials at which the galvanostatic profiles plateaued, indicating these materials may be charging via a Faradaic process, which is useful for battery technology. Unfortunately, there were stability issues with both materials, where CV repeats after the galvanostatic measurements revealed almost complete loss of all redox features for both polymers. However,

this model system enables a broader understanding of ionic conductivity (by examining capacitance) with this property decoupled from charge carrier mobility for the first time in OECT applications.

In order to develop this project, further techniques that were inaccessible to the author could be employed, such as in situ GIWAXS, to observe the structural changes occurring during applied potentials (CV), and electrochemical quartz crystal microbalance with dissipation monitoring (EQCM-d) which is able to provide additional insight into the uptake and retention of aqueous ions by the bulk of the polymer. Additionally, a separate study could be conducted to better understand the impact of annealing on OECT performance. This would require a different polymer series that is operable in OECT devices, however they would require some of the series to present melting and crystallisation transitions by DSC after the first cycle, such that the additional order conferred by heating could be investigated.

Chapter 5

Experimental procedures

5.1 General experimental

All reactions were performed in oven-dried glassware under a nitrogen atmosphere using standard Schlenk techniques unless otherwise stated. Commercially available chemicals were purchased from Sigma Aldrich, TCI or Thermo Fisher Scientific and used as received unless otherwise stated. Water was purified by an Elix® UV-10 system. Brine refers to a saturated aqueous solution of NaCl. *In vacuo* refers to the use of a rotary evaporator connected to a diaphragm pump. Column chromatography was performed on Geduran® silica gel, particle size 40–63 μm or with Biotage ZIP columns, using the indicated solvents. Reactions were monitored by thin-layer chromatography with silica gel 60 F_{254} plates and visualised by either UV irradiation or staining with potassium permangnate. Preparative gel permeation chromatography (recycling preparative HPLC) was performed using a LaboACE LC-5060 instrument with a separation line containing 2HR and 2.5HR columns for small molecules or a 4HH column for polymers. Microwave experiments were performed in a Biotage Initiator V 2.3. Argon (99.999%) gas was purchased from Praxair.

Materials characterisation. ^{1}H and ^{13}C NMR spectra were recorded on a Bruker AV-400 (400 MHz) spectrometer at ambient temperature, unless otherwise stated. Chemical shifts are reported in units of parts per million (ppm, δ) for solutions in the stated deuterated solvent and coupling constants (J) are given in Hz. The splitting patterns are reported as s (singlet), d (doublet), t (triplet), q (quartet), p (pentet) and m (multiplet). The chemical shifts were referenced using residual chloroform (^{1}H NMR: 7.26 ppm, ^{13}C NMR: 77.4 ppm), acetone (^{1}H NMR: 2.09 ppm, ^{13}C NMR: 30.6 ppm), DCM (^{1}H NMR: 5.30 ppm, ^{13}C NMR: 53.5 ppm) or dimethylsulfoxide (^{1}H NMR: 2.54 ppm, ^{13}C NMR: 40.5 ppm) peaks as an internal standard. Infrared absorption spectra were recorded using an Agilent Technologies Cary 630 FTIR spectrometer in the neat form, with the exception of the polymers, which were drop cast onto the measuring crystal. Low resolution mass spectra (m/z) were recorded on an Agilent 1260

Infinity II with Diode Array and Single Quadrupole Detectors in solutions of MeOH or acetonitrile. A selected peak is reported in Daltons and the intensity is given as a percentage of the base peak. High resolution mass spectrometry (HRMS) was run on a Bruker microTOF ESI by the mass spectrometry department, Chemistry Research Laboratory, University of Oxford. UV-Vis absorption spectra were recorded on UV-1601 (λ_{max} 1100 nm) and a UV-2600 (λ_{max} 1400 nm) Shimadzu UV-Vis spectrometers. Thermogravimetric analysis (TGA) analysis was carried out on a Mettler Toledo instrument, heating from 30.0°C to 105.0 °C (34.99 K/min), keeping the temperature at 105.0 °C for 10.0 min and heating from 105.0 to 600.0 °C (10.0 K/min) under nitrogen flow (50 mL/min). Differential scanning calorimetry (DSC) was performed on a TA-DSC Q100 from -10 °C to 290 °C under a nitrogen atmosphere, with a heating/cooling rate of 10 °C/min. Number average (*M*n) and weight average (*M*w) molecular weights in either chloroform or dimethylformamide at 40 °C were determined using an Agilent Technologies 1260 infinity GPC at 40 °C, using two PLgel 10 micrometer Mixed-B columns in series (300 × 7.5 mm), and calibrated against polystyrene standards ($Đ$ < 1.10). Photoelectron spectroscopy in air (PESA) was carried out on a KP Technology APS02 system. Grazing incidence wide-angle X-ray scattering (GIWAXS) was conducted at the Advanced Photon Source (APS) at Argonne National Laboratory using an incident beam energy of 10.92 keV and an incident angle of 0.14º or at Stanford Synchrotron Radiation Lightsource using a Rayonix MAR-225 area detector and an incident beam energy of 12.73 keV and an incidence angle of approximately 0.1° was employed. Raw scattering data were processed using GIXSGUI[260] and analysed using a custom MATLAB script. Coherence lengths in the backbone and lamellar directions can be extracted from GIWAXS data using pseudo-Voigt peak fits.

Inductively coupled plasma mass spectrometry (ICP-MS). Element concentrations were determined based on dry polymer weight. Samples were digested in TraceMetal® grade concentrated nitric acid under elevated temperature (200 °C) and pressure in fluoropolymer

pressure vessels in a CEM MARS5 microwave digestion system. Digested samples were diluted with 2% v/v nitric acid prior to analysis to target an estimated 1-100 µg/L in the analytical solution. Analysis was performed on an Agilent 8900 ICP-MS attached to an Agilent SPS-4 autosampler. The sample introduction system also includes a standard Scott double pass cooled spray chamber operated at 2 °C, a 2.5mm i.d. Agilent glass torch, and a 200 µl/min Micromist nebulizer. The ICP-MS was fitted with standard nickel cones and operated in no gas mode. Before analysis, all solutions were further diluted by 50% by teeing in an internal standard solution of 2 µg/L platinum and rhodium (High Purity Standards) prepared with 2% v/v nitric acid to correct for instrumental drift. Procedural blanks were run in parallel with samples and averaged 14 ng contributing to less than 2% of the analytical signal and are regarded as negligible. Reproducibility is estimated to be 2.8% RSD from repeated analyses (n=11) over 2 analytical sessions of an in-house QC sample prepared from a polymer of know Pd composition.

Cyclic voltammetry. Cyclic voltammograms were recorded using an Autolab PGSTAT101 with a standard three-electrode setup with a working electrode, a platinum wire counter electrode and a Ag/AgCl reference electrode, calibrated against the ferrocene/ferrocinium redox couple (Fc/Fc+). The polymers were deposited by drop-casting chloroform solutions (5 mg/mL) on a glassy carbon electrode. The measurements were carried out in either an anhydrous 0.1 M acetonitrile solution of tetrabutylammonium hexafluorophosphate ($TBAPF_6$) or a 0.1 M NaCl aqueous solution as the supporting electrolyte at a scan rate of 100 mV/s. The electrolyte solutions were degassed with nitrogen for 30 minutes prior to performing the measurement. Ionisation potentials were obtained using the equation $IP = (E_{ox} – E_{Fc} + 4.8\ V)$ and electron affinities using $EA = (E_{red} – E_{Fc} + 4.8\ V)$, where E_{Fc} was found to be 0.41 V versus Ag/AgCl.

Spectroelectrochemical analysis. The polymers were deposited by spin-coating chloroform solutions (5 mg/mL) at 1500 rpm on ITO-coated glass slides. The spectroelectrochemical measurements were performed in a 0.1 M $NaCl_{(aq)}$ solution using a standard three-electrode setup, with the ITO substrate as the working electrode, a platinum mesh counter electrode (active area 25 × 35 mm) and a Ag/AgCl reference electrode. The ITO substrate was then placed within a cuvette holder, which was inserted into the UV-1800 Shimadzu UV-Vis spectrometer. Each potential was applied for 5 s before recording the optical spectra.

OECT fabrication and characterisation. All devices were fabricated using previously reported photolithographic procedures.[71,261] The OECT devices featured a channel width of 100 µm and a channel length of 10 µm. For the OECT devices in **Chapter 2**, the substrates underwent a pre-deposition surface treatment to promote adhesion of the polymer to the channels and electrodes.[262] For Chapters 3 and 4, the substrates underwent a pre-deposition ozone treatment, then the polymer solutions were deposited by spin-coating at 500-1000 rpm for 45 seconds from chloroform solutions (5 mg/mL) and allowed to dry before peeling off the sacrificial Parylene C layer. The samples were rinsed in deionised water and dried before testing with no further processing. All measurements were performed using an external Ag/AgCl pellet electrode (diameter = 2 mm, height = 2 mm) as the gate in a 0.1 M NaCl aqueous solution in ambient conditions. The I-V characteristics were recorded on a National Instruments PXIe-1082 system using custom-made LabView scripts. The mobility of the OECT channel was determined by applying a sinusoidal voltage pulse at the gate electrode at varying frequencies. A custom MATLAB script was employed to extract the electron transit time as previously described.[159]

OFET fabrication and characterisation. All OFET films were prepared and characterised under a nitrogen atmosphere. Borosilicate substrates were cleaned by sequential ultrasonication in a dilute Extran 300 detergent solution and deionized water for 30 minutes each. Then the

substrates were cleaned with acetone and isopropyl alcohol by ultrasonication for 10 minutes each. As source-drain electrodes, 35 nm of Au with 5 nm of Al as the sticking layer was thermally evaporated at 2×10^{-6} mbar. The substrates with patterned Au/Al source-drain contacts were subjected to a UV-ozone treatment step for 20 min. The channel width and length of the transistors were 1000 μm/40 μm. Before the film deposition, the polymers were dissolved in anhydrous chloroform. The solutions were kept under stirring on a hot plate at room temperature for overnight. As gate dielectric, the mixture of Cytop (CTL-809M) and its solvent (CT-SOLV 180) with a volume ratio of 2:1 was spin-coated at 1200 rpm for 60 s. The Cytop film was then thermally annealed at 50°C for 2 h before the deposition of Al as a gate electrode. The electrical characteristics of the OTFTs were monitored by a probe station placed in an N_2-filled glove box that is connected to an Agilent B1500A semiconductor parameter analyzer. The saturation-regime mobility (μ_{sat}) of the transistor was determined using the equation $\mu_{sat} = {2L}/{W C_i}\left(\frac{d{I_{DS}}^{1/2}}{dV_G}\right)^2$, where I_D is the source–drain current, C_i is the capacitance per unit area, L is the channel length, W is the channel width, and V_G is the gate voltage.

Electrochemical impedance spectroscopy. Electrochemical impedance spectroscopy was performed under ambient conditions in a 0.1 M $NaCl_{(aq)}$ solution with a potentiostat (IviumStat) and a standard three-electrode setup using a polymer-coated gold working electrode (600 μm x 600 μm), a Ag/AgCl reference electrode and a Pt wire counter electrode. The measurements were carried out with a 10 mV sine wave potential above the threshold for the polymer, using frequencies from 0 Hz to 100 kHz. Analysis was performed with custom MATLAB tools.

Galvanostatic charging measurements. Prior to deposition, the rotating ring disk electrode (RRDE) was cleaned and polished with Al_2O_3 (particle size 0.05 μm) to a mirror finish. To create polymer films, 13 μL of polymer solutions (5 mg/mL) were drop cast onto the glassy

carbon disk of an RRDE (E6R1, Pt ring, polyether ether ketone (PEEK) shrouded, Pine Research) and the electrode was rotated at 500 r.p.m. for 2 minutes.

Three-electrode electrochemical measurements were conducted in an alkaline-resistant PTFE cell (AF01CKT1001, Pine Research Instrumentation) using a VSP-300 potentiostat (Biologic), with a leakless Ag/AgCl reference electrode (ET069, eDAQ), a graphite rod counter electrode (AFCTR3B, Pine Research Instrumentation) and the polymer-coated RRDE working electrode. The electrolyte was degassed with Ar for 30 minutes prior to electrochemical characterisation. For each experiment, the uncompensated resistance, *R*, was measured at open circuit voltage (polymer is in the pristine, neutral state) through electrochemical impedance spectroscopy (EIS) at the high frequency intercept and *iR* correction was completed manually during the data analysis phase.

The films were then cycled five times between 0.1 V and –1.0 V vs. Ag/AgCl at 5 mV s^{-1} scan rate. Following the cyclic voltammetry measurements, the films were charged at a constant current that corresponded to charging rates of C and C/2. The charging rates of C and C/2 result in fully charging the electrode within one hour and two hours, respectively. To calculate the currents needed to achieve the different rates, the theoretical capacity of every electrode was calculated according to the following formula, where $Conc_{polymer}$ is the concentration of the polymer solution (g mL^{-1}), *V* is the volume drop cast onto the RRDE (mL), $M_{monomer}$ is the molecular weight of a monomer unit (g mol^{-1}), *A* is Avogadro's number, *n* is the number of electrons a monomer unit can hold and *e* is the charge of an electron (1.6 × 10^{-19} C):

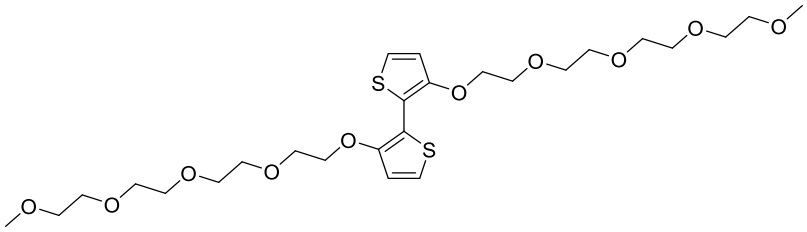
$$Capacity\ [C] = \frac{Conc_{polymer}\, V\, A\, n\, e}{M_{monomer}} \quad \frac{[C\ g\ mol^{-1}]}{[g\ mol^{-1}]}.$$

The currents used for charging at the different rates (I_c and $I_{C/2}$) were calculated by dividing the calculated theoretical capacity by the time over which the full charge is desired (3600 seconds or 7200 seconds, respectively).

5.2 Synthetic procedures for Chapter 2

The synthesis in this chapter is detailed in an accepted manuscript.[211]

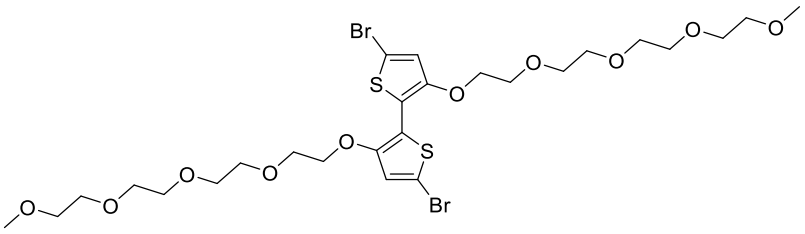
*3,3'-bis((2,5,8,11-tetraoxatridecan-13-yl)oxy)-2,2'-bithiophene (**g$_4$T2**)*



Copper(I) iodide (0.470 g, 2.47 mmol, 0.2 equiv.) and potassium tert-butoxide (4.16 g, 37.1 mmol, 3.0 equiv.) were dissolved in tetraethylene glycol (24 mL, 123 mmol, 10 equiv.) under a nitrogen atmosphere and stirred at room temperature for 30 minutes. To this, 3,3'-dibromo-2,2'-bithiophene (4.00 g, 12.3 mmol, 1.0 equiv.) and the reaction mixture was heated to 100 °C overnight. The reaction mixture was cooled to room temperature and washed through a frit with DCM (200 mL). The filtrate was then washed with a solution of ammonium chloride (2x 150 mL), a solution of 1 M HCl (2x 150 mL), water (2x 150mL) then brine (150 mL). The organic phase was dried over magnesium sulfate and excess solvent was removed *in vacuo*. The crude product was purified by silica column chromatography employing a 1:1 v/v mixture of ethyl acetate:petroleum ether as the eluent (R_f = 0.25). The final product was obtained as a pale yellow oil (4.54 g, 7.84 mmol, 64% yield): ^{1}H NMR (400 MHz, $CDCl_3$) δ 7.21 (dd, *J* = 5.5, 1.8 Hz, 2H), 6.97 (dd, *J* = 5.5, 1.9 Hz, 1H), 6.90 (dd, *J* = 5.7, 2.0 Hz, 1H), 4.32 (t, *J* = 5.6Hz, 2H), 3.84 (dd, *J* = 5.6, 4.3 Hz, 2H), 3.76 – 3.58 (m, 12H), 3.59 – 3.48 (m, 2H), 3.35 (s, 3H); ^{13}C NMR (101 MHz, $CDCl_3$) δ 154.3, 130.6, 130.1, 124.8, 123.8, 116.9, 113.2, 107.6, 72.0, 71.5, 71.0, 70.7, 70.7, 70.6, 70.0, 59.1. HRMS (ESI-ToF): 579.7322 [M+H$^+$] (calc. 579.7320).

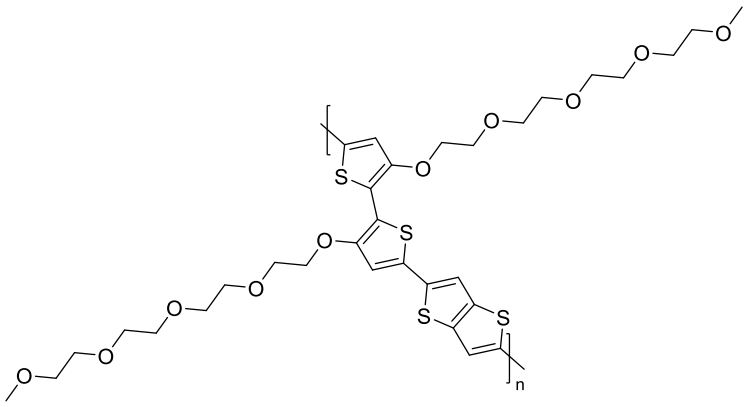
13,13'-((5,5'-dibromo-[2,2'-bithiophene]-3,3'-diyl)bis(oxy))bis(2,5,8,11-tetraoxatridecane)

(g$_4$T2Br$_2$)



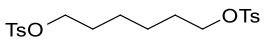
g$_4$T2 (4.49 g, 7.76 mmol, 1.0 equiv.) was dissolved in anhydrous THF (120 mL) under a nitrogen atmosphere. The reaction mixture was cooled to 0 °C and kept in the dark, while N-bromosuccinimide (3.04 g, 17.1 mmol, 2.2 equiv.) was added in four portions over 10 minutes. The solution was stirred at room temperature for 40 minutes, before the addition of DCM (150 mL). The reaction mixture was quenched with an aqueous solution of sodium metabisulfite and sodium hydrogen carbonate (3x 80 mL), then washed with water (3x 100 mL) and dried over sodium sulfate. Excess solvent was removed under reduced pressure. The crude material was purified by silica column chromatography employing a 1:1 v/v mixture of ethyl acetate:petroleum ether as the solvent system (R_f = 0.40). The final product was obtained as a colourless oil (5.16 g, 6.75 mmol, 87% yield): ^{1}H NMR (400 MHz, Acetone-d_6) δ 7.15 (s, 2H), 4.33 – 4.26 (m, 3H), 3.90 – 3.82 (m, 5H), 3.67 (ddd, *J* = 5.9, 3.9, 1.1 Hz, 5H), 3.66 – 3.52 (m, 18H), 3.50 – 3.41 (m, 2H), 3.27 (s, 6H); ^{13}C NMR (101 MHz, Acetone-d_6) δ 206.1, 121.0, 72.7, 72.6, 71.4, 71.4, 71.3, 71.1, 70.6, 58.8. HRMS (ESI-ToF): 736.5249 [M+H$^+$] (calc. 736.5255).

p(g$_4$T2-TT)



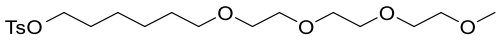
This polymer was synthesised by Dr Adam Marks. **g$_4$T2Br$_2$** (525.74 mg, 0.714 mmol, 1.0 equiv.), 2,5-bis(trimethylstannyl)-thieno[3,2-*b*]thiophene (332.52 mg, 0.714 mmol, 1.0 equiv.) and tetrakis(triphenylphosphine)palladium(0) (16.50 mg, 14.278 µmol, 0.02 equiv.) were dissolved in 1:1 v/v mixture of anhydrous degassed dimethylformamide:chlorobenzene (9.6 mL total volume). The resulting solution was degassed for an additional 10 minutes and the reaction was heated 110 °C overnight. The crude polymer solution was cooled to room temperature and precipitated into methanol, and the polymer was purified utilising Soxhlet extractions with: hexane, ethyl acetate, acetone, methanol, tetrahydrofuran and dichloromethane. The polymer was then dissolved in chloroform and excess solvent was removed *in vacuo*. The final product was collected by reprecipitating the polymer into methanol and collecting it by suction filtration. **p(g$_4$T2-TT)** was obtained as a dark blue solid (393.05 mg, 0.550 mmol, 77% yield): ^{1}H NMR (400 MHz, DMSO-d_6) δ 7.33 (br s), 7.09 (br s), 4.37 (br s), 3.91-3.44 (br m), 3.27 (br s); GPC (DMF, 40 °C): M_n = 83.4 kDa, M_w = 112.7 kDa.

Hexane-1,6-diyl bis(4-methylbenzenesulfonate)



Hexane-1,6-diol (10.0 g, 84.6 mmol, 1.0 equiv.) was dissolved in pyridine (40 mL) under ambient conditions. The reaction mixture was cooled to 0 °C and 4-toluenesulfonyl chloride (35.5 g, 186 mmol, 3.1 equiv.) was added in 4 portions, then stirred at room temperature for 30 minutes. The mixture was stored in the fridge overnight, then poured into 250 mL 2M HCl. The mixture was extracted with DCM (3 x 250 mL) and the organic fraction was washed with water (3 x 200 mL) then brine (1 x 200 mL) and dried over anhydrous Na_2SO_4. The solvent was removed *in vacuo* and the crude product was recrystallised from methanol to obtain the product as a white crystalline solid (31.14 g, 73.01 mmol, 86% yield): ^{1}H NMR (400 MHz, $CDCl_3$) δ 7.77 (d, *J* = 8 Hz, 4H), 7.34 (d, *J* = 8 Hz, 4H), 3.98 (t, *J* = 6.4 Hz, 4H), 2.45 (s, 6H), 1.63 – 1.55 (m, 4H), 1.30 – 1.23 (m, 4H); ^{13}C NMR (101 MHz, $CDCl_3$) δ 144.9, 133.3, 130.0, 128.0, 70.4, 28.8, 24.9, 21.8. HRMS (ESI-ToF): 427.5410 [$M+H^+$] (calc. 427.5418).

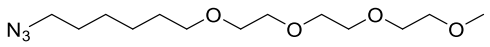
2,5,8,11-tetraoxaheptadecan-17-yl 4-methylbenzenesulfonate



Sodium hydride (60%, 2.38 g, 59.5 mmol, 1.5 equiv.) was dissolved in dry THF (50 mL) and the reaction mixture was cooled to 0 °C. Triethylene glycol monomethyl ether (6.35 mL, 39.7 mmol, 1.0 equiv.) was added dropwise, then the mixture was brought to room temperature and stirred for 30 minutes. The reaction mixture was heated to 65 °C for 1 hour, then cooled back to 0 °C. Separately, hexane-1,6-diyl bis(4-methylbenzenesulfonate) (16.9 g, 39.7 mmol, 1.0 equiv.) was dissolved in dry THF (50 mL) and this mixture was transferred to the first solution via canula. The reaction mixture was then stirred at room temperature for 1 hour, then heated to 55 °C overnight. The reaction was then cool to room temperature and poured over ice water. This mixture was extracted with chloroform (2 x 150 mL), then the organic portion was washed

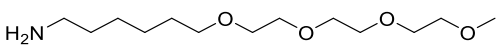
with water (3 x 150 mL) and brine (1 x 150 mL) and dried over Na_2SO_4. The solvent was removed *in vacuo* and the crude product was purified by silica column chromatography employing a 2:1 v/v mixture of ethyl acetate:petroleum ether as the solvent system (R_f = 0.30). The final product was dried by high vacuum and obtained as a colourless oil (5.65 g, 13.5 mmol, 34% yield): ^{1}H NMR (400 MHz, $CDCl_3$) δ 7.76 – 7.69 (m, 2H), 7.33 – 7.26 (m, 2H), 3.96 (t, *J* = 6.5 Hz, 2H), 3.63 – 3.55 (m, 8H), 3.54 – 3.47 (m, 4H), 3.36 (t, *J* = 6 Hz, 2H), 3.32 (s, 3H), 2.40 (s, 3H), 1.64 – 1.41 (m, 4H), 1.34 – 1.16 (m, 4H); ^{13}C NMR (101 MHz, $CDCl_3$) δ 144.6, 133.2, 129.8, 127.8, 71.9, 71.1, 70.6, 70.5, 70.4, 70.1, 59.0, 29.4, 28.7, 25.5, 25.2, 21.6. HRMS (ESI-ToF): 419.5460 (calc. 419.5402).

17-azido-2,5,8,11-tetraoxaheptadecane



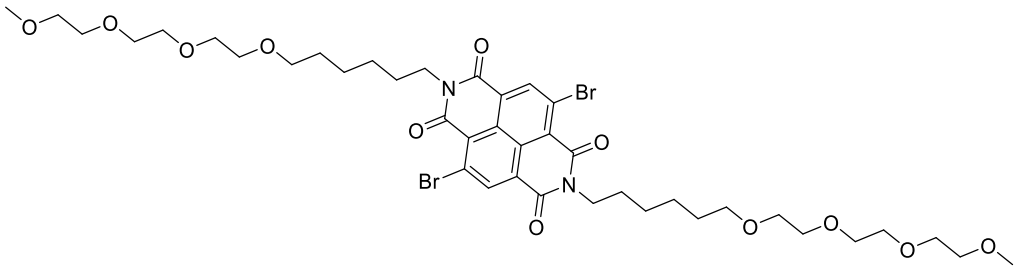
2,5,8,11-tetraoxaheptadecan-17-yl 4-methylbenzenesulfonate (3.75 g, 8.96 mmol, 1.0 equiv.) was dissolved in dry DMF (35 mL) and cool to 0 °C. To this, sodium azide (0.870 g, 13.4 mmol, 1.5 equiv.) was added and the mixture was heated to 100 °C for 2 hours. Subsequently, the reaction mixture was cooled to room temperature and ethyl acetate (200 mL) was added. The precipitate was filtered and the filtrate was washed with water (3 x 200 mL) and brine (1 x 150 mL) and dried over Na_2SO_4, before the solvent was removed *in vacuo*. The crude product was pure and used directly without further purification as a colourless oil (2.23 g, 7.71 mmol, 86% yield): ^{1}H NMR (400 MHz, $CDCl_3$) 3.59 – 3.49 (m, 8H), 3.49 – 3.39 (m, 4H), 3.33 (t, *J* = 6.6 Hz, 2H), 3.25 (s, 3H), 3.14 (t, *J* = 6.9 Hz, 2H), 1.48 (ddt, *J* = 8.2, 5.4, 1.2 Hz, 4H), 1.33 – 1.20 (m, 4H); ^{13}C NMR (101 MHz, $CDCl_3$) δ 71.8, 71.0, 70.4, 70.4, 70.3, 69.9, 58.8, 51.2, 29.3, 28.6, 26.4, 25.5. HRMS (ESI-ToF): 290.3760 [$M+H^+$] (calc. 290.3761).

2,5,8,11-tetraoxaheptadecan-17-amine



17-azido-2,5,8,11-tetraoxaheptadecane (2.20 g, 7.60 mmol, 1.0 equiv.) was dissolved in dry THF (40 mL) and cooled to 0 °C. Triphenylphosphine (2.99g, 11.4 mmol,1.5 equiv.) was added in and the mixture was stirred at room temperature for 2 hours. The reaction mixture was heated to 50 °C for 1 hour, then returned to room temperature, before deionised water (0.2 mL) was added. The reaction was stirred overnight at room temperature, then diluted with water (200 mL). The aqueous portion was washed with diethyl ether (3 x 200 mL), then concentrated *in vacuo* to obtain the pure product as a pale yellow oil (1.82 g, 69.2 mmol, 91% yield): ^{1}H NMR (400 MHz, $CDCl_3$) δ 3.71 – 3.59 (m, 9H), 3.59 – 3.50 (m, 4H), 3.43 (t, *J* = 6.7 Hz, 2H), 3.36 (s, 3H), 2.67 (t, *J* = 7.0 Hz, 2H), 1.56 (m, 2H), 1.47 – 1.39 (m, 2H), 1.38 – 1.28 (m, 4H); ^{13}C NMR (101 MHz, $CDCl_3$) δ 71.9, 71.4, 70.6, 70.6, 70.5, 70.1, 59.0, 42.1, 33.5, 29.5, 26.7, 26.0. HRMS (ESI-ToF): 264.3769 [$M+H^+$] (calc. 264.3780).

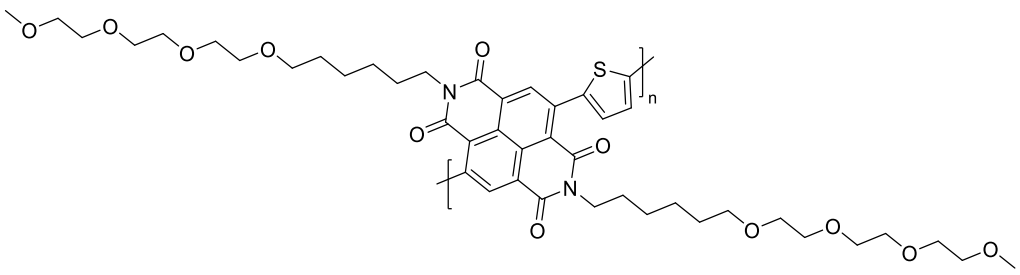
*4,9-dibromo-2,7-di(2,5,8,11-tetraoxaheptadecan-17-yl)benzo[lmn][3,8]phenanthroline-1,3,6,8(2H,7H)-tetraone (**C_6g_3NDI-Br_2**)*



The procedure for preparing the monomer was modified as follows.[139] 2,6-dibromonaphthalene-1,4,5,8-tetracarboxylic dianhydride ($NDABr_2$, 1.60 g, 3.76 mmol 1.0 equiv.) and zinc acetate (1.04 g, 7.51 mmol, 2.0 equiv.) were dissolved in anhydrous *o*-xylene (80 mL). The reaction mixture was heated to 90 °C, then 2,5,8,11-tetraoxaheptadecan-17-amine (2.08 g, 7.89 mmol, 2,1 equiv.) was added dropwise. The solution was heated to 125 °C

for 2 hours, then cooled to room temperature and diluted with chloroform (200 mL). The reaction mixture was washed with water (3x 150 mL), dried over magnesium sulfate and the excess solvent was removed under reduced pressure. The crude product was purified using silica column chromatography with ethyl acetate as the solvent system (R_f = 0.25). The final product was obtained as a pale yellow solid (0.683 g, 0.745 mmol, 20% yield): ^{1}H NMR (400 MHz, $CDCl_3$) δ 8.99 (s, 2H), 4.22 – 4.16 (m, 4H), 3.68 – 3.62 (m, 16H), 3.60 – 3.52 (m, 8H), 3.46 (t, *J* = 6.6 Hz, 4H), 3.37 (s, 6H), 1.75 (m, 4H), 1.61 (t, *J* = 6.8 Hz, 4H), 1.44 (d, *J* = 3.7 Hz, 8H); ^{13}C NMR (101 MHz, $CDCl_3$) δ 160.9, 139.2, 127.9, 125.5, 72.1, 71.4, 70.8, 70.8, 70.7, 70.2, 59.2, 41.7, 29.7, 28.0, 27.1, 26.0. HRMS (ESI-ToF): 917.6977 [M+H$^+$] (calc. 917.6990).

p(C$_6$g$_3$NDI-T)



C$_6$g$_3$NDI-Br$_2$ (306.50 mg, 0.334 mmol, 1.0 equiv.), 2,5-bis(trimethylstannyl)thiophene (137.00 mg, 0.334 mmol, 1.0 equiv.), tris(dibenzylideneacetone)dipalladium(0) (6.12 mg, 6.68 µmol, 0.02 equiv.) and tris(*o*-methoxyphenyl)phosphine (9.45 mg, 26.7 µmol, 0.08 equiv.) were dissolved in anhydrous degassed chlorobenzene (6 mL). The resulting solution was degassed for an additional 10 minutes and the reaction was heated 130 °C overnight. The crude polymer solution was cooled to room temperature and precipitated into a 2:1 v/v mixture of ethyl acetate:hexane, and the polymer was purified via Soxhlet extractions with: hexane, ethyl acetate, acetone, methanol, tetrahydrofuran and dichloromethane. The polymer was then dissolved in chloroform and excess solvent was removed *in vacuo*. The final product was

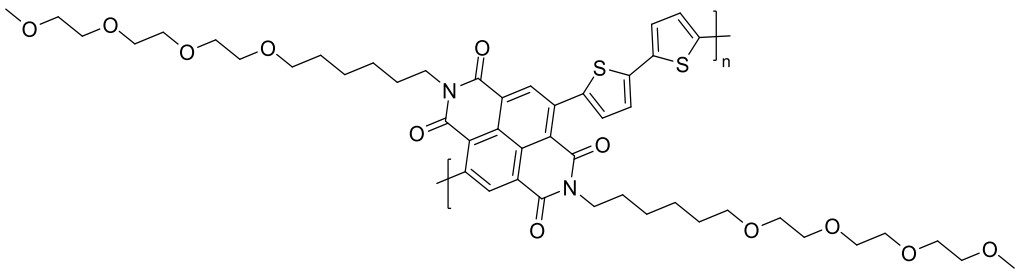
collected by reprecipitating the polymer into a 2:1 v/v mixture of ethyl acetate:hexane and collecting it by suction filtration. **p(C_6g_3NDI-T)** was obtained as a dark blue solid (264.43 mg, 0.304 mmol, 91% yield): ^{1}H NMR (400 MHz, $CDCl_3$) δ 8.97 (s), 7.47 (br s), 4.19 (br s), 3.65 – 3.62 (m), 3.58 – 3.52 (m), 3.45 (t), 3.36 (s), 1.63 – 1.59 (br m), 1.44 (br s); GPC (chloroform, 40 °C): M_n = 42.4 kDa, M_w = 87.4 kDa.

5.3 Synthetic procedures for Chapter 3

All polymers in this chapter utilise the **C_6g_3NDI-Br_2** monomer, which was synthesised as reported in the previous chapter.

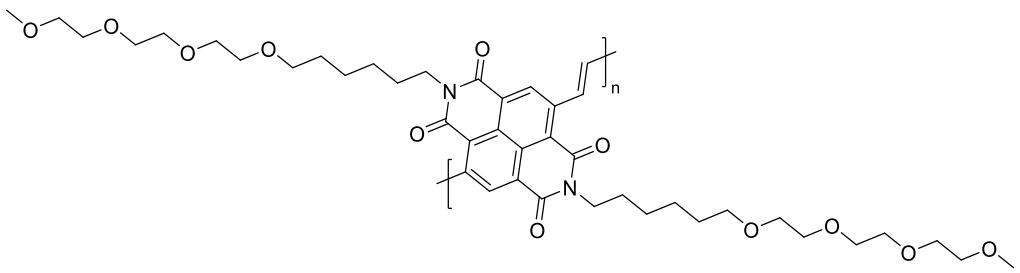
A new batch of **p(C_6g_3NDI-T)** was synthesized (herein called **pNDI-T**) as reported in the previous chapter, and the following GPC data was obtained: GPC (chloroform, 40 °C): M_n = 17.4 kDa, M_w = 31.3 kDa.

pNDI-T2



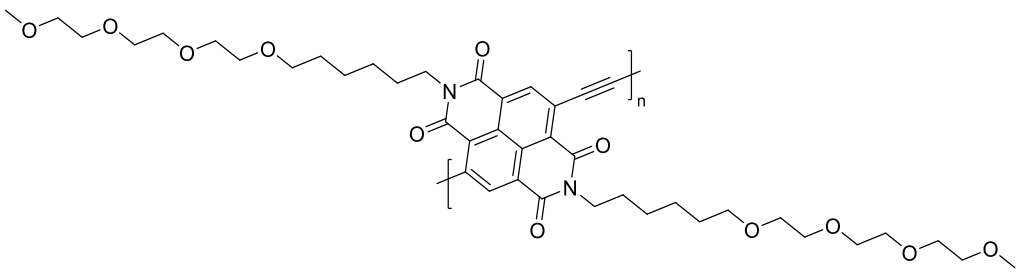
pNDI-T2 was synthesized according to literature,[139] in a yield of 71%. The following GPC data was obtained: GPC (chloroform, 40 °C): M_n = 14.7 kDa, M_w = 23.1 kDa.

pNDI-V



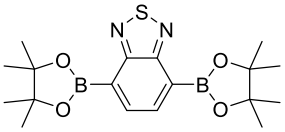
C$_6$g$_3$NDI-Br$_2$ (142.92 mg, 0.156 mmol), trans-1,2-bis(tributylstannyl)ethene (94.50 mg, 0.156 mmol, 1.0 equiv.), tris(dibenzylideneacetone)dipalladium(0) (2.86 mg, 3.12 µmol, 0.02 equiv.) and tris(*o*-methoxyphenyl)phosphine (4.41 mg, 12.5 µmol, 0.08 equiv.) were dissolved in anhydrous degassed chlorobenzene (3 mL). The resulting solution was degassed for an additional 10 minutes and the reaction was heated at 130 °C overnight. The crude polymer solution was cooled to room temperature and precipitated into a 2:1 v/v mixture of ethyl acetate:hexane, and the polymer was purified via Soxhlet extractions with: hexane, ethyl acetate, acetone and methanol. The polymer was then dissolved in chloroform and excess solvent was removed *in vacuo*. The final product was collected by reprecipitating the polymer into a 2:1 v/v mixture of ethyl acetate:hexane and collecting it by suction filtration. **pNDI-V** was obtained as a dark red solid (95.45 mg, 0.122 mmol, 78% yield): ^{1}H NMR (400 MHz, $CDCl_3$) δ 9.24 (s), 9.00 (s), 4.25 (br s), 3.90 – 3.45 (m), 3.43 – 3.27 (m), 2.28 – 1.37 (m); GPC (chloroform, 40 °C): M_n = 18.8 kDa, M_w = 30.9 kDa.

pNDI-A



C$_6$g$_3$NDI-Br$_2$ (131.91 mg, 0.144 mmol), bis(trimethylstannyl)acetylene (50.60 mg, 0.144 mmol, 1.0 equiv.), tris(dibenzylideneacetone)dipalladium(0) (2.64 mg, 2.883 µmol, 0.02 equiv.) and tris(*o*-methoxyphenyl)phosphine (4.07 mg, 11.532 µmol, 0.08 equiv.) were dissolved in anhydrous degassed chlorobenzene (3 mL). The resulting solution was degassed for an additional 10 minutes and the reaction was heated at 130 °C overnight. The crude polymer solution was cooled to room temperature and precipitated into a 1:1 v/v mixture of ethyl acetate:hexane, and the polymer was purified via Soxhlet extractions with: hexane, ethyl acetate, acetone and methanol. The polymer was then dissolved in chloroform and excess solvent was removed *in vacuo*. The final product was collected by reprecipitating the polymer into a 1:1 v/v mixture of ethyl acetate:hexane and collecting it by suction filtration. **pNDI-V** was obtained as a dark red solid (14.21 mg, 18.2 µmol, 13% yield): ^{1}H NMR (400 MHz, $CDCl_3$) δ 9.07 (br s), 7.81 (br s), 4.19 (br s), 3.74 – 3.29 (m), 2.10 – 1.18 (m); GPC (chloroform, 40 °C): M_n = 11.3 kDa, M_w = 20.3 kDa.

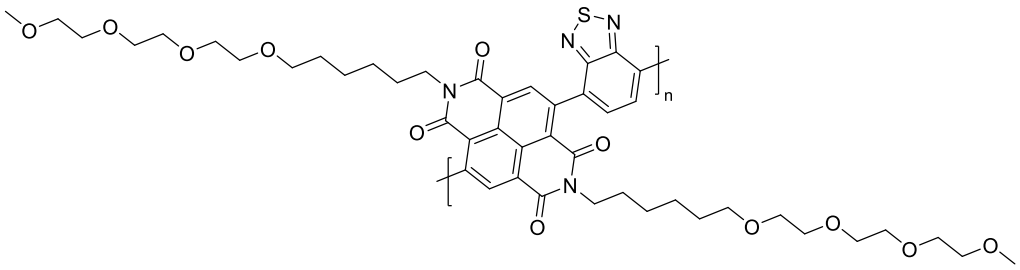
*2,1,3-Benzothiadiazole-4,7-bis(boronic acid pinacol ester) (**BT**)*



This procedure was adapted from literature.[219] 4,7-dibromobenzo[c][1,2,5]thiadiazole (1.00 g, 3.40 mmol, 1.0 equiv.), bis(pinacolato)diboron (2.00 g, 7.80 mmol, 2.3 equiv.), [1,1′-

bis(diphenylphosphino)ferrocene]dichloropalladium(II) (80.0 mg, 0.109 mmol, 0.03 equiv.) and potassium acetate (2.00 g, 20.0 mmol, 5.9 equiv.) were dried under high vacuum. To this mixture, anhydrous 1,4-dioxane (15 mL) was added and the reaction was heated at 85 °C overnight. The reaction mixture was cooled and quenched with water (50 mL). The mixture was extracted into DCM (3 x 60 mL) and the combined organic portions were dried over sodium sulfate and the solution was filtered before the solvent was removed *in vacuo*. The crude mixture was purified by silica column chromatography employing a 1:10 v/v mixture of ethyl acetate:petroleum ether as the solvent system (R_f = 0.12). The major fraction was further purified by recrystallisation from hexane. The final product was obtained as an off white solid (0.788 g, 2.03 mmol, 59% yield): ^{1}H NMR (400 MHz, $CDCl_3$) δ 8.13 (s, 2H), 1.44 (s, 24H); ^{13}C NMR (101 MHz, $CDCl_3$) δ 155.5, 129.0, 127.2, 88.1, 24.7. HRMS (ESI-ToF): 388.1797 [M+H$^+$] (calc. 388.1800).

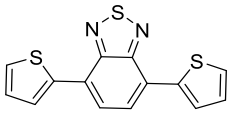
pNDI-BT



This procedure was adapted from literature.[219] **C_6g_3NDI-Br_2** (105.68 mg, 0.115 mmol) and 2,1,3-benzothiadiazole-4,7-bis(boronic acid pinacol ester) (44.74 mg, 0.115 mmol, 1.0 equiv.) were dried under high vacuum, then degassed DMF (3.2 mL) and aqueous K_2CO_3 (2 M, 0.32 mL) were added and degassed for a further 30 mins. Tetrakis(triphenylphosphine)palladium(0) (2.66 mg, 2.30 µmol, 0.02 equiv.) was added and the solution was heated at 140 °C for 72 hours. The crude polymer solution was cooled to room temperature and precipitated into a 2:1 v/v mixture of ethyl acetate:hexane, and the polymer was purified via Soxhlet extractions with:

hexane, ethyl acetate and methanol, then collected in chloroform and excess solvent was removed *in vacuo*. The final product was collected by reprecipitating the polymer into a 2:1 v/v mixture of ethyl acetate:hexane and collecting it by suction filtration. **pNDI-BT** was obtained as an orange solid (70.32 mg, 0.122 mmol, 69% yield): ^{1}H NMR (400 MHz, $CDCl_3$) δ 9.04 (br s), 7.99 (br s), 4.06 (br s), 3.68 – 3.62 (m), 3.58 – 3.52 (m), 3.46 – 3.42 (m), 3.38 – 3.35 (m), 1.37 (br s); GPC (chloroform, 40 °C): M_n = 16.2 kDa, M_w = 30.2 kDa.

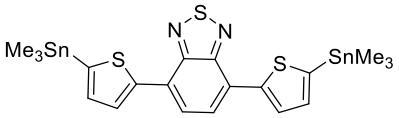
4,7-Di(thiophen-2-yl)benzo[c][1,2,5]thiadiazole



This procedure was adapted from literature.[218] To a mixture of 4,7-dibromobenzo[c][1,2,5]thiadiazole (1.37 g, 4.67 mmol, 1.0 equiv.), tris(dibenzylideneacetone)dipalladium(0) (85.5 mg, 93.4 µmol, 0.02 equiv.) and tris(o-tolyl)phosphine (114 mg, 378 µmol, 0.08 equiv.) under a nitrogen atmosphere, degassed toluene (50 mL) was added. To this, tributyl(thiophen-2-yl)stannane (4.53 g, 12.1 mmol, 2.6 equiv.) was added slowly and the reaction mixture was stirred at 110 °C overnight. Subsequently, the reaction mixture was cooled to room temperature, poured over a saturated aqueous solution of NH_4Cl and extracted with ethyl acetate (3 x 100 mL). The organic portions were washed with water (3 x 150 mL) and dried over Na_2SO_4. The filtrate was then passed through a silica plug and the solvent was removed *in vacuo*. The crude product was purified using silica column chromatography employing a 1:3 v/v mixture of ethyl acetate:petroleum ether as the solvent system (R_f = 0.20). The major fraction was further purified by recrystallisation from methanol. The final product was obtained as red needles (1.01 g, 3.36 mmol, 72% yield): ^{1}H NMR (400 MHz, $CDCl_3$) δ 8.06 (d, J = 3.8, 2H), 7.76 (d, J = 2.3 Hz, 2H), 7.43 (dd, J = 5.2, 1.1 Hz, 2H), 7.19 (dd, J = 5.1, 3.7 Hz, 2H); ^{13}C NMR (101 MHz, $CDCl_3$)

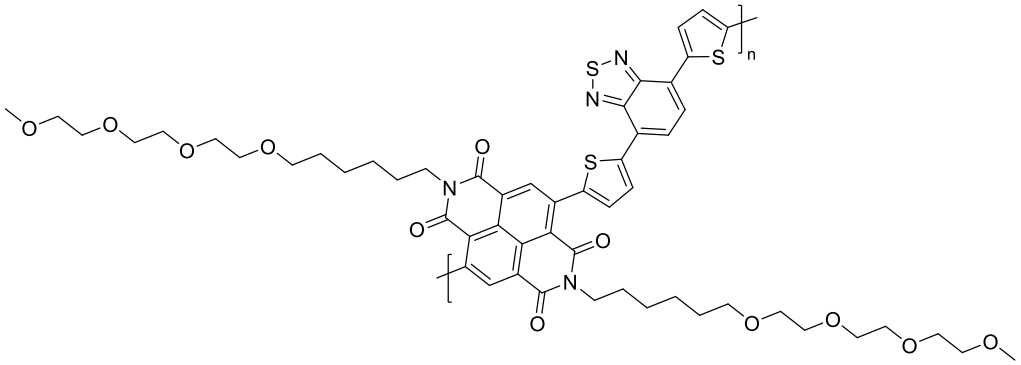
δ 152.5, 139.4, 128.0, 127.5, 126.8, 125.9, 125.7. HRMS (ESI-ToF): 301.4122 [M+H$^+$] (calc. 301.4120).

*4,7-bis(5-(trimethylstannyl)thiophen-2-yl)benzo[c][1,2,5]thiadiazole (**TBTT**)*



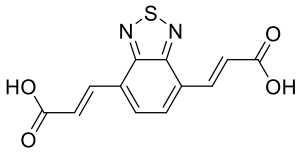
This procedure was adapted from literature.[218] 4,7-Di(thiophen-2-yl)benzo[c][1,2,5]thiadiazole (0.30 g, 1.00 mmol, 1.0 equiv.) was dissolved in dry THF (12 mL) and cooled to -78 °C. Lithium diisopropylamide solution (0.1 M in THF/hexanes, 3.0 mL, 3.00 mmol, 3.0 equiv.) was added dropwise and the solution turned from dark red, through green, blue and finally dark purple. The reaction mixture was stirred at -78 °C for 2 hours, then trimethyltin chloride solution (0.1 M in hexanes, 3.0 mL, 3.00 mmol, 3.0 equiv.) was added dropwise. The reaction mixture was stirred at room temperature overnight, then diluted with DCM. This was washed with water (3 x 150 mL) then brine (1 x 150 mL) and dried over Na_2SO_4, before the solvent was removed *in vacuo*. The crude mixture was dissolved in the minimum amount of DCM, then methanol was added and the product was left to precipitate. The precipitate was further purified by preparative gel permeation chromatography in THF to give the final product as a yellow solid (0.146 g, 0.232 mmol, 23% yield): ^{1}H NMR (400 MHz, $CDCl_3$) δ 8.19 (d, *J* = 3.5 Hz, 2H), 7.88 (s, 2H), 7.30 (d, *J* = 3.5 Hz, 2H), 0.44 (s, 18H); ^{13}C NMR (101 MHz, $CDCl_3$) δ 136.1, 128.4, 125.8, -8.2. HRMS (ESI-ToF): 627.0260 [M+H$^+$] (calc. 627.0255).

pNDI-TBTT



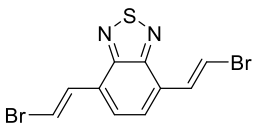
C$_6$g$_3$NDI-Br$_2$ (100.00 mg, 0.109 mmol, 1.0 equiv.), 4,7-bis(5-(trimethylstannyl)thiophen-2-yl)benzo[c][1,2,5]thiadiazole (68.29 mg, 0.109 mmol, 1.0 equiv.), tris(dibenzylideneacetone)dipalladium(0) (2.00 mg, 2.184 µmol, 0.02 equiv.) and tris(*o*-methoxyphenyl)phosphine (3.08 mg, 8.715 µmol, 0.02 equiv.) were dissolved in anhydrous degassed DMF (4 mL). The resulting solution was degassed for an additional 10 minutes and the reaction was heated 100 °C for 10 minutes. The crude polymer solution was cooled to room temperature and precipitated into a 2:1 v/v mixture of ethyl acetate:hexane, and the polymer was purified via Soxhlet extractions with: hexane, ethyl acetate, acetone and methanol. The polymer was then dissolved in chloroform and excess solvent was removed *in vacuo*. The final product was collected by reprecipitating the polymer into a 2:1 v/v mixture of ethyl acetate:hexane and collecting it by suction filtration. **pNDI-TBTT** was obtained as a dark blue solid (91.31 mg, 0.865 mmol, 79% yield): ^{1}H NMR (400 MHz, $CDCl_3$) δ 8.88 (br s), 8.23 – 8.18 (m), 8.02 – 7.93 (m), 7.49 – 7.47 (m), 4.16 (br s), 3.78 (br s), 3.65 – 3.61 (m), 3.56 – 3.51 (m), 3.44 – 3.35 (m), 1.73 (br s), 1.41 (br s); GPC (chloroform, 40 °C): M_n = 6.9 kDa, M_w = 7.9 kDa.

(2E,2'E)-3,3'-(benzo[c][1,2,5]thiadiazole-4,7-diyl)diacrylic acid



This procedure was adapted from literature.[220] 4,7-Dibromobenzo[c][1,2,5]thiadiazole (0.790 g, 2.69 mmol, 1.0 equiv.), $Pd(OAc)_2$ (12.1 mg, 5.40 µmol, 0.02 equiv.) and tri(o-tolylphosphine) (32.7 mg, 10.8 µmol, 0.04 equiv.) were dissolved in dry acetonitrile (24 ml), dry THF (12 ml) and triethylamine (3.7 ml). The reaction mixture was heated to 60 °C and acrylic acid (0.580 g, 8.06 mmol, 3.0 equiv.) was added dropwise. The mixture was heated to reflux overnight, then cooled and the solvent removed *in vacuo*. The residue was dissolved in a solution of water (400 mL) and triethylamine (3.4 mL) and stirred for 1 hour, before filtering. The filtrate was acidified with HCl (1 M) until the pH reached 3. The precipitate was collected by filtration and recrystallised from THF/hexane, dissolving in hot THF and adding this solution dropwise to hexane. The precipitate was collected for a final time by filtration to yield a yellow-orange powder (0.284 g, 1.05 mmol, 39% yield): ^{1}H NMR (400 MHz, DMSO-d_6) δ 12.66 (br s, 2H) 8.13 (s, 2H), 8.02 (d, J = 16.0 Hz, 2H), 7.40 (d, J = 16.0 Hz, 2H); unable to obtain ^{13}C NMR in chloroform-*d* or dimethyl sulfoxide-d_6. HRMS (ESI-ToF): 276.0215 [$M+H^+$] (calc. 276.0205).

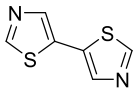
*4,7-bis((E)-2-bromovinyl)benzo[c][1,2,5]thiadiazole (**VBTV**)*



This procedure was adapted from literature.[220] (2E,2'E)-3,3'-(benzo[c][1,2,5]thiadiazole-4,7-diyl)diacrylic acid (0.280 g, 1.01 mmol, 1.0 equiv.) was suspended in acetonitrile (10 mL). To this, a solution of lithium acetate dihydrate (83.0 mg, 0.810 mmol, 0.8 equiv.) in water (3 mL)

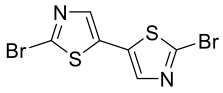
was added. The reaction mixture was cooled to 0 °C and N-bromosuccinimide (0.380 g, 2.13 mmol, 2.1 equiv.) was added in three portions. The reaction mixture was brough to room temperature and stirred for 2 hours. Subsequently, water (40 mL) was added and the mixture was filtered to collect the orange solid. The crude mixture was purified by silica column chromatography employing hexane as the solvent system (R_f = 0.35). The major fraction was recrystallised from hexane to isolate a yellow solid (0.238 g, 0.687 mmol, 68% yield): ^{1}H NMR (400 MHz, Chloroform-*d*) δ 8.03 (d, *J* = 13.8 Hz, 2H), 7.42 (d, *J* = 13.8 Hz, 2H), 7.39 (s, 2H); ^{1}H NMR (101 MHz, Chloroform-*d*) δ 152.7, 133.2, 128.2, 128.1, 114.1. HRMS (ESI-ToF): 345.8606 [M+H$^+$] (calc. 345.8599).

5,5'-bithiazole



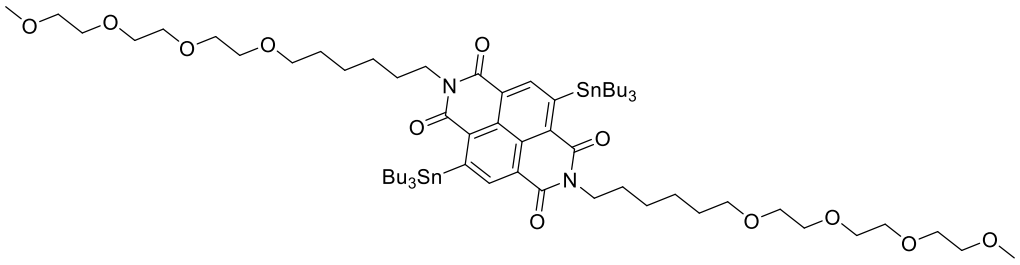
This procedure was adapted from literature.[223] 5-bromothiazole (2.00 g, 12.2 mmol, 1.0 equiv.), tetrabutylammonium bromide (1.98 g, 6.15 mmol, 0.5 equiv.), and $Pd(OAc)_2$ (0.139 g, 0.620 mmol, 0.05 equiv.) were dissolved into toluene (30 mL). To this, *N*,*N*-diisopropylethylamine (1.59 g, 2.14 mL, 12.3 mmol, 1.05 equiv.) was added and the mixture was heated at reflux overnight. The reaction mixture was cooled to room temperature and water (50 mL) was added. The mixture was extracted with DCM (3 x 75 mL), and the combined organic phase was dried with brine, then sodium sulfate and concentrated *in vacuo*. The crude residue was purified by silica column chromatography employing a 1:1 v/v mixture of ethyl acetate:petroleum ether as the solvent system (R_f = 0.25). The pure product was obtained as a white solid (0.841 g, 5.00 mmol, 41% yield): ^{1}H NMR (400 MHz, Chloroform-*d*) δ 8.80 (d, *J* = 0.7 Hz, 2H), 8.01 (d, *J* = 0.7 Hz, 2H); ^{13}C NMR (101 MHz, Chloroform-*d*) δ 152.7, 141.3, 128.1. HRMS (ESI-ToF): 167.9828 [M+H$^+$] (calc. 167.9818).

*2,2'-dibromo-5,5'-bithiazole (**Tz2**)*



This procedure was adapted from literature.[223] 5,5'-bithiazole (0.100 g, 0.590 mmol, 1.0 equiv.) was dissolved in dry chloroform (10 mL). The reaction was cooled to 0 °C and kept in the dark and N-bromosuccinimide (0.423 g, 2.38 mmol, 4.0 equiv.) and a spatula of silica gel (~0.05 g) were added. The reaction mixture was stirred at 70 °C in the dark for 72 hours. The mixture was quenched with a solution of sodium metabisulfite in saturated sodium hydrogen carbonate (3 x 50 mL) and extracted with chloroform (2 x 75 mL). The combined organic phase was with brine then sodium sulfate and concentrated *in vacuo*. The crude product was purified by silica column chromatography employing a 1:1 v/v mixture of ethyl acetate:petroleum ether as the solvent system (R_f = 0.10). The pure product was isolated as a white solid (61.4 mg, 0.188, 32% yield): ^{1}H NMR (400 MHz, Chloroform-*d*) δ 7.61 (s, 2H); ^{13}C NMR (101 MHz, Chloroform-*d*) δ 140.4, 136.2, 130.6. HRMS (ESI-ToF): 326.0408 [M+H^{+}] (calc. 326.0305).

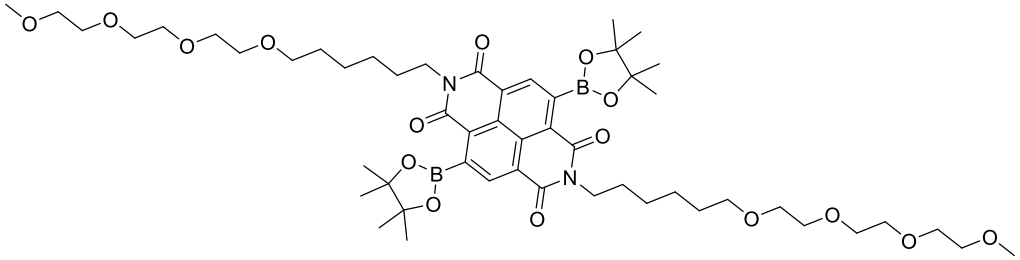
2,7-di(2,5,8,11-tetraoxaheptadecan-17-yl)-4,9-bis(tributylstannyl)benzo[lmn][3,8]phenanthroline-1,3,6,8(2H,7H)-tetraone



This procedure was adapted from literature.[229] **C$_6$g$_3$NDI-Br$_2$** (0.516 g, 0.563 mmol, 1.0 equiv.), 1,1,1,2,2,2-hexabutyldistannane (0.669 g, 0.58 mL, 1.15 mmol, 2.05 equiv.) and tri(o-tolyl)phosphine (34.3 mg, 0.113 mmol, 0.2 equiv.) were dissolved in dry toluene (10 mL). The solution was degassed with nitrogen for 20 minutes. Tris(dibenzylideneacetone)dipalladium

(25.77 mg, 28.0 µmol, 0.05 equiv.) was added and the reaction was heated to 90 ºC for 24 hours. Additional portions of tri(o-tolyl)phosphine (34.3 mg, 0.113 mmol, 0.2 equiv.) and tris(dibenzylideneacetone)dipalladium (25.77 mg, 28.0 µmol, 0.05 equiv.) were added and the reaction was stirred at 90 ºC for an additional 24 hours. Portions of tri(o-tolyl)phosphine (34.3 mg, 0.113 mmol, 0.2 equiv.) and tris(dibenzylideneacetone)dipalladium (25.77 mg, 28.0 µmol, 0.05 equiv.) were added a final time and the reaction was heated at 90 ºC for one further day. After cooling, the solvent was removed under vacuum then the residue was purified by silica column chromatography employing a 4:1 v/v mixture of ethyl acetate:petroleum ether as the solvent system (R_f = 0.20). The final product was obtained as pale yellow solid (0.442 g, 0.331 mmol, 56% yield): ^{1}H NMR (400 MHz, Chloroform-*d*) δ 8.99 (s, 2H), 4.21 (q, *J* = 7.6, 7.1 Hz, 4H), 3.70 – 3.61 (m, 16H), 3.61 – 3.52 (m, 8H), 3.46 (t, *J* = 6.7 Hz, 4H), 3.37 (s, 6H), 1.73 (t, *J* = 7.3 Hz, 4H), 1.68 – 1.48 (m, 28H), 1.48 – 1.39 (m, 8H), 1.39 – 1.26 (m, 12H), 0.91 – 0.81 (m, 18H); ^{13}C NMR (101 MHz, Chloroform-*d*) δ 165.2, 163.1, 154.6.3, 138.1, 132.2, 127.1, 123.4, 72.1, 71.5, 70.8, 70.8, 70.7, 70.2, 59.2, 29.7, 29.4, 28.3, 27.6, 27.1, 26.1, 13.9, 11.7. HRMS (ESI-ToF): 1336.6213 [M+H$^+$] (calc. 1336.6089).

2,7-di(2,5,8,11-tetraoxaheptadecan-17-yl)-4,9-bis(4,4,5,5-tetramethyl-1,3,2-dioxaborolan-2-yl)benzo[lmn][3,8]phenanthroline-1,3,6,8(2H,7H)-tetraone

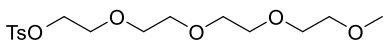


This procedure was adapted from literature.[219,233] **C$_6$g$_3$NDI-Br$_2$** (0.200 g, 0.218 mmol, 1.0 equiv.), bis(pinacolato)diboron (0.127 g, 0.502 mmol, 2.3 equiv.), [1,1′-bis(diphenylphosphino)ferrocene]dichloropalladium(II) (3.20 mg, 44.0 µmol, 0.03 equiv.) and

potassium acetate (0.126 g, 1.29 mmol, 5.9 equiv.) were dried under high vacuum. To this mixture, anhydrous 1,4-dioxane (3 mL) was added and the reaction was heated at 85 °C overnight. The reaction mixture was cooled to room temperature and quenched with water (25 mL). The mixture was extracted with DCM (3 x 25 mL). The combined organic portions were dried over sodium sulfate and the solution was filtered before the solvent was removed under reduced pressure. The crude mixture was purified by silica column chromatography employing ethyl acetate as the solvent system (R_f = 0.20). The final product was obtained as pale yellow solid (0.116 g, 0.115 mmol, 52% yield): ^{1}H NMR (400 MHz, Chloroform-*d*) δ 8.87 (s, 2H), 4.22 – 4.16 (m, 4H), 3.68 – 3.62 (m, 16H), 3.60 – 3.52 (m, 8H), 3.46 (t, *J* = 6.6 Hz, 4H), 3.37 (s, 6H), 1.75 (m, 4H), 1.61 (t, *J* = 6.8 Hz, 4H), 1.50 (s, 24H), 1.44 (d, *J* = 3.7 Hz, 8H); ^{13}C NMR (101 MHz, $CDCl_3$) δ 160.9, 139.2, 127.9, 125.5, 72.1, 71.4, 70.8, 70.8, 70.7, 70.2, 59.2, 41.7, 29.7, 28.0, 27.1, 26.0, 24.7. HRMS (ESI-ToF): 1010.5780 [M+H$^+$] (calc. 1010.5694).

5.4 Synthetic procedures for Chapter 4

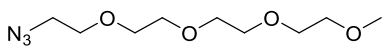
*2,5,8,11-tetraoxatridecan-13-yl 4-methylbenzenesulfonate (**g$_4$OTs**)*



Tetraethylene glycol monomethyl ether (5.98 g, 28.7 mmol, 1.0 equiv.) was dissolved in THF (20 mL) and cooled to 0 °C. To this, a solution of NaOH (1.72 g, 43.0 mmol, 1.5 equiv.) in water (20 mL) was added and the reaction mixture was stirred for 15 minutes. To this solution, 4-toluenesulfonyl chloride (5.75 g, 30.2 mmol, 1.05 equiv.) in THF (20 mL) was added and the reaction was stirred for 4 hours. Following this, DCM (200 mL) was added to the reaction mixture, which was then washed with water (3 x 150 mL) and brine (1 x 150 mL), then dried over $MgSO_4$. The solvent was removed *in vacuo* and the crude product was purified by silica column chromatography employing a 1:1 v/v ethyl acetate:hexane eluent as the solvent system (R_f = 0.30). This yielded the pure product as a colourless oil (4.87 g, 13.4 mmol, 47% yield):

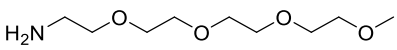
7.80 (d, *J* = 8 Hz, 2H), 7.34 (d, *J* = 8 Hz, 2H), 4.16 (t, *J* = 8 Hz, 2H), 3.69 (t, *J* = 8 Hz, 2H), 3.63 – 3.58 (m, 10H), 3.54 – 3.51 (m, 2H), 3.37 (s, 3H), 2.45 (s, 3H); ^{13}C NMR (101 MHz, $CDCl_3$) δ 144.7, 132.9, 129.8, 127.8, 72.5, 71.9, 70.8 70.6, 70.5, 70.4, 69.2, 68.7, 58.9, 21.5. HRMS (ESI-ToF): 362.1394 [M+H$^+$] (calc. 362.1390).

*13-azido-2,5,8,11-tetraoxatridecane (**g$_4$N$_3$**)*



2,5,8,11-tetraoxatridecan-13-yl 4-methylbenzenesulfonate (4.80 g, 13.2 mmol) was dissolved in dry DMF (70 mL) and cooled to 0 °C. Sodium azide (1.20 g, 18.5 mmol, 1.5 equiv.) was added, then the reaction mixture was heated to 100 °C for 1.5 hours. Then, the reaction mixture was cooled to room temperature and ethyl acetate (200 mL) was added. The precipitate was filtered and the filtrate was washed with water (3 x 200 mL) and brine (1 x 150 mL) and dried over Na_2SO_4, before the solvent was removed *in vacuo*. The crude product was pure and used directly without further purification as a colourless oil (1.77 g, 7.59 mmol, 57% yield): ^{1}H NMR (400 MHz, $CDCl_3$) δ 3.70 – 3.60 (m, 12H), 3.54 (t, *J* = 4.8 Hz, 2H), 3.41 – 3.36 (m, 5H); ^{13}C NMR (101 MHz, $CDCl_3$) δ 72.0, 70.8, 70.7, 70.7, 70.6, 70.5, 70.0, 59.0, 50.7. HRMS (ESI-ToF): 233.1369 [M+H$^+$] (calc. 233.1375).

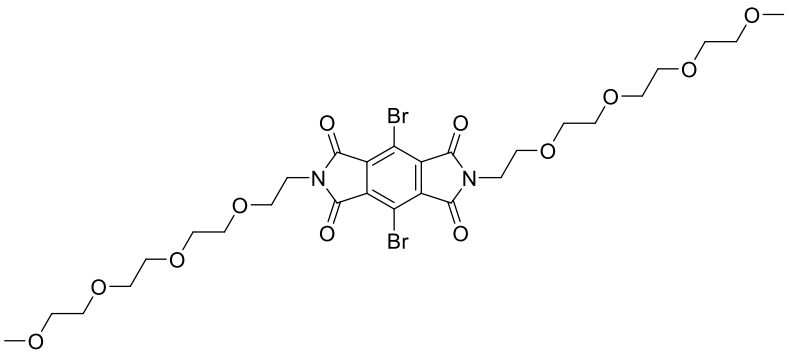
*2,5,8,11-tetraoxatridecan-13-amine (**g$_4$NH$_2$**)*



13-azido-2,5,8,11-tetraoxatridecane (1.61 g, 6.90 mmol) was dissolved in dry THF (20 mL) and cooled to 0 °C. Triphenylphosphine (2.72g, 10.4 mmol,1.5 equiv.) was added in and the mixture was stirred at room temperature for 2 hours. The reaction mixture was heated to 50 °C for 1 hour, then returned to room temperature, before deionised water (0.2 mL) was added. The reaction was stirred overnight at room temperature, then diluted with water (200 mL). The

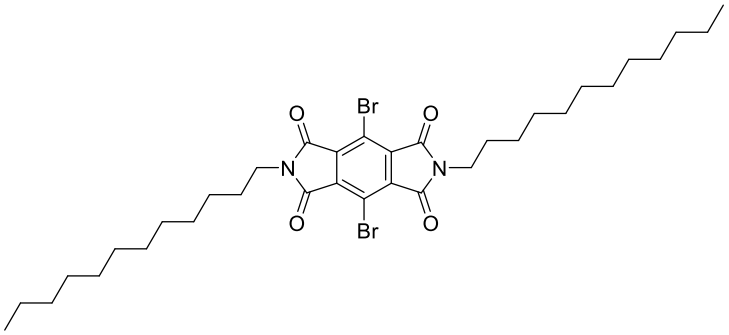
aqueous portion was washed with diethyl ether (3 x 200 mL), then concentrated *in vacuo* to obtain the pure product as a pale yellow oil (1.33 g, 6.42 mmol, 93% yield): ^{1}H NMR (400 MHz, $CDCl_3$) δ 3.71 – 3.58 (m, 11H), 3.58 – 3.48 (m, 4H), 3.38 (s, 3H), 2.91 – 2.84 (m, 2H); ^{13}C NMR (101 MHz, $CDCl_3$) δ 73.3, 72.1, 70.7, 70.6, 70.5, 59.2, 41.9. HRMS (ESI-ToF): 207.1460 [M+H$^+$] (calc. 207.1481).

*4,8-dibromo-2,6-di(2,5,8,11-tetraoxatridecan-13-yl)pyrrolo[3,4-f]isoindole-1,3,5,7(2H,6H)-tetraone (**gPMDI**)*



4,8-dibromo-1H,3H-benzo[1,2-c:4,5-c']difuran-1,3,5,7-tetraone (0.300 g, 0.800 mmol, 1.0 equiv.) was dissolved in glacial acetic acid (8 mL) and heated to 80 °C. 2,5,8,11-tetraoxatridecan-13-amine (0.410 g, 1.99 mmol, 2.5 equiv.) was added dropwise, then the reaction mixture was heated to 120 °C overnight. Subsequently, the reaction mixture was cooled to room temperature and the solvent was removed under reduced pressure. The crude mixture was purified by silica column chromatography employing a 98:2 v/v ethyl acetate:methanol eluent as the solvent system (R_f = 0.18), to yield the product as a white solid (0.430 g, 0.570 mmol, 72% yield): ^{1}H NMR (400 MHz, $CDCl_3$) δ 3.94 (t, *J* = 5.6 Hz, 4H), 3.77 (t, *J* = 5.6 Hz, 4H), 3.68 – 3.58 (m, 22H), 3.55 – 3.49 (m, 4H), 3.36 (s, 6H); ^{13}C NMR (101 MHz, $CDCl_3$) δ 163.4, 136.4, 114.3, 72.1, 70.8, 70.7, 70.6, 70.2, 67.5, 59.2, 38.4. HRMS (ESI-ToF): 754.0780 [M+H$^+$] (calc. 754.0771).

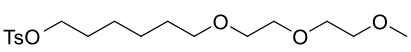
*4,8-dibromo-2,6-didodecylpyrrolo[3,4-f]isoindole-1,3,5,7(2H,6H)-tetraone (**aPMDI**)*



4,8-dibromo-1H,3H-benzo[1,2-c:4,5-c']difuran-1,3,5,7-tetraone (80.0 mg, 0.213 mmol, 1.0 equiv.) was dissolved in glacial acetic acid (2 mL) and heated to 80 °C. Dodecanamine (98.6 mg, 0.532 mmol, 2.5 equiv.) was added dropwise, then the reaction mixture was heated to 120 °C overnight. Subsequently, the reaction mixture was cooled to room temperature and the solvent was removed under reduced pressure. The crude mixture was purified by a silica plug employing chloroform as the eluent, to yield the product as a white solid (0.103 mg, 0.145 mmol, 68% yield): ^{1}H NMR (400 MHz, $CDCl_3$) δ 3.77 – 3.68 (m, 4H), 1.68 (d, *J* = 7.5 Hz, 4H), 1.38 – 1.18 (m, 36H), 0.92 – 0.82 (m, 6H); ^{13}C NMR (126 MHz, $CDCl_3$) δ 163.6, 136.3, 114.2, 39.3, 32.1, 29.8, 29.7, 29.6, 29.5, 29.2, 28.4, 27.0, 22.8, 14.3. HRMS (ESI-ToF): 710.2118 [$M+H^+$] (calc. 710.2117).

Hexane-1,6-diyl bis(4-methylbenzenesulfonate) was synthesised as reported in **Chapter 2**.

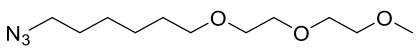
6-(2-(2-methoxyethoxy)ethoxy)hexyl 4-methylbenzenesulfonate



Sodium hydride (60%, 1.62 g, 40.6 mmol, 1.5 equiv.) was dissolved in dry THF (250 mL) and the reaction mixture was cooled to 0 °C. Diethylene glycol monomethyl ether (5.00 mL, 36.9 mmol, 1.0 equiv.) was added dropwise, then the mixture was brought to room temperature and stirred for 30 minutes. The reaction mixture was heated to 65 °C for 1 hour, then cooled back

to 0 °C. *6-(2-*(2-methoxyethoxy)ethoxy)hexyl 4-methylbenzenesulfonate (47.2 g, 111 mmol, 3.0 equiv.) added in one portion to the reaction mixture, which was stirred at room temperature for 1 hour, then heated to 55 °C overnight. The reaction was then cool to room temperature and poured over ice water. This mixture was extracted with DCM (2 x 200 mL), then the organic portion was washed with water (3 x 150 mL) and brine (1 x 150 mL) and dried over Na_2SO_4. The solvent was removed *in vacuo* and the crude product was purified by silica column chromatography employing a 1:1 v/v mixture of ethyl acetate:petroleum ether as the solvent system (R_f = 0.30). The final product was dried by high vacuum and obtained as a colourless oil (8.66 g, 23.1 mmol, 62% yield): ^{1}H NMR (400 MHz, $CDCl_3$) δ 7.78 (d, *J* = 8.3, 2H), 7.34 (d, *J* = 8.0 Hz, 2H), 4.00 (dt, *J* = 13.1, 6.4 Hz, 2H), 3.69 – 3.52 (m, 8H), 3.46 – 3.35 (m, 5H), 2.45 (s, 3H), 1.70 – 1.47 (m, 4H), 1.34-1.24 (m, 4H); ^{13}C NMR (101 MHz, $CDCl_3$) δ 144.9, 133.3, 130.0, 128.0, 72.1, 71.3, 70.8, 70.7, 70.4, 70.2, 59.2, 29.5, 28.8, 25.6, 25.4, 24.9, 21.8. HRMS (ESI-ToF): 374.1770 [$M+H^+$] (calc. 374.1760).

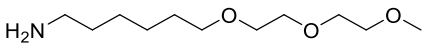
1-azido-6-(2-(2-methoxyethoxy)ethoxy)hexane



6-(2-(2-methoxyethoxy)ethoxy)hexyl 4-methylbenzenesulfonate (7.00 g, 18.7 mmol, 1.0 equiv.) was dissolved in dry DMF (70 mL) and cool to 0 °C. To this, sodium azide (1.82 g, 28.0 mmol, 1.5 equiv.) was added and the mixture was heated to 100 °C overnight. The reaction was cooled to room temperature and ethyl acetate (150 mL) was added. The precipitate was removed by filtration and the filtrate was washed with water (3 x 150 mL) and brine (1 x 150 mL) and dried over Na_2SO_4, before the solvent was removed *in vacuo*. The crude product was pure and used directly without further purification as a colourless oil (3.49 g, 14.2 mmol, 76% yield): ^{1}H NMR (400 MHz, $CDCl_3$) δ 3.65 – 3.60 (m, 2H), 3.60 – 3.51 (m, 4H), 3.44 (t, *J* = 6.6 Hz, 2H), 3.36 (s, 3H), 3.25 (dt, *J* = 7.9, 6.9 Hz, 2H), 1.64 – 1.53 (m, 6H), 1.42 – 1.32 (m, 4H);

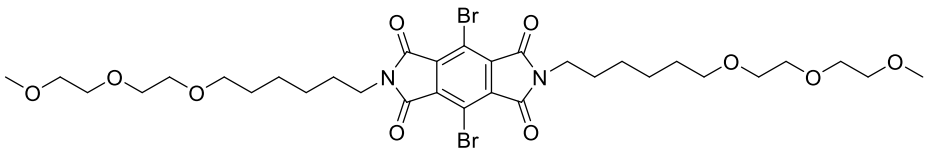
^{13}C NMR (101 MHz, $CDCl_3$) δ 72.1, 71.3, 70.8, 70.6, 70.2, 59.1, 51.4, 29.6, 28.8, 26.6, 25.8. HRMS (ESI-ToF): 245.1737 [M+H$^+$] (calc. 245.1738).

6-(2-(2-methoxyethoxy)ethoxy)hexan-1-amine



1-azido-6-(2-(2-methoxyethoxy)ethoxy)hexane (3.50 g, 14.3 mmol, 1.0 equiv.) was dissolved in dry THF (40 mL) and cooled to 0 °C. Triphenylphosphine (5.61 g, 21.4 mmol,1.5 equiv.) was added in and the mixture was stirred at room temperature for 2 hours. Deionised water (0.4 mL) was added and the reaction was stirred overnight at room temperature, then diluted with water (200 mL). The aqueous portion was washed with diethyl ether (3 x 200 mL) and concentrated *in vacuo*. The crude product was purified by an acid-base work up, by dissolving in DCM (100 mL), then extracting into aqueous HCl (2 M, 100 mL). The aqueous phase was basified and extracted with DCM (3 x 100 mL). The organic phase was dried over Na_2SO_4 and concentrated under reduced pressure to obtain the pure product as a colourless oil (1.70 g, 7.75 mmol, 54% yield): ^{1}H NMR (400 MHz, $CDCl_3$) δ 3.68 – 3.52 (m, 8H), 3.45 (t, *J* = 6.7 Hz, 2H), 3.37 (s, 3H), 2.67 (td, *J* = 7.0, 2.8 Hz, 2H), 1.63 – 1.52 (m, 2H), 1.50 – 1.39 (m, 2H), 1.33 (m, 6H); ^{13}C NMR (101 MHz, $CDCl_3$) δ 72.1, 71.6, 70.8, 70.7, 70.2, 59.2, 42.3, 34.0, 29.7, 26.9, 26.1. HRMS (ESI-ToF): 219.1828 [M+H$^+$] (calc. 219.1834).

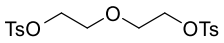
*4,8-dibromo-2,6-bis(6-(2-(2-methoxyethoxy)ethoxy)hexyl)pyrrolo[3,4-f]isoindole-1,3,5,7(2H,6H)-tetraone (**agPMDI**)*



4,8-dibromo-1H,3H-benzo[1,2-c:4,5-c']difuran-1,3,5,7-tetraone (0.120 g, 0.319 mmol, 1.0 equiv.) was dissolved in glacial acetic acid (4 mL) and heated to 80 °C. 6-(2-(2-

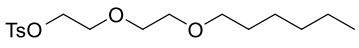
methoxyethoxy)ethoxy)hexan-1-amine (0.175 g, 0.798 mmol, 2.5 equiv.) was added dropwise, then the reaction mixture was heated to 120 °C overnight. Subsequently, the reaction mixture was cooled to room temperature and the solvent was removed *in vacuo*. The crude mixture was purified by silica column chromatography employing a 98:2 v/v chloroform:methanol eluent as the solvent system (R_f = 0.40) to yield the product as a pale yellow solid (0.060 g, 0.0771 mmol, 24% yield): ^{1}H NMR (400 MHz, $CDCl_3$) δ 3.73 (t, *J* = 7.3 Hz, 4H), 3.65 (dt, *J* = 5.7, 2.6 Hz, 8H), 3.57 (ddd, *J* = 12.0, 6.0, 3.9 Hz, 8H), 3.45 (td, *J* = 6.6, 2.7 Hz, 4H), 3.38 (s, 6H), 1.75 – 1.67 (m, 4H), 1.63 – 1.58 (m, 4H); 1.46 – 1.32 (m, 8H); ^{13}C NMR (126 MHz, $CDCl_3$) δ 163.6, 136.3, 114.3, 72.1, 71.3, 70.8, 70.7, 70.6, 59.2, 39.2, 29.6, 28.3, 26.8, 25.8.

oxybis(ethane-2,1-diyl) bis(4-methylbenzenesulfonate)



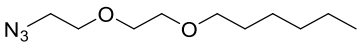
Diethylene glycol (22.4 g, 211 mmol, 1.0 equiv.) was dissolved in pyridine (53 mL, 654 mmol, 3.1 equiv.) and DCM (100 mL) under ambient conditions. The reaction mixture was cooled to 0 °C and 4-toluenesulfonyl chloride (88.5 g, 464 mmol, 2.2 equiv.) was added in 4 portions, then stirred at room temperature for one hour. The mixture was poured into 250 mL 2M HCl. The mixture was extracted with DCM (3 x 250 mL) and the organic fraction was washed with water (3 x 200 mL) then brine (1 x 200 mL) and dried over anhydrous Na2SO4. The solvent was removed in vacuo and the crude product was recrystallised from DCM and diethyl ether to obtain the product as a white crystalline solid (50.5 g, 122 mmol, 58% yield): ^{1}H NMR (400 MHz, $CDCl_3$) δ 7.80 (d, *J* = 8.5 Hz, 4H), 7.34 (d, *J* = 8.2 Hz, 4H), 4.08 (dq, *J* = 4.7, 2.5 Hz, 4H), 3.60 (qd, *J* = 3.3, 1.6 Hz, 4H), 2.44 (s, 6H); ^{13}C NMR (101 MHz, $CDCl_3$) δ 145.1, 132.9, 130.0, 128.0, 69.1, 68.8, 21.7. HRMS (ESI-ToF): 414.0807 [$M+H^+$] (calc. 414.0808).

2-(2-(hexyloxy)ethoxy)ethyl 4-methylbenzenesulfonate



Sodium hydride (60%, 1.43 g, 35.9 mmol, 1.5 equiv.) was dissolved in dry THF (200 mL) and the reaction mixture was cooled to 0 °C. Hexanol (3.00 mL, 23.9 mmol, 1.0 equiv.) was added dropwise, then the mixture was brought to room temperature and stirred for 30 minutes. The reaction mixture was heated to 65 °C for 1 hour, then cooled back to 0 °C. oxybis(ethane-2,1-diyl) bis(4-methylbenzenesulfonate) (29.7 g, 71.7 mmol, 3.0 equiv.) was added in one portion to the reaction mixture, which was then stirred at room temperature for 1 hour, then heated to 55 °C overnight. The reaction was cool to room temperature and poured over ice water. This mixture was extracted with DCM (2 x 150 mL), then the organic portion was washed with water (3 x 150 mL) and brine (1 x 150 mL) and dried over Na_2SO_4. The solvent was removed *in vacuo* and the crude product was purified by silica column chromatography employing a 1:3 v/v mixture of ethyl acetate:petroleum ether as the solvent system (R_f = 0.25). The final product was dried by high vacuum and obtained as a colourless oil (4.12 g, 12.0 mmol, 50% yield): ^{1}H NMR (400 MHz, $CDCl_3$) δ 7.80 (d, *J* = 8.5 Hz, 2H), 7.34 (d, *J* = 8.2 Hz, 2H), 4.16 (t, *J* = 4.9 Hz, 2H), 3.69 (dd, *J* = 5.7, 4.1 Hz, 2H), 3.60 – 3.47 (m, 5H), 3.41 (t, *J* = 6.8 Hz, 2H), 2.44 (s, 3H), 1.37 – 1.23 (m, 8H), 0.92 – 0.85 (m, 3H); ^{13}C NMR (101 MHz, $CDCl_3$) δ 144.9, 133.1, 129.9, 128.1, 71.7, 70.9, 70.1, 69.4, 63.2, 31.7, 29.7, 25.9, 22.7, 14.2. HRMS (ESI-ToF): 344.1650 [$M+H^+$] (calc. 344.1657).

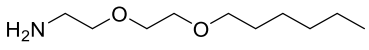
1-(2-(2-azidoethoxy)ethoxy)hexane



2-(2-(hexyloxy)ethoxy)ethyl 4-methylbenzenesulfonate (1.10 g, 3.19 mmol, 1.0 equiv.) was dissolved in dry DMF (15 mL) and cool to 0 °C. To this, sodium azide (0.310 g, 4.80 mmol, 1.5 equiv.) was added and the mixture was heated to 100 °C for 2.5 hours. Subsequently, the

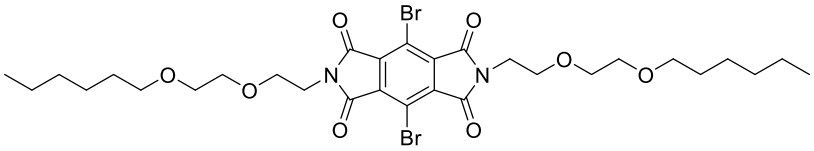
reaction mixture was cooled to room temperature and ethyl acetate (150 mL) was added. The precipitate was filtered and the filtrate was washed with water (3 x 150 mL) and brine (1 x 150 mL) and dried over Na_2SO_4, before the solvent was removed *in vacuo*. The crude product was pure and used directly without further purification as a colourless oil (0.678 g, 3.15 mmol, 99% yield): ^{1}H NMR (400 MHz, $CDCl_3$) δ 3.71 – 3.63 (m, 2H), 3.62 – 3.57 (m, 2H), 3.46 (t, *J* = 6.8 Hz, 2H), 3.39 (t, *J* = 5.1 Hz, 2H), 1.58 (dq, *J* = 8.2, 6.6 Hz, 2H), 1.41 – 1.21 (m, 8H), 0.94 – 0.82 (m, 3H); ^{13}C NMR (101 MHz, $CDCl_3$) δ 77.4, 71.8, 70.9, 70.3, 70.2, 50.9, 31.8, 29.7, 25.9, 22.8, 14.2. HRMS (ESI-ToF): 215.1640 [M+H$^+$] (calc. 215.1644).

2-(2-(hexyloxy)ethoxy)ethan-1-amine



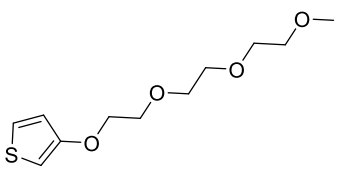
1-(2-(2-azidoethoxy)ethoxy)hexane (0.680 g, 3.16 mmol, 1.0 equiv.) was dissolved in dry THF (10 mL) and cooled to 0 °C. Triphenylphosphine (1.24 g, 4.74 mmol,1.5 equiv.) was added in and the mixture was stirred at room temperature for 2 hours. Deionised water (0.2 mL) was added and the reaction was stirred overnight at room temperature, then diluted with water (200 mL). The aqueous portion was washed with diethyl ether (3 x 200 mL), then concentrated *in vacuo*. The crude product was purified by an acid-base work up, by dissolving in DCM (100 mL), then extracting into aqueous HCl (2 M, 100 mL). The aqueous phase was basified and extracted with DCM (3 x 100 mL). The organic phase was dried over Na_2SO_4 and concentrated under reduced pressure to obtain the pure product as a colourless oil (0.551 g, 2.91 mmol, 92% yield): ^{1}H NMR (400 MHz, $CDCl_3$) δ 3.65 – 3.41 (m, 8H), 2.88 (t, *J* = 5.1 Hz, 2H), 1.65 – 1.51 (m, 2H), 1.41 – 1.22 (m, 6H), 0.96 – 0.82 (m, 3H); ^{13}C NMR (101 MHz, $CDCl_3$) δ 73.3, 71.7, 70.5, 70.2, 41.8, 31.8, 29.7, 25.9, 22.8, 14.2. HRMS (ESI-ToF): 189.1731 [M+H$^+$] (calc. 189.1729).

*4,8-dibromo-2,6-bis(2-(2-(hexyloxy)ethoxy)ethyl)pyrrolo[3,4-f]isoindole-1,3,5,7(2H,6H)-tetraone (**gaPMDI**)*



4,8-dibromo-1H,3H-benzo[1,2-c:4,5-c']difuran-1,3,5,7-tetraone (0.200 g, 0.532 mmol, 1.0 equiv.) was dissolved in glacial acetic acid (4.5 mL) and heated to 80 °C. 2-(2-(hexyloxy)ethoxy)ethan-1-amine (0.252 g, 1.33 mmol, 2.5 equiv.) was added dropwise, then the reaction mixture was heated to 120 °C overnight. Subsequently, the reaction mixture was cooled to room temperature and the solvent was removed under reduced pressure. The crude mixture was purified by silica column chromatography employing a 98:2 v/v ethyl acetate:methanol eluent as the solvent system (R_f = 0.25). The product was further purified by recrystallisation from ethyl acetate to yield the product as a white solid (0.088 g, 0.122 mmol, 23% yield): ^{1}H NMR (400 MHz, $CDCl_3$) δ 3.95 (t, *J* = 5.6 Hz, 4H), 3.79 (t, *J* = 5.6 Hz, 4H), 3.68 – 3.62 (m, 4H), 3.56 – 3.51 (m, 4H), 3.40 (t, *J* = 6.8 Hz, 4H), 1.51 (q, *J* = 7.1 Hz, 4H), 1.32 – 1.21 (m, 12H), 0.90 – 0.83 (m, 6H); ^{13}C NMR (126 MHz, $CDCl_3$) δ 163.5, 136.4, 114.3, 71.8, 70.2, 70.1, 67.5, 38.3, 31.8, 29.7, 25.9, 22.8, 14.2. HRMS (ESI-ToF): 718.1286 [$M+H^+$] (calc. 718.1288).

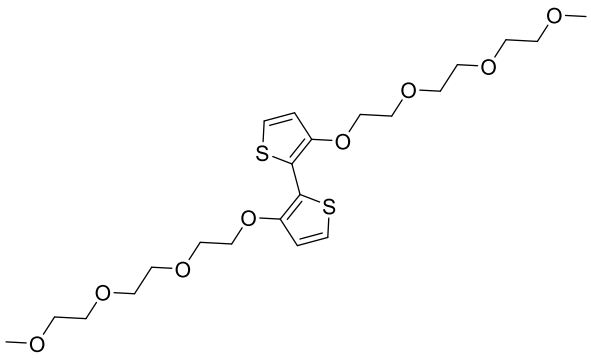
3-(2-(2-(2-methoxyethoxy)ethoxy)ethoxy)thiophene



Following a modified literature procedure,[49] 3-methoxythiophene (5.00 g, 43.8 mmol, 1.0 equiv.), triethylene glycol monomethyl ether (9.40 g, 57.0 mmol, 1.5 equiv.) and *p*-toluenesulfonic acid (0.840 g, 4.4 mmol, 0.1 equiv.) were dissolved in dry toluene (45 mL).

The reaction mixture was heated at reflux overnight. Following this, the reaction mixture was quenched with water (70 mL) and the aqueous phase was extracted with dichloromethane (3 x 100 mL). The combined organic layers were then washed with water (2 x 150 mL) and brine (1 x 150 mL), before drying over magnesium sulfate. The solvent was removed *in vacuo* and the crude product was purified by silica column chromatography with an eluent system of 1:2 v/v mixture of ethyl acetate:petroleum ether (R_f = 0.20). The final product was obtained as a clear colorless oil (6.12 g, 24.9 mmol, 57% yield): ^{1}H NMR (400 MHz, $CDCl_3$, δ) 7.17 (dd, *J* = 5.3, 3.1 Hz, 1H), 6.77 (dd, *J* = 5.3, 1.6 Hz, 1H), 6.27 (dd, *J* = 3.1, 1.6 Hz, 1H), 4.15 – 4.10 (m, 2H), 3.87 – 3.83 (m, 2H), 3.78 – 3.63 (m, 6H), 3.58 – 3.53 (m, 2H), 3.39 (s, 3H); ^{13}C NMR (101 MHz, $CDCl_3$) δ: 157.6, 124.6, 119.6, 97.5, 71.9, 70.8, 70.7, 70.6, 69.7, 69.6, 59.0. HRMS (ESI-ToF): 246.0294 [$M+H^+$] (calc. 246.0296).

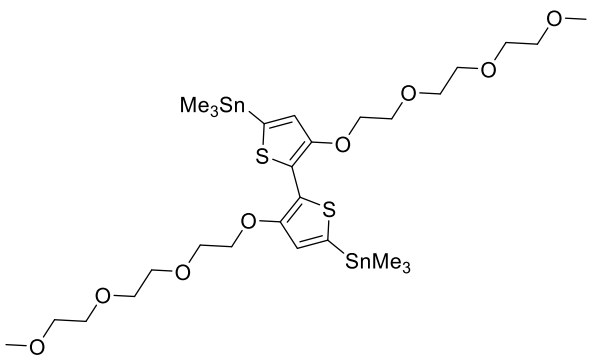
*3,3'-bis(2-(2-(2-methoxyethoxy)ethoxy)ethoxy)-2,2'-bithiophene (**g_3T2**)*



Following a modified literature procedure,[49] 3-(2-(2-(2-methoxyethoxy)ethoxy)ethoxy)thiophene (4.21 g, 17.2 mmol, 1.0 equiv.) was dissolved in dry THF (40 mL). The solution was cooled to -78 °C and *n*-BuLi in hexanes (1.6 M, 12.9 mL, 20.6 mmol, 1.2 equiv.) was added dropwise. The reaction mixture was brought to -40 °C and stirred for 1 hour. Separately, iron acetylacetonate (6.07 g, 17.2 mmol, 1.0 equiv.) was dissolved in dry THF (80 mL), then the lithiated species was transferred by canula to this solution. The reaction mixture was heated at reflux for 3 hours. Then, the reaction mixture was cooled to

room temperature and passed through a silica plug and excess solvent was removed *in vacuo*. The crude product was purified by silica column chromatography with an eluent system of 3:1 v/v mixture of ethyl acetate:petroleum ether (R_f = 0.25). The product was isolated as a white solid (5.74, 11.7 mmol, 68% yield): ^{1}H NMR (400 MHz, $CDCl_3$) 7.09 (d, *J* = 5.6 Hz, 2H), 6.87 (d, *J* = 5.5 Hz, 2H), 4.26 (t, *J* = 4.9 Hz, 4H), 3.94 (dd, *J* = 5.5, 4.6 Hz, 4H), 3.81 – 3.76 (m, 4H), 3.73 – 3.66 (m, 8H), 3.59 – 3.54 (m, 4H), 3.39 (s, 6H). ^{13}C NMR (100 MHz, $CDCl_3$): δ 151.8, 122.1, 116.4, 114.9, 72.1, 71.5, 71.0, 70.8, 70.7, 70.3, 59.0. HRMS (ESI-ToF): 490.1689 [M+H$^+$] (calc. 490.1694).

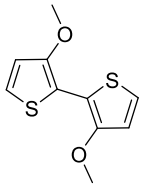
(3,3'-bis(2-(2-(2-methoxyethoxy)ethoxy)ethoxy)-[2,2'-bithiophene]-5,5'-diyl)bis(trimethylstannane)



Following a modified literature procedure,[49] **g$_3$T2** (1.00 g, 2.04 mmol, 1.0 equiv.) was dissolved in anhydrous THF (160 mL) and the reaction mixture was cooled to -30 °C. To this reaction mixture, *n*-BuLi in hexanes (2.5 M, 3.2 mL, 8.15 mmol, 4.0 equiv.) was added dropwise and the mixture was stirred at -30 °C for one hour. Subsequently, trimethyltin chloride in hexanes (1 M, 9.0 mL, 8.97 mmol, 4.4 equiv.) was added dropwise, then the reaction was brought to room temperature and stirred overnight. The reaction mixture was quenched with water (100 mL) and extracted with diethyl ether (2 x 150 mL). The combined organic phases were dried over sodium sulfate and excess solvent was removed *in vacuo*. The yellow oil was dissolved in acetonitrile (150 mL) and washed with hexane (3 x 150 mL) to remove tin

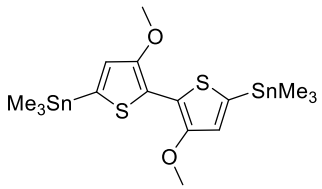
residues. The acetonitrile was again removed under reduced pressure to afford the title compound as an off white solid (1.02 g, 1.25 mmol, 61% yield): ^{1}H NMR (400 MHz, CD_2Cl_2) δ 6.99 (s, 2H), 4.31 – 4.26 (m, 4H), 3.94 – 3.89 (m, 4H), 3.78 – 3.72 (m, 4H), 3.68 – 3.60 (m, 8H), 3.58 – 3.50 (m, 4H), 3.35 (s, 6H), 0.41 (s, 18H); 13C NMR (101 MHz, CD_2Cl_2) δ 153.6, 134.3, 124.2, 120.9, 71.9, 71.5, 70.9, 70.6, 70.4, 70.1, 58.6, -8.7. HRMS (ESI-ToF): 816.0982 [M+H$^+$] (calc. 816.0985).

*3,3'-dimethoxy-2,2'-bithiophene (**OMeT2**)*



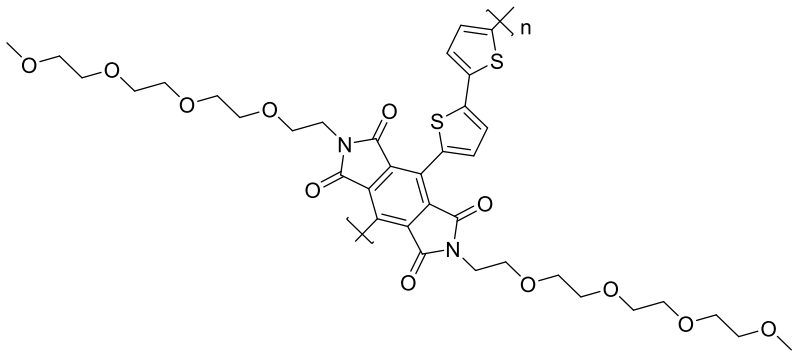
Following a modified literature procedure,[49] 3-methoxythiophene (6.15 g, 53.9 mmol, 1.0 equiv.) was dissolved in dry THF (50 mL). The solution was cooled to -78 °C and *n*-BuLi in hexanes (2.5 M, 21.6 mL, 53.9 mmol, 1.0 equiv.) was added dropwise. The reaction mixture was brought to -20 °C and stirred for 2 hours. Separately, iron acetylacetonate (20.0 g, 56.6 mmol, 1.05 equiv.) was dissolved in dry THF (170 mL), then the lithiated species was transferred via canula to this solution. The reaction mixture was heated at reflux for 4 hours. Then, the reaction mixture was cooled to room temperature and passed through a silica plug and excess solvent was removed *in vacuo*. The crude product was purified by silica column chromatography with an eluent system of 7:3 v/v mixture of petroleum ether:DCM (R_f = 0.40). The product was isolated as a white solid (5.12, 22.6 mmol, 42% yield): ^{1}H NMR (400 MHz, $CDCl_3$) δ 7.09 (d, *J* = 5.5 Hz, 2H), 6.86 (d, *J* = 5.6 Hz, 2H), 3.92 (s, 6H); ^{13}C NMR (101 MHz, $CDCl_3$) δ 152.8, 121.9, 115.7, 113.5, 58.8. HRMS (ESI-ToF): 226.0127 [M+H$^+$] (calc. 226.0126).

(3,3'-dimethoxy-[2,2'-bithiophene]-5,5'-diyl)bis(trimethylstannane)



Following a modified literature procedure,[49] **OMeT2** (0.890 g, 3.93 mmol, 1.0 equiv.) was dissolved in anhydrous THF (50 mL) and the reaction mixture was cooled to -78 °C. To this reaction mixture, *n*-BuLi in hexanes (2.5 M, 6.3 mL, 15.7 mmol, 4.0 equiv.) was added dropwise and the mixture was stirred at room temperature for one hour. Subsequently, trimethyltin chloride in hexanes (1 M, 15.7 mL, 15.7 mmol, 4.0 equiv.) was added dropwise, then the reaction was brought to room temperature and stirred overnight. The reaction mixture was quenched with water (100 mL) and extracted with diethyl ether (2 x 150 mL). The combined organic phases were dried over magnesium sulfate and excess solvent was removed *in vacuo*. The crude product was recrystallized from acetonitrile to afford the title compound as an off white solid (1.80 g, 3.26 mmol, 83% yield): ^{1}H NMR (400 MHz, acetone-d_6) δ 6.91 (s, 2H), 3.97 (s, 6H), 0.37 (s, 18H); ^{13}C NMR (101 MHz, acetone-d_6) δ 155.7, 134.8, 124.3, 59.1, -8.4. HRMS (ESI-ToF): 551.9418 [M+H^{+}] (calc. 551.9412).

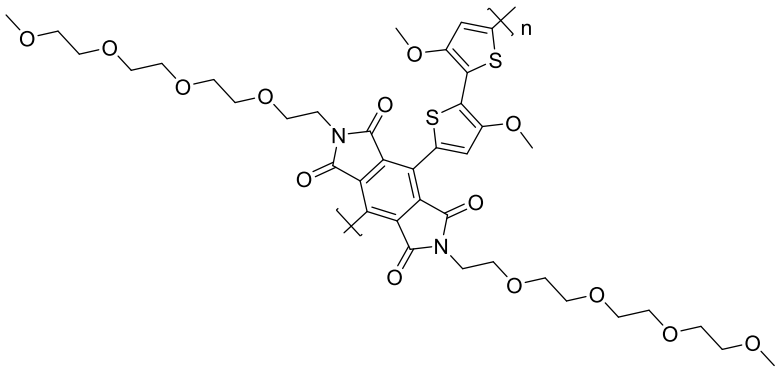
p(gPMDI-T2)



gPMDI (64.88 mg, 86.0 µmol, 1.0 equiv.), 5,5′-bis(trimethylstannyl)-2,2′-bithiophene (42.30 mg, 86.0 µmol, 1.0 equiv.), tris(dibenzylideneacetone)dipalladium(0) (1.58 mg, 1.72 µmol,

0.02 equiv.) and tris(*o*-methoxyphenyl)phosphine (2.43 mg, 6.88 µmol, 0.08 equiv.) were dissolved in anhydrous degassed chlorobenzene (1.8 mL). The resulting solution was degassed for an additional 10 minutes and the reaction was heated at 135 °C in a microwave for 4 hours. The crude polymer solution was cooled to room temperature and precipitated into a 1:1 v/v mixture of ethyl acetate:hexane, and the polymer was purified via Soxhlet extractions with: hexane, ethyl acetate, acetone and methanol. The polymer was then dissolved in chloroform and excess solvent was removed *in vacuo*. The final product was collected by reprecipitating the polymer into a 1:1 v/v mixture of ethyl acetate:hexane and collecting it by suction filtration. **p(PMDI-T2)** was obtained as an orange/yellow solid (42.10 mg, 55.5 µmol, 65% yield): ^{1}H NMR (400 MHz, $CDCl_3$) δ 7.36 (d), 7.19 (d), 3.86 (s), 3.74 (t), 3.69 – 3.59 (m), 3.54 – 3.52 (m), 3.36 (s); GPC (chloroform, 40 °C): M_n = 28.5 kDa, M_w = 43.8 kDa.

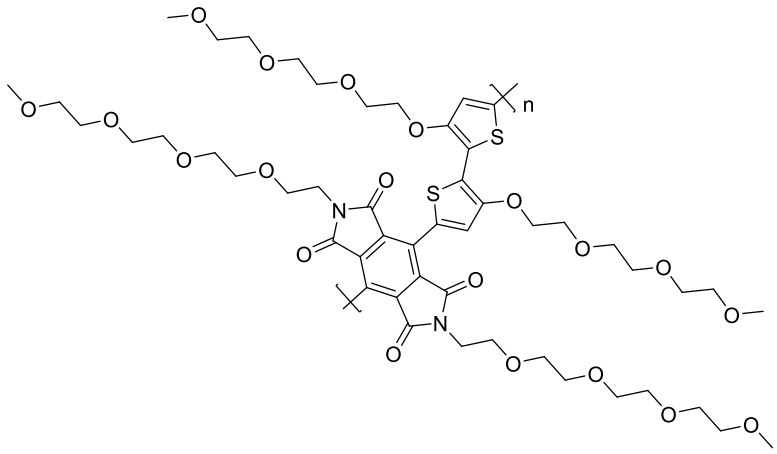
p(gPMDI-OMeT2)



gPMDI (52.68 mg, 69.8 µmol, 1.0 equiv.), (3,3'-dimethoxy-[2,2'-bithiophene]-5,5'-diyl)bis(trimethylstannane) (38.59 mg, 69.8 µmol, 1.0 equiv.), tris(dibenzylideneacetone)dipalladium(0) (1.28 mg, 1.40 µmol, 0.02 equiv.) and tris(*o*-methoxyphenyl)phosphine (1.97 mg, 5.59 µmol, 0.08 equiv.) were dissolved in anhydrous degassed chlorobenzene (1.5 mL). The resulting solution was degassed for an additional 10 minutes and the reaction was heated at 135 °C in a microwave for 3 hours. The crude polymer solution was cooled to room temperature and precipitated into a 1:1 v/v mixture of ethyl

acetate:hexane, and the polymer was purified via Soxhlet extractions with: hexane, ethyl acetate, acetone and methanol. The polymer was then dissolved in chloroform and excess solvent was removed *in vacuo*. The final product was collected by reprecipitating the polymer into a 1:1 v/v mixture of ethyl acetate:hexane and collecting it by suction filtration. **p(PMDI-OMeT2)** was obtained as a red solid (50.11 mg, 61.2 µmol, 88% yield): ^{1}H NMR (400 MHz, $CDCl_3$) δ 4.03 (s), 3.86 (s), 3.75 (d), 3.69 – 3.59 (m), 3.54 – 3.52 (m), 3.36 (s); GPC (chloroform, 40 °C): M_n = 30.9 kDa, M_w = 71.8 kDa.

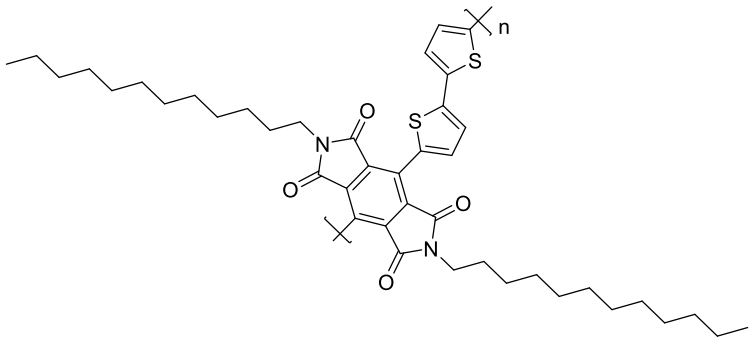
p(gPMDI-g$_3$T2)



gPMDI (64.75 mg, 85.8 µmol, 1.0 equiv.), (3,3'-bis(2-(2-(2-methoxyethoxy)ethoxy)ethoxy)-[2,2'-bithiophene]-5,5'-diyl)bis(trimethylstannane) (70.06 mg, 85.8 µmol, 1.0 equiv.), tris(dibenzylideneacetone)dipalladium(0) (1.57 mg, 1.72 µmol, 0.02 equiv.) and tris(*o*-methoxyphenyl)phosphine (2.43 mg, 6.87 µmol, 0.08 equiv.) were dissolved in anhydrous degassed chlorobenzene (1.9 mL). The resulting solution was degassed for an additional 10 minutes and the reaction was heated at 135 °C in a microwave for 3 hours. The crude polymer solution was cooled to room temperature and precipitated into a 1:1 v/v mixture of ethyl acetate:hexane, and the polymer was purified via Soxhlet extractions with: hexane, ethyl acetate, acetone and methanol. The polymer was then dissolved in chloroform and excess solvent was removed *in vacuo*. The final product was collected by reprecipitating the polymer

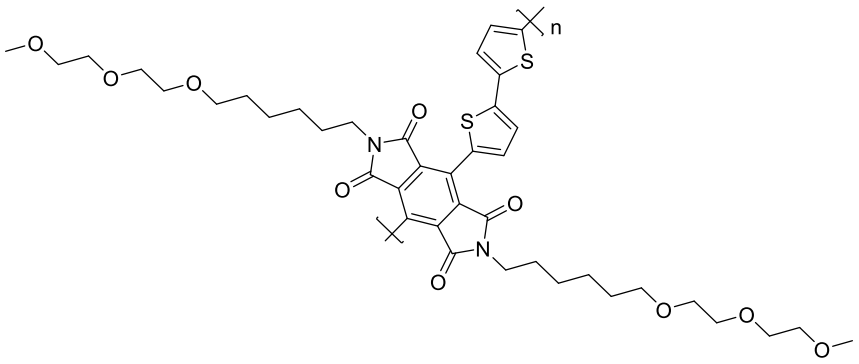
into a 1:1 v/v mixture of ethyl acetate:hexane and collecting it by suction filtration. **p(PMDI-g_3T2)** was obtained as a dark red solid (47.92 mg, 44.2 µmol, 52% yield): ^{1}H NMR (400 MHz, $CDCl_3$) δ 7.04 (s), 4.35 (s), 3.94 (s), 3.78 – 3.73 (m), 3.67 – 3.61 (m), 3.54 – 3.51 (m), 3.37 – 3.31 (m); GPC (chloroform, 40 °C): M_n = 21.6 kDa, M_w = 36.8 kDa.

p(aPMDI-T2)



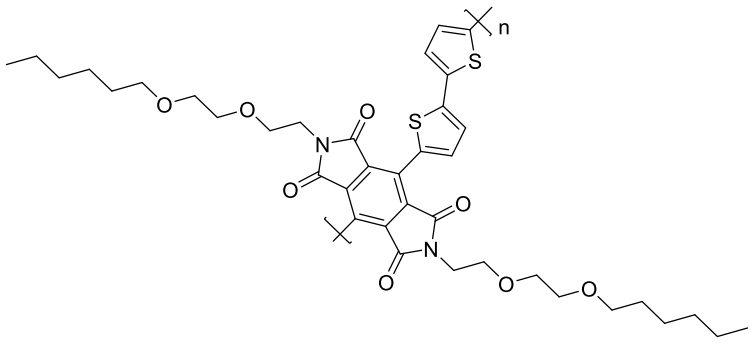
aPMDI (70.11 mg, 98.7 µmol, 1.0 equiv.), 5,5′-bis(trimethylstannyl)-2,2′-bithiophene (48.53 mg, 98.7 µmol, 1.0 equiv.), tris(dibenzylideneacetone)dipalladium(0) (1.81 mg, 1.97 µmol, 0.02 equiv.) and tris(*o*-methoxyphenyl)phosphine (2.79 mg, 7.89 µmol, 0.08 equiv.) were dissolved in anhydrous degassed chlorobenzene (2.1 mL). The resulting solution was degassed for an additional 10 minutes and the reaction was heated at 135 °C in a microwave for 2.5 hours. The crude polymer solution was cooled to room temperature and precipitated into a 1:1 v/v mixture of ethyl acetate:hexane, and the polymer was purified via Soxhlet extractions with: hexane, ethyl acetate, acetone and methanol. The polymer was then dissolved in chloroform and excess solvent was removed *in vacuo*. The final product was collected by reprecipitating the polymer into a 1:1 v/v mixture of ethyl acetate:hexane and collecting it by suction filtration. **p(aPMDI-T2)** was obtained as red solid (33.0 mg, 46.2 µmol, 47% yield): ^{1}H NMR (400 MHz, $CDCl_3$) δ 7.38 (d), 7.22 (d), 3.63 (br s), 1.65 (br s), 1.32 – 1.27 (m), 1.24 (s), 0.87 (t); GPC (chloroform, 40 °C): M_n = 13.1 kDa, M_w = 22.4 kDa.

p(agPMDI-T2)



agPMDI (41.60 mg, 53.3 µmol, 1.0 equiv.), 5,5′-bis(trimethylstannyl)-2,2′-bithiophene (26.22 mg, 53.3 µmol, 1.0 equiv.), tris(dibenzylideneacetone)dipalladium(0) (0.98 mg, 1.07 µmol, 0.02 equiv.) and tris(*o*-methoxyphenyl)phosphine (1.51 mg, 4.26 µmol, 0.08 equiv.) were dissolved in anhydrous degassed chlorobenzene (1.2 mL). The resulting solution was degassed for an additional 10 minutes and the reaction was heated at 135 °C in a microwave for 2.5 hours. The crude polymer solution was cooled to room temperature and precipitated into a 1:1 v/v mixture of ethyl acetate:hexane, and the polymer was purified via Soxhlet extractions with: hexane, ethyl acetate, acetone and methanol. The polymer was then dissolved in chloroform and excess solvent was removed *in vacuo*. The final product was collected by reprecipitating the polymer into a 1:1 v/v mixture of ethyl acetate:hexane and collecting it by suction filtration. **p(aPMDI-T2)** was obtained as red solid (30.4 mg, 38.8 µmol, 73% yield): ^{1}H NMR (400 MHz, $CDCl_3$) δ 7.38 (d), 7.22 (d), 3.67 – 3.60 (m), 3.64 – 3.60 (m), 3.58 – 3.53 (m), 3.44 (t), 3.37 (s), 1.59 – 1.53 (m), 1.39 – 1.31 (m); GPC (chloroform, 40 °C): M_n = 19.7 kDa, M_w = 25.4 kDa.

p(gaPMDI-T2)



gaPMDI (58.68 mg, 81.7 µmol, 1.0 equiv.), 5,5′-bis(trimethylstannyl)-2,2′-bithiophene (40.17 mg, 81.7 µmol, 1.0 equiv.), tris(dibenzylideneacetone)dipalladium(0) (1.50 mg, 1.63 µmol, 0.02 equiv.) and tris(*o*-methoxyphenyl)phosphine (2.31 mg, 6.53 µmol, 0.08 equiv.) were dissolved in anhydrous degassed chlorobenzene (1.8 mL). The resulting solution was degassed for an additional 10 minutes and the reaction was heated at 135 °C in a microwave for 2.5 hours. The crude polymer solution was cooled to room temperature and precipitated into a 1:1 v/v mixture of ethyl acetate:hexane, and the polymer was purified via Soxhlet extractions with: hexane, ethyl acetate, acetone and methanol. The polymer was then dissolved in chloroform and excess solvent was removed *in vacuo*. The final product was collected by reprecipitating the polymer into a 1:1 v/v mixture of ethyl acetate:hexane and collecting it by suction filtration. **p(aPMDI-T2)** was obtained as red solid (49.8 mg, 68.9 µmol, 84% yield): ^{1}H NMR (400 MHz, $CDCl_3$) δ 7.36 (d) 7.18 (d), 3.87 (br s), 3.75 (t), 3.66 – 3.62 (m), 3.56 – 3.52 (m), 3.43 (t), 1.57 – 1.49 (m), 1.36 – 1.22 (m), 0.92 – 0.82 (m); GPC (chloroform, 40 °C): M_n = 36.8 kDa, M_w = 60.7 kDa.

Bibliography

1. About the Super Retina display and Super Retina XDR display on your iPhone. https://support.apple.com/en-gb/HT208191.
2. 2022 55" S95B OLED 4K Quantum HDR Smart TV. https://www.samsung.com/uk/tvs/oled-tv/s95b-55-inch-oled-4k-smart-tv-qe55s95batxxu/.
3. OLED R - Rollable design. https://www.lg.com/global/lg-signature/rollable-oled-tv-r.
4. Why The Boeing 787 Has Dimmable Windows. https://simpleflying.com/boeing-787-dimmable-windows-why/.
5. Mazzio, K. A. & Luscombe, C. K. The future of organic photovoltaics. *Chem. Soc. Rev.* **44**, 78–90 (2014).
6. Kim, M. *et al.* Donor–Acceptor-Conjugated Polymer for High-Performance Organic Field-Effect Transistors: A Progress Report. *Adv. Funct. Mater.* **30**, 1904545 (2020).
7. Russ, B., Glaudell, A., Urban, J. J., Chabinyc, M. L. & Segalman, R. A. Organic thermoelectric materials for energy harvesting and temperature control. *Nat. Rev. Mater.* **1**, 16050 (2016).
8. Sze, S. M. & Ng, K. K. *Physics of Semiconductor Devices*. (Wiley, 2006). doi:10.1002/9780470068328.
9. Moss, T. S. *Handbook on semiconductors*. (Elsevier Science Publishers, 1992).
10. Bredas, J. L. Mind the gap! *Mater. Horizons* **1**, 17–19 (2014).
11. Bronstein, H., Nielsen, C. B., Schroeder, B. C. & McCulloch, I. The role of chemical design in the performance of organic semiconductors. *Nat. Rev. Chem.* **4**, 66–77 (2020).
12. Bubnova, O. & Crispin, X. Towards polymer-based organic thermoelectric generators. *Energy Environ. Sci.* **5**, 9345–9362 (2012).
13. Zhan, C. G., Nichols, J. A. & Dixon, D. A. Ionization potential, electron affinity, electronegativity, hardness, and electron excitation energy: Molecular properties from density functional theory orbital energies. *J. Phys. Chem. A* **107**, 4184–4195 (2003).
14. Martin, R. E. & Diederich, F. Linear Monodisperse π-Conjugated Oligomers: Model Compounds for Polymers and More. *Angew. Chemie Int. Ed.* **38**, 1350–1377 (1999).
15. Yamashita, Y. Organic semiconductors for organic field-effect transistors. *Sci. Technol. Adv. Mater.* **10**, 24313 (2009).
16. Brédas, J. L., Calbert, J. P., Da Silva Filho, D. A. & Cornil, J. Organic semiconductors: A theoretical characterization of the basic parameters governing charge transport. *Proc. Natl. Acad. Sci. U. S. A.* **99**, 5804–5809 (2002).
17. Fratini, S., Nikolka, M., Salleo, A., Schweicher, G. & Sirringhaus, H. Charge transport in high-mobility conjugated polymers and molecular semiconductors. *Nat. Mater.* **19**, 491–502 (2020).

18. Giannini, S., Carof, A. & Blumberger, J. Crossover from Hopping to Band-Like Charge Transport in an Organic Semiconductor Model: Atomistic Nonadiabatic Molecular Dynamics Simulation. *J. Phys. Chem. Lett.* **9**, 3116–3123 (2018).

19. Coropceanu, V. *et al.* Charge transport in organic semiconductors. *Chem. Rev.* **107**, 926–952 (2007).

20. Schweicher, G. *et al.* Molecular Semiconductors for Logic Operations: Dead-End or Bright Future? *Adv. Mater.* **32**, 1905909 (2020).

21. Fratini, S., Mayou, D. & Ciuchi, S. The transient localization scenario for charge transport in crystalline organic materials. *Adv. Funct. Mater.* **26**, 2292–2315 (2016).

22. Kim, D. H. *et al.* Molecular weight-induced structural transition of liquid-crystalline polymer semiconductor for high-stability organic transistor. *Adv. Funct. Mater.* **21**, 4442–4447 (2011).

23. Pasveer, W. F. *et al.* Unified description of charge-carrier mobilities in disordered semiconducting polymers. *Phys. Rev. Lett.* **94**, 1–4 (2005).

24. Gu, K. *et al.* Assessing the Huang-Brown Description of Tie Chains for Charge Transport in Conjugated Polymers. *ACS Macro Lett.* **7**, 1333–1338 (2018).

25. Onorato, J. W. & Luscombe, C. K. Morphological effects on polymeric mixed ionic/electronic conductors. *Mol. Syst. Des. Eng.* **4**, 310–324 (2019).

26. Goh, C., Kline, R. J., McGehee, M. D., Kadnikova, E. N. & Fŕchet, J. M. J. Molecular-weight-dependent mobilities in regioregular poly(3-hexyl- thiophene) diodes. *Appl. Phys. Lett.* **86**, 1–3 (2005).

27. Noriega, R. *et al.* A general relationship between disorder, aggregation and charge transport in conjugated polymers. *Nat. Mater.* **12**, 1038–1044 (2013).

28. Takacs, C. J. *et al.* Remarkable order of a high-performance polymer. *Nano Lett.* **13**, 2522–2527 (2013).

29. Gu, K., Onorato, J. W., Luscombe, C. K. & Loo, Y. L. The Role of Tie Chains on the Mechano-Electrical Properties of Semiconducting Polymer Films. *Adv. Electron. Mater.* **6**, 1–8 (2020).

30. Chen, Z., Zheng, Y., Yan, H. & Facchetti, A. Naphthalenedicarboximide- vs Perylenedicarboximide-Based Copolymers. Synthesis and Semiconducting Properties in Bottom-Gate N-Channel Organic Transistors. *J. Am. Chem. Soc.* **131**, 8–9 (2009).

31. Pandey, M., Kumari, N., Nagamatsu, S. & Pandey, S. S. Recent advances in the orientation of conjugated polymers for organic field-effect transistors. *J. Mater. Chem. C* **7**, 13323–13351 (2019).

32. Shi, J., Li, Y., Jia, M., Xu, L. & Wang, H. Organic semiconductors based on annelated $β$-oligothiophenes and its application for organic field-effect transistors. *J. Mater. Chem.* **21**, 17612–17614 (2011).

33. Fornari, R. P., Rowe, P., Padula, D. & Troisi, A. Importance and Nature of Short-Range Excitonic Interactions in Light Harvesting Complexes and Organic Semiconductors. *J. Chem. Theory Comput.* **13**, 3754–3763 (2017).

34. Venkateshvaran, D. *et al.* Approaching disorder-free transport in high-mobility

conjugated polymers. *Nature* **515**, 384–388 (2014).

35. McCulloch, I. *et al.* Liquid-crystalline semiconducting polymers with high charge-carrier mobility. *Nat. Mater.* **5**, 328–333 (2006).

36. Wang, X.-Y. *et al.* Azaborine Compounds for Organic Field-Effect Transistors: Efficient Synthesis, Remarkable Stability, and BN Dipole Interactions. *Angew. Chemie* **125**, 3199–3202 (2013).

37. Okamoto, T., Suzuki, T., Tanaka, H., Hashizume, D. & Matsuo, Y. Tetracene Dicarboxylic Imide and Its Disulfide: Synthesis of Ambipolar Organic Semiconductors for Organic Photovoltaic Cells. *Chem. Asian J.* **7**, 105–111 (2012).

38. Onwubiko, A. *et al.* Fused electron deficient semiconducting polymers for air stable electron transport. *Nat. Commun.* **9**, 416 (2018).

39. Fu, C., Beldon, P. J. & Perepichka, D. F. H-Bonding Control of Supramolecular Ordering of Diketopyrrolopyrroles. *Chem. Mater.* **29**, 2979–2987 (2017).

40. Griggs, S., Marks, A., Bristow, H. & McCulloch, I. n-Type organic semiconducting polymers: stability limitations, design considerations and applications. *J. Mater. Chem. C* **9**, 8099–8128 (2021).

41. Kleinhenz, N., Yang, L., Zhou, H., Price, S. C. & You, W. Low-band-gap polymers that utilize quinoid resonance structure stabilization by thienothiophene: Fine-tuning of HOMO level. *Macromolecules* **44**, 872–877 (2011).

42. Mcculloch, I. *et al.* Design of Semiconducting Indacenodithiophene Polymers for High Performance Transistors and Solar Cells. *Acc. Chem. Res.* **45**, 714–722 (2012).

43. Belletéte, M., Leclerc, M. & Durocher, G. Potentialities of Semiempirical Calculations (AMPAC and INDO/S) in Determining the Conformation and Electronic Properties of 2,2/-Bithiophene: A New Joint Experimental and Theoretical Approach. *J. Phys. Chem.* **98**, 9450–9456 (1994).

44. Casanovas, J., Zanuy, D. & Alemán, C. Structural and electronic effects induced by carboxylic acid substitution in isomeric 2,2′-bithiophenes and oligothiophenes: A computational study. *Polymer (Guildf).* **46**, 9452–9460 (2005).

45. Müllen, K. & Pisula, W. Donor–Acceptor Polymers. *J. Am. Chem. Soc.* **137**, 9503–9505 (2015).

46. Duan, C., Huang, F. & Cao, Y. Recent development of push–pull conjugated polymers for bulk-heterojunction photovoltaics: rational design and fine tailoring of molecular structures. *J. Mater. Chem.* **22**, 10416 (2012).

47. Yan, Z., Sun, B. & Li, Y. Novel stable (3E,7E)-3,7-bis(2-oxoindolin-3-ylidene)benzo[1,2-b:4,5-b′]difuran-2,6(3H,7H)-dione based donor-acceptor polymer semiconductors for n-type organic thin film transistors. *Chem. Commun.* **49**, 3790–3792 (2013).

48. Song, H. *et al.* Donor-Acceptor Conjugated Polymers Based on Indacenodithiophene Derivative Bridged Diketopyrrolopyrroles: Synthesis and Semiconducting Properties. *Macromolecules* **50**, 2344–2353 (2017).

49. Moser, M. *et al.* Side Chain Redistribution as a Strategy to Boost Organic

Electrochemical Transistor Performance and Stability. *Adv. Mater.* **32**, 1–6 (2020).

50. Sommer, M. Conjugated polymers based on naphthalene diimide for organic electronics. *J. Mater. Chem. C* **2**, 3088–3098 (2014).

51. Nielsen, C. B., Turbiez, M. & McCulloch, I. Recent Advances in the Development of Semiconducting DPP-Containing Polymers for Transistor Applications. *Adv. Mater.* **25**, 1859–1880 (2013).

52. Chen, X. *et al.* n -Type Rigid Semiconducting Polymers Bearing Oligo(Ethylene Glycol) Side Chains for High-Performance Organic Electrochemical Transistors. *Angew. Chemie Int. Ed.* **60**, 9368–9373 (2021).

53. Stalder, R., Mei, J., Graham, K. R., Estrada, L. A. & Reynolds, J. R. Isoindigo, a versatile electron-deficient unit for high-performance organic electronics. *Chem. Mater.* **26**, 664–678 (2014).

54. Wang, Y. *et al.* Naphthodithiophenediimide-Benzobisthiadiazole-Based Polymers: Versatile n-Type Materials for Field-Effect Transistors and Thermoelectric Devices. *Macromolecules* **50**, 857–864 (2017).

55. Nakano, M., Osaka, I. & Takimiya, K. Naphthodithiophene diimide (NDTI)-based semiconducting copolymers: From ambipolar to unipolar N-type polymers. *Macromolecules* **48**, 576–584 (2015).

56. Yue, W. *et al.* Azaisoindigo conjugated polymers for high performance n-type and ambipolar thin film transistor applications. *J. Mater. Chem. C* **4**, 9704–9710 (2016).

57. Kim, G. *et al.* Acceptor–acceptor type isoindigo-based copolymers for high-performance n-channel field-effect transistors. *Chem. Commun.* **50**, 2180--2183 (2014).

58. Dai, Y.-Z. *et al.* Embedding electron-deficient nitrogen atoms in polymer backbone towards high performance n-type polymer field-effect transistors †. *Chem. Sci.* **7**, 5753–5757 (2016).

59. Hwang, Y.-J., Ren, G., Murari, N. M. & Jenekhe, S. A. n-Type Naphthalene Diimide−Biselenophene Copolymer for All Polymer Bulk Heterojunction Solar Cells. *Macromolecules* **45**, 9056−9062 (2012).

60. Zhao, Z. *et al.* High-Performance, Air-Stable Field-Effect Transistors Based on Heteroatom-Substituted Naphthalenediimide-Benzothiadiazole Copolymers Exhibiting Ultrahigh Electron Mobility up to 8.5 cm V^{-1} s^{-1}. *Adv. Mater.* **29**, 1602410 (2017).

61. Shi, K. *et al.* Toward High Performance n-Type Thermoelectric Materials by Rational Modification of BDPPV Backbones. *J. Am. Chem. Soc.* **137**, 6979–6982 (2015).

62. Han, J. *et al.* Dichlorinated Dithienylethene-Based Copolymers for Air-Stable n-Type Conductivity and Thermoelectricity. *Adv. Funct. Mater.* **31**, 2005901 (2021).

63. Kang, B. *et al.* Side-Chain-Induced Rigid Backbone Organization of Polymer Semiconductors through Semifluoroalkyl Side Chains. *J. Am. Chem. Soc.* **138**, 3679–3686 (2016).

64. Wang, Y. & Takimiya, K. Naphthodithiophenediimide–Bithiopheneimide Copolymers for High-Performance n-Type Organic Thermoelectrics: Significant Impact of

Backbone Orientation on Conductivity and Thermoelectric Performance. *Adv. Mater.* **32**, 2002060 (2020).

65. Zheng, Y.-Q. *et al.* Strong Electron-Deficient Polymers Lead to High Electron Mobility in Air and Their Morphology-Dependent Transport Behaviors. *Adv. Mater.* **28**, 7213–7219 (2016).

66. Lei, T., Dou, J.-H., Cao, X.-Y., Wang, J.-Y. & Pei, J. A BDOPV-Based Donor-Acceptor Polymer for High-Performance n-Type and Oxygen-Doped Ambipolar Field-Effect Transistors. *Adv. Mater.* **25**, 6589–6593 (2013).

67. Roncali, J. Molecular Engineering of the Band Gap of $π$-Conjugated Systems: Facing Technological Applications. *Macromol. Rapid Commun.* **28**, 1761–1775 (2007).

68. Lei, T., Wang, J. Y. & Pei, J. Roles of flexible chains in organic semiconducting materials. *Chem. Mater.* **26**, 594–603 (2014).

69. Moia, D. *et al.* Design and evaluation of conjugated polymers with polar side chains as electrode materials for electrochemical energy storage in aqueous electrolytes. *Energy Environ. Sci.* **12**, 1349–1357 (2019).

70. Szweda, R., Chendo, C., Charles, L., Baxter, P. N. W. & Lutz, J. F. Synthesis of oligoarylacetylenes with defined conjugated sequences using tailor-made soluble polymer supports. *Chem. Commun.* **53**, 8312–8315 (2017).

71. Giovannitti, A. *et al.* Controlling the mode of operation of organic transistors through side-chain engineering. *Proc. Natl. Acad. Sci. U. S. A.* **113**, 12017–12022 (2016).

72. Giovannitti, A. *et al.* N-type organic electrochemical transistors with stability in water. *Nat. Commun.* **7**, 13066 (2016).

73. Nielsen, C. B. *et al.* Molecular Design of Semiconducting Polymers for High-Performance Organic Electrochemical Transistors. *J. Am. Chem. Soc.* **138**, 10252–10259 (2016).

74. Kang, K. *et al.* 2D coherent charge transport in highly ordered conducting polymers doped by solid state diffusion. *Nat. Mater.* **15**, 896–902 (2016).

75. Marks, A. *et al.* Synthetic Nuances to Maximize n-Type Organic Electrochemical Transistor and Thermoelectric Performance in Fused Lactam Polymers. *J. Am. Chem. Soc.* **144**, 4642–4656 (2022).

76. Sarhan, A. A. O. & Bolm, C. Iron(III) chloride in oxidative C–C coupling reactions. *Chem. Soc. Rev.* **38**, 2730–2744 (2009).

77. Lu, Y., Shi, G., Li, C. & Liang, Y. Thin Polypyrrole Films Prepared by Chemical Oxidative Polymerization. *J Appl Polym Sci* **70**, 2169–2172 (1998).

78. Myers, R. E. Chemical oxidative polymerization as a synthetic route to electrically conducting polypyrroles. *J. Electron. Mater. 1986 152* **15**, 61–69 (1986).

79. Stefan, M. C., Bhatt, M. P., Sista, P. & Magurudeniya, H. D. Grignard metathesis (GRIM) polymerization for the synthesis of conjugated block copolymers containing regioregular poly(3-hexylthiophene). *Polym. Chem.* **3**, 1693–1701 (2012).

80. Holcombe, T. W., Woo, C. H., Kavulak, D. F. J., Thompson, B. C. & Fréchet, J. M. J.

All-Polymer Photovoltaic Devices of Poly(3-(4- n -octyl)-phenylthiophene) from Grignard Metathesis (GRIM) Polymerization. *J. Am. Chem. Soc.* **131**, 14160–14161 (2009).

81. Stille, J. K. The Palladium-Catalyzed Cross-Coupling Reactions of Organotin Reagents with Organic Electrophiles[New Synthetic Methods(58)]. *Angew. Chemie Int. Ed. English* **25**, 508–524 (1986).

82. Miyaura, N. & Suzuki, A. Palladium-Catalyzed Cross-Coupling Reactions of Organoboron Compounds. *Chem. Rev.* **95**, 2457–2483 (1995).

83. Sakamoto, J., Rehahn, M., Wegner, G. & Schlüter, A. D. Suzuki Polycondensation: Polyarylenes à la Carte. *Macromol. Rapid Commun.* **30**, 653–687 (2009).

84. Carrillo, J. A., Turner, M. L. & Ingleson, M. J. A General Protocol for the Polycondensation of Thienyl N -Methyliminodiacetic Acid Boronate Esters To Form High Molecular Weight Copolymers. *J. Am. Chem. Soc.* **138**, 13361–13368 (2016).

85. Lennox, A. J. J. & Lloyd-Jones, G. C. Transmetalation in the Suzuki-Miyaura Coupling: The Fork in the Trail. *Angew. Chemie Int. Ed.* **52**, 7362–7370 (2013).

86. Chen, H. *et al.* Acene Ring Size Optimization in Fused Lactam Polymers Enabling High n-Type Organic Thermoelectric Performance. *J. Am. Chem. Soc.* **143**, 260–268 (2021).

87. Melling, D., Martinez, J. G. & Jager, E. W. H. Conjugated Polymer Actuators and Devices: Progress and Opportunities. *Adv. Mater.* **31**, 1808210 (2019).

88. Li, K. *et al.* Lattice-contraction triggered synchronous electrochromic actuator. *Nat. Commun.* **9**, 4798 (2018).

89. Guo, K. *et al.* Rapid single-molecule detection of COVID-19 and MERS antigens via nanobody-functionalized organic electrochemical transistors. *Nat. Biomed. Eng.* **5**, 666–677 (2021).

90. Romele, P. *et al.* Multiscale real time and high sensitivity ion detection with complementary organic electrochemical transistors amplifier. *Nat. Commun.* **11**, 3743 (2020).

91. Spyropoulos, G. D., Gelinas, J. N. & Khodagholy, D. Internal ion-gated organic electrochemical transistor: A building block for integrated bioelectronics. *Sci. Adv.* **5**, eaau7378 (2019).

92. Khodagholy, D. *et al.* Organic electronics for high-resolution electrocorticography of the human brain. *Sci. Adv.* **2**, e1601027 (2016).

93. Rivnay, J. *et al.* Organic electrochemical transistors. *Nat. Rev. Mater.* **3**, 17086 (2018).

94. Jonas, F. *et al.* Polythiophenes, process for their preparation and their use. (1989).

95. Groenendaal, L., Jonas, F., Freitag, D., Pielartzik, H. & Reynolds, J. R. Poly(3,4-ethylenedioxythiophene) and Its Derivatives: Past, Present, and Future. *Adv. Mater.* **12**, 481–494 (2000).

96. Rivnay, J. *et al.* Structural control of mixed ionic and electronic transport in conducting polymers. *Nat. Commun.* **7**, 11287 (2016).

97. Giridharagopal, R. *et al.* Electrochemical strain microscopy probes morphology-induced variations in ion uptake and performance in organic electrochemical transistors. *Nat. Mater.* **16**, 1–6 (2017).

98. Zeglio, E. & Inganäs, O. Active Materials for Organic Electrochemical Transistors. *Adv. Mater.* **30**, 1800941 (2018).

99. Moser, M., Ponder, J. F., Wadsworth, A., Giovannitti, A. & McCulloch, I. Materials in Organic Electrochemical Transistors for Bioelectronic Applications: Past, Present, and Future. *Adv. Funct. Mater.* **29**, 1807033 (2019).

100. Keyes, R. W. Physical limits of silicon transistors and circuits. *Reports Prog. Phys.* **68**, 2701–2746 (2005).

101. Tsumura, A., Koezuka, H. & Ando, T. Macromolecular electronic device: Field-effect transistor with a polythiophene thin film. *Appl. Phys. Lett.* **49**, 1210–1212 (1986).

102. Koezuka, H., Tsumura, A. & Ando, T. Field-effect transistor with polythiophene thin film. *Synth. Met.* **18**, 699–704 (1987).

103. Horowitz, G. Organic Field-Effect Transistors. *Adv. Mater.* **10**, 365–377 (1998).

104. Allard, S., Forster, M., Souharce, B., Thiem, H. & Scherf, U. Organic Semiconductors for Solution-Processable Field-Effect Transistors (OFETs). *Angew. Chemie Int. Ed.* **47**, 4070–4098 (2008).

105. Letizia, J. A. *et al.* n-channel polymers by design: Optimizing the interplay of solubilizing substituents, crystal packing, and field-effect transistor characteristics in polymeric bithiophene-imide semiconductors. *J. Am. Chem. Soc.* **130**, 9679–9694 (2008).

106. Facchetti, A. π-Conjugated polymers for organic electronics and photovoltaic cell applications. *Chem. Mater.* **23**, 733–758 (2011).

107. Singh, T. B. *et al.* High-Performance Ambipolar Pentacene Organic Field-Effect Transistors on Poly(vinyl alcohol) Organic Gate Dielectric. *Adv. Mater.* **17**, 2315–2320 (2005).

108. Veres, J., Ogier, S., Lloyd, G. & De Leeuw, D. Gate insulators in organic field-effect transistors. *Chem. Mater.* **16**, 4543–4555 (2004).

109. Hallani, R. K. *et al.* Low-Temperature Cross-Linking Benzocyclobutene Based Polymer Dielectric for Organic Thin Film Transistors on Plastic Substrates. *J. Org. Chem.* **85**, 277–283 (2020).

110. Paterson, A. F. *et al.* Recent Progress in High-Mobility Organic Transistors: A Reality Check. *Adv. Mater.* **30**, 1801079 (2018).

111. Yang, J., Zhao, Z., Wang, S., Guo, Y. & Liu, Y. Insight into High-Performance Conjugated Polymers for Organic Field-Effect Transistors. *Chem* **4**, 2748–2785 (2018).

112. Kim, J.-H. J. J.-S. *et al.* Naphthalene Diimide Copolymers by Direct Arylation Polycondensation as Highly Stable Supercapacitor Electrode Materials. *Macromolecules* **51**, 954–965 (2018).

113. Kim, S. H. *et al.* Electrolyte-Gated Transistors for Organic and Printed Electronics.

Adv. Mater. **25**, 1822–1846 (2013).

114. Braga, D., Ha, M., Xie, W. & Frisbie, C. D. Ultralow contact resistance in electrolyte-gated organic thin film transistors. *Appl. Phys. Lett.* **97**, 193311 (2010).

115. White, H. S., Kittlesen, G. P. & Wrighton, M. S. Chemical Derivatization of an Array of Three Gold Microelectrodes with Polypyrrole : Fabrication of a Molecule-Based Transistor. *J. Am. Chem. Soc.* **106**, 5375–5377 (1984).

116. Giovannitti, A. *et al.* The Role of the Side Chain on the Performance of N-type Conjugated Polymers in Aqueous Electrolytes. *Chem. Mater.* **30**, 2945–2953 (2018).

117. Rivnay, J. *et al.* High-performance transistors for bioelectronics through tuning of channel thickness. *Sci. Adv.* **1**, e1400251 (2015).

118. Bredas, J. L. & Street, G. B. Polarons, Bipolarons, and Solitons in Conducting Polymers. *Acc. Chem. Res.* **18**, 309–315 (1985).

119. Flagg, L. Q. *et al.* Polymer Crystallinity Controls Water Uptake in Glycol Side-Chain Polymer Organic Electrochemical Transistors. *J. Am. Chem. Soc.* **141**, 4345–4354 (2019).

120. Stavrinidou, E. *et al.* Direct Measurement of Ion Mobility in a Conducting Polymer. *Adv. Mater.* **25**, 4488–4493 (2013).

121. Bernards, D. A. & Malliaras, G. G. Steady-state and transient behavior of organic electrochemical transistors. *Adv. Funct. Mater.* **17**, 3538–3544 (2007).

122. Inal, S., Malliaras, G. G. & Rivnay, J. Benchmarking organic mixed conductors. *Nat. Commun.* **8**, 1767 (2017).

123. Khodagholy, D. *et al.* In vivo recordings of brain activity using organic transistors. *Nat. Commun.* **4**, 1575 (2013).

124. Zeglio, E. *et al.* Conjugated Polyelectrolyte Blends for Electrochromic and Electrochemical Transistor Devices. *Chem. Mater.* **27**, 6385–6393 (2015).

125. Moser, M. *et al.* Polaron Delocalization in Donor–Acceptor Polymers and its Impact on Organic Electrochemical Transistor Performance. *Angew. Chemie Int. Ed.* **60**, 7777–7785 (2021).

126. Wang, Y. *et al.* Hybrid Alkyl–Ethylene Glycol Side Chains Enhance Substrate Adhesion and Operational Stability in Accumulation Mode Organic Electrochemical Transistors. *Chem. Mater.* **31**, 9797–9806 (2019).

127. Paulsen, B. D., Tybrandt, K., Stavrinidou, E. & Rivnay, J. Organic mixed ionic–electronic conductors. *Nat. Mater.* **19**, 13–26 (2020).

128. Lill, A. T. *et al.* Organic Electrochemical Transistors Based on the Conjugated Polyelectrolyte PCPDTBT-SO3K (CPE-K). *Adv. Mater.* **1908120**, 1–9 (2020).

129. Schmode, P. *et al.* High-Performance Organic Electrochemical Transistors Based on Conjugated Polyelectrolyte Copolymers. *Chem. Mater.* **31**, 5286–5295 (2019).

130. Marks, A., Griggs, S., Gasparini, N. & Moser, M. Organic Electrochemical Transistors: An Emerging Technology for Biosensing. *Adv. Mater. Interfaces* **9**, 2102039 (2022).

131. Nilsson, D. *et al.* Bi-stable and Dynamic Current Modulation in Electrochemical Organic Transistors. *Adv. Mater.* **14**, 51–54 (2002).

132. Takano, T., Masunaga, H., Fujiwara, A., Okuzaki, H. & Sasaki, T. PEDOT Nanocrystal in Highly Conductive PEDOT:PSS Polymer Films. *Macromolecules* **45**, 3859–3865 (2012).

133. Keene, S. T. *et al.* Enhancement-Mode PEDOT:PSS Organic Electrochemical Transistors Using Molecular De-Doping. *Adv. Mater.* **32**, 2000270 (2020).

134. Inal, S. *et al.* A High Transconductance Accumulation Mode Electrochemical Transistor. *Adv. Mater.* **26**, 7450–7455 (2014).

135. Hallani, R. K. *et al.* Regiochemistry-Driven Organic Electrochemical Transistor Performance Enhancement in Ethylene Glycol-Functionalized Polythiophenes. *J. Am. Chem. Soc.* **143**, 11007–11018 (2021).

136. Moser, M. *et al.* Controlling Electrochemically Induced Volume Changes in Conjugated Polymers by Chemical Design: from Theory to Devices. *Adv. Funct. Mater.* **31**, 2100723 (2021).

137. Giovannitti, A. *et al.* Energetic Control of Redox-Active Polymers toward Safe Organic Bioelectronic Materials. *Adv. Mater.* **32**, 1908047 (2020).

138. Maria, I. P. *et al.* The Effect of Alkyl Spacers on the Mixed Ionic-Electronic Conduction Properties of N-Type Polymers. *Adv. Funct. Mater.* **31**, 2008718 (2021).

139. Ohayon, D. *et al.* Influence of Side Chains on the n-Type Organic Electrochemical Transistor Performance. *ACS Appl. Mater. Interfaces* **13**, 4253–4266 (2021).

140. Maria, I. P. *et al.* Enhancing the Backbone Coplanarity of n-Type Copolymers for Higher Electron Mobility and Stability in Organic Electrochemical Transistors. *Chem. Mater.* **34**, 8593–8602 (2022).

141. Surgailis, J. *et al.* Mixed Conduction in an N-Type Organic Semiconductor in the Absence of Hydrophilic Side-Chains. *Adv. Funct. Mater.* 2010165 (2021) doi:10.1002/adfm.202010165.

142. Tang, H. *et al.* A solution-processed n-type conducting polymer with ultrahigh conductivity. *Nat. 2022* 1–2 (2022) doi:10.1038/s41586-022-05295-8.

143. Wang, Y. *et al.* Green Synthesis of Lactone-Based Conjugated Polymers for n-Type Organic Electrochemical Transistors. *Adv. Funct. Mater.* 2111439 (2022) doi:10.1002/ADFM.202111439.

144. Wu, H. *et al.* Influence of Molecular Weight on the Organic Electrochemical Transistor Performance of Ladder-Type Conjugated Polymers. *Adv. Mater.* **34**, 2106235 (2022).

145. Arnold, F. E. & Van Deusen, R. L. Preparation and Properties of High Molecular Weight, Soluble Oxobenz[de]imidazobenzimidazoisoquinoline Ladder Polymer. *Macromolecules* **2**, 497–502 (1969).

146. Sun, H. *et al.* Complementary Logic Circuits Based on High-Performance n-Type Organic Electrochemical Transistors. *Adv. Mater.* **30**, 1704916 (2018).

147. Sun, H., Gerasimov, J., Berggren, M. & Fabiano, S. N-Type organic electrochemical

transistors: Materials and challenges. *J. Mater. Chem. C* **6**, 11778–11784 (2018).

148. Moser, M. *et al.* Ethylene Glycol-Based Side Chain Length Engineering in Polythiophenes and its Impact on Organic Electrochemical Transistor Performance. *Chem. Mater.* **32**, 6618–6628 (2020).

149. Elasser, A. & Chow, T. P. Silicon carbide benefits and advantages for power electronics circuits and systems. *Proc. IEEE* **90**, 969–986 (2002).

150. Pappa, A. M. *et al.* Direct metabolite detection with an n-type accumulation mode organic electrochemical transistor. *Sci. Adv.* **4**, eaat0911 (2018).

151. Li, W., Jin, J., Xiong, T., Yu, P. & Mao, L. Fast-Scanning Potential-Gated Organic Electrochemical Transistors for Highly Sensitive Sensing of Dopamine in Living Rat Brain. *Angew. Chemie* **134**, (2022).

152. van de Burgt, Y. *et al.* A non-volatile organic electrochemical device as a low-voltage artificial synapse for neuromorphic computing. *Nat. Mater.* **16**, 414–418 (2017).

153. Gkoupidenis, P., Koutsouras, D. A. & Malliaras, G. G. Neuromorphic device architectures with global connectivity through electrolyte gating. *Nat. Commun.* **8**, 15448 (2017).

154. Tybrandt, K., Kollipara, S. B. & Berggren, M. Organic electrochemical transistors for signal amplification in fast scan cyclic voltammetry. *Sensors Actuators, B Chem.* **195**, 651–656 (2014).

155. Wustoni, S. *et al.* Membrane-Free Detection of Metal Cations with an Organic Electrochemical Transistor. *Adv. Funct. Mater.* **29**, 1904403 (2019).

156. Pierre, A., Doris, S. E., Lujan, R. & Street, R. A. Monolithic Integration of Ion-Selective Organic Electrochemical Transistors with Thin Film Transistors on Flexible Substrates. *Adv. Mater. Technol.* **4**, 1800577 (2019).

157. Zhang, L. *et al.* Highly selective and sensitive sensor based on an organic electrochemical transistor for the detection of ascorbic acid. *Biosens. Bioelectron.* **100**, 235–241 (2018).

158. Pappa, A.-M. *et al.* Organic Transistor Arrays Integrated with Finger-Powered Microfluidics for Multianalyte Saliva Testing. *Adv. Healthc. Mater.* **5**, 2295–2302 (2016).

159. Rivnay, J. *et al.* Organic electrochemical transistors for cell-based impedance sensing. *Appl. Phys. Lett.* **106**, 043301 (2015).

160. Hempel, F. *et al.* PEDOT:PSS organic electrochemical transistors for electrical cell-substrate impedance sensing down to single cells. *Biosens. Bioelectron.* **180**, 113101 (2021).

161. Ohayon, D. *et al.* Biofuel powered glucose detection in bodily fluids with an n-type conjugated polymer. *Nat. Mater.* **19**, 456–463 (2020).

162. Rashid, R. B. *et al.* Ambipolar inverters based on cofacial vertical organic electrochemical transistor pairs for biosignal amplification. *Sci. Adv.* **7**, eabh1055 (2021).

163. Qing, X. *et al.* Wearable Fiber-Based Organic Electrochemical Transistors as a

Platform for Highly Sensitive Dopamine Monitoring. *ACS Appl. Mater. Interfaces* **11**, 13105–13113 (2019).

164. Coppedè, N. *et al.* Human stress monitoring through an organic cotton-fiber biosensor. *J. Mater. Chem. B* **2**, 5620–5626 (2014).

165. Keene, S. T. *et al.* Wearable Organic Electrochemical Transistor Patch for Multiplexed Sensing of Calcium and Ammonium Ions from Human Perspiration. *Adv. Healthc. Mater.* **8**, 1901321 (2019).

166. Parlak, O., Keene, S. T., Marais, A., Curto, V. F. & Salleo, A. Molecularly selective nanoporous membrane-based wearable organic electrochemical device for noninvasive cortisol sensing. *Sci. Adv.* **4**, (2018).

167. Li, H., Kim, F. S., Ren, G. & Jenekhe, S. A. High-mobility n-type conjugated polymers based on electron-deficient tetraazabenzodifluoranthene diimide for organic electronics. *J. Am. Chem. Soc.* **135**, 14920–14923 (2013).

168. De Leeuw, D. M., Simenon, M. M. J., Brown, A. R. & Einerhand, R. E. F. Stability of n-type doped conducting polymers and consequences for polymeric microelectronic devices. *Synth. Met.* **87**, 53–59 (1997).

169. Di Pietro, R., Fazzi, D., Kehoe, T. B. & Sirringhaus, H. Spectroscopic Investigation of Oxygen- and Water-Induced Electron Trapping and Charge Transport Instabilities in n-type Polymer Semiconductors. *J. Am. Chem. Soc.* **134**, 14877–14889 (2012).

170. Sudakov, I. *et al.* The Interplay of Stability between Donor and Acceptor Materials in a Fullerene-Free Bulk Heterojunction Solar Cell Blend. *Adv. Energy Mater.* **10**, 2002095 (2020).

171. Usta, H. *et al.* Design, synthesis, and characterization of ladder-type molecules and polymers. air-stable, solution-processable n-channel and ambipolar semiconductors for thin-film transistors via experiment and theory. *J. Am. Chem. Soc.* **131**, 5586–5608 (2009).

172. Zhan, X. *et al.* Rylene and Related Diimides for Organic Electronics. *Adv. Mater.* **23**, 268–284 (2011).

173. Savva, A. *et al.* Solvent Engineering for High-Performance n-Type Organic Electrochemical Transistors. *Adv. Electron. Mater.* **5**, 1900249 (2019).

174. Flagg, L. Q., Giridharagopal, R., Guo, J. & Ginger, D. S. Anion-Dependent Doping and Charge Transport in Organic Electrochemical Transistors. *Chem. Mater.* **30**, 5380–5389 (2018).

175. Cendra, C. *et al.* Role of the Anion on the Transport and Structure of Organic Mixed Conductors. *Adv. Funct. Mater.* **29**, 1807034 (2019).

176. Guardado, J. O. & Salleo, A. Structural Effects of Gating Poly(3-hexylthiophene) through an Ionic Liquid. *Adv. Funct. Mater.* **27**, 1701791 (2017).

177. Savva, A. *et al.* Influence of Water on the Performance of Organic Electrochemical Transistors. *Chem. Mater.* **31**, 927–937 (2019).

178. Savva, A. *et al.* Balancing Ionic and Electronic Conduction for High-Performance Organic Electrochemical Transistors. *Adv. Funct. Mater.* **30**, 1907657 (2020).

179. Brinkmann, M. & Rannou, P. Molecular Weight Dependence of Chain Packing and Semicrystalline Structure in Oriented Films of Regioregular Poly(3-hexylthiophene) Revealed by High-Resolution Transmission Electron Microscopy. *Macromolecules* **42**, 1125–1130 (2009).

180. Khan, J. I. *et al.* P3HT Molecular Weight Determines the Performance of P3HT:O-IDTBR Solar Cells. *Sol. RRL* **3**, 1900023 (2019).

181. Liu, F. *et al.* Molecular Weight Dependence of the Morphology in P3HT:PCBM Solar Cells. *Appl. Mater. Interfaces Interfaces* **6**, 19876−19887 (2014).

182. Zen, A. *et al.* Effect of Molecular Weight and Annealing of Poly(3-hexylthiophene)s on the Performance of Organic Field-Effect Transistors. *Adv. Funct. Mater.* **14**, 757–764 (2004).

183. Kline, R. J., McGehee, M. D., Kadnikova, E. N., Liu, J. & Fréchet, J. M. J. Controlling the Field-Effect Mobility of Regioregular Polythiophene by Changing the Molecular Weight. *Adv. Mater.* **15**, 1519–1522 (2003).

184. Bracher, C. *et al.* The effect of residual palladium catalyst on the performance and stability of PCDTBT:PC70BM organic solar cells. *Org. Electron.* **27**, 266–273 (2015).

185. Koch, F. P. V. *et al.* The impact of molecular weight on microstructure and charge transport in semicrystalline polymer semiconductors–poly(3-hexylthiophene), a model study. *Prog. Polym. Sci.* **38**, 1978–1989 (2013).

186. Kosco, J. *et al.* The Effect of Residual Palladium Catalyst Contamination on the Photocatalytic Hydrogen Evolution Activity of Conjugated Polymers. *Adv. Energy Mater.* **8**, 1802181 (2018).

187. Troshin, P. A. *et al.* Impedance Measurements as a Simple Tool to Control the Quality of Conjugated Polymers Designed for Photovoltaic Applications. *Adv. Funct. Mater.* **20**, 4351–4357 (2010).

188. Kroon, R. *et al.* Polar Side Chains Enhance Processability, Electrical Conductivity, and Thermal Stability of a Molecularly p-Doped Polythiophene. *Adv. Mater.* **29**, 1700930 (2017).

189. Guo, X. & Watson, M. D. Conjugated polymers from naphthalene bisimide. *Org. Lett.* **10**, 5333–5336 (2008).

190. Liu, J., Loewe, R. S. & McCullough, R. D. Employing MALDI-MS on Poly(alkylthiophenes): Analysis of Molecular Weights, Molecular Weight Distributions, End-Group Structures, and End-Group Modifications. *Macromolecules* **32**, 5777–5785 (1999).

191. Moser, M. *et al.* Propylene and butylene glycol: new alternatives to ethylene glycol in conjugated polymers for bioelectronic applications. *Mater. Horizons* **9**, 973–980 (2022).

192. Feng, K. *et al.* Fused Bithiophene Imide Dimer-Based n-Type Polymers for High-Performance Organic Electrochemical Transistors. *Angew. Chemie Int. Ed.* **60**, 24198–24205 (2021).

193. Savagian, L. R. *et al.* Balancing Charge Storage and Mobility in an Oligo(Ether) Functionalized Dioxythiophene Copolymer for Organic- and Aqueous- Based

Electrochemical Devices and Transistors. *Adv. Mater.* **30**, 1804647 (2018).

194. Shin, Y. H. *et al.* Synthesis and Aggregation Behavior of a Glycolated Naphthalene Diimide Bithiophene Copolymer for Application in Low-Level n-Doped Organic Thermoelectrics. *Macromolecules* **53**, 5158–5168 (2020).

195. Jeong, D. *et al.* High-Performance n -Type Organic Electrochemical Transistors Enabled by Aqueous Solution Processing of Amphiphilicity-Driven Polymer Assembly. *Adv. Funct. Mater.* **32**, 2111950 (2022).

196. Gross, Y. M. & Ludwigs, S. P(NDI2OD-T2) revisited – Aggregation control as key for high performance n-type applications. *Synth. Met.* **253**, 73–87 (2019).

197. Brinkmann, M. *et al.* Segregated versus Mixed Interchain Stacking in Highly Oriented Films of Naphthalene Diimide Bithiophene Copolymers. *ACS Nano* **6**, 10319–10326 (2012).

198. Sachs, M. *et al.* Tracking Charge Transfer to Residual Metal Clusters in Conjugated Polymers for Photocatalytic Hydrogen Evolution. *J. Am. Chem. Soc.* **142**, 14574–14587 (2020).

199. Krebs, F. C., Nyberg, R. B. & Jørgensen, M. Influence of Residual Catalyst on the Properties of Conjugated Polyphenylenevinylene Materials: Palladium Nanoparticles and Poor Electrical Performance. *Chem. Mater.* **16**, 1313–1318 (2004).

200. Michaelson, H. B. The work function of the elements and its periodicity. *J. Appl. Phys.* **48**, 4729–4733 (1977).

201. Gu, D., Dey, S. K. & Majhi, P. Effective work function of Pt, Pd, and Re on atomic layer deposited HfO2. *Appl. Phys. Lett.* **89**, 082907 (2006).

202. Jia, H. *et al.* Engineering donor–acceptor conjugated polymers for high-performance and fast-response organic electrochemical transistors. *J. Mater. Chem. C* **9**, 4927–4934 (2021).

203. Wang, Y. *et al.* The effect of the donor moiety of DPP based polymers on the performance of organic electrochemical transistors. *J. Mater. Chem. C* **9**, 13338–13346 (2021).

204. Luo, X. *et al.* Designing Donor–Acceptor Copolymers for Stable and High-Performance Organic Electrochemical Transistors. *ACS Macro Lett.* **10**, 1061–1067 (2021).

205. Kim, Y. *et al.* Strain-Engineering Induced Anisotropic Crystallite Orientation and Maximized Carrier Mobility for High-Performance Microfiber-Based Organic Bioelectronic Devices. *Adv. Mater.* **33**, 2007550 (2021).

206. Gasperini, A. & Sivula, K. Effects of Molecular Weight on Microstructure and Carrier Transport in a Semicrystalline Poly(thieno)thiophene. *Macromolecules* **46**, 9349–9358 (2013).

207. Björklund, N. *et al.* The effects of metal impurities in poly[(2,5-bis(3-decylthiophen-2-yl)thieno[2,3-b]thiophene] on field-effect transistor properties. *Org. Electron.* **10**, 215–221 (2009).

208. Brixi, S. *et al.* Air and temperature sensitivity of n-type polymer materials to meet and

exceed the standard of N2200. *Sci. Rep.* **10**, 4014 (2020).

209. Jones, B. A., Facchetti, A., Wasielewski, M. R. & Marks, T. J. Tuning orbital energetics in arylene diimide semiconductors. Materials design for ambient stability of n-type charge transport. *J. Am. Chem. Soc.* **129**, 15259–15278 (2007).

210. Quinn, J. T. E., Zhu, J., Li, X., Wang, J. & Li, Y. Recent progress in the development of n-type organic semiconductors for organic field effect transistors. *J. Mater. Chem. C* **5**, 8654–8681 (2017).

211. Griggs, S. *et al.* The effect of residual palladium on the performance of organic electrochemical transistors. *Nat. Commun.* **13**, 7964 (2022).

212. Geng, Y. *et al.* A theoretical discussion on the relationships among molecular packings, intermolecular interactions, and electron transport properties for naphthalene tetracarboxylic diimide derivatives. *J. Mater. Chem.* **21**, 15558–15566 (2011).

213. Chua, L. L. *et al.* General observation of n-type field-effect behaviour in organic semiconductors. *Nature* **434**, 194–199 (2005).

214. Zhang, L., Colella, N. S., Cherniawski, B. P., Mannsfeld, S. C. B. & Briseno, A. L. Oligothiophene semiconductors: Synthesis, characterization, and applications for organic devices. *ACS Appl. Mater. Interfaces* **6**, 5327–5343 (2014).

215. Shi, S. *et al.* Ultranarrow Bandgap Naphthalenediimide-Dialkylbifuran-Based Copolymers with High-Performance Organic Thin-Film Transistors and All-Polymer Solar Cells. *Macromol. Rapid Commun.* **41**, 2000144 (2020).

216. Liu, G., Xiao, C., Negri, F., Li, Y. & Wang, Z. Dodecatwistarene Imides with Zigzag-Twisted Conformation for Organic Electronics. *Angew. Chemie* **132**, 2024–2028 (2020).

217. Ly, J. T. *et al.* Efficient Electron Mobility in an All-Acceptor Napthalenediimide-Bithiazole Polymer Semiconductor with Large Backbone Torsion. *ACS Appl. Mater. Interfaces* **10**, 40070–40077 (2018).

218. Livi, F. *et al.* Influence of Side Chain Position on the Electrical Properties of Organic Solar Cells Based on Dithienylbenzothiadiazole-alt-phenylene Conjugated Polymers. *Macromolecules* **48**, 3481–3492 (2015).

219. Gu, C. *et al.* Optical, electrochemical, and photovoltaic properties of conjugated polymers with dithiafulvalene as side chains. *J. Appl. Polym. Sci.* **132**, 41508 (2015).

220. Alsalme, A. M., Alghamdi, A. A. B., Alhamdani, A. A. G. Q. & Iraqi, A. Synthesis and Properties of Alternating Vinylene-Benzothiadiazole-Based Copolymers with Carbazole and Fluorene Derivatives for Photovoltaic Applications. *Int. J. Electrochem. Sci.* **9**, 1920–1941 (2014).

221. Kuang, C., Yang, Q., Senboku, H. & Tokuda, M. Stereoselective Synthesis of (E)-β-Arylvinyl Bromides by Microwave-Induced Hunsdiecker-Type Reaction. *Synthesis (Stuttg).* 1319–1325 (2005) doi:10.1055/s-2005-865283.

222. Usta, H. *et al.* Perfluoroalkyl-Functionalized Thiazole–Thiophene Oligomers as N-Channel Semiconductors in Organic Field-Effect and Light-Emitting Transistors. *Chem. Mater.* **26**, 6542–6556 (2014).

223. Liu, D. *et al.* Design of wide-bandgap polymers with deeper ionization potential enables efficient ternary non-fullerene polymer solar cells with 13% efficiency. *J. Mater. Chem. A* **7**, 14153–14162 (2019).

224. Wunderlich, S. H. & Knochel, P. (tmp)2Zn·2 MgCl2·2 LiCl: A Chemoselective Base for the Directed Zincation of Sensitive Arenes and Heteroarenes. *Angew. Chemie Int. Ed.* **46**, 7685–7688 (2007).

225. Varma, R. S. Solvent-free organic syntheses. *Green Chem.* **1**, 43–55 (1999).

226. Onitsuka, S., Jin, Y. Z., Shaikh, A. C., Furuno, H. & Inanaga, J. Silica Gel-Mediated Organic Reactions under Organic Solvent-Free Conditions. *Molecules* **17**, 11469–11483 (2012).

227. Seetula, J. A. Catalytic bromination of anthracene on silica gel. *J. Mol. Catal. A Chem.* **231**, 153–159 (2005).

228. Mohan Reddy, B., Venkata Ramana Kumar, V., Chinna Gangi Reddy, N. & Mahender Rao, S. Silica gel catalyzed α-bromination of ketones using N-bromosuccinimide: An easy and rapid method. *Chinese Chem. Lett.* **25**, 179–182 (2014).

229. Polander, L. E. *et al.* Stannyl derivatives of naphthalene diimides and their use in oligomer synthesis. *Org. Lett.* **14**, 918–921 (2012).

230. Sawadjoon, S., Orthaber, A., Sjöberg, P. J. R., Eriksson, L. & Samec, J. S. M. Equilibrium study of Pd(dba)2 and P(OPh)3 in the Pd-catalyzed allylation of aniline by allyl alcohol. *Organometallics* **33**, 249–253 (2014).

231. Donaldson, J. D. & Grimes, S. M. The inorganic chemistry of tin. in *Chemistry of Tin* 10 (Springer Netherlands, 1998). doi:10.1007/978-94-011-4938-9_3.

232. Bulfield, D. & Huber, S. M. Synthesis of Polyflourinated Biphenyls; Pushing the Boundaries of Suzuki–Miyaura Cross Coupling with Electron-Poor Substrates. *J. Org. Chem.* **82**, 13188–13203 (2017).

233. Lyall, C. L., Shotton, C. C., Pérez-Salvia, M., Pantoş, G. D. & Lewis, S. E. Direct core functionalisation of naphthalenediimides by iridium catalysed C–H borylation. *Chem. Commun.* **50**, 13837–13840 (2014).

234. Wang, S. *et al.* A Chemically Doped Naphthalenediimide-Bithiazole Polymer for n-Type Organic Thermoelectrics. *Adv. Mater.* **30**, 1–6 (2018).

235. Alsufyani, M. *et al.* Lactone Backbone Density in Rigid Electron-Deficient Semiconducting Polymers Enabling High n-type Organic Thermoelectric Performance. *Angew. Chemie Int. Ed.* **61**, (2022).

236. Bi, Z., Naveed, H. B., Mao, Y., Yan, H. & Ma, W. Importance of Nucleation during Morphology Evolution of the Blade-Cast PffBT4T-2OD-Based Organic Solar Cells. *Macromolecules* **51**, 6682–6691 (2018).

237. Österholm, A. M., Ponder, J. F., De Keersmaecker, M., Shen, D. E. & Reynolds, J. R. Disentangling Redox Properties and Capacitance in Solution-Processed Conjugated Polymers. *Chem. Mater.* **31**, 2971–2982 (2019).

238. Heinze, J., Frontana-Uribe, B. A. & Ludwigs, S. Electrochemistry of Conducting Polymers—Persistent Models and New Concepts. *Chem. Rev.* **110**, 4724–4771 (2010).

239. Trefz, D. *et al.* Electrochemical Investigations of the N-Type Semiconducting Polymer P(NDI2OD-T2) and Its Monomer: New Insights in the Reduction Behavior. *J. Phys. Chem. C* **119**, 22760–22771 (2015).

240. Larsson, O., Laiho, A., Schmickler, W., Berggren, M. & Crispin, X. Controlling the Dimensionality of Charge Transport in an Organic Electrochemical Transistor by Capacitive Coupling. *Adv. Mater.* **23**, 4764–4769 (2011).

241. Ghosh, R. *et al.* Anisotropic Polaron Delocalization in Conjugated Homopolymers and Donor-Acceptor Copolymers. *Chem. Mater.* **31**, 7033–7045 (2019).

242. Arvind, M. *et al.* Quantitative Analysis of Doping-Induced Polarons and Charge-Transfer Complexes of Poly(3-hexylthiophene) in Solution. *J. Phys. Chem. B* **124**, 7694–7708 (2020).

243. Tait, C. E. *et al.* Spin–spin interactions and spin delocalisation in a doped organic semiconductor probed by EPR spectroscopy. *Phys. Chem. Chem. Phys.* **23**, 13827–13841 (2021).

244. Hua, C. *et al.* Through-Space Intervalence Charge Transfer as a Mechanism for Charge Delocalization in Metal–Organic Frameworks. *J. Am. Chem. Soc.* **140**, 6622–6630 (2018).

245. Sirringhaus, H. *et al.* Two-dimensional charge transport in self-organized, high-mobility conjugated polymers. *Nature* **401**, 685–688 (1999).

246. Chang, J. F. *et al.* Molecular-weight dependence of interchain polaron delocalization and exciton bandwidth in high-mobility conjugated polymers. *Phys. Rev. B* **74**, 115318 (2006).

247. Wang, A. *et al.* Solution-Processable Redox-Active Polymers of Intrinsic Microporosity for Electrochemical Energy Storage. *J. Am. Chem. Soc.* **144**, 17198–17208 (2022).

248. Zhou, X. *et al.* Tuning the Charge-Transport Property of Pyromellitic Diimide-Based Conjugated Polymers towards Efficient Field-Effect Transistors. *Asian J. Org. Chem.* **3**, 209–215 (2014).

249. Hashemi, D., Ma, X., Ansari, R., Kim, J. & Kieffer, J. Design principles for the energy level tuning in donor/acceptor conjugated polymers. *Phys. Chem. Chem. Phys.* **21**, 789–799 (2019).

250. Duan, J. *et al.* Highly Efficient Mixed Conduction in N-type Fused Small Molecule Semiconductors. *Adv. Funct. Mater.* **32**, 2203937 (2022).

251. Koklu, A. *et al.* Convection Driven Ultrarapid Protein Detection via Nanobody-Functionalized Organic Electrochemical Transistors. *Adv. Mater.* 2202972 (2022) doi:10.1002/ADMA.202202972.

252. Nehls, B. S. *et al.* Semiconducting Polymers via Microwave-Assisted Suzuki and Stille Cross-Coupling Reactions. *Adv. Funct. Mater.* **14**, 352–356 (2004).

253. Raj, M. R. *et al.* A comparative study on the thermal- and microwave-assisted Stille coupling polymerization of a benzodithiophene-based donor–acceptor polymer (PTB7). *J. Mater. Chem. A* **5**, 3330–3335 (2017).

254. Zhang, Z. & Dubay, K. H. The Sequence of a Step-Growth Copolymer Can Be Influenced by Its Own Persistence Length. *J. Phys. Chem. B* **125**, 3426–3437 (2021).

255. Schmode, P. *et al.* The Key Role of Side Chain Linkage in Structure Formation and Mixed Conduction of Ethylene Glycol Substituted Polythiophenes. *ACS Appl. Mater. Interfaces* **12**, 13029–13039 (2020).

256. Jones, A. L. *et al.* Branched Oligo(ether) Side Chains: A Path to Enhanced Processability and Elevated Conductivity for Polymeric Semiconductors. *Adv. Funct. Mater.* **31**, 2102688 (2021).

257. Zhang, L. & Gong, H. Improvement in flexibility and volumetric performance for supercapacitor application and the effect of Ni–Fe ratio on electrode behaviour. *J. Mater. Chem. A* **3**, 7607–7615 (2015).

258. Zindy, N. *et al.* Pyromellitic Diimide-Based Copolymers and Their Application as Stable Cathode Active Materials in Lithium and Sodium-Ion Batteries. *Chem. Mater.* **30**, 6821–6830 (2018).

259. Biesheuvel, P. M., Porada, S. & Dykstra, J. E. The difference between Faradaic and non-Faradaic electrode processes. (2018).

260. Jiang, Z. GIXSGUI: A MATLAB toolbox for grazing-incidence X-ray scattering data visualization and reduction, and indexing of buried three-dimensional periodic nanostructured films. *J. Appl. Crystallogr.* **48**, 917–926 (2015).

261. Khodagholy, D. *et al.* High transconductance organic electrochemical transistors. *Nat. Commun.* **4**, 2133 (2013).

262. Bi, X., Crum, B. P. & Li, W. Super hydrophobic Parylene-C produced by consecutive O2 and SF6 plasma treatment. *J. Microelectromechanical Syst.* **23**, 628–635 (2014).

Appendix

Functionalisation of organic mixed ionic-electronic polymers for bioelectronic applications

A1 General information and attributions

Polymer **P3-OTs** was synthesised in collaboration with Kate Chamberlain as partial fulfilment of her MChem degree. The OECT characteristics for **P3-OTs** were measured in collaboration with Dr Xiaolei Zhao (McCulloch Group, University of Oxford). Fluorescence was measured by the author with the assistance of Dr Robert Hein (Beer Group, University of Oxford). Cyclic voltammetry in aqueous and organic electrolytes was conducted by the author, other electrochemical and chronoamperometry measurements, as well as OECT characteristics, for **P4** were conducted by Dr David Ohayon (Inal Group, KAUST).

A2 Introduction

Due to the mixed transport of organic mixed ionic-electronic conductors (OMIECs), they are particularly suited to be employed as the channel material in organic electrochemical transistors (OECTs) on account of their low operational voltages and ability to transduce an ionic signal into a "readable" electronic output.[1] The latter property is particularly important as these materials and devices are able to bridge the gap between the ionic signals generated by biological systems with the electronic outputs required for electronic circuits and computational devices. This, combined with the biological compatibility conferred by organic materials, due to their soft nature and ability to operate in a volumetric regime,[2] renders OECTs a promising technology for sensing applications in healthcare settings.[3] However, while this simple conversion process is directly applicable to the amplification of electrophysiological signals,[4–6] it is not applicable to more complex biological phenomena, for example monitoring of metabolic pathways.

One of the most critical requirements for OECT-based biosensors, such as metabolite sensors[7,8] or pathogen detectors,[9,10] is selectivity towards the biomolecule in question. This requires the biofunctionalisation of one of the OECTs components with a specific recognition element.

Currently, the most common OECT biofunctionalisation strategy is biofunctionalisation of the gate electrode.[11–13] Biofunctionalisation of the gate electrode is not ideal given its two-dimensional and indirect sensing nature. This limits the number of sensing units that can be incorporated, and leads to a greater susceptibility towards side reactions.[11] A more convenient biofunctionalisation approach is therefore the biofunctionalisation of the OMIEC itself. To this end, drop-casting of the biofunctionalisation element onto the OMIEC has shown some success,[3] however as the sensing element is not covalently attached to the OMIEC it is prone to surface delamination and consequently the sensing performance decreases or is completely lost. The use of chemical mediators in the electrolyte has also been trialled, however, the often toxic nature of the chemical mediator limits the practical in vivo applications of this approach.[14]

To overcome the aforementioned limitations, this chapter focuses on the functionalisation of the OMIEC itself through post-polymerisation chemistry, leading to the formation of a covalent bond between the biological recognition motif or other sensing aid and the OMIEC.[15] By introducing reactive end groups to the polymer sidechains, it is proposed that a polymer may covalently bond to a range of redox mediators or sensing elements, including enzymes or a single strand of DNA or RNA, otherwise known as an aptamer, which are expected to confer a high degree of selectivity and sensitivity to the device.

Design of a p-type OMIEC for OECT application was based around a field effect transistor (FET) based-biosensors which has been proven to demonstrate selectivity towards serotonin, dopamine and glucose when the associated aptamer was bound to the FET active material.[16] As the aptamer is negatively charged, when it rearranges its conformation to encapsulate the biomolecule, the movement of charge closer to or further from the semiconductor channel alters the transconductance of the device, acting as a sensing event (**Figure A1**). A p-type OMIEC with reactive end groups could allow for this concept to be developed in OECTs,

mimicking this mode of operation, with the aptamer covalently bound to the OECT channel material. A p-type polymer with an attached aptamer that rearranges as per **Figure A1** in the presence of a biomolecule would result in the mobile holes in the OMIEC moving towards the negatively charged aptamer backbone. This would act similarly to aqueous ions in compensating the charges, which may reduce charge carrier mobility as holes become localised near the aptamers or impact the volumetric capacitance by requiring fewer ions in the bulk to compensate the injected charges. In either of these hypothesised scenarios, the transconductance would observe a decrease, which would be recorded as a sensing event.

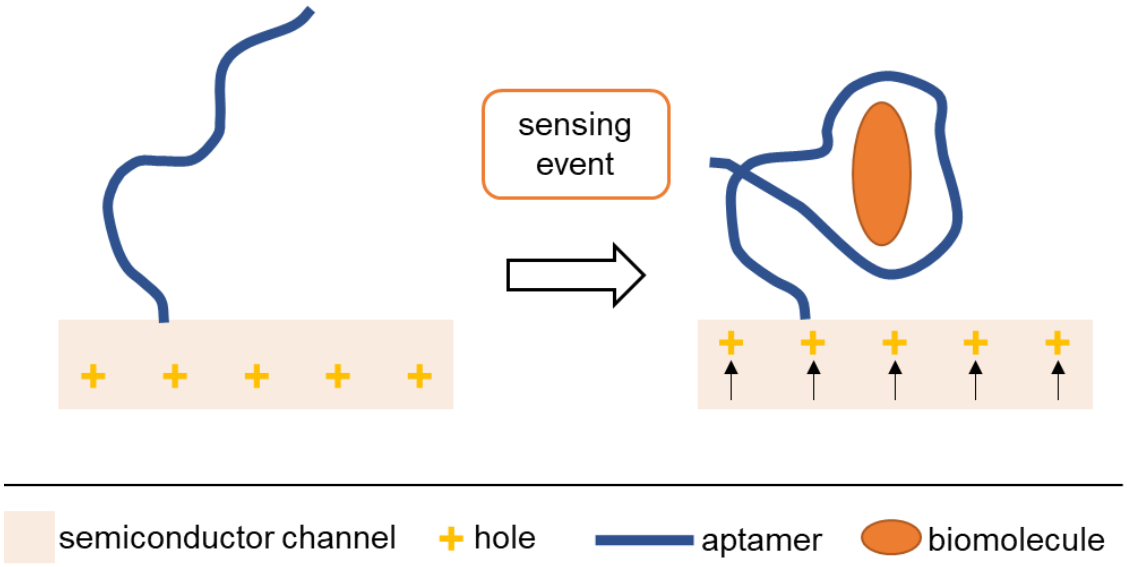


Figure A1. Schematic of the sensing event for a p-type semiconducting channel, whereby the aptamer reorientates to accommodate the specific biomolecule, and the holes in the semiconductor are attracted towards the negatively charged aptamer (single strand of DNA). By using an aptamer, the sensing event only occurs in the presence of the biomolecule for which the aptamer is selective.

Next, an n-type OMIEC with reactive end groups was proposed, such that an electron mediator, for example ferrocene (Fc), could be covalently bonded to the polymer. N-type polymers are particularly favourable for this application as they are able to accept electrons that are generated

by a biological event, such as metabolite sensing using an enzyme. Typically, Fc is dispersed in the aqueous electrolyte,[17] where it is able to shuttle electrons from the gate electrode to the glucose oxidase (GOx) enzyme (**Figure A2**), due to the low redox potentials of the Fc^+/Fc redox couple. However, as ferrocene is biologically toxic, its dispersion in an aqueous electrolyte makes it impractical for safe sensing applications. Instead, it was thought that by covalently attaching it to the OMIEC, it would retain its mediator abilities without harmful diffusion of it into biological systems. Additionally, as ferrocene is not a biomolecule itself, it is more synthetically robust, enabling the use of a wide range of conditions for its attachment. The use of Fc as an electron mediator was initially demonstrated with a Pt gate electrode,[17] but has since been reported with a PEDOT:PSS gate electrode.[14] Whilst PEDOT:PSS is able to undergo volumetric operation, applying it as the gate electrode restricts this to a two dimensional sensing nature. As a proof-of-concept, the designed polymer will first be applied as the gate electrode to mimic the device architecture of those reported in literature,[14] after which optimisation of the device using the functionalisable polymer as the channel can continue.

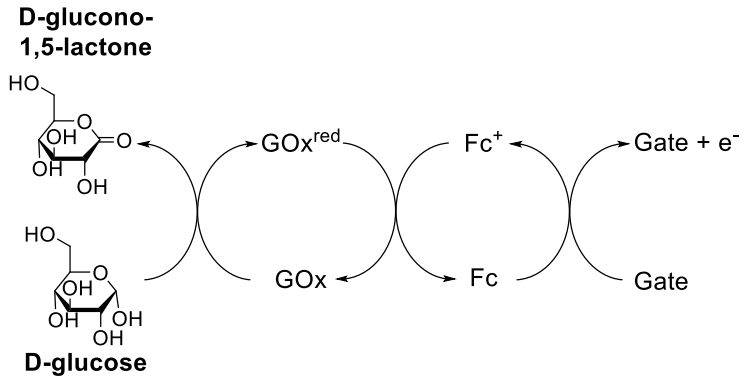


Figure A2. The reaction cycle for the detection of glucose employing glucose oxidase (Gox).[14] The process requires an electron mediator to complete the redox cycle, which can either be O_2/H_2O_2 or ferrocenium /ferrocene (Fc^+/Fc). The use of Fc prevents the formation of toxic hydrogen peroxide.

These concepts are yet to be translated to OECTs, thus this chapter highlights the advantages conferred by post-polymerisation functionalisation of polymers in OECTs. Whilst there is now a small literature precedent for functionalising transistor materials,[18,19] this is yet to be demonstrated on glycolated OMIEC materials. To do this, both a p-type polythiophene and an n-type naphthalene diimide (NDI)-based polymer bearing reactive end groups on the side chains were prepared (**Figure A3**). These end groups can be displaced directly via S_N2, or the reactive end group can be substituted with a more optimal group, such as a maleimide or azide, which is able to undergo Michael addition or "click" chemistry with mild reaction conditions. As biomolecules are often unable to withstand high temperatures, toxic solvents or extreme pH values, these conditions offer biological compatibility, making them ideal for sensing purposes.

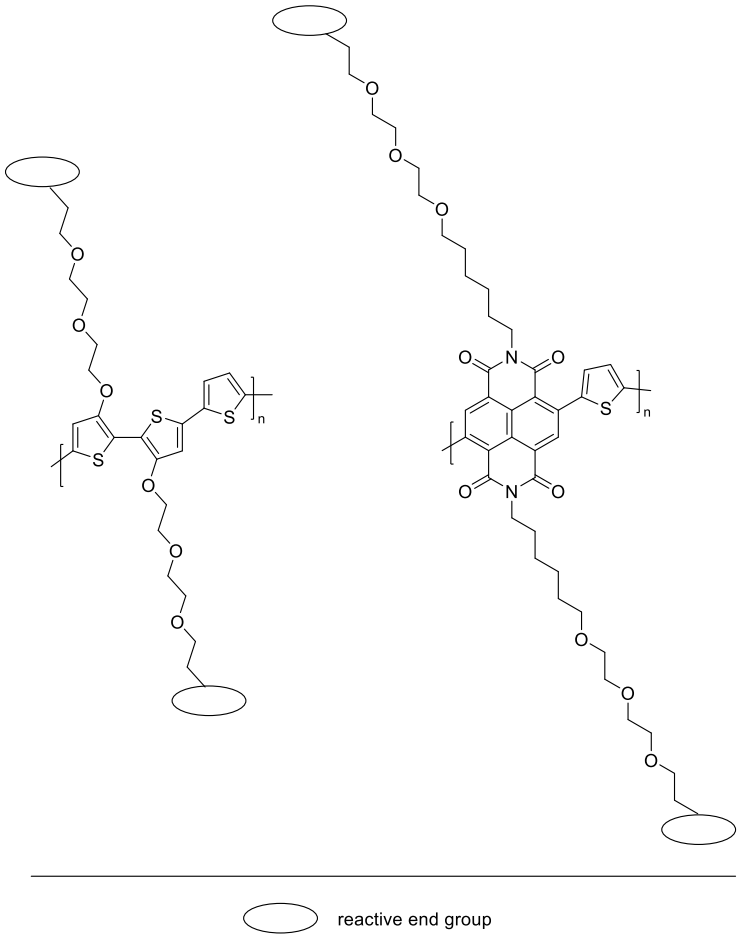


Figure A3. Proposed structures of the functionalisable p-type polythiophene and n-type NDI-based polymers.

A3 P-type functionalisable polymer

A3.1 Synthesis

Efforts towards the synthesis of a p-type polymer with reactive end groups commenced with a target random polythiophene copolymer containing terminal bromide groups on the sidechains (**P1**, **Figure A4**). The rationale for this structure was that the glycolated monomer has previously been reported in literature,[20–23] and the ratio of glycolated to (alkylated) functionalisable monomer could be readily changed to impart sufficient solubility for processing in organic solvents, whilst also controlling the degree of functionalisation that is possible. By selecting a reactive sidechain with an alkoxy group closest to the backbone, it was predicted that the energetics would be minimally affected by the ratio of the two sidechains, as the electron donating oxygen remained adjacent to the backbone in all variations.

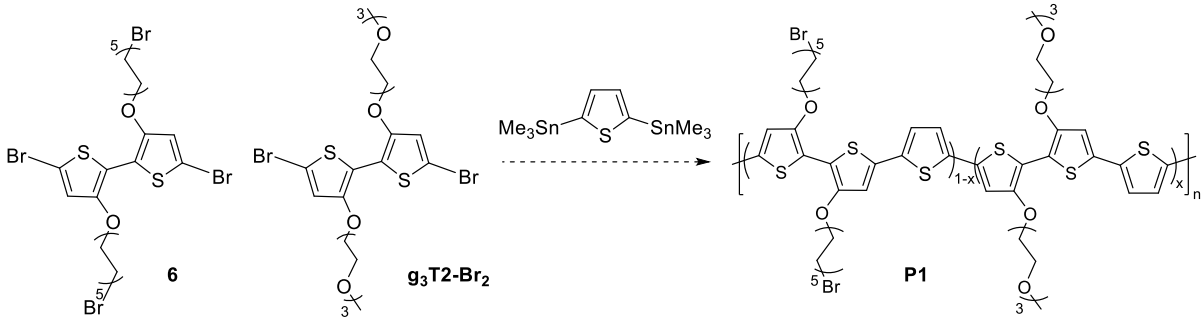


Figure A4. Proposed structure of a random polythiophene copolymer with terminal reactive groups.

The first step required a large excess of 1,10-decanediol (**Figure A5**), in a bid to minimise the disubstitution of thiophene onto a single chain, which was then separated from the product (**1**) by vacuum distillation. The terminal alcohol group was then protected using triisopropylsilyl ether (TIPS) to allow for the bromination and subsequent Ni-mediated coupling of two thiophene units, to reach intermediate **4**. A number of other routes were attempted, including copper chloride and in situ Stille conditions, however despite altering concentrations and

temperatures, optimisation of these routes was not achieved, and the reactions failed. With the bithiophene unit in place, the sidechain termini were deprotected in good yields to regenerate the free alcohol group (**5**). Appel conditions were then attempted to transform the alcohol into a bromide group (**6**), with no success. An alternative route was devised, installing the maleimide unit onto the monomer (**7**), as it is able to directly undergo mild thiol-ene click chemistry (specifically via a Michael addition) with a thiol on the biomolecule, to form a covalent attachment. This reaction was successfully performed on a free alcohol (hexanol) using literature conditions,[24] then the reaction was optimised by performing it in a microwave for one hour, instead of overnight. However, when either of these conditions were employed on the core, the thiophene peaks in the NMR significantly shifted, indicating that the core itself either reacts under these conditions or degrades.

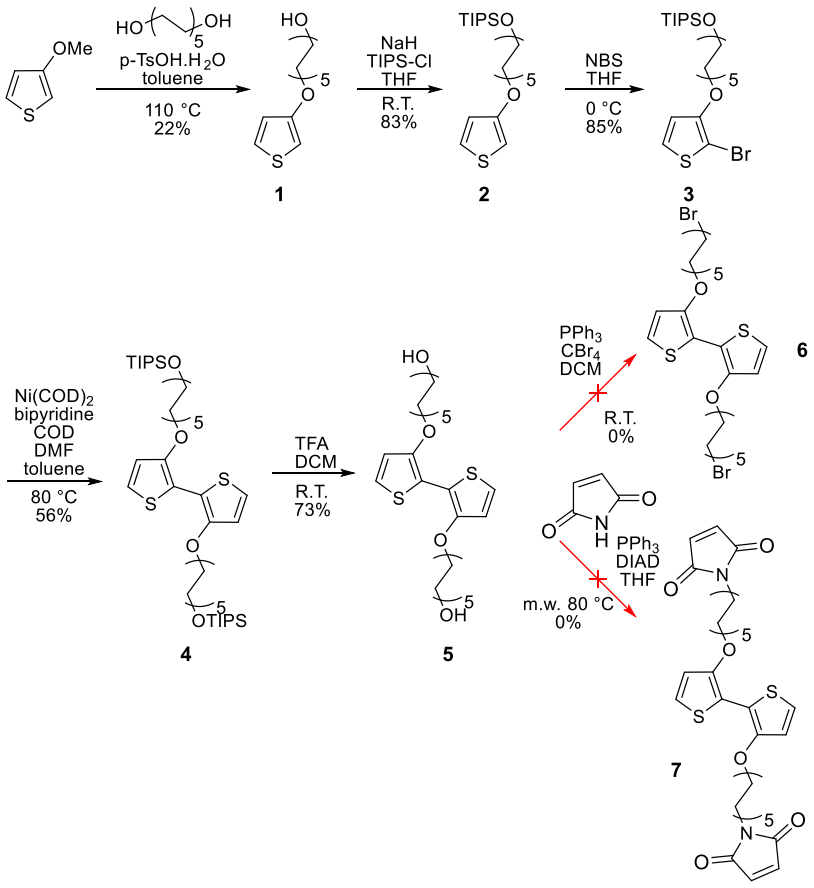


Figure A5. Synthetic routes to the proposed reactive end group monomer.

Initially, an alkylated sidechain was selected to accommodate the reactive end groups for synthetic ease, however after several unsuccessful attempts a new structure was proposed (**P2**, **Figure A6**). The synthetic strategy was adapted to functionalise a glycolated sidechain, thus the only variable became whether the sidechain contained functionality (i.e., only the percentage of reactive end groups changes, rather than also the alkyl:glycol ratio and therefore the hydrophilicity of the polymer).

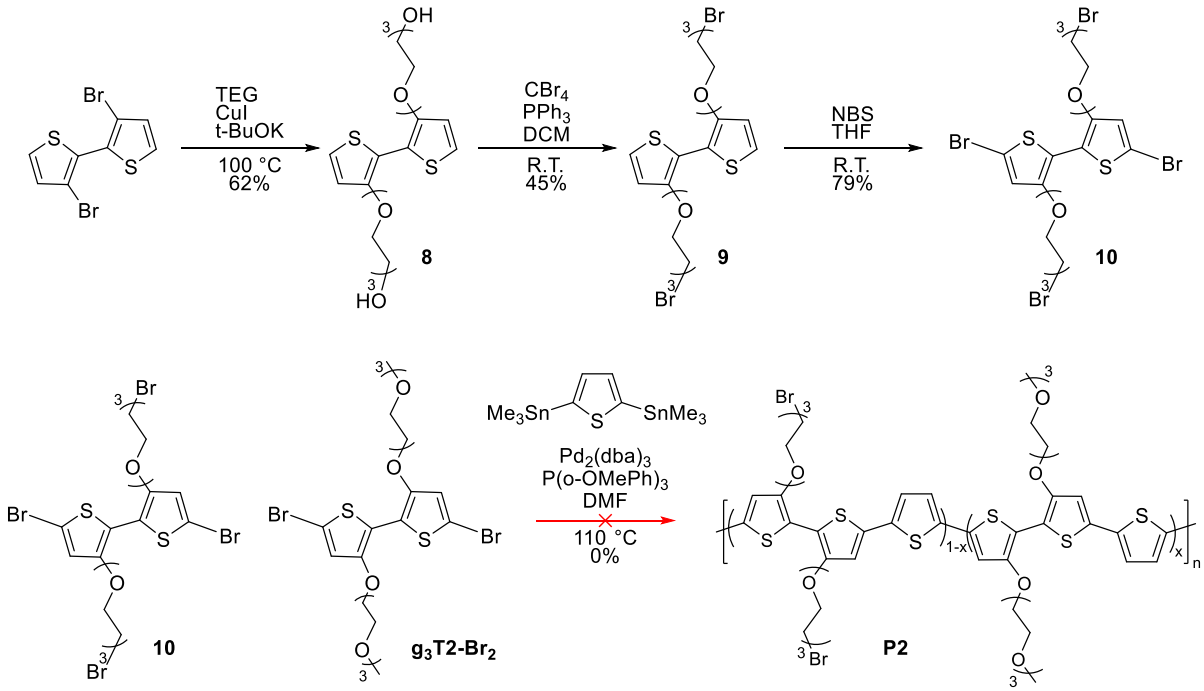


Figure A6. Adapted synthetic route to fully glycolated p-type polymer.

In this case, as the sidechain was added directly to the pre-formed bithiophene core, there was no need for protecting groups, which eliminated two yield-costly steps. Additionally, the Appel conditions worked in moderate yields on the glycolated sidechains, to obtain intermediate **9**. This indicates that perhaps there was either a solubility difference between the two materials which accounts for the difference in reactivity, or the alkylated derivative was not sufficiently purified, such that the Appel reagents were interacting instead with residual by-products. Following a successful bromination to yield the monomer unit, the polymerisation was attempted using five different ratios of the functional monomer (**10**), 0%, 10%, 25%, 50% and

100%. Unfortunately, when the percentage of **10** was increased above 10%, the polymerisation was deemed unsuccessful as it resulted in an insoluble residue which could not be dissolved from the Soxhlet thimble in hot chloroform or chlorobenzene. It was hypothesised that the bromide terminal groups were reducing the solubility of the polymerisation, thus the synthesis depicted in **Figure A6** was reproduced using the longer (and therefore more solubilising) tetraethylene glycol sidechains. Unfortunately, this did not result in a more positive outcome, thus it is likely that instead of the issue being related to inherent solubility, there is a cross-linking, miscoupling or degradation reaction occurring with the brominated termini, which may be light-activated.[25,26] Whilst the 10% derivative appeared soluble, by XPS, there appeared to be no bromide signals, indicating that this polymer is most likely just pure **p(g3T2-T)** (i.e., only **g$_3$T2Br$_2$** polymerised and **10** remained unreacted), and the NMR corroborated this.

The final attempt at introducing reactive end groups onto a p-type polymer was proposed, using tosyl termini (**Figure A7**), rationalising that these do not have literature precedent for undergoing light-activated reactions.[27] The initial step to introduce the glycol chains remained the same, with **8** synthesised in good yields of 62%. The next step involved typical tosylation conditions to transform the relatively unreactive alcohol into a somewhat more reactive tosyl group (**11**), followed by bromination of the 5 and 5' positions to produce the final monomer (**12**). Monomer **12** was then thoroughly purified using column chromatography and carried forward into both a two- and three-monomer Stille polymerisation, using a 1:1 of **12**:bis(trimethylstannyl)thiophene (**P3-OTS-100%**) and a 0.5:0.5:1 ratio of **12**: **g$_3$T2-Br$_2$**:bis(trimethylstannyl)thiophene (**P3-50%**).

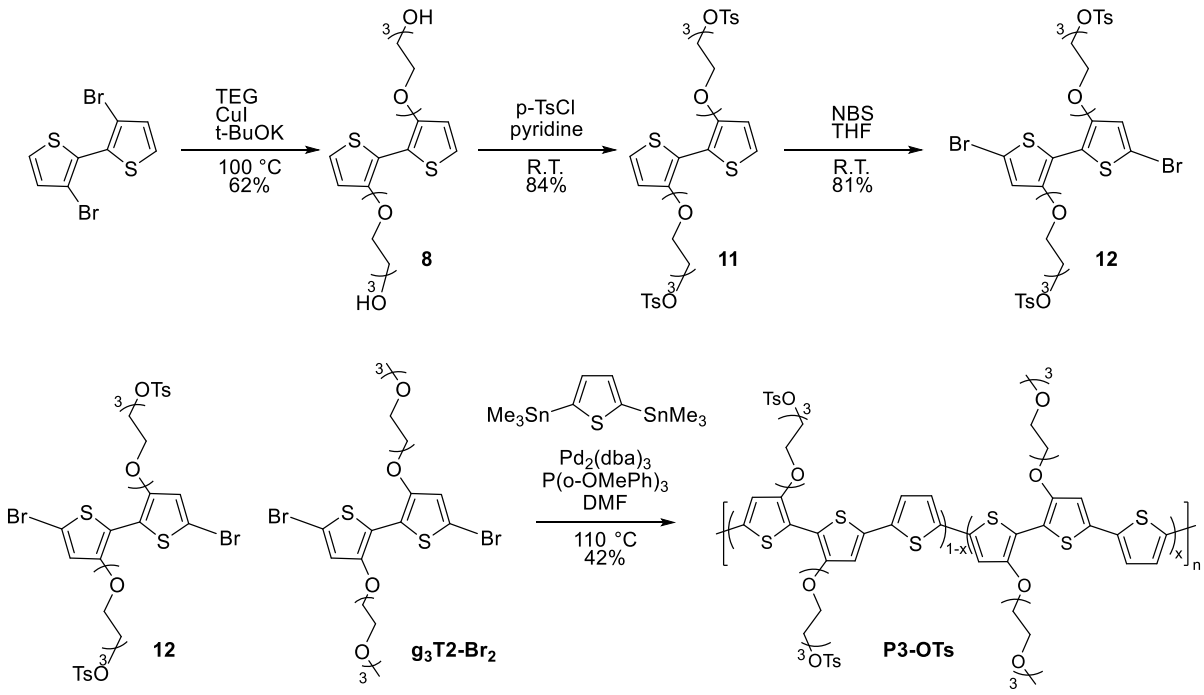


Figure A7. Synthetic route to the proposed tosyl terminated polythiophene-based random copolymer.

The successful synthesis of **P3-OTs-100%** (i.e. where x=0 in **Figure A7**) was indicated by an NMR of the polymer in DMSO-d_6 (**Figure A8**), which clearly depicts the broad peaks associated with the thiophene-based backbone and the glycolated sidechains. Additionally, there are three further sharper peaks, two doublets at 7.59 ppm and 7.12 ppm and a singlet at 2.29 ppm, which align with the tosyl group as seen in the monomer NMR spectrum. The sharpness of these peaks also supports the theory that they have remained at the end of the sidechains where they are not subjected to the broadening that occurs along and adjacent to the polymer backbone. This is due to a lesser degree of molecular rotation, as well as the same proton from neighbouring repeat units being situated in slightly different chemical environments. Herein, **P3-OTs-100%** remained the focus of attention due to the ease with which the polymer could be characterised compared to polymers with varying proportions of functionality. Finally, **p(g3T2-T)** was synthesised according to literature procedures for use as a control polymer.[21,23]

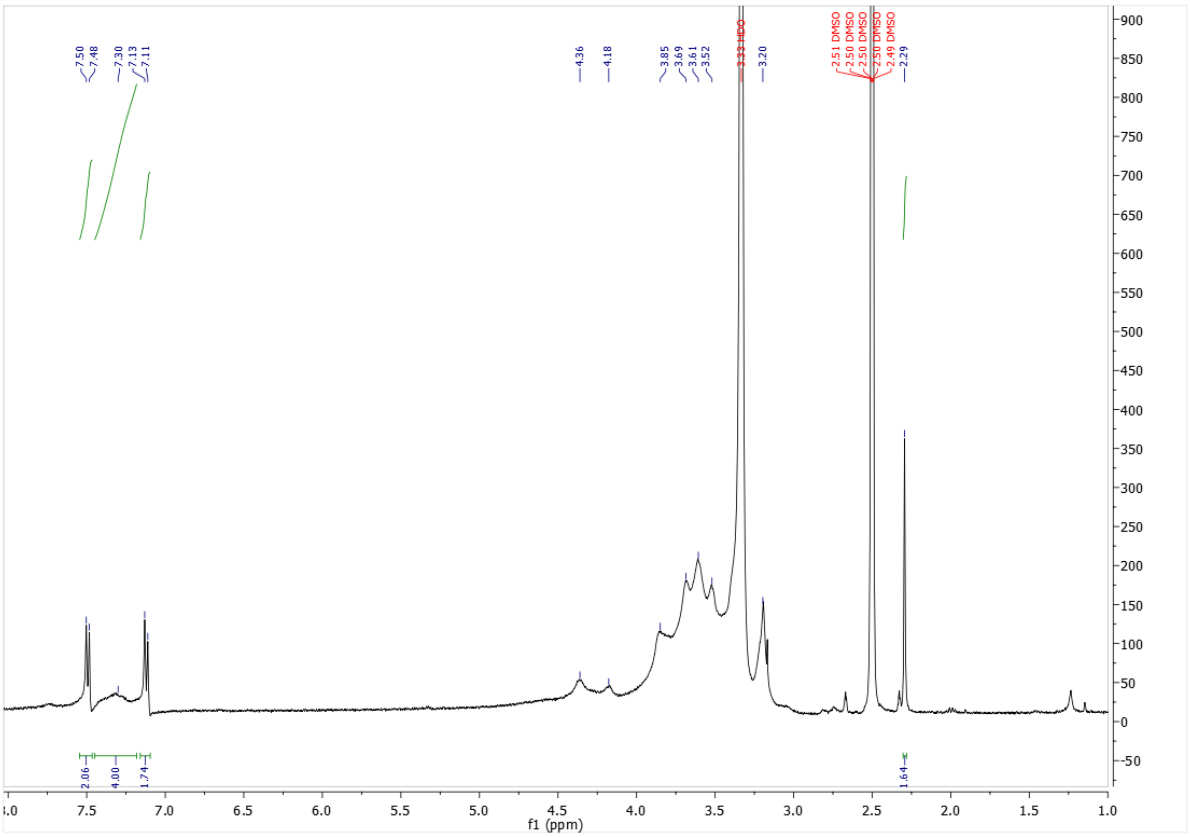


Figure A8. ^{1}H NMR spectrum of polymer **P3-OTs-100%** in DMSO-d_6.

A3.2 Polymer functionalisation

Following the successful synthesis of **P3**, test reactions to functionalise the polymer were conducted. This began with the aim of converting the tosyl group into a maleimide group to enable mild thiol-ene conditions to be used[28–30] for the attachment of a biomolecule, such as an enzyme or aptamer. To test this concept, triethylene glycol monomethyl ether was employed as a model system to emulate the sidechain of the polymer. By tosylating this (**Figure A9**), the conditions for polymer functionalisation could be optimised on a less precious system. To begin, literature conditions[31] were replicated to synthesise a protected maleimide derivative via Diels Alder (**Figure A9**). Maleimide alone is not nucleophilic enough to displace a tosyl group, however when "protected" by furan, the electronics of the molecule alter such that this becomes possible.[32]

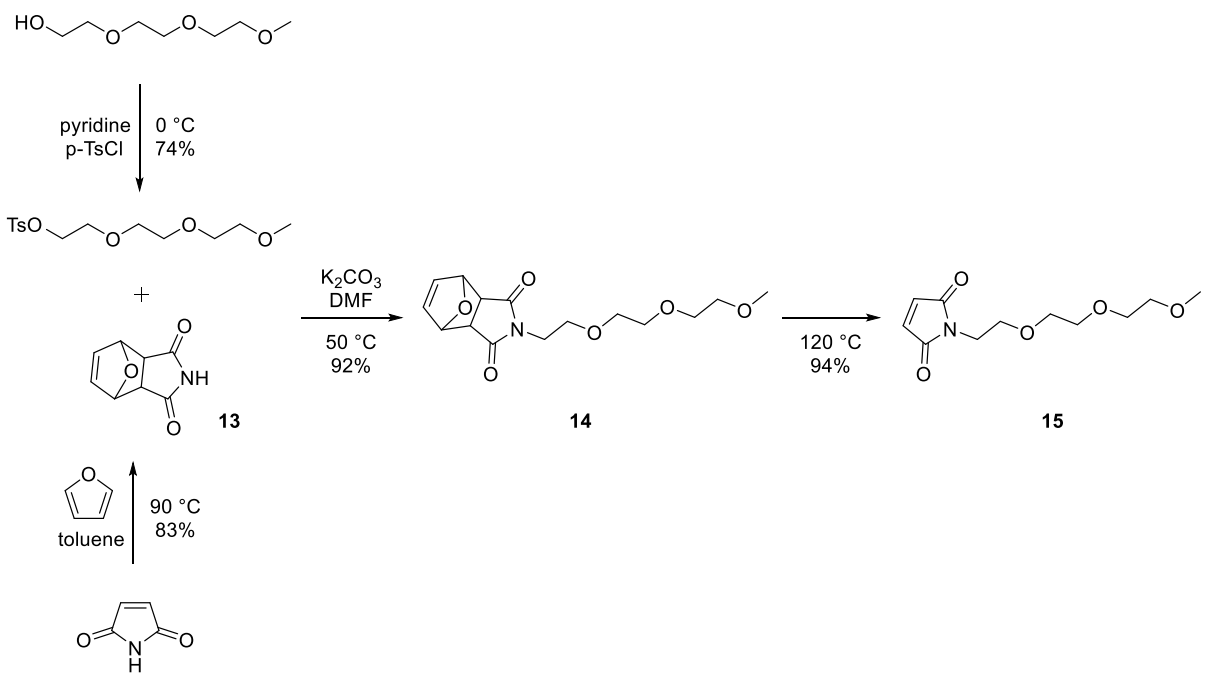


Figure A9. Synthetic route for the test reaction of maleimide attachment to **P3**.

Next, the S_N2 reaction was optimised, to improve the reaction yields from 42% on the initial attempt, to 92%. This was achieved by ensuring that the potassium carbonate was oven-dried before use to ensure the deprotonation step reached completion, as well as increasing the temperature from the initial attempt from 40 to 50 °C. By both NMR and HRMS, the synthesis of **14** was confirmed, then a retro Diels Alder produced the free maleimide terminal group. For ease of synthesis, it was also shown that these two steps could be telescoped, with a total yield of 88%, which was useful to note for the translation of this route to **P3-OTs-100%**.

In order to easily denote the attachment of a thiol onto the polymer, a fluorescent marker was selected, namely anthracene-9-ylmethanethiol (**Figure A10**). This was synthesised following literature conditions[33] and a test reaction with **15** was performed. On the first attempt, the reaction conditions were those detailed in **Figure A10**, without the use of the phosphate buffered saline (PBS) solution. This resulted in a poor yield of only 33%, which was improved by controlling the pH between 6.8 and 7.4, where the yield was improved to 90%. The use of PBS is beneficial because it makes these conditions biocompatible, indicating that they are

likely to suit reactions with an aptamer or enzyme. Furthermore, high yields are necessary when performing these reactions on a polymer, as unreacted reactive end groups on the polymer may undergo undesired chemistries and interfere with the sensing element.

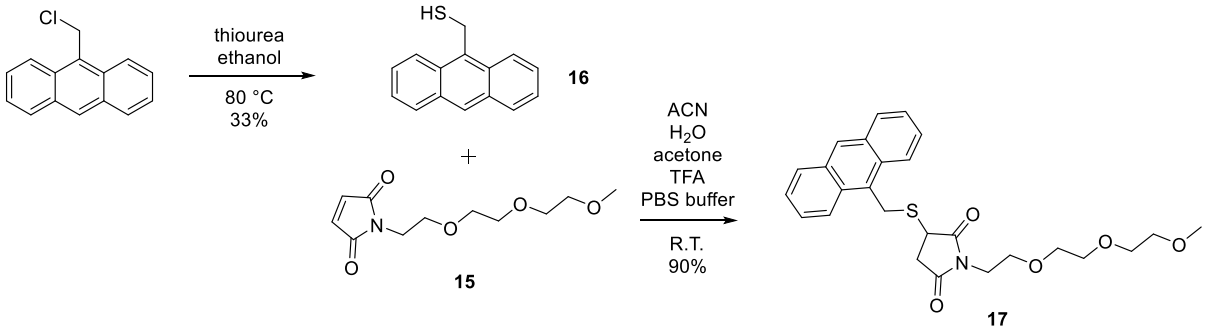


Figure A10. Synthetic route for the test reactions of the thiol-ene click reaction between maleimide and a thiol anthracene derivative.

Once optimised, these conditions were then transferred to the polymer, to first transform the reactive tosyl end groups into maleimide derivatives, then attach the fluorescent marker (**Figure A11**). By telescoping the first two steps, as previously discussed, a yield of 88% was achieved. ^{1}H NMR proved difficult to accurately interpret due to the broadness of the spectrum, however the peaks ascribed to the tosyl group were no longer present, and a distinct singlet at 6.69 ppm appeared in the spectra, which can be attributed to the protons attached to the C=C bond of the maleimide, aligning with the ^{1}H NMR of **15**. Following this, the anthracene marker was attached using the biocompatible thiol-ene click conditions developed in the synthesis of **17**, with a yield of 95% reported. Due to the bulky nature of the anthracene groups, the solubility of this polymer decreased significantly, and became processable in DMF only. Beyond this proof-of-concept study, this indicates that it would be necessary to in fact reduce the percentage of reactive end groups in the polymer to maintain solubility to allow for processing. This would also be a logical approach when considering the use of biomolecules because the length scales of an aptamer are on the same order of magnitude as those of a polymer. Thus, having an aptamer attached to every repeat unit would not only be unnecessary

but potentially detrimental to the hypothesised mechanism of operation, due to the high aptamer concentration inhibiting each other's movement. With the anthracene marker installed onto the polymer (**P3-Anth-100%**), the characterisation of this polymer is detailed in **Section A3.5**. Before this, it was necessary to fully characterise both the control and tosyl polymers (**p(g3T2-T)** and **P3-OTs-100%**), to understand the impact of reactive end groups on the optoelectronic, physical and electrochemical properties and OECT performance.

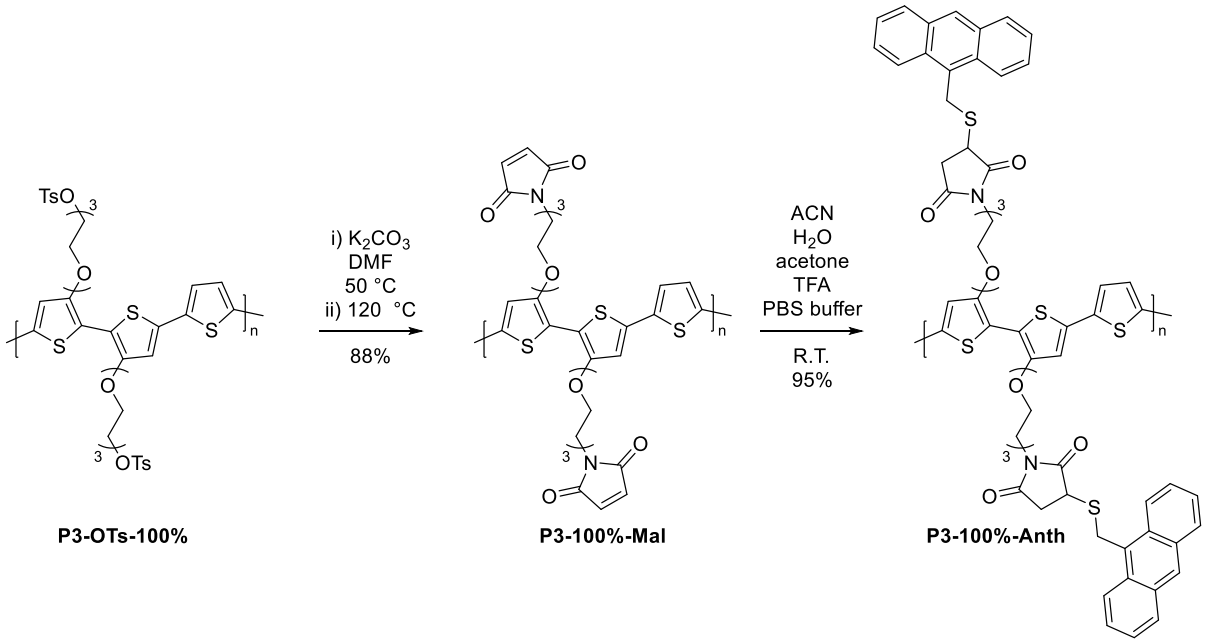


Figure A11. Synthetic route for the functionalisation of **P3-OTs-100%** with a fluorescent marker via a maleimide derivative.

A3.3 Optoelectronic, electrochemical and physical properties

The physical and optoelectronic properties of the p-type control and functionalisable polymers (**p(g3T2-T)** and **P3-OTs-100%**, respectively) are set out in **Table A1**. The number average molecular weights were determined by GPC in DMF at 40 °C with respect to PMMA standards. The M_n values of the two polymers are comparable, thus any differences in properties can accurately be attributed to differences in the polymer structures themselves rather than being dependant on molecular weight.

Table A1. Summary of the properties of the control polymer, **p(g3T2-T)** and the p-type functionalisable polymer **P3-OTs-100%**.

Polymer	M_n (kDa) [$Đ$] [a]	$E_{g,opt}$ (eV) [b]	$\lambda_{max,sol}$ (nm) [c]	IP (eV) [d]	IP (eV) [e]	T_d (°C) [f]
p(g3T2-T)	22.2 [1.57]	1.66	569	4.66	4.66	305
P3-OTs-100%	19.2 [1.33]	1.60	545	4.72	5.05	221

[a] Number-average molecular weight (M_n) and dispersity ($Đ$) measured by GPC vs PMMA standards in dimethylformaldehyde at 40 °C. [b] Optical band gap estimated from thin film UV-Vis absorption onset. [c] Peak wavelength obtained from solution UV-Vis absorption spectra in chloroform. [d] The IP was calculated by finding the oxidation onset potential and using it to calculate IP by: $IP = 4.8 + E_O - E_f$ where $E_f = 0.44$ V. Oxidation onset found from the cyclic voltammogram of polymer thin films on glassy carbon electrode with 0.1 M tetrabutylammonium hexafluorophosphate as the supporting electrolyte using a platinum rod counter electrode and a silver/silver chloride reference electrode. [e] Measured by photoelectron spectroscopy in air. [f] Temperature for 5% weight-loss (i.e., decomposition) from thermogravimetric analysis.

The UV-Vis absorption spectra of the polymers were measured in both dilute chloroform solutions and as thin films on glass substrates (**Figure A12(a)** and **(b)**, respectively). UV-Vis absorption and fluorescence measurements for **P3-Anth-100%** were also conducted and are discussed in **Section A3.5** as evidence for the proof-of-concept functionalisation. Surprisingly, the π–π* (HOMO-LUMO) transition in solution is blue-shifted for the functionalisable polymer compared to the control. Given the polymers have the same polythiophene backbone, this indicates that the reactive end groups are acting to significantly alter the aggregation in solution, which results in $\lambda_{max,sol}$ shifting from 569 nm for the control polymer to 545 nm for **P3-OTs-100%**. The trend remains consistent when measuring the polymers as thin films, where the π–π* transition shifts from 655 nm to 586 nm. This also indicates that, unsurprisingly, the introduction of functionality on the sidechains impacts the microstructure of the thin films. Numerically, this translates to a smaller optical bandgap for the polymer with reactive end groups, of 1.60 eV, compared to 1.68 eV for **p(g3T2-T)**, which is comparable to

literature.[23] Both polymers also display somewhat of a broad peak ≈ 900 nm, which is ascribed to the presence of polarons on the polymer backbone. As these measurements were conducted in an ambient atmosphere, this most likely indicates that there is some ambient doping, whereby the polymer is interacting with oxygen, as is common for polythiophene-based polymers.[20]

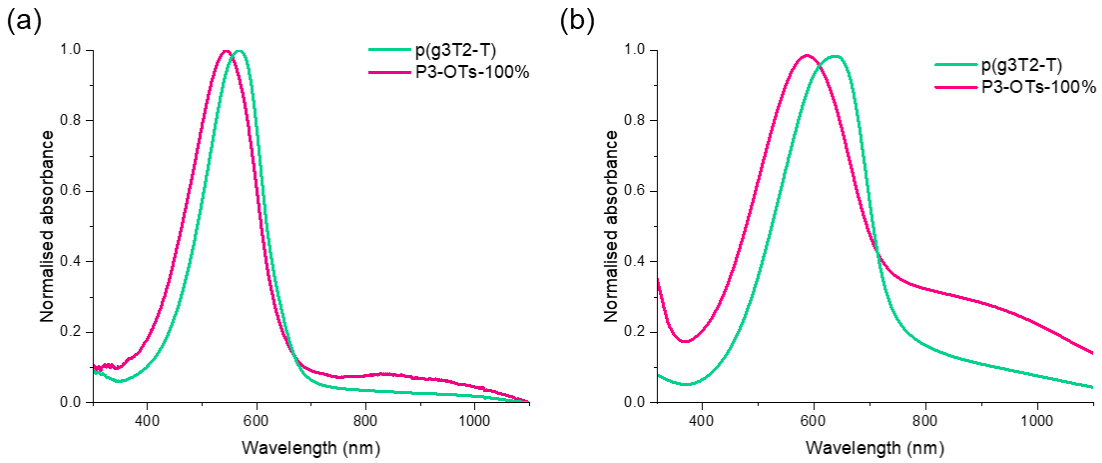


Figure A12. Normalised UV-Vis absorption spectra (a) in dilute chloroform solutions and (b) as thin films spin-coated onto glass substrates at 600 rpm for 45 seconds for **p(g3T2-T)** and **P3-OTs-100%**.

Photoelectron spectroscopy in air (PESA) was conducted to measure the ionisation potential (IP) of the polymers. This is determined by using photons of known energy to excite photoelectrons from a material's surface, whereby any excess energy is converted to kinetic energy of the emitted electron. By recording the number and kinetic energy of the electrons emitted at each photon energy, the IP can be extracted from tangents to the baseline (i.e., where the incident photons do not have enough energy to eject an electron) and the emission yield. This technique uses polymer thin films, which were spin coated onto indium tin oxide (ITO)-coated glass slides. PESA resulted in values of 4.67 eV and 5.01 eV for **p(g3T2-T)** and **P3-OTs-100%**, respectively (**Table A1**).

The ionisation potentials of p-type polymers can also be determined by cyclic voltammetry (CV) in 0.1 M tetrabutylammonium hexafluorophosphate ($TBAPF_6$) in acetonitrile, using a polymer-coated glassy carbon working electrode, a Pt wire counter electrode and an Ag/AgCl reference electrode. Promisingly, both polymers displayed only p-type (oxidative) behaviour, with repeated cycling of both polymers overlaying their original cycle, indicating good reversibility of the materials (**Figure A13**). Using this method, **p(g3T2-T)** had an oxidation onset potential of -0.01 V, compared to **P3-OTs-100%**, which had E_{ox} = 0.07 V. This small difference translated to IPs of 4.65 V for the control polymer and 4.73 V for the polymer with reactive end groups. These values appear more reasonable for the two materials due to the identical backbones, which are typically considered the part of a polymer to influence the energy levels.

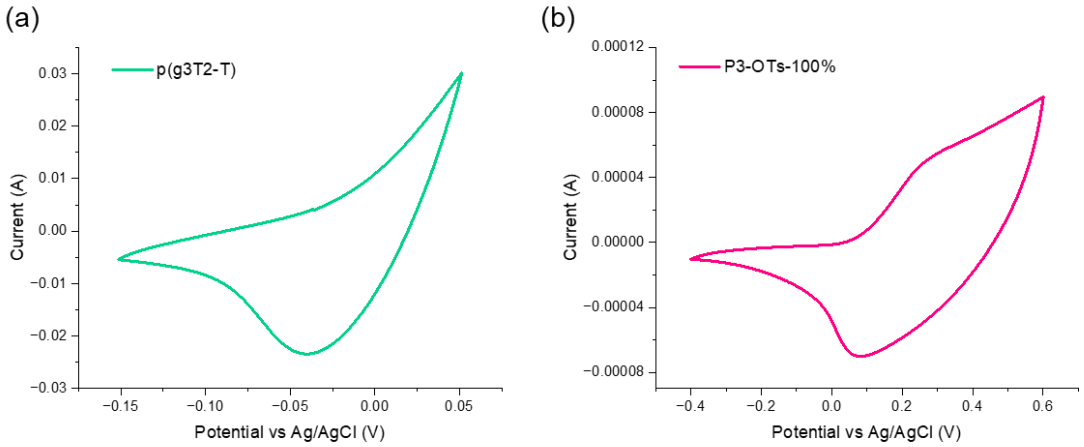


Figure A13. Cyclic voltammograms of (a) **p(g3T2-T)** and (b) **P3-OTs-100%** determined by cyclic voltammetry of the polymer thin films on a glassy carbon working electrode vs Ag/AgCl in acetonitrile with 0.1 M tetrabutylammonium hexafluorophosphate as the supporting electrolyte, using a platinum rod counter electrode. By drawing tangents to extract the oxidation onset potential (E_O), IP can be calculated using: $IP = 4.8 + E_O - E_f$. E_f is the average potential of the oxidation and reduction peaks in ferrocene and was found to be +0.44 V.

The IP values for the control polymer remain consistent across both techniques, indicating this is a reasonable estimate for the HOMO. Conversely, there is a reasonable discrepancy between the calculated values for **P3-OTs-100%** with each of the two methods. This may indicate that the packing in two different thin film samples (one drop cast onto glassy carbon, the other spin coated onto ITO coated glass) varies significantly, whereas **p(g3T2-T)** remains more consistent.

The electrochemical activity of the polymers was then examined using CV in aqueous 0.1 M NaCl electrolyte to understand the operation of the polymers in conditions more representative of their destined application, OECT devices. Both polymers showed discrete oxidation behaviour with good reversibility and similar voltammogram shapes to those measured in the organic electrolyte (**Figure A14**). Interestingly, in the aqueous electrolyte, the onset of oxidation is lower for **P3-OTs-100%** (at 0.02 V compared to 0.13 V for **p(g3T2-T)**), indicating that it is more able to accommodate ions. If this trend is consistent when in an OECT device, this results in a transistor that is easier to turn on, producing a more efficient device, the reverse of the trend in the organic electrolyte. It is possible that the larger tosyl reactive end groups (*c.f.* small, unreactive methyl termini) disrupt the microstructure such that hydrated ions are more easily able to penetrate into the bulk to volumetrically dope the material.

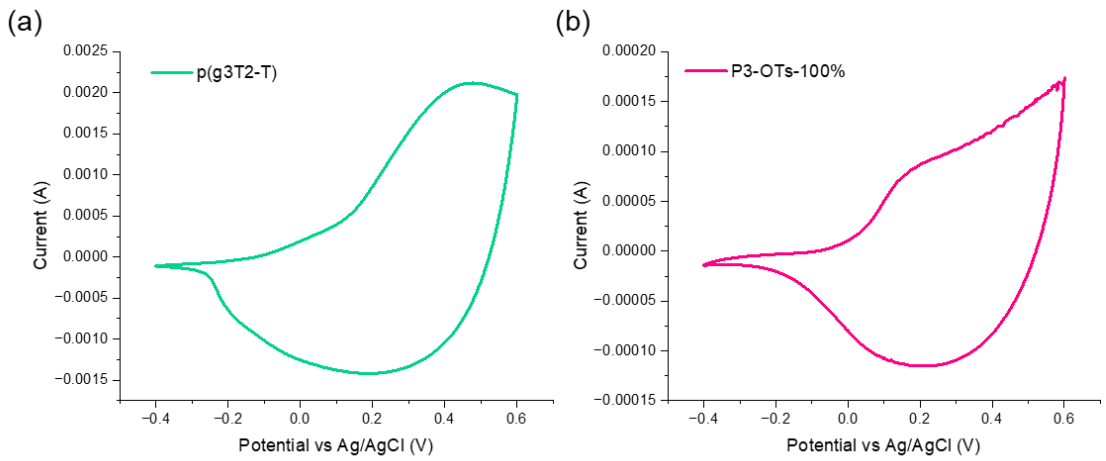


Figure A14. Cyclic voltammetry of (a) **p(g3T2-T)** and (b) **P3-OTs-100%** drop cast onto a glassy carbon working electrode, using an Ag/AgCl reference and platinum wire counter electrode. The electrolyte was degassed 0.1 M $NaCl_{(aq)}$ solution and a scan rate of 0.1 V s^{-1} was used. The second and third cycles are shown; the first cycle is not presented as this cycle is typically associated with the reorganisation of polymer chains or break-in effects.[34,35]

To further understand the impact of the reactive end group on the polymers properties, the thermal stability was investigated using thermogravimetric analysis (TGA). The polymers were heated to 500 °C under nitrogen, and the temperature at which a 5% mass loss was recorded was taken to be the degradation temperature (T_d). The traces are shown in **Figure A15**. The values (**Table A1**) indicate that the polymer with reactive end groups, **P3-OTs-100%**, has a lower degradation temperature than **p(g3T2-T)**, where T_d = 221 and 305 °C, respectively. Fortunately, 221 °C still provides sufficiently high thermal stability to undergo a range of annealing temperatures, and indicates stability to any further reaction conditions required for functionalisation, especially biocompatible conditions, which will likely be no more than 50 °C.

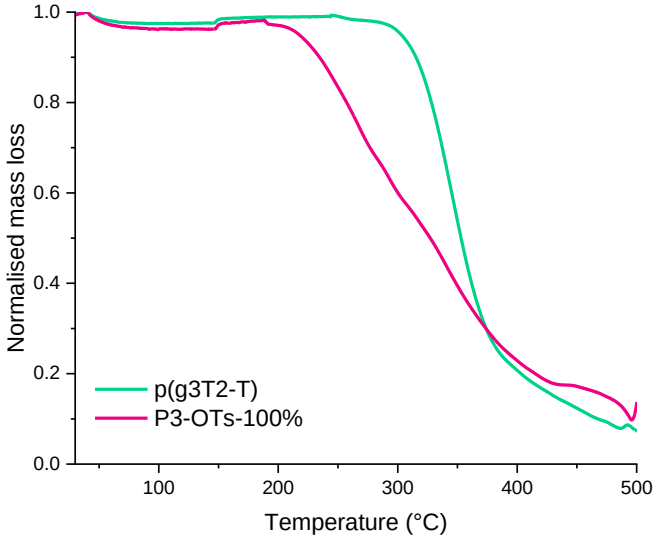


Figure A15. Thermogravimetric analysis traces of the two polymers, **p(g3T2-T)** and **P3-OTs-100%**. Polymers were heated under nitrogen flow (50 mL/min), using the following conditions: [1] 30.0 to 105.0 °C, 34.99 K/min, [2] hold at 105.0 °C for 10.00 min, [3] 105.0 to 500.0 °C, 10.00 K/min.

A3.4 OECT characteristics

To understand the impact of the reactive end group on OECT performance, devices were fabricated and tested in 0.1 M aqueous NaCl solution in ambient conditions. An Ag/AgCl pellet constituted the gate electrode and pre-printed gold was used as the source and drain electrodes, with the OMIEC as the channel material. As **p(g3T2-T)** is widely reported in literature,[21,23] **P3-OTs-100%** was tested in the same device conditions to understand how its performance compared. **Table A2** sets out the performance of the functionalisable polymer, and comparative literature values for **p(g3T2-T)**, and the output and transfer characteristics are displayed in **Figure A16**.

Table A2. Steady-state OECT performance of **P3-OTs-100%**.

Polymer	V_T [V] [a]	d [nm] [b]	g_m [mS] [c]	[μC^*] [F V^{-1} cm^{-1} s^{-1}] [d]	C^* [F cm^{-3}] [e]	μ_{OECT} [cm^2 V^{-1} s^{-1}] [f]
p(g3T2-T)[*]	-0.18 ± 0.01	63	3.03 ± 0.21	135 ± 9	211 ± 18	0.16 ± 0.01
P3-OTs-100%	-0.16 ± 0.02	361[†]	7.40 ± 1.06	22 ± 0.6	288 ± 12	0.062 ± 0.001

[a] Threshold voltage extracted from a plot of $\sqrt{I_D}$ versus V_G. [b] Thin film thickness measured by Dektak profilometer. [c] Peak OECT transconductance. [d] [μC^*] calculated for the highest performing channel from the slope of g_m with known channel dimensions and applied bias. [e] C^* values extracted from Randles circuit fits from electrochemical impedance curves of the polymers coated on Au electrodes in 0.1 M aqueous NaCl solution. [f] OECT mobility calculated by an impedance matching method.[36] [*] The values for **p(g3T2-T)** were taken from literature.[23] [†] The thickness of **P3-OTs-100%** is significantly larger than the control polymer as it was drop cast to ensure the OECT devices produced sufficient signal.

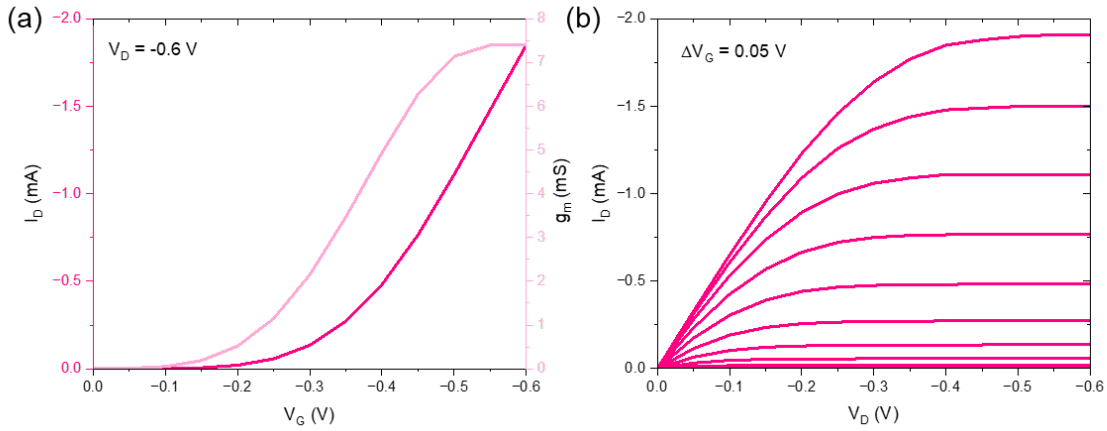


Figure A16. Performance of OECTs averaged across 6 devices, where W = 100 µm and L = 10 µm in aqueous 0.1 M NaCl solution in ambient conditions. The panels present (a) transfer and transconductance (g_m) curves and (b) the output characteristics of **P3-OTs-100%**.

As expected from the polythiophene backbone and performance of the control polymer, **P3-OTs-100%** displayed pure p-type accumulation mode performance. The threshold voltages aligned with the trend observed in oxidation potential in aqueous CVs, indicating that the polymer with reactive end groups required a lower potential (i.e., a V_T closer to zero) to turn

the device on, making it a more efficient device. When examining the performance of the two polymers by comparing their μC^* product, the functionalisable polymer appears to have a performance ~5 times lower than the control. To further investigate this, electrochemical impedance spectroscopy (EIS) was conducted to extract a volumetric capacitance. This indicates that C^* is 36% larger for **P3-OTs-100%**, suggesting it is better able to accommodate ions, which corroborates the hypothesis that the polymer has more free volume available due to the bulky tosyl end groups, which limit packing into ordered, crystalline domains. Conversely, this significantly impinges on the mobility, which is a factor of 5 smaller than the control polymer, likely for this same reason. GIWAXS or STM measurements would be required to verify this, though as this is not the primary focus of this research project, it is outside of the scope of the study. Having successfully operated an OECT device, the functionalisation step was optimised.

A3.5 Proof-of-concept functionalisation data

The synthetic procedures of the functionalisation are detailed in **Section A3.2**, however this section describes the evidence to suggest successful functionalisation. Typical characterisation techniques used for small molecules become more cumbersome on polymers due to the comparatively large nature of the molecules. For example, polymer NMRs are much broader and accurate integration of the peaks may be unfeasible. Furthermore, ^{13}C NMR of polymers is not viable, as achieving a high enough concentration of a relatively insoluble material (compared to small molecules) is often not possible. Mass techniques, such as MALDI are sometimes accessible for polymers depending on the molecular weight of the material, however for heavier chains, they are often considered an underestimation of the molecular weight. MALDI was attempted with these materials, however there was limited success with the typical trans-2-[3-(4-tert-Butylphenyl)-2-methyl-2-propenylidene]-malononitrile (DCTB) matrix, as has previously been reported for polymers.[20,37,38]

Instead, a fluorescent marker (an anthracene derivative) was selected to provide supporting evidence for the functionalisation of the polymer. By performing the functionalisation reaction, then precipitating the polymer and washing it with copious amounts of methanol (a solvent in which the anthracene derivative was readily soluble), it was presumed that any remaining fluorescence observed was attributed to anthracene molecules covalently bonded to the polymer. Firstly, the UV-Vis absorption of a solution of anthracene-9-ylmethanethiol in chloroform was measured to understand the peak(s) relating to this species in a UV-Vis spectrum and to suggest the wavelength at which to excite when collecting the fluorescence spectra. The most intense peak attributed to anthracene was at 373 nm, thus this was used as the excitation wavelength for fluorescence measurements. Next, the fluorescence of anthracene-9-ylmethanethiol was collected and is presented in **Figure A17(a)**. Anthracene-9-ylmethanethiol displays the expected anthracene fluorescence peaks between 380 and 450 nm, which corresponds to the π^*-π transition, with a well-defined vibrational fine structure. The peak at 396 nm is common to both the absorption and emission spectra and is attributed to the 0-0 transition between the vibration levels of π and π^* states.

Then, the UV-Vis absorption spectrum of the control polymer (**p(g3T2-T)**) mixed with anthracene-9-ylmethanethiol (1:1.3 w/w, the mass ratio of polymer:anthracene if every end group reacted with the marker) in chloroform was measured to understand what the ratio of peaks would be in this spectrum after 100% conversion (**Figure A17(b)**). The corresponding fluorescence spectrum was acquired, to ensure that the polymer backbone did not quench the anthracene emission. If this had been the case, then a new marker with a different emission wavelength would have been required. Promisingly though, the emission spectrum of the mixture shows the clearly defined anthracene peaks, identical to the anthracene-9-ylmethanethiol spectrum.

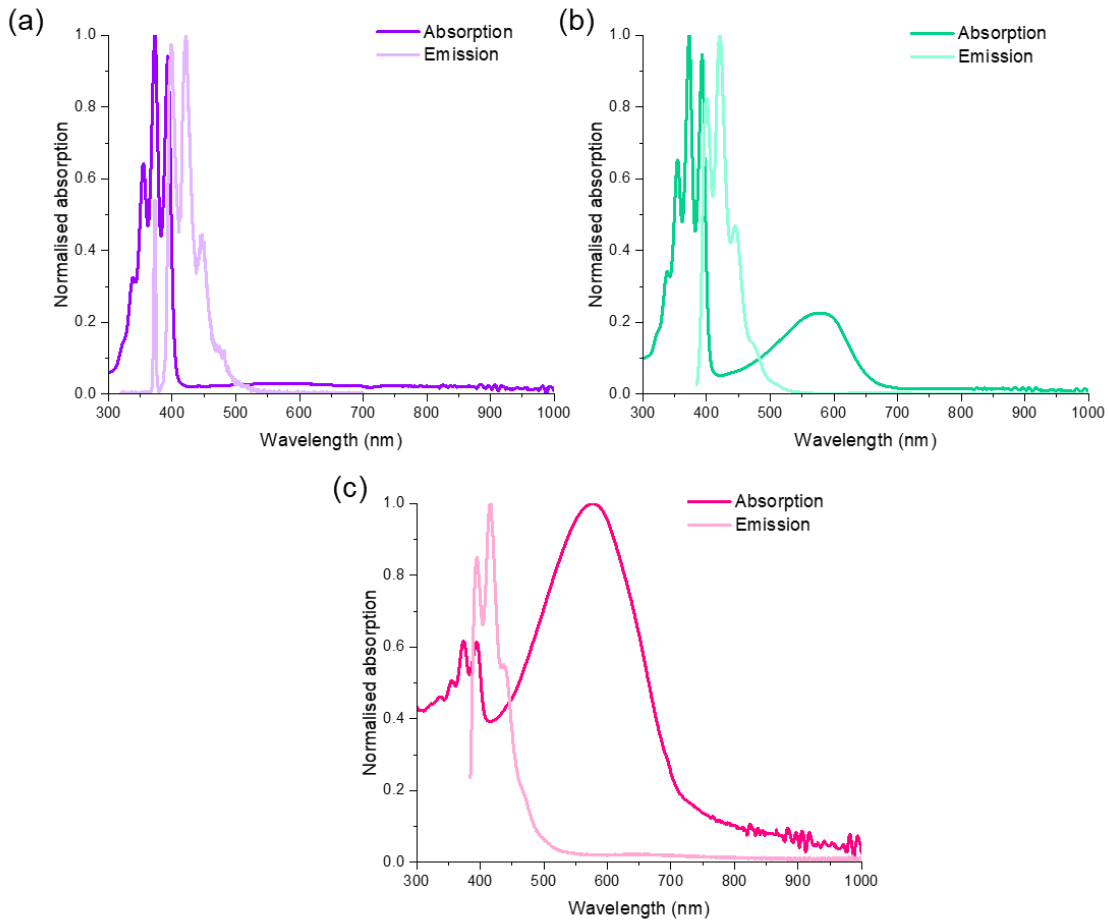


Figure A17. UV-Vis absorption and fluorescence spectra for (a) anthracene-9-ylmethanethiol, (b) a X:Y w/w mixture of anthracene-9-ylmethanethiol and **p(g3T2-T)** and (c) **P3-Anth-100%** measured in chloroform solution. Fluorescence spectra are measuring using an excitation wavelength of 373 nm.

Using this information, the UV-Vis and fluorescence spectra of **P3-Anth-100%** were measured (**Figure A17(c)**). Again, these spectra show presence of the anthracene peaks, however there is a clear difference between the ratio of the anthracene:polymer peaks in the UV-Vis absorption spectrum. As the polymer peak is significantly larger than that in **Figure A17(b)**, this indicates that there is a degree of polymer that did not react.

A3.6 Conclusions and future work

This work has developed a p-type polymer with reactive end groups for post-polymerisation functionalisation. The significant synthetic efforts concluded with a solution processable material with reactive termini on the sidechains, namely tosyl groups, which proved inert to the polymerisation and processing conditions. The p-type polymer, **P3-OTs-100%**, showed similar optoelectronic and electrochemical properties to the control polymer, **p(g3T2-T)**, as expected, due to the identical polythiophene backbone. The tosyl reactive end groups were first demonstrated to react cleanly with a furan protected maleimide derivative, followed by a Diels Alder to reveal the maleimide group. This was then able to undergo mild thiol-ene click chemistry (via a Michael addition mechanism) to install a fluorescent anthracene marker. Using fluorescence spectroscopy, it was possible to qualitatively infer the degree of functionalisation of the polymer to understand that there was likely some remaining unreacted maleimide groups present.

Whilst the required conditions for the functionalisation step are already biocompatible due to the solvents and temperature employed, further work is required to first optimise the yield of the functionalisation, ensuring there are no unreacted maleimide groups remaining. Next, repetition of this step using a biorecognition unit, such as an enzyme or aptamer, is required to realise the end goal of the project. Due to the size of the biorecognition element, this step should be conducted on a surface (instead of in solution as demonstrated in this work). This will prevent the large aptamer or enzyme from occupying free volume in the bulk of the OMIEC, reducing the C^* and disrupting the crystallinity such that charge carrier mobility is inhibited. Furthermore, enzymes or aptamers are not compatible with the solvents required for solubilising the polymer, hence, to achieve a uniform thin film, this step must be conducted before introduction of this unit.

In order to characterise these surface binding events, surface plasmon resonance (SPR) could be utilised. This is an optical technique, whereby the reaction is conducted in a flow cell and light is shone onto the surface of the sample. A detector measures the refractive index of the sample without the presence of the desired biorecognition unit to obtain a baseline, then when the binding event occurs between the polymer and the biorecognition unit, the refractive index changes to denote such an event. By using SPR, it would be possible to understand the degree of reaction between the polymer and the sensing unit. It would also be feasible to continue the SPR experiment and pass through a number of biomolecules, recording the binding event when the biorecognition unit senses the relevant biomolecule. Finally, this functionalisation step should be conducted with the OMIEC in situ as the channel material in an OECT device, and the transistor can be operated as a biosensor, as has recently been demonstrated for a PEDOT-based OECT.[39]

A4 N-type functionalisable polymer

A4.1 Synthesis

Learning from the synthetic struggles of **Section A3.1**, tosyl end groups were also selected for the n-type polymer. The choice of polymer backbone was based on the reported high performance of the non-functionalisable derivative, which has been optimised for OECT performance,[40] and the availability of this material for use as a control (due to the work in **Chapters 2** and **3**). The synthesis commenced with the sidechain, which was prepared via a very similar procedure to that detailed in **Chapter 2**, aside from the use of triethylene glycol in place of triethylene glycol monomethyl ether (**Figure A18**). Fortunately, due to the order of synthesis, there was no need for protecting groups, thus the sidechain was synthesised in four steps.

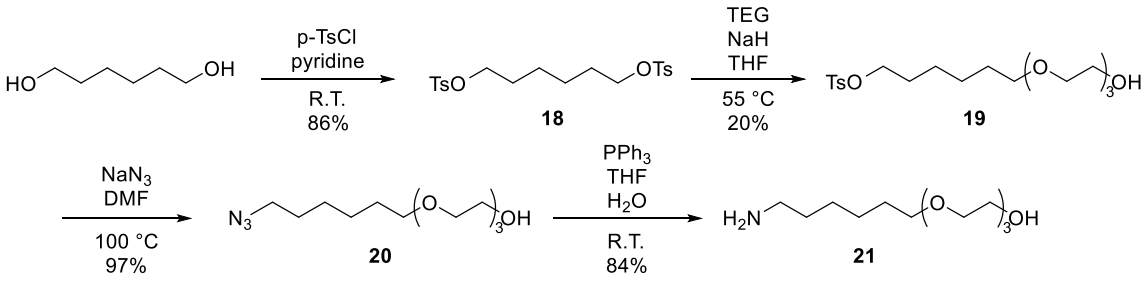


Figure A18. Synthetic route to the functionalisable sidechain for attachment to the NDI core.

Initially, attempts at a functionalisable sidechain involved introducing the tosyl group before attachment to the NDI core, which was unsuccessful due to its high reactivity interfering with the desired reaction. Instead, it was proposed that the sidechain with the free alcohol was attached to the NDI core, followed by an in situ tosylation before the polymerisation. Unfortunately, under the typical acidic or Lewis acid reaction conditions used for attachment of the sidechains to NDA, via a ring-opening/closure mechanism,[37,38,40,41] this favoured the self-attack of the sidechain. Thus, it was deemed that a protecting group was required to enable the attachment of the sidechains. Whilst various options were investigated, including tetrahydropyranyl (THP) and triisopropylsilyl ether (TIPS), ultimately, by using a carboxylic acid during the attachment of the sidechain, the conditions were appropriate to simultaneously promote the ring-opening/closure mechanism and protect the free alcohol, preventing it from self-attack. The conditions for this were replicated from literature, where Giovannitti et al. were aiming for the ester sidechains on the polymer.[41] The authors noted, however, that these materials were unstable in acid, with the ester group detaching.[41] This knowledge was advantageous and resulted in a simple procedure to remove the ester group, exposing the free alcohol, in very high yields of 98%. Additionally, due to the poor solubility of this material, purification was simplified, with only an aqueous work up required to achieve optimal purity. The final tosylation step to achieve the monomer required an extended reaction time of 72 hours, with only a meagre 11% yield achieved, however, as sufficient material was isolated for polymerisation, this step was not further optimised.

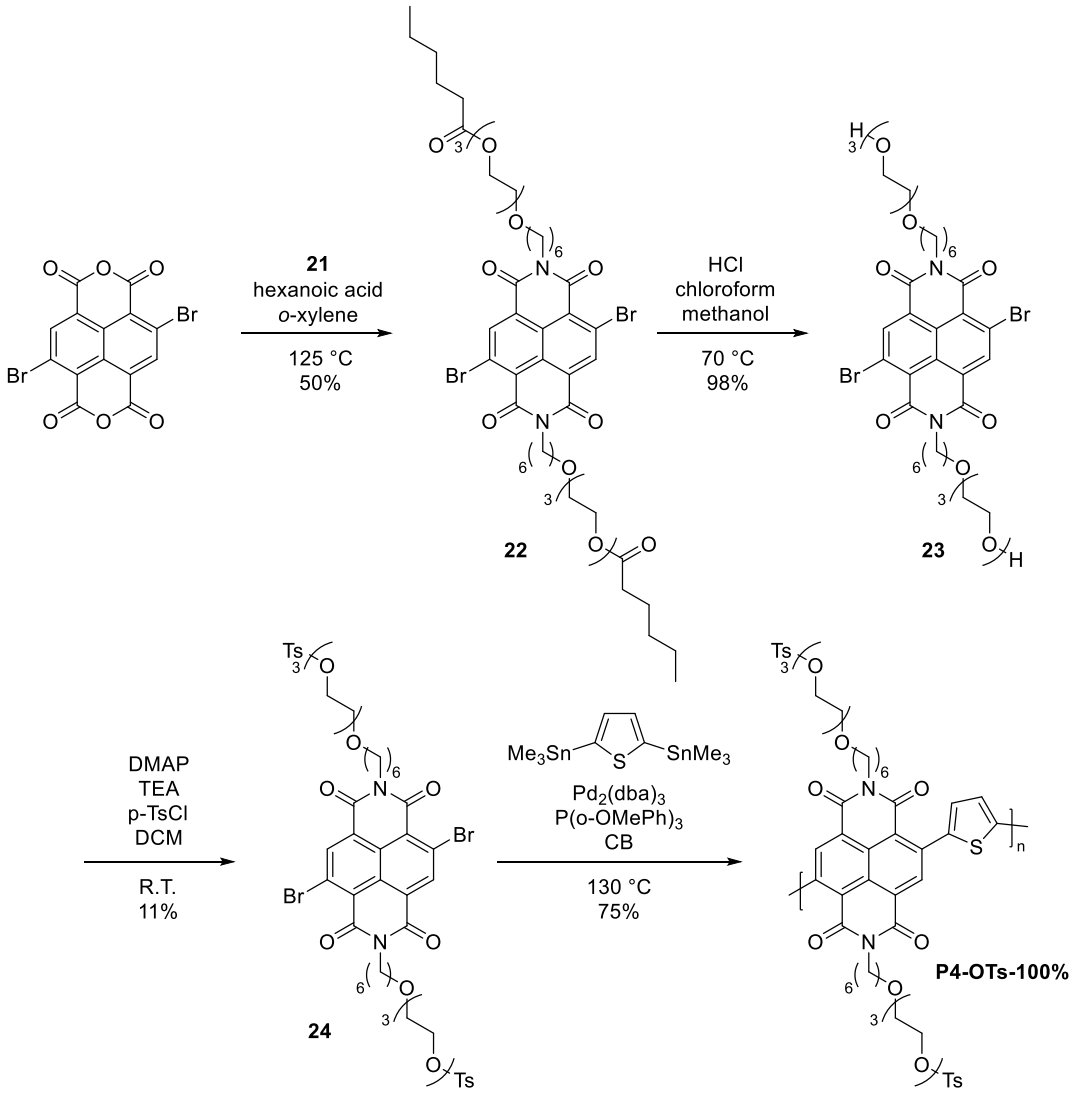


Figure A19. Synthetic route to the functionalisable NDI-based polymer, **P4-OTs-100%**.

A4.2 Polymer functionalisation

In this case, biocompatible conditions were less of a necessity as the goal was to covalently attach ferrocene as an electron mediator for redox processes with enzymes. On account of this, it was possible to instead use traditional click chemistry between an alkyne and an azide. As Fc is commercially available as ethynylferrocene, it was decided that the polymer reactive group should be substituted for an azide. This was first tested on a linear glycol chain (**g_3OTs**), to produce **g_3N_3** in a yield of 58% (**Figure A20**). The yield of this step was lower than expected, which is potentially due to the partial solubility of the product in the aqueous phase of the work

up, which caused a significant reduction in yield. This is not an issue moving forward as the work up for this will be altered when applied to a polymer. Finally, the click conditions were selected due to precedent in the group, and were successful in attaching the ferrocene (**g_3Fc**), as verified by HRMS and ^{1}H and ^{13}C NMR.

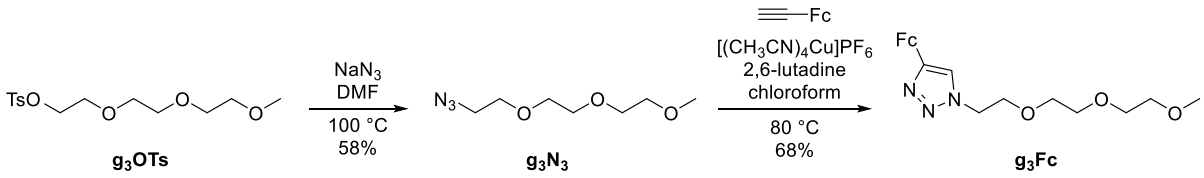


Figure A20. Synthetic route for the test reactions of the alkyne-azide click reaction.

These conditions were then applied to polymer **P4-OTs-100%**, with a total yield of ~50%. The final product (**P4-Fc-100%**) was collected as a blue powder, with a significantly different appearance to **P4-OTs-100%**, whereby the typical metallic lustre of these OMIEC polymers had decreased. The solubility of the polymer in chloroform also decreased, to the point of no longer being processable in the solvent. As such, the polymer containing 50% of the reactive end group monomer was synthesised (**P4-OTs-50%, Figure A21**) which overcame the solubility issue, ensuring it could be sufficiently purified and spin cast onto device substrates. The use of an azide as an intermediate proved convenient when characterising the material. The azide functionality introduced an easily identifiable FTIR signal at 2108 cm^{-1}, which was not present in **P4-OTs** or **P4-Fc** but was clearly observed in **P4-N_3** (**Figure A22**). Additionally, the same ^{1}H NMR signals as reported for the p-type polymer were present for **P4-OTs** (two doublets at 7.75 ppm and 7.32 ppm and a singlet at 2.43 ppm), but were no longer present after the functionalisation with the azide. Further convincing evidence for the azide formation was the shift in NMR signal of the methyl protons neighbouring the reactive end group, which moved from 4.13 ppm for the tosyl group to 3.37 ppm for the azide.

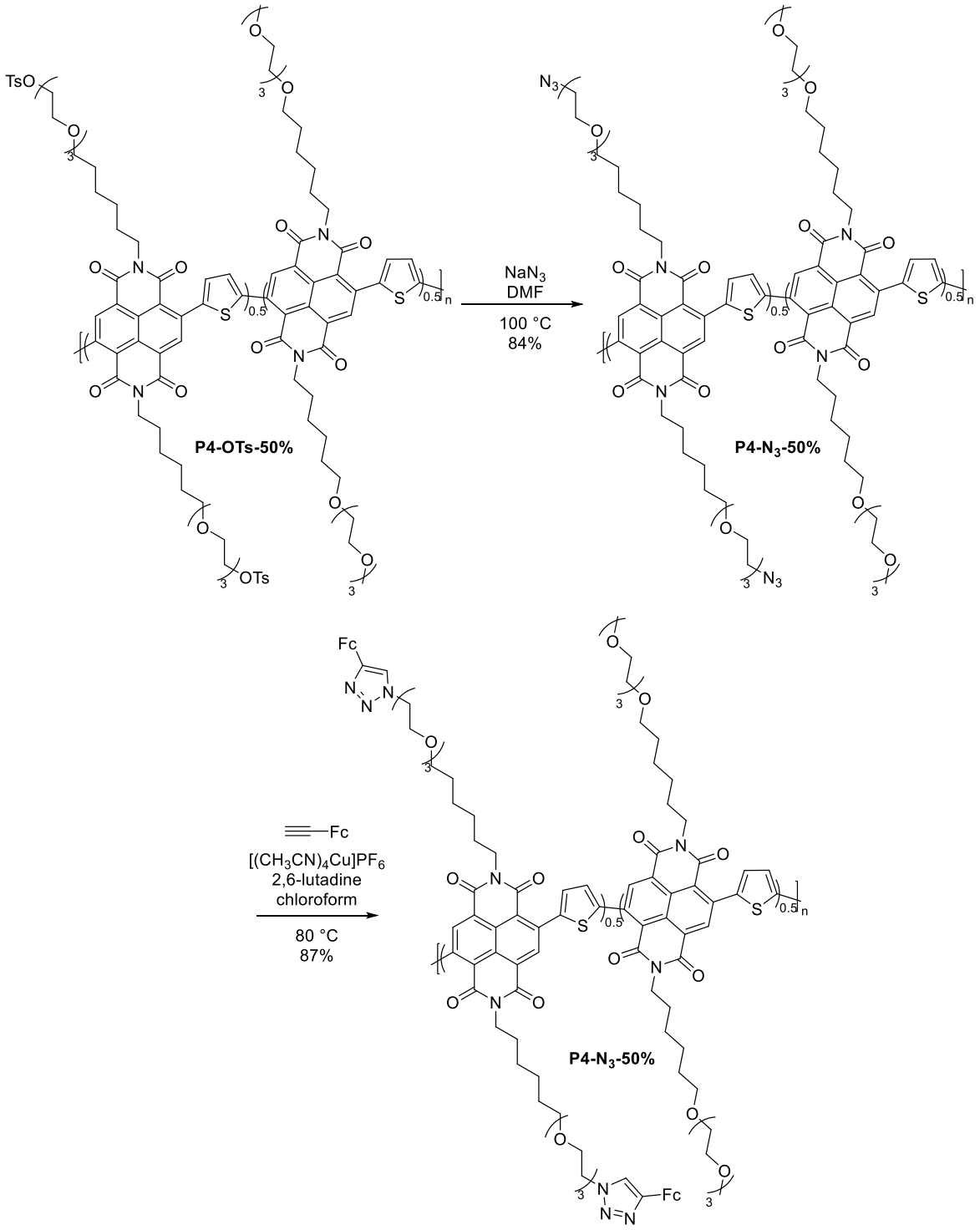


Figure A21. Synthetic route for the functionalisation of **P4-OTs-50%**, via an azide derivative, to attach ferrocene (Fc).

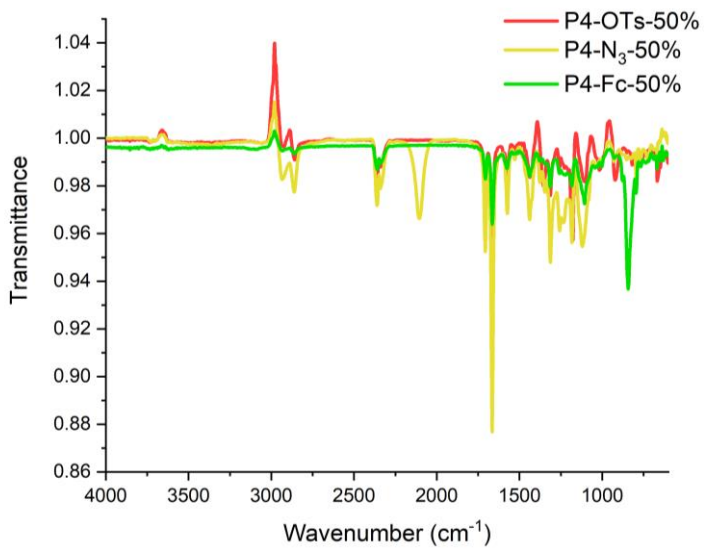


Figure A22. FTIR spectra for the progressive functionalisation of **P4-50%**, with the azide peak displayed at 2108 cm^{-1} and only present in **P4-N3-50%**.

A4.3 Optoelectronic and physical properties

The physical and optoelectronic properties of the control polymer (**pNDI-T**) and the polymer with reactive end groups, at each stage of polymer functionalisation (**P4-OTs-50%**, **P4-N3-50%** and **P4-Fc-50%**) are set out in **Table A3** and discussed herein. The molecular weight of **P4** was not repeated beyond the initial measurement as the polymer chain length was assumed to be unchanging as this was not the target for the reaction site. Furthermore, as the solubility varied somewhat throughout the functionalisation, to prevent column blockage of the GPC, it was decided that this additional data was not necessary.

Table A3. Summary of the properties of the control polymer, **pNDI-T** and the n-type functionalisable polymer at each step of functionalisation.

Polymer	M_n (kDa) [$Đ$] [a]	$E_{g,opt}$ (eV) [b]	$\lambda_{max,sol}$ (nm) [c]	EA (eV) [d]	IP (eV) [e]
pNDI-T*	17.4 [1.80]	1.72	323, 540	4.19	6.11
P4-OTs-50%	23.8 [1.80]	1.75	322, 540	4.22	6.08
P4-N_3-50%	- §	1.73	323, 539	4.22	6.10
P4-Fc-50%	- §	1.74	315, 542	4.22	- †

[a] Number-average molecular weight (M_n) and dispersity ($Đ$) measured by GPC vs polystyrene standards in chloroform at 40 °C. [b] Optical band gap estimated from thin film UV-Vis absorption onset. [c] Peak wavelength obtained from solution UV-Vis absorption spectra in chloroform. [d] The EA was calculated by finding the reduction onset potential and using it to calculate EA by: $EA = 4.8 + E_R - E_f$ where E_f = 0.44 V. Reduction onset was extracted from the cyclic voltammogram of polymer thin films on glassy carbon electrode with 0.1 M tetrabutylammonium hexafluorophosphate as the supporting electrolyte using a platinum rod counter electrode and a silver/silver chloride reference electrode. [e] Measured by photoelectron spectroscopy in air. * The data for **pNDI-T** is reproduced from **Chapter 3**. § M_n was assumed to be unchanged versus the polymer pre-functionalisation so was not remeasured. † The uniformity of the film was insufficient to obtain a reasonable PESA spectrum.

The optoelectronic properties of the functionalisable polymers further support the hypothesis that the post-polymerisation functionalisation reactions are occurring solely at the end of the sidechains as the polymer properties, largely controlled by the electronics of the polymer backbone, are consistent across the series. The shapes of the UV-Vis absorption spectra for the tosyl and azide derivatives of **P4** remain consistent with the control polymer, **pNDI-T**, both in solution and as thin films, though the peaks broaden and vary in intensity for the Fc derivative (**Figure A23**). This is due to greater accessibility of the vibrational and rotational states for the Fc-functionalised polymer, which is likely on account of the bulky end groups inhibiting adequate packing, thus providing more free space of rotation.

The thin films also all display an increasing peak to 300 nm (**Figure A23(b)**), which is indicative of Rayleigh scattering. This phenomenon is typically observed when a sample contains particles that are smaller than the wavelength of the light, thus the light is scattered by the particles and are not recorded by the detector so are artificially reported as absorbance.[42] This is typically an observation in solution, however as these measurements were conducted in very dilute solutions, this was not noted. Instead, this is seen for the thin film measurements, which may indicate that the polymers have not formed uniform thin films.

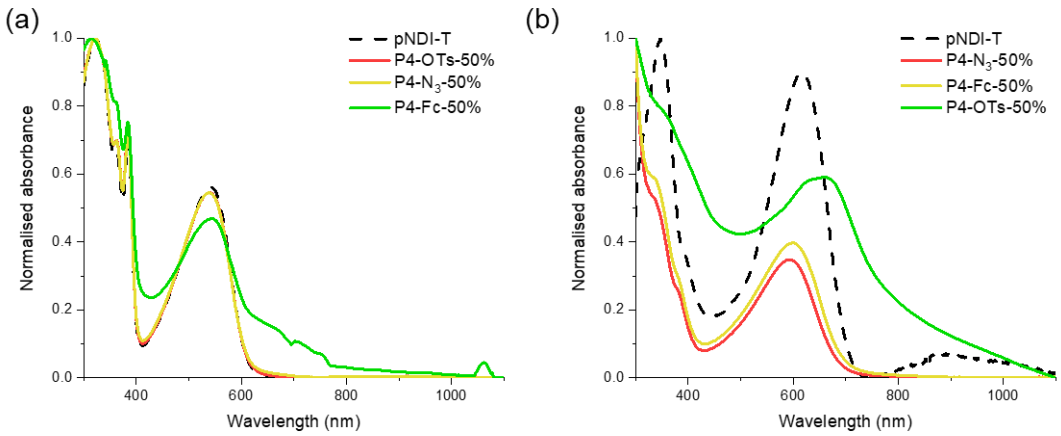


Figure A23. Normalised UV-Vis absorption spectra (a) in dilute chloroform solutions and (b) as thin films spin coated onto glass substrates at 600 rpm for 45 seconds for **pNDI-T**, **P4-OTs-50%**, **P4-N$_3$-50%** and **P4-Fc-50%**.

Next, an estimate of the HOMO was obtained using photoelectron spectroscopy in air (PESA), whereby the control polymer and all derivatives of the functionalisable polymer presented an IP of ~6.1 eV. The minor differences potentially occur from the method used to extract IP, rather than true variations in electronics of the polymers. The Fc-functionalised **P4** did not record a reasonable spectrum by PESA, likely due to the reduced solubility of this polymer compared to the other three. This resulted in a visibly non-uniform film, thus scattering dominated and a reasonable estimate for the HOMO was not achieved.

Finally, the polymers were subjected to CV in 0.1 M $TBAPF_6$ in acetonitrile to obtain the electron affinity values as an approximation for the LUMO level (**Figure A24**). Again, the values obtained for EA are constant across the series (**Table A3**), as the onset of reduction is unchanging for the three polymers. This value is also consistent with the value obtained for **pNDI-T**, indicating that the reactive end groups have a limited impact on the energy levels of the polymer.

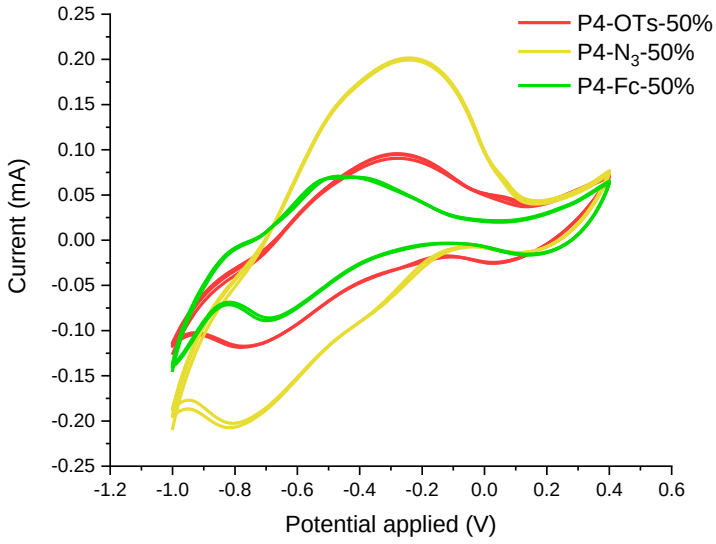


Figure A24. Cyclic voltammograms of polymer thin films of the three derivatives of **P4** on a glassy carbon working electrode vs Ag/AgCl in acetonitrile with 0.1 M tetrabutylammonium hexafluorophosphate as the supporting electrolyte, using a platinum rod counter electrode and a 0.1 Vs^{-1} scan rate. By drawing tangents to extract the reduction onset potential (E_R), EA can be calculated using: $EA = 4.8 + E_R - E_f$. E_f is the average potential of the oxidation and reduction peaks in ferrocene and was found to be 0.44 V.

A4.4 Electrochemical activity in aqueous media

Typically, without an electron mediator, a polymer in combination with an enzyme will undergo redox and generate hydrogen peroxide as a toxic by-product, when sensing is conducted in an oxygen-rich environment.[43] For the desired bioelectronic sensing applications,

it is not feasible for sensing to be conducted in an inert atmosphere, hence an alternative solution is required. In this case, ferrocene was selected as the electron mediator as it has been demonstrated to remove the dependence of the process on ambient species.[14] The novelty of this system is the covalent attachment of Fc to the OMIEC, instead of using Fc in the electrolyte solution.

First, to verify the attachment of Fc to the polymer, cyclic voltammograms were obtained using a potential window to more positive potentials of +0.8 V and a slower scan rate of 0.05 Vs^{-1} in aqueous electrolyte (0.1 M NaCl). From this, it was possible to visualise the Fc/Fc^{+} redox couple, which was expected between ~+0.4 V and +0.5 V.[44] The results are presented in **Figure A25** (solid line), where the peaks at +0.39 V and +0.52 V are observed and are ascribed to the Fc/Fc^{+} redox couple. It should be noted that the ferrocene peaks in particular are relatively unstable, with the oxidation peak being poorly defined, and the intensity of the reduction peak decreasing with each cycle. It is possible that the polymer backbone is quenching the ferrocene, for example an electron is transferred from Fc to **P4**, hence oxidation of Fc is not well defined when the potential is increased to ~+0.5 V. The lack of stability or other interference with this redox couple will hamper potential sensing applications, however as a proof-of-concept, this system was taken forward for further sensing experiments.

Next, the CV was repeated in an inert (N_2-saturated) atmosphere (**Figure A25,** dashed line) to determine whether the redox was proceeding via a ferrocene or oxygen mediator. This revealed that the peaks were sharper and more consistent on repeated cycles when operated in an inert environment, which indicates that in an ambient atmosphere, the redox process is likely proceeding via both oxygen and ferrocene mediators.

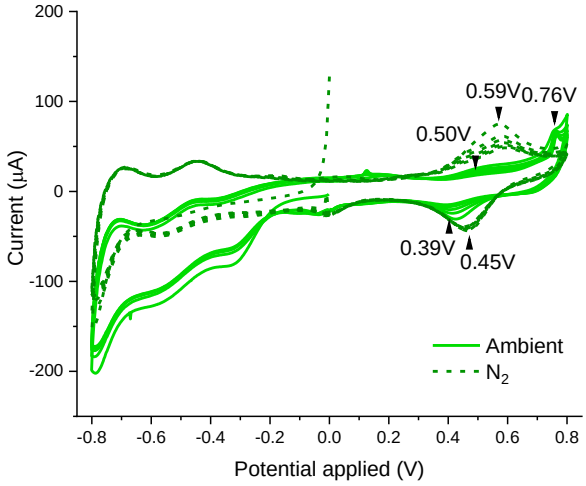


Figure A25. Cyclic voltammogram of polymer thin film of **P4-Fc-50%** on a glassy carbon working electrode vs Ag/AgCl in 0.1 M aqueous NaCl solution, using a platinum rod counter electrode and a 0.05 Vs^{-1} scan rate. The ensure uniformity of the films, films were drop cast from 1 mg/mL solutions in chloroform. The solid line indicates the voltammogram obtained under ambient conditions and the dashed line under inert, nitrogen-saturated atmosphere.

A4.5 OECT characteristics

Finally, **P4-Fc-50%** was tested for its sensing capabilities. This began by initially using the well-documented methods of fabricating an OECT device using **P4-Fc-50%** as the gate electrode and **pNDI-T** (the control polymer) as the OMIEC channel. Whilst this is not optimal due to not taking advantage of the volumetric nature of **P4-Fc-50%**, if this is proven successful for sensing, the device structure can then be developed by using the functionalisable polymer as the OMIEC layer of an OECT. The transfer and transconductance curves were recorded as usual and are presented in **Figure A26(a)**. This proves that it is possible to operate an OECT device using the ferrocene-functionalised polymer, which shows promise, despite its relatively low performance (g_m = 26.3 mS). To understand how the material acted as a sensor, the transistor substrate was then subjected to chronoamperometry experiments (**Figure A26(b)**). By applying a square wave potential and viewing the response of the device, it is possible to

see the response to stimuli. By using glucose oxidase (GOx), the enzyme capable of detecting glucose, physically adsorbed to the surface of the gate electrode, and introducing increasing concentrations of glucose, it exposes the sensing abilities of the device. The sensing range appears to begin ~1 mM, however the stabilisation time after the introduction of glucose is slow and not entirely reversible (visible by the response to each addition being a broad peak and by the baseline not flattening, respectively).

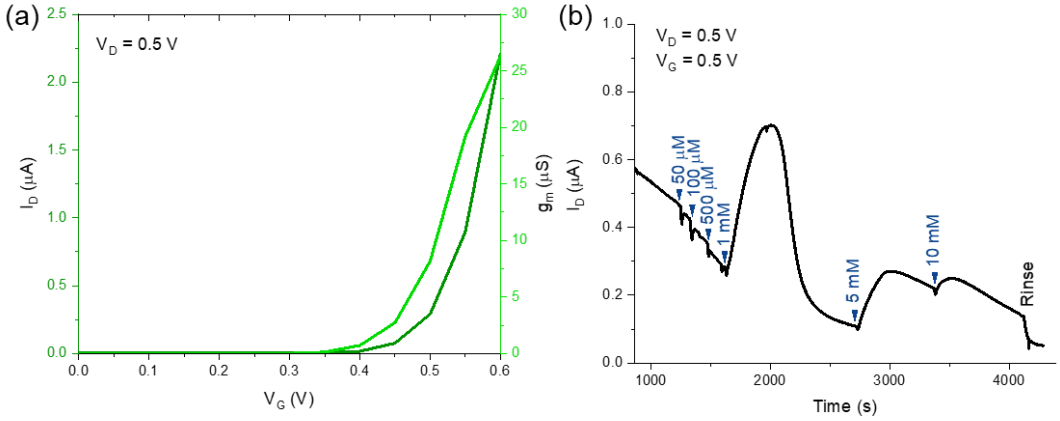


Figure A26. (a) Transfer and transconductance of OECTs averaged across 6 devices, using **P4-Fc-50%** as the gate electrode and **pNDI-T** as the channel material, where the channel dimensions are W = 50 µm and L = 50 µm in aqueous 0.1 M NaCl solution in ambient conditions. (b) Chronoamperometry measurements conducted using the same OECT device with 10 µL of glucose oxidase (GOx) in phosphate buffered saline (PBS) in the aqueous electrolyte, to which varying concentrations from 50 µM to 10 mM of glucose solution were added and the response was measured.

A4.6 Conclusions and future work

Section A4 details the work in designing, synthesising and characterising n-type polymers with reactive end groups, namely **P4-100%** and **P4-50%**. The latter was developed due to solubility issues with the former, whereby **P4-100%** pre-functionalisation was insufficiently soluble to undergo both standard characterisation and post-polymerisation reactions in solution. The **P4-**

50% series overcame these issues and azidation of the tosyl groups was successful, proven by both NMR and FTIR. From this, alkyne-azide click conditions were used to produce a solution processable derivative with ferrocene covalently attached to the sidechain termini.

Polymer characterisation indicated that both the azide and ferrocene derivates had very similar optoelectronic properties to the control polymer with methyl terminated sidechains, **pNDI-T**. The electrochemical properties of **P4-OTs-50%** and **P4-N_3-50%** were also very similar to **pNDI-T**, however when introducing the ferrocene units, the polymer displayed clear redox peaks by cyclic voltammetry for the reduction and oxidation of ferrocene. This was noticeably more reversible in an inert atmosphere, which may suggest that in ambient environments, oxygen is partially acting as a mediator for the redox process. **P4-Fc-50%** was then inserted into an OECT device as the gate electrode, with **pNDI-T** as the channel. The device switched on and recorded a reasonable transconductance of 26.3 mS. Using chronoamperometry measurements, with glucose oxidase physically adsorbed to the surface of the gate electrode, it was possible to visualise the sensing capabilities of the polymer. This technique showed that the detection level began at ~1 mM of glucose, although the stabilisation of the device was slow and was not fully reversible.

Future work for this polymer would involve measuring different thicknesses of the OMIEC with the aim of improving the stabilisation time and reversibility of the sensing regime. Furthermore, it is necessary to prove the selectivity of this polymer/mediator/enzyme combination towards glucose only, by testing other biomolecules and verifying no response. The set up should also be measured with other biorecognition units to demonstrate the versatility of this method. Beyond this, it would also be convenient to functionalise the polymer directly with the enzyme, and apply it as the semiconducting channel in the OECT device (rather than the gate electrode, as demonstrated in this work), which would allow the device to take full advantage of the bulk nature of the mixed conduction polymer. It is thought that this

might improve the detection range of the polymer, with it able to sense biomolecules at concentrations lower than 1 mM.

A5 Experimental procedures for Appendix

A5.1 General experimental

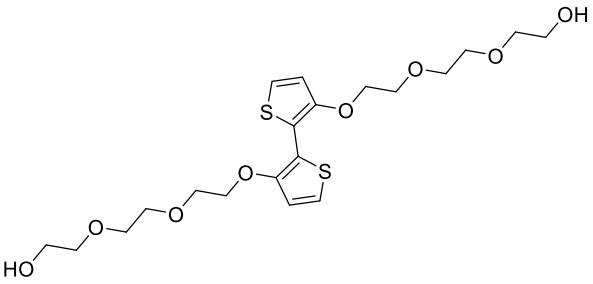
Chronoamperometry measurements. To evaluate the sensor performance, the gate electrode was functionalized with the **P4-Fc-50%** polymer (500 x 500 µm), while the channel was coated with **pNDI-T** n-type polymer. GOx in PBS (10 mg/ml) was drop cast on the device's active area (channel and gate) and left for 30 minutes to physically adsorb. The current–voltage characteristics of the devices were recorded using a Keithley 2602A dual source meter. Changes in the drain current of the OECT at a constant source–drain (V_d = 0.5 V) and gate voltages were measured in real-time. After a steady baseline was obtained for the drain current (current at zero analyte concentration), the real-time changes in response to subsequent additions of increasing concentrations of glucose into the electrolyte were monitored. For all the experiments, the electrolyte volume was kept at 40 µl. Solutions of the enzyme and glucose were stored at 4 °C.

All other measurements were conducted as per the details in Chapter 5.

A5.2 Synthetic procedures for the p-type polymer

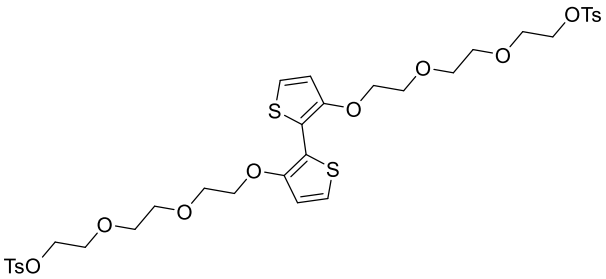
The synthesis of the p-type polymer and the relevant test reactions were conducted in part by Kate Chamberlain as partial fulfilment of her MChem degree.

*2,2'-(((((2,2'-bithiophene]-3,3'-diylbis(oxy))bis(ethane-2,1-diyl))bis(oxy))bis(ethane-2,1-diyl))bis(oxy))bis(ethan-1-ol) (**8**)*



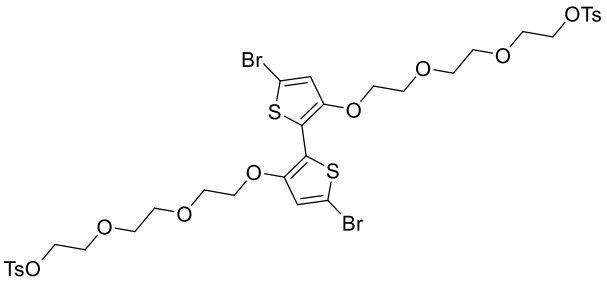
Triethylene glycol (41.8 g, 277.7 mmol, 15.0 equiv.) was added to copper iodide (0.70 g, 3.70 mmol, 0.20 equiv.) and potassium tert-butoxide (6.22 g, 55.6 mmol, 3.0 equiv.). The mixture was stirred at room temperature for 30 minutes, then 3,3'-dibromo-2,2'-bithiophene (6.00 g, 18.5 mmol, 1.0 equiv.) was added. The solution was heated at 100 °C overnight, then cooled and filtered. The reaction mixture was extracted with DCM and washed with aqueous hydrochloric acid (2 M, 100 mL), saturated ammonium chloride (100 mL), water (100 mL), and brine (100 mL). The organic phase was dried over sodium sulfate and concentrated *in vacuo*. The crude product was purified by silica column chromatography employing a 9:1 v/v mixture of ethyl acetate:methanol as the eluent (R_f = 0.15) to give the desired product as a colourless oil (5.31 g, 11.5 mmol, 62 %): ^{1}H NMR (400 MHz, $CDCl_3$) δ 7.09 (s, 2H), 6.86 (s, 2H), 4.26 (s, 4H), 3.90 (s, 4H), 3.77 – 3.66 (m, 12H), 3.62 – 3.58 (m, 4H). ^{13}C NMR (101 MHz, $CDCl_3$) δ 151.7, 122.1, 116.7, 114.7, 77.4, 77.1, 76.7, 72.5, 72.5, 71.4, 71.0, 70.5, 70.1, 61.8. HRMS (ESI-ToF): 462.1388 [$M+H^+$] (calc. 462.1380).

*((((([2,2'-bithiophene]-3,3'-diylbis(oxy))bis(ethane-2,1-diyl))bis(oxy))bis(ethane-2,1-diyl))bis(oxy))bis(ethane-2,1-diyl) bis(4-methylbenzenesulfonate) (**11**)*



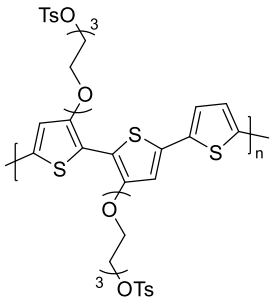
2,2'-((((([2,2'-bithiophene]-3,3'-diylbis(oxy))bis(ethane-2,1-diyl))bis(oxy))bis(ethane-2,1-diyl))bis(oxy))bis(ethan-1-ol) (2.23 g, 4.82 mmol, 1.0 equiv.) was dissolved in pyridine (40 mL) at 0 °C. P-tosyl chloride (1.92 g, 10.1 mmol, 2.1 equiv.) was added and the mixture was stirred at 0 °C for 30 minutes, then left in the fridge overnight. The solution was extracted with DCM then washed with 2M hydrochloric acid (3 x 100 mL), water (2 x 100 mL) and brine (100 mL). The organic layer was dried, filtered and concentrated *in vacuo*. The crude product was purified by silica column chromatography employing ethyl acetate as the eluent (R_f = 0.25), to yield the product as a yellow oil (3.12 g, 4.05 mmol, 84%): ^{1}H NMR (400 MHz, $CDCl_3$) δ 7.78 (d, 4H), 7.32 (d, 4H), 7.08 (d, 2H), 6.84 (d, 2H), 4.25 – 4.20 (m, 4H), 4.17 – 4.12 (m, 4H), 3.88 – 3.84 (m, 4H), 3.71 – 3.65 (m, 8H), 3.63 – 3.57 (m, 4H), 2.42 (s, 6H). ^{13}C NMR (101 MHz, $CDCl_3$): δ (ppm) 129.8, 128.0, 122.0, 116.6, 71.4, 70.9, 70.8, 70.1, 69.3, 68.8. HRMS (ESI-ToF): 770.1544 [$M+H^+$] (calc. 770.1559).

*((((((5,5'-dibromo-[2,2'-bithiophene]-3,3'-diyl)bis(oxy))bis(ethane-2,1-diyl))bis(oxy))bis(ethane-2,1-diyl))bis(oxy))bis(ethane-2,1-diyl) bis(4-methylbenzenesulfonate) (**12**)*



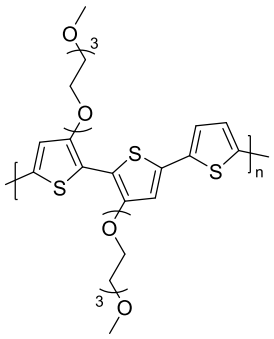
Intermediate **11** (0.80 g, 1.04 mmol, 1.0 equiv.) was dissolved in dry THF (25 mL) and the reaction mixture was cooled to 0 °C. N-bromosuccinimde (0.41 g, 2.28 mmol, 2.2 equiv.) was added in the dark and the reaction mixture was stirred for 30 minutes. The solution was diluted with DCM (100 mL) and washed with a solution of sodium hydrogen carbonate and sodium metabisulfite (3 x 75 mL), followed by water (2 x 100 mL) and brine (100 mL), then dried and concentrated *in vacuo*. The crude product was purified by silica column chromatography employing a 4:1 v/v mixture of ethyl acetate:petroleum ether as the eluent (R_f = 0.25), to give the product as a dark yellow oil (0.76 g, 0.54 mmol, 81%): ^{1}H NMR (400 MHz, Acetone-d_6) δ 7.76 (d, 4H), 7.34 (d, 4H), 6.87 (s, 2H), 4.16 (m, 4H), 4.11 (m, 4H), 3.80 (m, 4H), 3.67 – 3.60 (m, 8H), 3.58 (m, 4H), 2.42 (s, 6H). ^{13}C NMR (101 MHz, Acetone-d_6) δ 151.7, 145.9, 131.0, 128.9, 121.2, 110.5, 72.8, 71.5, 71.5, 70.8, 70.8, 69.6, 30.6, 30.4, 30.2, 30.0, 29.8, 29.6, 29.4, 21.7. HRMS (ESI-ToF): 927.9800 [M+H$^+$] (calc. 927.9744).

P3-OTs-100%



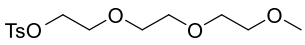
Monomer **12** (95.1 mg, 102 µmol, 1.0 equiv.), 2,5-bis(trimethylstannyl)thiophene (42.00 mg, 102 µmol, 1.0 equiv.), tris(dibenzylideneacetone)dipalladium(0) (1.9 mg, 2.15 µmol, 0.02 equiv.) and tris(o-methoxyphenyl)phosphine (2.9 mg, 8.61 µmol, 0.08 equiv.) were dissolved in dry DMF (1.4 mL). The solution was degassed for 10 minutes then heated at 110 °C overnight. The mixture was cooled room temperature, suspended in chloroform (5 mL) and precipitated in a 1:1 v/v mixture of EA and hexane (60mL). It was filtered through a thimble and then Soxhlet extractions were carried out in hexane, EA, acetone, and chloroform. Excess solvent of the chloroform fraction was removed under reduced pressure. The product was re-dissolved in the minimum amount of chloroform then precipitated in a 1:1 v/v mixture of EA and hexane (40 mL). **P3-OTs-100%** was collected by filtration as a dark purple solid (62.47 mg, 73.4 µmol, 72%): ^{1}H NMR (400 MHz, DMSO) δ 7.49 (d), 7.30 (m), 7.12 (d), 4.36 (br s), 4.18 (br s), 3.85-3.52 (m), 2.29 (s). GPC (DMF, 40 °C): M_n = 19.2 kDa, M_w = 25.5 kDa.

p(g$_3$T2-T)



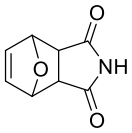
p(g$_3$T2-T) was synthesised according to literature procedures[21,23] and used as a control polymer. GPC (DMF, 40 °C): M_n = 22.2 kDa, M_w = 34.9 kDa.

*2-(2-(2-methoxyethoxy)ethoxy)ethyl 4-methylbenzenesulfonate (**g$_3$OTs**)*



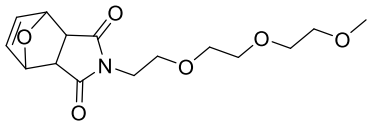
Triethylene glycol monomethyl ether (5.00 g, 30.5 mmol, 1.0 equiv.) was dissolved in pyridine (20 mL) and the mixture was cooled to 0 °C. 4-Toluenesulfonyl chloride (6.97 g, 36.5 mmol, 1.2 equiv.) was added in three portions and stirred at 0 °C for 30 mins. The reaction was then left in the fridge overnight, before quenching with HCl (2 M, 100 mL), then extracted into DCM (200 mL). The organic layer was washed with HCl (2 M, 3 x 100 mL), water (3 x 150 mL), then brine (1 x 150 mL), before drying over Na_2SO_4. The solvent was removed under reduced pressure and the crude product was pure and used without further purification as a colourless oil (7.17 g, 22.5 mmol, 74% yield): ^{1}H NMR (400 MHz, $CDCl_3$) δ 7.80 (d, J = 8 Hz, 2H), 7.34 (d, J = 8 Hz, 2H), 4.16 (t, J = 4.8 Hz, 2H), 3.69 (t, J = 4.8 Hz, 2H), 3.63 – 3.58 (m, 6H), 3.54 – 3.51 (m, 2H), 3.37 (s, 3H), 2.45 (s, 3H); ^{13}C NMR (101 MHz, $CDCl_3$) δ 144.7, 132.9, 129.8, 127.8, 127.8, 71.8, 70.6, 70.4, 69.2, 68.5, 58.9, 21.5. HRMS (ESI-ToF): 318.1137 [M+H$^+$] (calc. 318.1171).

*10-oxa-4-azatricyclo[5.2.1.0,2,6]dec-8-ene-3,5-dione (**13**)*



Maleimide (9.99g, 103 mmol, 1.0 equiv.) was dissolved in toluene (60 mL). Furan (12.8 g, 216 mmol, 2.1 equiv.) was added to the solution, which was then stirred at 90 °C overnight. After cooling the reaction mixture to room temperature, the resulting precipitate was filtered and washed with toluene. The precipitate was dried *in vacuo*, giving the product as a white powder (14.1 g, 85.4 mmol, 83%): ^{1}H NMR (400 MHz, $CDCl_3$) δ 7.98 (s, 1H), 6.52 (t, *J* = 1.0 Hz, 2H), 5.32 (t, *J* = 1.0 Hz, 2H), 2.89 (s, 2H). ^{13}C NMR (101 MHz, $CDCl_3$) δ 175.8, 136.6, 81.0, 48.7. HRMS (ESI-ToF): 165.0428 [$M+H^+$] (calc. 165.0422).

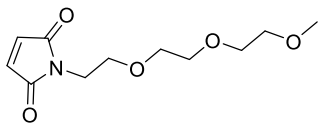
*2-(2-(2-(2-methoxyethoxy)ethoxy)ethyl)-3a,4,7,7a-tetrahydro-1H-4,7-epoxyisoindole-1,3(2H)-dione (**14**)*



10-oxa-4-azatricyclo[5.2.1.0,2,6]dec-8-ene-3,5-dione (0.39 g, 2.38 mmol, 1.5 equiv.) and potassium carbonate (0.33 g, 2.36 mmol, 1.5 equiv.) were dissolved in dry DMF (40 mL). The solution was stirred under nitrogen and then 1 (0.50g, 1.57 mmol, 1.0 equiv.) was added dropwise. The reaction mixture was stirred overnight at 50 °C then cooled and extracted into DCM (100 mL) and washed with water (3 x 100 mL) and brine (100 mL). The organic layer was dried and concentrated *in vacuo*, to obtain the product as a yellow oil (0.68 g, 2.19 mmol, 92%): ^{1}H NMR (400 MHz, $CDCl_3$) δ 6.51 (s, 2H), 5.26 (s, 2H), 3.69 (d, *J* = 12.8 Hz, 2H), 3.64 (s, 8H), 3.53 (d, *J* = 9.7 Hz, 2H), 3.37 (s, 3H), 2.85 (s, 2H). ^{13}C NMR (101 MHz, $CDCl_3$) δ

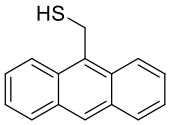
176.1, 136.6, 80.9, 72.0, 70.6, 70.1, 67.1, 59.0, 47.5, 38.2. HRMS (ESI-ToF): 311.1340 [M+H$^+$] (calc. 311.1369).

*1-(2-(2-(2-methoxyethoxy)ethoxy)ethyl)-1H-pyrrole-2,5-dione (**15**)*



Toluene (20 mL) was added to 2-(2-(2-(2-methoxyethoxy)ethoxy)ethyl)-3a,4,7,7a-tetrahydro-1H-4,7-epoxyisoindole-1,3(2H)-dione (2.61 g, 8.51 mmol, 1.0 equiv.). The reaction mixture was stirred under nitrogen at 120 °C overnight. It was then cooled and the solvent was removed to afford the product (1.95g, 8.01 mmol, 94%) as a brown oil: ^{1}H NMR (400 MHz, $CDCl_3$) δ 6.69 (s, 2H), 3.73 (d, *J* = 12.3 Hz, 2H), 3.66 – 3.58 (m, 8H), 3.53 (d, *J* = 9.7 Hz, 2H), 3.37 (s, 3H). ^{13}C NMR (101 MHz, $CDCl_3$) δ 170.7, 134.1, 77.3, 77.0, 76.7, 71.9, 70.6, 70.1, 67.8, 59.0, 37.2. HRMS (ESI-ToF): 243.1100 [M+H$^+$] (calc. 243.1111).

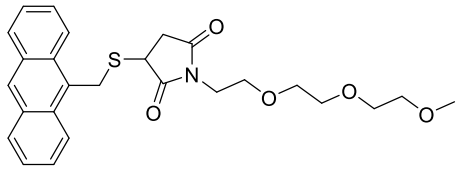
*Anthracene-9-ylmethanethiol (**16**)*



Anthracene-9-ylmethanethiol was synthesised following a procedure detailed in literature.[33] 9-(chloromethyl)anthracene (1.00 g, 4.41 mmol, 1.0 equiv.) and thiourea (0.67 g, 8.82 mmol, 2.0 equiv.) were dissolved in ethanol (10 mL). The reaction mixture was stirred at 80 °C for 2 h and a yellow precipitate formed. The mixture was cooled, filtered and the collected precipitate washed with diethyl ether. The precipitate was dissolved in ethanol (10 mL) and aqueous sodium hydroxide (3 M, 5 mL) was added. The mixture was refluxed for 1 h at 110 °C then cooled and filtered. On addition of a solution of hydrochloric acid (2 mL) in water (5 mL), a precipitate formed, which was then filtered and washed with water. The crude product was

extracted into DCM and washed with water (3 x 100 mL) and brine (100 mL). The organic layer was dried over magnesium sulfate and concentrated *in vacuo*, before being recrystallised from acetonitrile to yield the product as a yellow solid (0.328 g, 1.46 mmol, 33%): ^{1}H NMR (400 MHz, $CDCl_3$) δ 8.41 (s, 1H), 8.27 (dq, *J* = 8.9, 1.0 Hz, 2H), 8.06 – 7.96 (m, 2H), 7.59 (ddd, *J* = 8.9, 6.5, 1.4 Hz, 2H), 7.53 – 7.44 (m, 2H), 4.74 (d, *J* = 6.8 Hz, 2H), 1.97 (t, *J* = 6.8 Hz, 1H). ^{13}C NMR (101 MHz, $CDCl_3$) δ 151.73, 122.06, 116.66, 114.73, 77.37, 77.05, 76.73, 72.49, 72.47, 71.38, 70.97, 70.46, 70.07, 61.78. LS-GCMS *m*/*z* (ESI^+) 224.1 $[M + H]^+$.

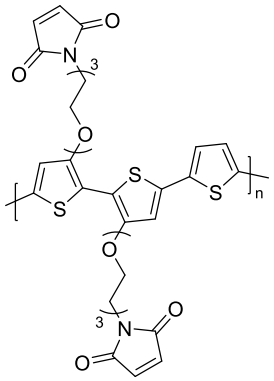
3-((anthracen-9-ylmethyl)thio)-1-(2-(2-(2-methoxyethoxy)ethoxy)ethyl)pyrrolidine-2,5-dione ***(17)***



To a solution of **g_3OTs** (0.15 g, 0.67 mmol, 1.0 equiv.) in 1:1 water:acetonitrile + 0.1% TFA (50 mL), a solution of anthracene-9-ylmethanethiol (0.16 g, 0.67 mmol, 1.0 equiv.) in 2:1 acetonitrile:acetone (80 mL) was added. The pH of the reaction mixture was adjusted to 6.8-7.4 using phosphate buffered saline (PBS) solution (150 mL) before the mixture was stirred at room temperature for 2 h. The mixture was extracted into DCM, washed with water (3 x 100 mL) and brine (100 mL), and the organic phase was dried, filtered and concentrated *in vacuo*. The crude product was purified by column chromatography to give the title compound as a yellow oil (0.27 g, 0.60 mmol, 90%): ^{1}H NMR (400 MHz, CDCl3) δ 8.44 – 8.35 (m, 3H), 8.01 (ddt, J = 8.4, 1.4, 0.7 Hz, 2H), 7.58 (ddd, J = 8.9, 6.5, 1.4 Hz, 2H), 7.48 (ddd, J = 8.4, 6.5, 1.1 Hz, 2H), 5.20 – 5.07 (m, 2H), 3.86 (dd, J = 9.3, 4.1 Hz, 1H), 3.81 (dd, J = 6.7, 5.4 Hz, 2H), 3.73 (ddd, J = 6.7, 5.2, 2.1 Hz, 2H), 3.67 – 3.62 (m, 2H), 3.61 – 3.53 (m, 4H), 3.49 – 3.44 (m, 2H), 3.33 (s, 3H), 3.08 – 2.96 (m, 1H), 2.48 – 2.37 (m, 1H). ^{13}C NMR (101 MHz, CDCl3) δ

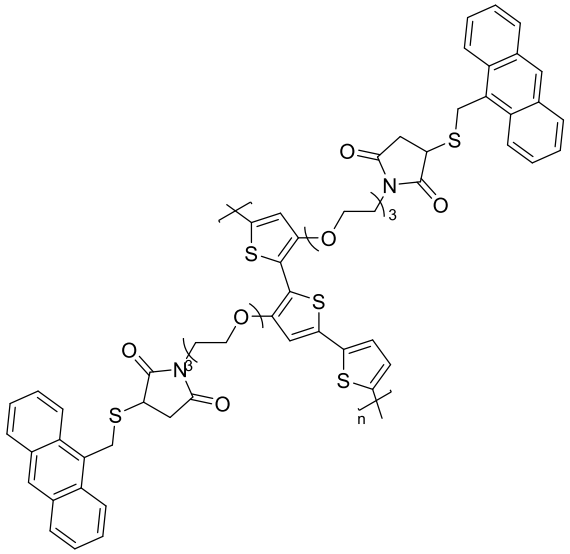
177.4, 174.6, 131.6, 130.3, 129.4, 128.1, 127.6, 126.7, 125.3, 124.1, 72.0, 70.7, 70.6, 70.2, 67.1, 59.1, 39.6, 38.6, 35.9, 29.0. HRMS (ESI-ToF): 467.1787 [M+H^+] (calc. 467.1766).

P3-Mal-100%



10-oxa-4-azatricyclo[5.2.1.0,2,6]dec-8-ene-3,5-dione (5.79 mg, 35.1 µmol, 1.5 equiv.) and potassium carbonate (4.85 mg, 35.1 µmol, 1.5 equiv.) were dissolved in dry DMF (1.5 mL). The solution was stirred under nitrogen and then **P3-OTs-100%** (20.00 mg, 23.4 µmol, 1.0 equiv.) was added dropwise. The reaction mixture was stirred overnight at 50 °C then cooled, precipitated into methanol and filtered. The polymer was then dispersed in toluene (2 mL) and the reaction mixture was stirred at 120 ℃ overnight. The solution was then cooled, precipitated into methanol and filtered to afford the product as a purple solid (14.41 mg, 20.59 µmol, 88%): ^{1}H NMR (400 MHz, $CDCl_3$) δ ^{1}H NMR (400 MHz, DMSO) δ 7.30 (m), 6.69 (s), 4.36 (br s), 4.18 (br s), 3.85-3.52 (m).

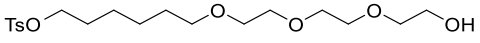
P3-Anth-100%



P3-Mal-100% (10.00 mg, 11.8 µmmol, 1.0 equiv.), anthracene-9-ylmethanethiol (15.8 mg, 70.5 µmmol, 6.0 equiv.) and potassium hydroxide (16.91 mg, 72.9 µmmol, 6.2 equiv.) were added to a microwave vial, to which DMF (1.5 mL) and water (0.1 mL) were added. After stirring the reaction mixture at room temperature overnight, it was precipitated in a 1:1 v/v mixture of EA:hexane (60 mL). The resulting precipitate was filtered and washed with methanol (4 x 50 mL) to afford the polymer functionalised with anthracene, **P3-Anth-100%** (11.21 mg, 11.2 µmmol, 95%): no conclusive NMR was obtained due to the insolubility of the material.

A5.3 Synthetic procedures for the n-type polymer

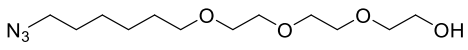
*6-(2-(2-(2-hydroxyethoxy)ethoxy)ethoxy)hexyl 4-methylbenzenesulfonate (**19**)*



Sodium hydride (60%, 6.19 g, 155 mmol, 1.1 equiv.) was dissolved in dry THF (500 mL) and the reaction mixture was cooled to 0 °C. Triethylene glycol (18.8 mL, 141 mmol, 1.0 equiv.) was added dropwise, then the mixture was brought to room temperature and stirred for 30 minutes. The reaction mixture was heated to 65 °C for 1 hour, then cooled back to 0 °C.

Hexane-1,6-diyl bis(4-methylbenzenesulfonate) (60.0 g, 141 mmol, 1.0 equiv.) was then added in four portions and the reaction mixture was then stirred at room temperature for 1 hour, then heated to 55 °C overnight. The reaction was then cool to room temperature and poured over ice water. This mixture was extracted with chloroform (2 x 250 mL), then the organic portion was washed with water (3 x 250 mL) and brine (1 x 200 mL) and dried over Na_2SO_4. The solvent was removed *in vacuo* and the crude product was purified by silica column chromatography employing ethyl acetate as the solvent system (R_f = 0.30). The final product was dried by high vacuum and obtained as a colourless oil (11.4 g, 28.1 mmol, 20% yield): ^{1}H NMR (400 MHz, $CDCl_3$) δ 7.82 – 7.75 (m, 2H), 7.39 – 7.31 (m, 2H), 4.02 (t, *J* = 6.5 Hz, 2H), 3.72 – 3.55 (m, 12H), 3.47 – 3.36 (m, 2H), 2.45 (s, 3H), 1.64 – 1.51 (m, 4H), 1.36 – 1.29 (m, 4H); ^{13}C NMR (101 MHz, $CDCl_3$) δ 144.6, 133.3, 129.8, 127.9, 72.5, 71.2, 70.6, 70.6, 70.6, 70.4, 70.1, 61.8, 29.3, 28.8, 25.5, 25.2, 21.6. HRMS (ESI-ToF): 405.5181 [M+H$^+$] (calc. 405.5184).

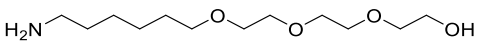
*2-(2-(2-((6-azidohexyl)oxy)ethoxy)ethoxy)ethan-1-ol (**20**)*



6-(2-(2-(2-hydroxyethoxy)ethoxy)ethoxy)hexyl 4-methylbenzenesulfonate (11.3 g, 27.9 mmol, 1.0 equiv.) was dissolved in dry DMF (90 mL) and cool to 0 °C. To this, sodium azide (2.70 g, 41.9 mmol, 1.5 equiv.) was added and the mixture was heated to 100 °C for 2 hours. The reaction mixture was then cooled to room temperature and ethyl acetate (400 mL) was added. The precipitate was filtered and the filtrate was washed with water (3 x 300 mL) and brine (1 x 250 mL) and dried over Na_2SO_4, before the solvent was removed *in vacuo*. The crude product was pure and used directly without further purification as a colourless oil (7.51 g, 27.2 mmol, 97% yield): ^{1}H NMR (400 MHz, $CDCl_3$) δ 3.75 – 3.53 (m, 10H), 3.45 (t, *J* = 6.7 Hz, 2H), 3.25 (t, *J* = 6.9 Hz, 2H), 1.59 (tddd, *J* = 8.7, 6.0, 4.4, 2.5 Hz, 4H), 1.45 – 1.30 (m, 4H);

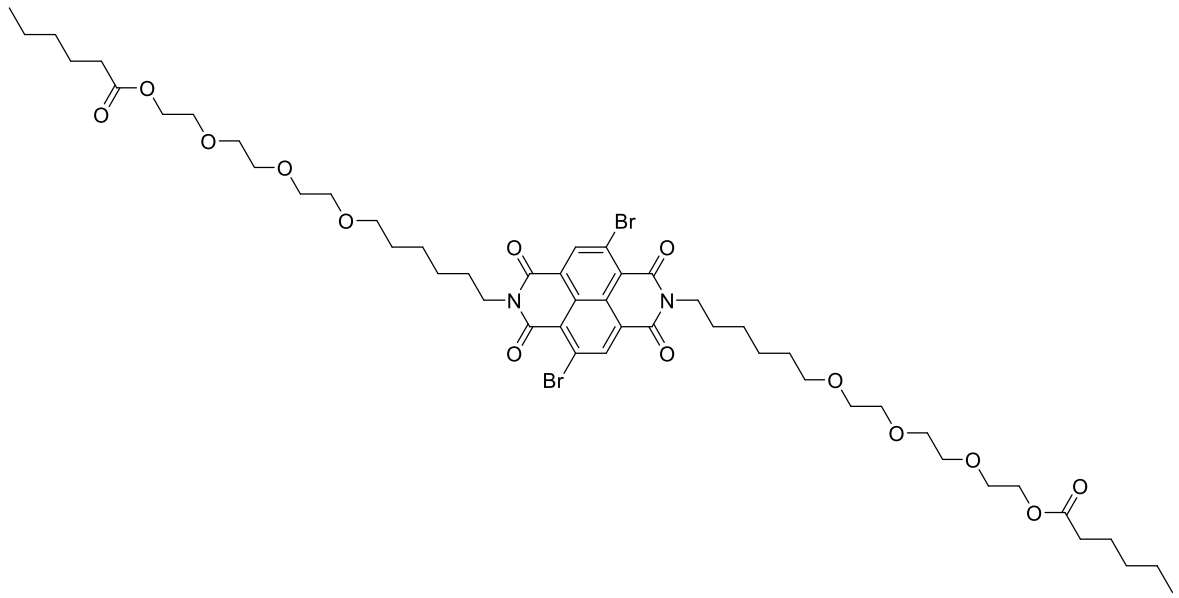
^{13}C NMR (101 MHz, $CDCl_3$) δ 72.6, 71.4, 70.8, 70.7, 70.5, 70.3, 70.2, 61.9, 51.5, 29.6, 28.9, 26.7, 25.8. HRMS (ESI-ToF): 276.3492 [M+H$^+$] (calc. 276.3499).

*2-(2-(2-((6-aminohexyl)oxy)ethoxy)ethoxy)ethan-1-ol (**21**)*



2-(2-(2-((6-azidohexyl)oxy)ethoxy)ethoxy)ethan-1-ol (7.50 g, 27.2 mmol, 1.0 equiv.) was dissolved in dry THF (100 mL) and cooled to 0 °C. Triphenylphosphine (10.7 g, 40.9 mmol, 1.5 equiv.) was added in and the mixture was stirred at room temperature for 2 hours. The reaction mixture was heated to 50 °C for 1 hour, then returned to room temperature, before deionised water (0.5 mL) was added. The reaction was stirred overnight at room temperature, then diluted with water (200 mL). The aqueous portion was washed with diethyl ether (3 x 250 mL), then concentrated *in vacuo* to obtain the pure product as a pale yellow oil (5.72 g, 22.9 mmol, 84% yield): ^{1}H NMR (400 MHz, $CDCl_3$) δ 3.77 – 3.70 (m, 2H), 3.67 – 3.57 (m, 10H), 3.49 – 3.43 (m, 2H), 2.71 (t, *J* = 6.9 Hz, 2H), 2.24 (br s, 2H), 1.62 – 1.56 (m, 2H), 1.51 – 1.43 (m, 2H), 1.36 (p, *J* = 3.7 Hz, 4H); ^{13}C NMR (101 MHz, $CDCl_3$) δ 72.8, 71.5, 70.8, 70.5, 70.2, 70.1, 61.7, 41.9, 33.1, 29.5, 26.5, 26.1. HRMS (ESI-ToF): 250.3520 [M+H$^+$] (calc. 250.3518).

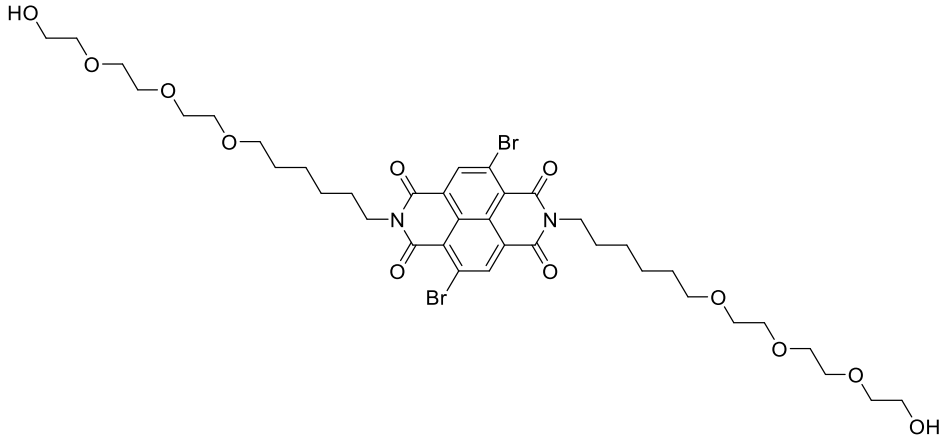
*(((((((4,9-dibromo-1,3,6,8-tetraoxo-1,3,6,8-tetrahydrobenzo[lmn][3,8]phenanthroline-2,7-diyl)bis(hexane-6,1-diyl))bis(oxy))bis(ethane-2,1-diyl))bis(oxy))bis(ethane-2,1-diyl))bis(oxy))bis(ethane-2,1-diyl) dihexanoate (**22**)*



2,6-dibromonaphthalene-1,4,5,8-tetracarboxylic dianhydride ($NDABr_2$, 0.621 g, 1.46 mmol, 1.0 equiv.) was suspended in anhydrous *o*-xylene (14 mL) and hexanoic acid (3.3 mL, 26.3 mmol, 18 equiv.) was added. The reaction mixture was heated to 100 °C, then 2-(2-(2-((6-aminohexyl)oxy)ethoxy)ethoxy)ethan-1-ol (0.800 g, 3.21 mmol, 2.2 equiv.) was added dropwise. The solution was heated to 125 °C for 2 hours, then cooled to room temperature and diluted with chloroform (100 mL). The reaction mixture was washed with water (3 x 100 mL), dried over magnesium sulfate and the excess solvent was removed under reduced pressure. The crude product was purified using silica column chromatography employing a 2:3 v/v mixture of ethyl acetate:petroleum ether as the solvent system (R_f = 0.20). The final product was obtained as a pale yellow solid (0.790 g, 0.728 mmol, 50% yield): ^{1}H NMR (400 MHz, $CDCl_3$) δ 8.99 (s, 2H), 4.23 – 4.21 (m, 4H), 3.72 – 3.68 (m, 4H), 3.67 – 3.62 (m, 16H), 3.58 (dt, *J* = 6.0, 2.5 Hz, 4H), 3.46 (t, *J* = 6.7 Hz, 4H), 2.31 (t, *J* = 7.6 Hz, 4H), 1.74 (q, *J* = 7.4 Hz, 4H), 1.66 – 1.56 (m, 8H), 1.43 (q, *J* = 3.0 Hz, 8H), 1.30 (tt, *J* = 5.6, 3.0 Hz, 8H), 0.92 – 0.86 (m,

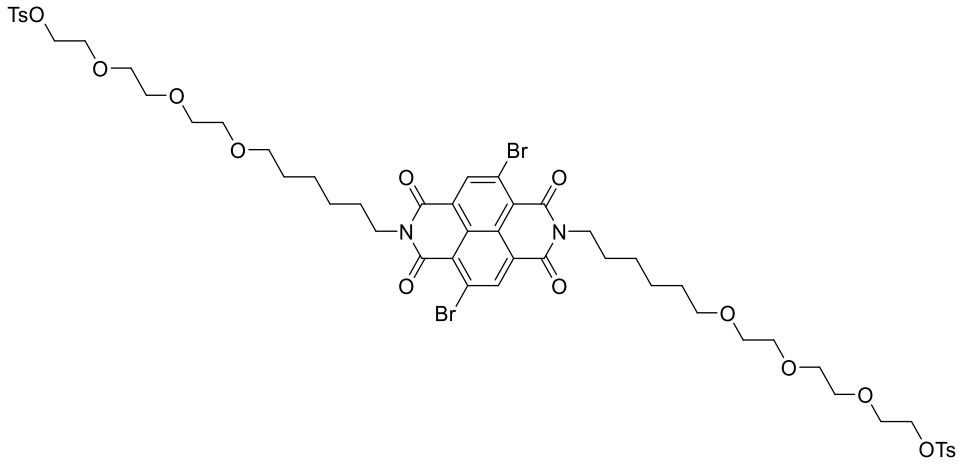
6H); ^{13}C NMR (101 MHz, $CDCl_3$) δ 160.7, 139.1, 128.3, 71.3, 70.7, 70.6, 70.6, 70.1, 69.2, 63.4, 41.5, 34.2, 31.3, 29.5, 27.9, 26.9, 25.8, 24.6, 22.3, 13.9. HRMS (ESI-ToF): 1085.9349 [M+H$^+$] (calc. 1085.9332).

4,9-dibromo-2,7-bis(6-(2-(2-(2-hydroxyethoxy)ethoxy)ethoxy)hexyl)benzo[lmn][3,8]phenanthroline-1,3,6,8(2H,7H)-tetraone ***(23)***



(((((((4,9-dibromo-1,3,6,8-tetraoxo-1,3,6,8-tetrahydrobenzo[lmn][3,8]phenanthroline-2,7-diyl)bis(hexane-6,1-diyl))bis(oxy))bis(ethane-2,1-diyl))bis(oxy))bis(ethane-2,1-diyl))bis(oxy))bis(ethane-2,1-diyl) dihexanoate (0.680 mg, 0.627 mmol, 1.0 equiv.) was dissolved in a mixture of chloroform (20 mL) and methanol (20 mL) under an ambient atmosphere. To this, concentrated hydrochloric acid (2 mL) was added and the reaction mixture was heated to 70 °C overnight. The reaction mixture was then cooled to room temperature and diluted with chloroform (100 mL). The organic fraction was washed with water (3 x 80 mL) and dried over Na_2SO_4 before the solvent was removed *in vacuo* to isolate the product as a yellow solid (0.547 mg, 0.616 mmol, 98% yield): ^{1}H NMR (400 MHz, $CDCl_3$) δ 8.92 (s, 2H), 4.17 – 4.07 (m, 4H), 3.69 – 3.49 (m, 24H), 3.40 (t, *J* = 6.6 Hz, 4H), 1.67 (q, *J* = 7.3 Hz, 4H), 1.55 (t, *J* = 6.7 Hz, 4H), 1.37 (dq, *J* = 6.7, 3.8 Hz, 8H); unable to obtain ^{13}C NMR in chloroform-*d* or dimethyl sulfoxide-d_6.

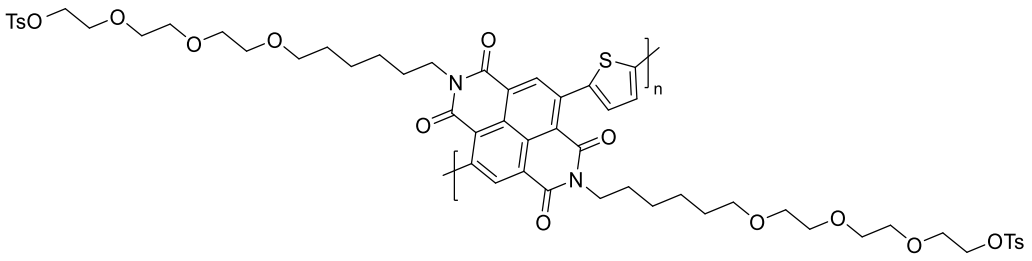
*(((((((4,9-dibromo-1,3,6,8-tetraoxo-1,3,6,8-tetrahydrobenzo[lmn][3,8]phenanthroline-2,7-diyl)bis(hexane-6,1-diyl))bis(oxy))bis(ethane-2,1-diyl))bis(oxy))bis(ethane-2,1-diyl))bis(oxy))bis(ethane-2,1-diyl) bis(4-methylbenzenesulfonate) (**24**)*



4,9-dibromo-2,7-bis(6-(2-(2-(2-hydroxyethoxy)ethoxy)ethoxy)hexyl)benzo[lmn][3,8]phenanthroline-1,3,6,8(2H,7H)-tetraone (0.622 g, 0.700 mmol, 1.0 equiv.) and 4-dimethylaminopyridine (36.2 mg, 0.296 mmol, 0.4 equiv.) were dissolved in dry DCM (20 mL). Subsequently, triethylamine (72.2 µL, 0.518 mmol, 0.7 equiv.) was added and the reaction mixture was cooled to 0 °C. Separately, 4-toluenesulfonyl chloride (0.667 g, 3.50 mmol, 5.0 equiv.) was dissolved in 20 mL dry DCM, and this was added to the original mixture. The reaction mixture was stirred at room temperature for 72 hours. It was then diluted with DCM (100 mL) and washed with water (3 x 120 mL) and brine (100 mL) before drying over Na_2SO_4 and removing the solvent under reduced pressure. The crude product was purified using silica column chromatography employing a 7:3 v/v mixture of ethyl acetate:petroleum ether as the solvent system, gradually increasing to a 92:8 v/v mixture of ethyl acetate:methanol to isolate the pure product as a yellow solid (99.9 mg, 82.7 µmol, 11% yield): ^{1}H NMR (400 MHz, $CDCl_3$) δ 8.96 (s, 2H), 7.80 – 7.71 (m, 4H), 7.37 – 7.29 (m, 4H), 4.19 – 4.15 (m, 4H), 3.70 – 3.65 (m, 4H), 3.61 – 3.53 (m, 20H), 3.44 (t, *J* = 6.6 Hz, 4H), 2.44 (s, 6H), 1.74 (p, *J* = 7.5 Hz, 4H), 1.60 (q, *J* = 6.7 Hz, 4H), 1.48 –

1.38 (m, 8H); ^{13}C NMR (101 MHz, $CDCl_3$) δ 171.2, 160.9, 160.9, 144.9, 139.1, 136.7, 133.2, 129.9, 128.4, 128.1, 127.9, 125.5, 124.2, 81.1, 71.4, 70.9, 70.8, 70.7, 70.2, 69.4, 68.8, 60.5, 47.8, 41.6, 29.6, 28.00, 27.1, 26.0, 21.8, 21.2, 14.3. HRMS (ESI-ToF): 1098.0068 [$M+H^+$] (calc. 1098.2071).

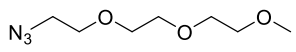
P4-OTs-100%



(((((((4,9-dibromo-1,3,6,8-tetraoxo-1,3,6,8-tetrahydrobenzo[lmn][3,8]phenanthroline-2,7-diyl)bis(hexane-6,1-diyl))bis(oxy))bis(ethane-2,1-diyl))bis(oxy))bis(ethane-2,1-diyl))bis(oxy))bis(ethane-2,1-diyl) bis(4-methylbenzenesulfonate) (38.56 mg, 0.032 mmol, 1.0 equiv.), 2,5-bis(trimethylstannyl)thiophene (13.20 mg, 0.032 mmol, 1.0 equiv.), tris(dibenzylideneacetone)dipalladium(0) (0.59 mg, 0.644 μmol, 0.02 equiv.) and tris(*o*-methoxyphenyl)phosphine (0.91 mg, 2.58 μmol, 0.08 equiv.) were dissolved in anhydrous degassed chlorobenzene (1 mL). The resulting solution was degassed for an additional 10 minutes and the reaction was heated 130 °C overnight. The crude polymer solution was cooled to room temperature and precipitated into a 2:1 v/v mixture of ethyl acetate:hexane, and the polymer was purified via Soxhlet extractions with: hexane, ethyl acetate, acetone and methanol. The polymer was extracted in chloroform and excess solvent was removed *in vacuo*. The final product was collected by reprecipitating the polymer into a 2:1 v/v mixture of ethyl acetate:hexane and collecting it by suction filtration. **P4-OTs-100%** was obtained as a dark blue solid (27.02 mg, 0.0240 mmol, 75% yield): ^{1}H NMR (400 MHz, $CDCl_3$) δ 8.95 (br s, 2H), 7.74 (d, *J* = 7.8 Hz, 4H), 7.47 (br s, 2H), 7.31 (d, *J* = 7.8 Hz, 4H), 4.27 – 4.05 (m, 8H), 3.72 –

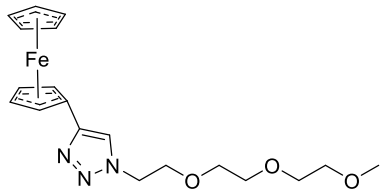
3.63 (m, 4H), 3.63 – 3.49 (m, 16H), 3.44 (t, J = 6.5 Hz, 4H), 2.43 (s, 6H), 1.75 (s, 8H), 1.43 (s, 8H); GPC (chloroform, 40 °C): M_n = 14.6 kDa, M_w = 23.2 kDa.

*1-azido-2-(2-(2-methoxyethoxy)ethoxy)ethane (**g₃N₃**)*



2-(2-(2-methoxyethoxy)ethoxy)ethyl 4-methylbenzenesulfonate (2.00 g, 6.29 mmol, 1.0 equiv.) was dissolved in dry DMF (30 mL) and cooled to 0 °C. Sodium azide (0.613 g, 9.43 mmol, 1.5 equiv.) was added, then the reaction mixture was heated to 100 °C for 2 hours. Subsequently, the reaction mixture was cooled to room temperature and ethyl acetate (200 mL) was added. The precipitate was filtered and the filtrate was washed with water (3 x 200 mL) and brine (1 x 150 mL) and dried over Na_2SO_4, before the solvent was removed *in vacuo*. The crude product was pure and used directly without further purification as a colourless oil (0.690 g, 3.65 mmol, 58% yield): ^{1}H NMR (400 MHz, $CDCl_3$) δ 3.71 – 3.63 (m, 8H), 3.58 – 3.52 (m, 2H), 3.41 – 3.36 (m, 5H); ^{13}C NMR (101 MHz, $CDCl_3$) δ 72.1, 70.9, 70.8, 70.7, 70.2, 59.2, 50.8. HRMS (ESI-ToF): 190.2139 [M+H$^+$] (calc. 190.2130).

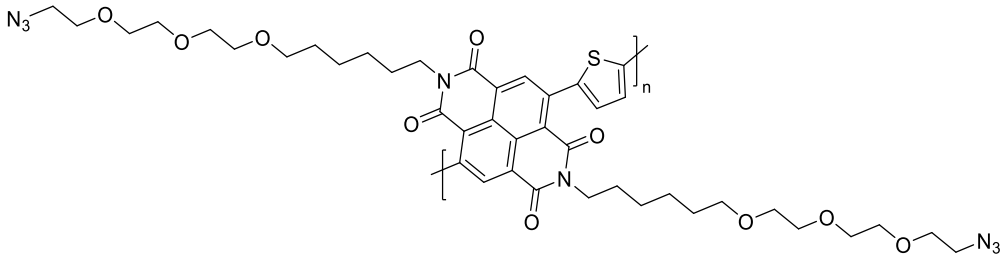
g₃Fc



g₃N₃ (4.50 mg, 0.0240 mmol, 1.0 equiv.), ethynylferrocene (50.02 mg, 0.238 mmol, 10 equiv.) and tetrakis(acetonitrile)copper(I) hexafluorophosphate (44.71 mg, 0.120 mmol, 5.0 equiv.) were sealed in a vial and purged with three vacuum/nitrogen cycles. To this, dry degassed chloroform (4 mL) was added, followed by 2,6-lutidine (0.28 mL, 2.40 mmol, 100 equiv.). The mixture was degassed for a further 2 minutes, then heated at 80 °C overnight. The solution was

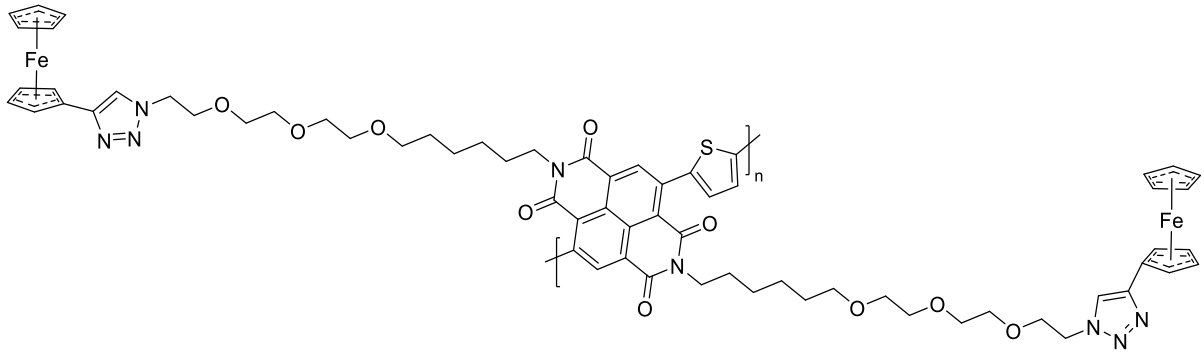
cooled to room temperature and diluted with chloroform (50 mL). The solution was passed through an aluminum oxide pad and the solvent was removed *in vacuo*. The crude product was purified using silica column chromatography employing ethyl acetate as the solvent system (R_f = 0.30). The final product was isolated as an orange oil (6.50 mg, 0.0160 mmol, 68% yield): ^{1}H NMR (400 MHz, $CDCl_3$) δ 7.61 (s, 1H), 4.84 (s, 2H), 4.65 – 4.31 (m, 4H), 4.14 (m, 5H), 3.88 (s, 2H), 3.74 – 3.46 (m, 8H), 3.37 (s, 3H); ^{13}C NMR (101 MHz, $CDCl_3$) δ 146.7, 120.5, 72.1, 70.8, 70.7, 69.9, 69.8, 68.9, 67.0, 60.5, 59.2, 50.4, 14.3. HRMS (ESI-ToF): 400.1312 [M+H$^+$] (calc. 400.1318).

P4-N$_3$-100%



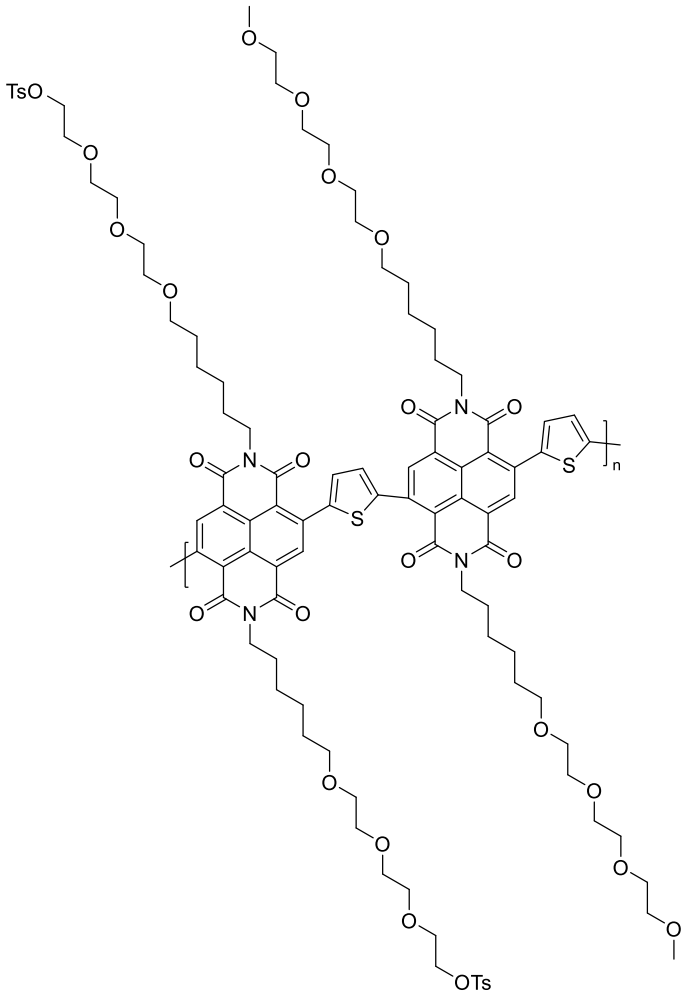
P4-OTs-100% (22.00 mg, 19.65 µmol, 1.0 equiv.) and sodium azide (5.11 mg, 78.60 µmol, 4.0 equiv.) were sealed in a microwave vial and dry degassed DMF (1 mL) was added. The reaction mixture was heated at 100 °C overnight, then cooled to room temperature, before precipitation into methanol. This was filtered and **P4-N$_3$** was collected as a dark blue solid (15.08 mg, 17.5 µmol, 89% yield): ^{1}H NMR (400 MHz, $CDCl_3$) δ 8.97 (br s, 2H), 7.47 (br s, 2H), 4.18 (br s, 4H), 3.66 (m, 16H), 3.57 (m, 4H), 3.46 (t, *J* = 6.5 Hz, 4H), 3.41 – 3.31 (m, 4H), 1.60 (d, *J* = 8.4 Hz, 8H), 1.44 (s, 8H).

P4-Fc-100%



P4-N_3-100% (10.00 mg, 11.61 µmol, 1.0 equiv.), ethynylferrocene (24.40 mg, 116.16 µmol, 10 equiv.) and tetrakis(acetonitrile)copper(I) hexafluorophosphate (21.60 mg, 57.95 µmol, 5.0 equiv.) were sealed in a vial and purged with three vacuum/nitrogen cycles. To this, dry degassed chloroform (2 mL) was added, followed by 2,6-lutidine (0.14 mL, 1.161 mmol, 100 equiv.). The mixture was degassed for a further 2 minutes, then heated at 80 °C overnight. The solution was cooled to room temperature and precipitated into methanol before filtration. **P4-Fc-100%** was collected as a dark blue solid (8.32 mg, 6.49 µmol, 54% yield): no NMR was obtained due to the insolubility of the material.

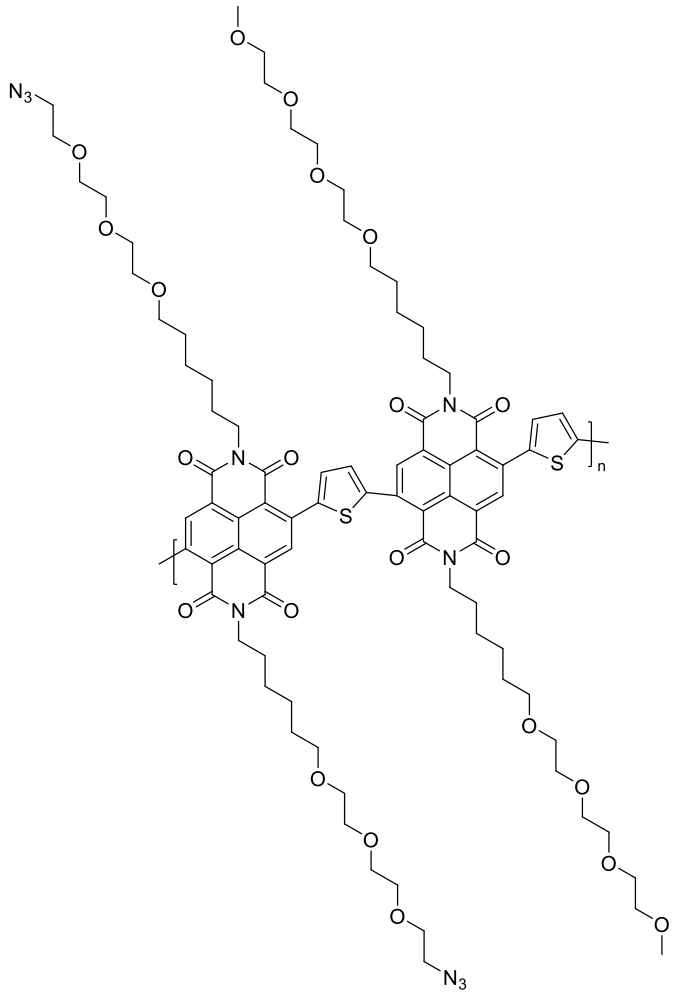
P4-OTs-50%



(((((((4,9-dibromo-1,3,6,8-tetraoxo-1,3,6,8-tetrahydrobenzo[lmn][3,8]phenanthroline-2,7-diyl)bis(hexane-6,1-diyl))bis(oxy))bis(ethane-2,1-diyl))bis(oxy))bis(ethane-2,1-diyl))bis(oxy))bis(ethane-2,1-diyl) bis(4-methylbenzenesulfonate) (19.53 mg, 0.016 mmol, 0.5 equiv.), **C_6g_3NDI-Br_2** (14.96 mg, 0.016 mmol, 0.5 equiv.), 2,5-bis(trimethylstannyl)thiophene (13.37 mg, 0.033 mmol, 1.0 equiv.), tris(dibenzylideneacetone)dipalladium(0) (0.60 mg, 0.655 µmol, 0.02 equiv.) and tris(*o*-methoxyphenyl)phosphine (0.92 mg, 2.61 µmol, 0.08 equiv.) were dissolved in anhydrous degassed chlorobenzene (1 mL). The resulting solution was degassed for an additional 10 minutes and the reaction was heated 130 °C overnight. The crude polymer solution was cooled to room temperature and precipitated into a 2:1 v/v mixture of ethyl acetate:hexane, and the polymer was purified via Soxhlet extractions with: hexane, ethyl

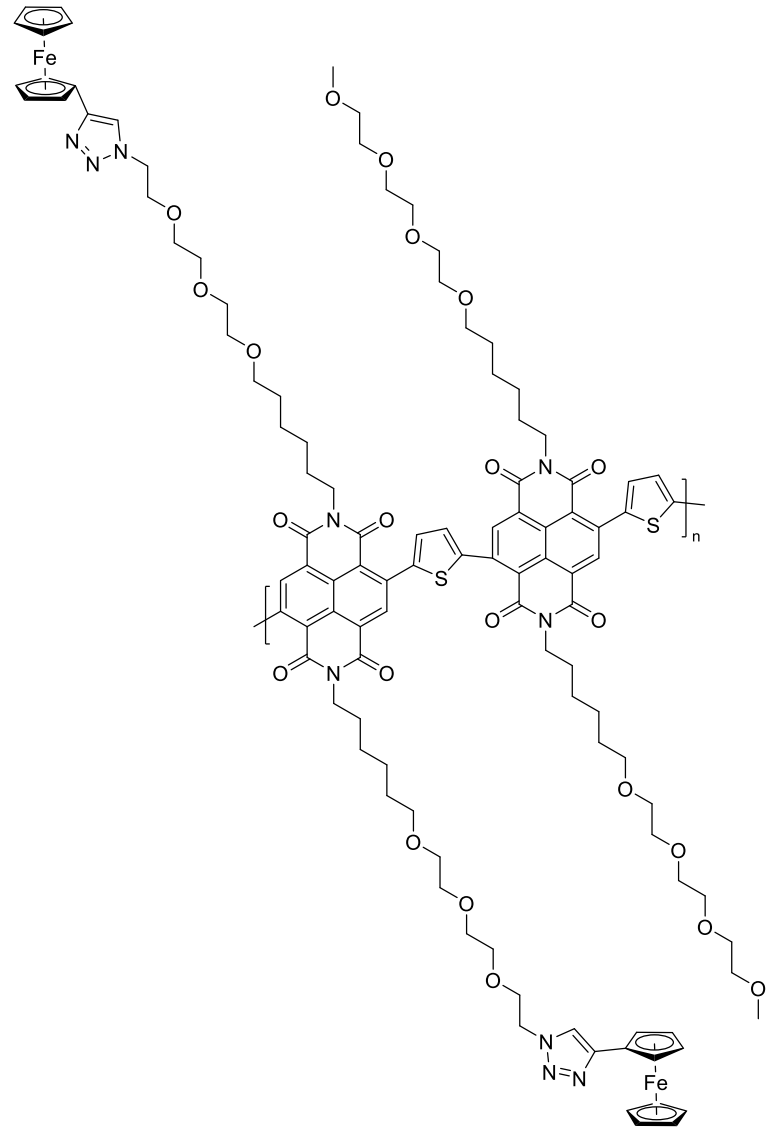
acetate, acetone and methanol. The polymer was extracted in chloroform and excess solvent was removed *in vacuo*. The final product was collected by reprecipitating the polymer into a 2:1 v/v mixture of ethyl acetate:hexane and collecting it by suction filtration. **P4-OTs-50%** was obtained as a dark blue solid (27.52 mg, 0.0140 mmol, 88% yield): ^{1}H NMR (400 MHz, $CDCl_3$) δ 8.97 (s, 2H), 7.75 (d, *J* = 8.0 Hz, 2H), 7.47 (s, 2H), 7.32 (d, *J* = 7.8 Hz, 2H), 4.16 – 4.10 (m, 4H), 3.68 – 3.60 (m, 4H), 3.59 – 3.50 (m, 16H), 3.44 (t, *J* = 6.7 Hz, 4H), 3.36 (s, 1.5H), 2.43 (s, 1.5H), 1.75 (s, 8H), 1.43 (s, 8H), 1.25 (s, 2H); GPC (chloroform, 40 °C): M_n = 23.8 kDa, M_w = 42.8 kDa.

P4-N$_3$-50%



P4-OTs-50% (20.00 mg, 10.21 µmol, 1.0 equiv.) and sodium azide (2.70 mg, 41.53 µmol, 4.0 equiv.) were sealed in a microwave vial and dry degassed DMF (1 mL) was added. The reaction mixture was heated at 100 °C overnight, then cooled to room temperature, before precipitation into methanol. This was filtered and **P4-N$_3$-50%** was collected as a dark blue solid (14.59 mg, 8.58 µmol, 84% yield): ^{1}H NMR (400 MHz, $CDCl_3$) δ 8.97 (br s, 2H), 7.47 (br s, 2H), 4.18 (s, 4H), 3.65 (m, 19H), 3.65 – 3.50 (m, 4H), 3.49 – 3.41 (m, 4H), 3.41 – 3.34 (m, 4H), 1.75 (s, 8H), 1.44 (s, 8H).

P4-Fc-50%



P4-N3-50% (12.40 mg, 14.59 µmol, 1.0 equiv.), ethynylferrocene (15.32 mg, 72.93 µmol, 5.0 equiv.) and tetrakis(acetonitrile)copper(I) hexafluorophosphate (13.59 mg, 36.46 µmol, 2.5 equiv.) were sealed in a vial and purged with three vacuum/nitrogen cycles. To this, dry degassed chloroform (2.2 mL) was added, followed by 2,6-lutidine (0.08 mL, 0.730 mmol, 50 equiv.). The mixture was degassed for a further 5 minutes, then heated at 80 °C overnight. The solution was cooled to room temperature and precipitated into methanol before filtration. **P4-Fc-50%** was collected as a dark blue solid (13.46 mg, 12.70 µmol, 87% yield): no NMR was obtained due to the insolubility of the material.

A6 References

1. Rivnay, J. *et al.* Organic electrochemical transistors. *Nat. Rev. Mater.* **3**, 17086 (2018).
2. Rivnay, J., Owens, R. M. & Malliaras, G. G. The Rise of Organic Bioelectronics. *Chem. Mater.* **26**, 679–685 (2014).
3. Pappa, A. M. *et al.* Direct metabolite detection with an n-type accumulation mode organic electrochemical transistor. *Sci. Adv.* **4**, eaat0911 (2018).
4. Khodagholy, D. *et al.* In vivo recordings of brain activity using organic transistors. *Nat. Commun.* **4**, 1575 (2013).
5. Khodagholy, D. *et al.* Organic electronics for high-resolution electrocorticography of the human brain. *Sci. Adv.* **2**, e1601027 (2016).
6. Spyropoulos, G. D., Gelinas, J. N. & Khodagholy, D. Internal ion-gated organic electrochemical transistor: A building block for integrated bioelectronics. *Sci. Adv.* **5**, eaau7378 (2019).
7. Pappa, A.-M. *et al.* Organic Transistor Arrays Integrated with Finger-Powered Microfluidics for Multianalyte Saliva Testing. *Adv. Healthc. Mater.* **5**, 2295–2302 (2016).
8. Ohayon, D. *et al.* Biofuel powered glucose detection in bodily fluids with an n-type conjugated polymer. *Nat. Mater.* **19**, 456–463 (2020).
9. Hai, W. *et al.* Human influenza virus detection using sialyllactose-functionalized organic electrochemical transistors. *Sensors Actuators B Chem.* **260**, 635–641 (2018).
10. He, R.-X. *et al.* Detection of bacteria with organic electrochemical transistors. *J. Mater. Chem.* **22**, 22072 (2012).
11. Wustoni, S. *et al.* Membrane-Free Detection of Metal Cations with an Organic Electrochemical Transistor. *Adv. Funct. Mater.* **29**, 1904403 (2019).
12. Bidinger, S. L. *et al.* Pulsed transistor operation enables miniaturization of electrochemical aptamer-based sensors. *Sci. Adv.* **8**, 4111 (2022).
13. Tan, S. T. M. *et al.* High-Gain Chemically Gated Organic Electrochemical Transistor. *Adv. Funct. Mater.* **31**, (2021).
14. Shim, N. Y. *et al.* All-Plastic Electrochemical Transistor for Glucose Sensing Using a Ferrocene Mediator. *Sensors* **9**, 9896–9902 (2009).
15. Tran, V. Van. Conjugated Polymers-Based Biosensors for Virus Detection: Lessons from COVID-19. *Biosensors* **12**, 748 (2022).
16. Nakatsuka, N. *et al.* Aptamer-field-effect transistors overcome Debye length limitations for small-molecule sensing. *Science* **362**, 319–324 (2018).
17. Cass, A. E. G. *et al.* Ferrocene-mediated enzyme electrode for amperometric determination of glucose. *Anal. Chem.* **56**, 667–671 (1984).
18. Tropp, J. *et al.* PEDOT-NHS as a Versatile Conjugated Polyelectrolyte for Bioelectronics. *Chem Rxiv* (2022).

19. Li, N. *et al.* A universal and facile approach for building multifunctional conjugated polymers for human-integrated electronics. *Matter* **4**, 3015–3029 (2021).

20. Giovannitti, A. *et al.* Controlling the mode of operation of organic transistors through side-chain engineering. *Proc. Natl. Acad. Sci. U. S. A.* **113**, 12017–12022 (2016).

21. Nielsen, C. B. *et al.* Molecular Design of Semiconducting Polymers for High-Performance Organic Electrochemical Transistors. *J. Am. Chem. Soc.* **138**, 10252–10259 (2016).

22. Moser, M. *et al.* Side Chain Redistribution as a Strategy to Boost Organic Electrochemical Transistor Performance and Stability. *Adv. Mater.* **32**, 1–6 (2020).

23. Moser, M. *et al.* Ethylene Glycol-Based Side Chain Length Engineering in Polythiophenes and its Impact on Organic Electrochemical Transistor Performance. *Chem. Mater.* **32**, 6618–6628 (2020).

24. Matuszak, N., Muccioli, G. G., Labar, G. & Lambert, D. M. Synthesis and in vitro evaluation of N-substituted maleimide derivatives as selective monoglyceride lipase inhibitors. *J. Med. Chem.* **52**, 7410–20 (2009).

25. Wang, G.-Z., Shang, R., Cheng, W.-M. & Fu, Y. Irradiation-Induced Heck Reaction of Unactivated Alkyl Halides at Room Temperature. *J. Am. Chem. Soc.* **139**, 18307–18312 (2017).

26. Yau, C. P. *et al.* Investigation of Radical and Cationic Cross-Linking in High-Efficiency, Low Band Gap Solar Cell Polymers. *Adv. Energy Mater.* **5**, 1401228 (2015).

27. Bunyaporn Todee *et al.* Synthesis and post-polymerization functionalization of a tosylated hyper-crosslinked polymer for fast and efficient removal of organic pollutants in water. *Mater. Chem. Front.* (2022) doi:10.1039/D2QM00633B.

28. Xu, Y., Xiong, X., Cai, L., Tang, Z. & Ye, Z. Thiol-ene click chemistry. *Prog. Chem.* **24**, 385–394 (2012).

29. Lowe, A. B. Thiol-ene 'click' reactions and recent applications in polymer and materials synthesis: A first update. *Polym. Chem.* **5**, 4820–4870 (2014).

30. Stolz, R. M. & Northrop, B. H. Experimental and Theoretical Studies of Selective Thiol−Ene and Thiol−Yne Click Reactions Involving N-Substituted Maleimides. *J. Org. Chem* **78**, 8105–8116 (2013).

31. Otsubo, T., Tanaka, T., Motoyanagi, J. & Minoda, M. An Alternating Glycopolymer Composed of Carbohydrate-carrying Maleimide and OH-functionalized Vinyl Ether— A New Synthetic Strategy for Glycosaminoglycan Mimics —. *https://doi.org/10.1246/cl.181015* **48**, 465–467 (2019).

32. Gevrek, T. N., Bilgic, T., Klok, H. A. & Sanyal, A. Maleimide-functionalized thiol reactive copolymer brushes: Fabrication and post-polymerization modification. *Macromolecules* **47**, 7842–7851 (2014).

33. Shanzer, A. & Libman, J. Total synthesis of enterobactin via an organotin template. *J. Chem. Soc. Chem. Commun.* 846–847 (1983) doi:10.1039/C39830000846.

34. Österholm, A. M., Ponder, J. F., De Keersmaecker, M., Shen, D. E. & Reynolds, J. R. Disentangling Redox Properties and Capacitance in Solution-Processed Conjugated

Polymers. *Chem. Mater.* **31**, 2971–2982 (2019).

35. Heinze, J., Frontana-Uribe, B. A. & Ludwigs, S. Electrochemistry of Conducting Polymers—Persistent Models and New Concepts. *Chem. Rev.* **110**, 4724–4771 (2010).

36. Rivnay, J. *et al.* Organic electrochemical transistors for cell-based impedance sensing. *Appl. Phys. Lett.* **106**, 043301 (2015).

37. Giovannitti, A. *et al.* The Role of the Side Chain on the Performance of N-type Conjugated Polymers in Aqueous Electrolytes. *Chem. Mater.* **30**, 2945–2953 (2018).

38. Maria, I. P. *et al.* The Effect of Alkyl Spacers on the Mixed Ionic-Electronic Conduction Properties of N-Type Polymers. *Adv. Funct. Mater.* **31**, 2008718 (2021).

39. Fenoy, G. E. *et al.* "Clickable" Organic Electrochemical Transistors. *JACS Au* (2022) doi:10.1021/jacsau.2c00515.

40. Ohayon, D. *et al.* Influence of Side Chains on the n-Type Organic Electrochemical Transistor Performance. *ACS Appl. Mater. Interfaces* **13**, 4253–4266 (2021).

41. Giovannitti, A. *et al.* N-type organic electrochemical transistors with stability in water. *Nat. Commun.* **7**, 13066 (2016).

42. Ives, J. T. & Reichert, W. M. Polymer thin film integrated optics: Fabrication and characterization of polystyrene waveguides. *J. Appl. Polym. Sci.* **36**, 429–443 (1988).

43. De La Fuente Durán, A. *et al.* Origins of hydrogen peroxide selectivity during oxygen reduction on organic mixed ionic-electronic conducting polymers. doi:10.26434/chemrxiv-2022-r3pkd.

44. Brisset, H., Navarro, A.-E., Moustrou, C., Perepichka, I. F. & Roncali, J. Electrogenerated conjugated polymers incorporating a ferrocene-derivatized-(3,4-ethylenedioxythiophene). *Electrochem. commun.* **6**, 249–253 (2004).